Galaxy Clusters in the Ultra-Low Radio-Frequency Era

A LOFAR LBA view
From Radio Galaxies to Diffuse Emission

Dissertation

zur Erlangung des Doktorgrades
an der Fakultät für Mathematik, Informatik und Naturwissenschaften
Fachereich Physik
der Universität Hamburg

vorgelegt von

Giulia Lusetti

Hamburg
2025

Gutachter der Dissertation:	Prof. Dr. Marcus Brüggen Prof. Dr. Francesco de Gasperin
Zusammensetzung der Prüfungskommission:	Prof. Dr. Marcus Brüggen Prof. Dr. Francesco de Gasperin Prof. Dr. Jochen Liske Prof. Dr. Jan-Torge Schindler Prof. Dr. Luisa Lucie-Smith
Vorsitzender der Prüfungskommission:	Prof. Dr. Jochen Liske
Datum der Disputation:	16.05.2025
Vorsitzender des Fach-Promotionsausschusses PHYSIK:	Prof. Dr. Wolfgang J. Parak
Leiter des Fachbereichs PHYSIK:	Prof. Dr. Markus Drescher
Dekan der Fakultät MIN:	Prof. Dr.-Ing. Norbert Ritter

Declaration on oath

I hereby declare and affirm that this doctoral dissertation is my own work and that I have not used any aids and sources other than those indicated.
If electronic resources based on generative artificial intelligence (gAI) were used in the course of writing this dissertation, I confirm that my own work was the main and value-adding contribution and that complete documentation of all resources used is available in accordance with good scientific practice. I am responsible for any erroneous or distorted content, incorrect references, violations of data protection and copyright law or plagiarism that may have been generated by the gAI.

Hamburg, den 11.04.2025

Giulia Lusetti

To my younger self,
who dreamed of doing research
and travel the world.
You made it.

Zusammenfassung

Galaxienhaufen entstehen an den Knotenpunkten kosmischer Filamente durch den gravitativen Kollaps anfänglicher Dichtefluktuationen im frühen Universum sowie durch die anschließende Akkretion von Gas und Substrukturen. Während dieses Prozesses wird eine große Menge Energie in Form von Schockwellen und Turbulenzen freigesetzt, die wiederum das Magnetfeld komprimieren und verstärken sowie Elementarteilchen auf relativistische Energien beschleunigen können. Aufgrund des $\sim \mu$G starken Magnetfeldes im Haufenplasma emittieren diese relativistischen Teilchen Synchrotronstrahlung im Radiobereich, die typischerweise als diffuse Quellen von Mpc-Ausmaß beobachtet wird – in Form von Radiohalos und -relikten. Radiorelikte sind länglich Quellen, die sich meist in den Außenbereichen der Haufen befinden und Schockwellen aufzeigen, die durch Haufenverschmelzungen ausgelöst wurden. Radiohalos hingegen sind zentral im Haufen gelegene Quellen, deren Ursprung auf durch die von Haufenverschmelzung erzeugte Turbulenzen zurückgeführt wird, welche eine Wiederbeschleunigung von Elektronen bewirken. Beobachtungen bei ultra-niedrigen Frequenzen ($\lesssim$ 100 MHz) sind entscheidend, um die Energieverteilung der Elektronen auf Hinweise zum zeitlichen Ablauf der Beschleunigungs- und Alterungsprozesse der strahlenden Teilchen zu prüfen. Bislang wurden nur wenige Galaxienhaufen in diesem Frequenzbereich untersucht, weshalb jedes neue Objekt einen wertvollen Beitrag zum Verständnis der nicht-thermischen Physik bei ultra-niedrigen Frequenzen liefert.

Eine weitere charakteristische Komponente von Haufen im Radiobereich sind Radiogalaxien. In Haufen zeigen die Materiestrahlen aktiver galaktischer Kerne (AGN) aufgrund ihrer Wechselwirkung mit dem sie umgebenden intracluster Medium (ICM) häufig eine besondere Morphologie. Durch diese Wechselwirkung spielen sie eine wichtige Rolle in der thermischen und dynamischen Entwicklung der Haufen und dienen gleichzeitig als Quelle relativistischer Teilchen im ICM. Diese leicht-relativistischen Teilchen können später durch großskalige Prozesse im Haufen wiederbeschleunigt werden und zur Bildung der oben genannten diffusen Radioquellen beitragen. Aufgrund ihrer charakteristisch steilen Spektren werden sowohl diffuse Haufenemissionen als auch AGN-Plasma bevorzugt bei niedrigen Radiofrequenzen ($\lesssim$ 300 MHz) untersucht, bei denen sie intrinsisch heller erscheinen. Allerdings sind interferometrische Radiobeobachtungen in diesem Bereich mit erheblichen technischen Herausforderungen verbunden, insbesondere durch die starke Beeinflussung durch ionosphärische Störungen, die richtungsabhängige systematische Fehler im Sichtfeld verursachen.

Mit der Einführung des LOw-Frequency ARray (LOFAR), insbesondere seines Low Band Antennas (LBA)-Systems, wurde ein neues Beobachtungsfenster eröffnet, das hochauflösende und empfindliche Aufnahmen in diesem Frequenzbereich ermöglicht. Der Zugang zu diesem ultra-niedrigen Frequenzbereich ist entscheidend, um Emission mit ultra-steilen Spektrum nachzuverfolgen, Alterungs- und Wiederbeschleunigungsprozesse kosmischer Elektronen zu untersuchen und fossiles Plasma aus früheren AGN-Aktivitätsphasen zu erfassen. In dieser Dissertation nutze ich die Möglichkeiten von LOFAR LBA, um eine Auswahl an Objekten zu untersuchen, die aufgrund ihrer besonderen Eigenschaften wichtige Einblicke in die nicht-thermische Physik von Galaxienhaufen liefern.

Im ersten Projekt dieser Arbeit habe ich die dynamische Wechselwirkung zwischen Radiogalaxien und dem umgebenden Medium im Galaxienhaufen ZwCl0634.1+4747 untersucht. Ich kombinierte Daten von vier Teleskopen, die Frequenzen zwischen 53 MHz und 1,5 GHz abdecken, für drei sogenannte Head-Tail-Radiogalaxien in diesem Haufen. Diese stellen vermutlich eine wichtige Quelle leicht relativistischer Elektronen im ICM dar und sind somit ein zentraler Bestandteil der (Wieder-)Beschleunigungsprozesse, die für die diffuse, großskalige Radioemission in Haufen verantwortlich sind. Für diese Untersuchung war die kombinierte Nutzung von LOFAR LBA- und HBA-Beobachtungen entscheidend, um das gesamte Ausmaß der Radiogalaxienschweife bis zu einer Entfernung von ~1 Mpc zu erfassen – darunter die längsten bekannten Head-Tail-Radiogalaxien – und um die spektralen Eigenschaften der AGN-Schweife zu charakterisieren. Ich stellte deutliche Abweichungen von reinen Alterungsmodellen fest, die auf Synchrotron- und inverse-Compton-Verlusten basieren. Abschließend untersuchte ich verschiedene physikalische Prozesse, die für dieses Verhalten verantwortlich sein könnten, und zeigte, dass durch Turbulenzen im Schweif verursachte Wiederbeschleunigung – ausgelöst durch die Wechselwirkung mit dem ICM – eine plausible Erklärung darstellt.

Im zweiten und dritten Projekt konzentrierte ich mich auf die Teilchenbeschleunigung in haufenverschmelzenden Galaxienhaufen durch die Untersuchung von Radiorelikten und Halos.

Das zweite Projekt befasst sich mit CIZA J2242.8+5301, einem wohlbekannten verschmelzenden Galaxienhaufen, der ein prototypisches Beispiel für ein Radiorelikt enthält. Für dieses Objekt führte ich die erste vollständige Reduktion und Kalibration von LOFAR LBA-Daten bei 45 MHz durch, wobei ich ein durch thermisches Rauschen begrenztes Bild mit $\sigma_{\rm rms} \sim 1.5$ mJy/beam erzielte. Durch die Kombination dieser Beobachtungen mit umfangreichen Multifrequenzdaten bis 3 GHz konnte ich integrierte und räumlich aufgelöste Spektralindizes sowie Karten der spektralen Krümmung erzeugen. Darüber hinaus ermöglichten die niederfrequenten Daten – die naturgemäß weniger von Strahlungsverlusten betroffen sind – eine direkte Abschätzung des Injektionsspektrums und damit der Mach-Zahlen der Schockfronten: $\mathcal{M}_N = 2.9 \pm 0.5$ und $\mathcal{M}_S = 2.9 \pm 0.8$ für das nördliche bzw. südliche Relikt. Schließlich untersuchte ich die Oberflächenhelligkeitverteilung des nördlichen Relikts – jener gut definierten Radiostruktur, die dem Haufen den Spitznamen „Sausage Cluster“ eingebracht hat. Ich stellte fest, dass der östliche Teil des nördlichen Relikts entgegen den Erwartungen ein bemerkenswert symmetrisches Profil zeigt, mit „Flügeln“ zu beiden Seiten des Maximums. Dies steht im Widerspruch zum Standardszenario, das von einer einzigen, scharfen Schockfront mit nachgelagerten Strahlungsverlusten ausgeht. Zur Erklärung modellierte ich das Oberflächenhelligkeitsprofil unter Berücksichtigung von Projektionseffekten, Magnetfeldvariationen und Schockdeformation, um eine realistischere Beschreibung der beobachteten Emission zu liefern.

Das dritte Projekt konzentriert sich auf das komplexe dreifachverschmelzende System Abell 746, in dem ich mehrere reliktartige Strukturen sowie das zentrale Radiohalo mithilfe von LOFAR LBA, HBA und ergänzenden höherfrequenten Daten analysierte. Ich bestätigte das Vorhandensein eines klassischen bogenförmigen Relikts im Nordwesten mit typischer spektraler Steilung (von $\alpha_{144}^{53} \sim -0.5$ am Haufenrand bis $\alpha_{144}^{53} \sim -2.5$ zum Haufenzentrum hin), was mit einer Alterung hinter einer Stoßfront mit $\mathcal{M}_{\mathrm{NW}} = 2.8 \pm 0.3$ übereinstimmt. Ähnlich niedrige Mach-Zahlen wurden für die anderen reliktartigen Strukturen (R1, R2, R3) abgeleitet, was auf eine ineffiziente Teilchenbeschleunigung hinweist und die Rolle fossilen Plasmas als Saatpopulation für die Wiederbeschleunigung unterstreicht. Schließlich zeigte sich, dass das zentrale Gebiet ein $\sim 1\,\mathrm{Mpc}$ großes Radiohalo mit einem ultra-steilen Spektrum ($\alpha_{144}^{53} \sim -1.6$) beherbergt, das durch Anpassung des Oberflächenhelligkeitsprofils charakterisiert wurde. Eine vollständige Abtrennung von diffuser, kontaminierender Emission war jedoch nicht möglich. Dieses Ergebnis stimmt mit Vorhersagen aus dem Szenario der turbulenten Wiederbeschleunigung überein, welches ultra-steile Halos bevorzugt in massearmen Haufen wie A746 erwartet.

Die Ergebnisse dieser Arbeiten belegen, dass die Kombination aus niedrig- und ultra- niedrigfrequenten Beobachtungen entscheidend ist, um die Population steilspektraler Radioquellen in Galaxienhaufen zu identifizieren und zu charakterisieren. Die in dieser Arbeit genutzte Synergie zwischen LOFAR HBA ($\sim$ 150 MHz) und LBA ($\sim$ 50 MHz) ermöglichte eine detaillierte Untersuchung der Spektralverteilung dieser Quellen und lieferte wertvolle Einblicke in Teilchenalterungs und -wiederbeschleunigungsprozesse, die bei höheren Frequenzen ($\sim$ GHz) verborgen geblieben wären.

Abstract

Galaxy clusters form at the intersection of cosmic filaments, via the gravitational collapse of initial density fluctuations in the early Universe and subsequent accretion of gas and substructures. During this process, large amounts of energy are released in the form of shocks and turbulence, which in turn can compress and amplify the magnetic field and accelerate particles to relativistic energies. Due to the presence of the $\sim \mu$G cluster magnetic field, these relativistic particles give rise to synchrotron radio emission, usually observed as Mpc-scale diffuse sources, in the form of radio halos and relics. Radio relics are elongated sources, usually found in the clusters' outskirts tracing cluster-merger-driven shock waves. Halos are centrally located sources, thought to originate from turbulence re-acceleration mechanisms that develop during cluster mergers. Observations at ultra-low frequencies ($\lesssim$ 100 MHz) are essential to constrain the shape of the electron energy distribution and detect spectral features that reflect the acceleration and ageing history of the emitting particles. To date, only a handful of galaxy clusters have been studied in this frequency range, making every new object a valuable contribution to the low-frequency view of non-thermal physics.

Another characteristic radio component of clusters are radio galaxies. In clusters, these jets and lobes of active galactic nuclei (AGN) oftentimes show a peculiar morphology due to the interaction with the surrounding intra-cluster medium (ICM). Via this interaction, they play an important role in the thermal and dynamical evolution of clusters, while also seeding relativistic particles into the ICM. This mildly relativistic particles can later be re-accelerated by cluster-scale processes, contributing to the formation of the above-mentioned diffuse sources. Due to their characteristic steep spectra, both diffuse cluster emission and AGN plasma are best studied at low radio frequencies ($\lesssim$ 300 MHz), where they are intrinsically brighter.

However, interferometric radio observations in this regime come with significant technical challenges. Above all, the strong influence of ionospheric disturbances which introduces direction-dependent systematic errors across the field of view. The advent of the LOw-Frequency ARray (LOFAR), and in particular its Low Band Antennas (LBA) system, has opened a new observational window, enabling high-sensitivity and high-resolution imaging in this frequency range. Accessing this ultra-low-frequency regime is essential for tracing ultra-steep-spectrum emission, studying the ageing and re-acceleration cosmic ray electrons, and tracing fossil plasma from past AGN activity. Throughout this thesis, I exploit the capabilities of LOFAR LBA to study a selection of objects that, due to their unique characteristics, provide important insights into non-thermal cluster physics.

In the first project of this thesis, I investigated the dynamical interaction between radio galaxies and the surrounding medium in the galaxy cluster ZwCl0634.1+4747. I combined data of four telescopes covering frequencies between 53 MHz and 1.5 GHz of three head-tail radio galaxies hosted by this cluster, which are likely important sources of seed populations of mildly relativistic electrons in the intra-cluster medium and thus key ingredients for the (re-)acceleration

processes responsible for diffuse, large-scale radio emission in clusters. For this work, the combined use of LOFAR LBA and HBA observations was crucial to detect the full extent of the radio galaxy tails up to a distance of ~ 1 Mpc, among the longest head-tailed radio galaxies known, and to characterize the spectral properties of the AGN-tails. I identified clear departures from a pure ageing models involving synchrotron and inverse-Compton losses. Lastly, I explored different possible physical processes responsible for this behavior, and showed that re-acceleration driven by turbulence into the tail via interaction with the ICM provides a viable explanation.

In the second and third projects, I focused on particle acceleration in merging galaxy clusters by studying radio relics and halos.

The second project is about CIZA J2242.8+5301, a well-known major merging galaxy cluster which hosts a prototypical example for a radio relic. For this object, I carried out the first full reduction and calibration of LOFAR LBA data at 45 MHz, where I achieved a thermal noise limited image with $\sigma_{\rm rms} \sim 1.5\,$mJy/beam. By combining these observations with extensive multi-frequency data up to 3 GHz, I derived integrated and spatially resolved spectral indices, as well as spectral curvature maps. Moreover, the low-frequency data, naturally less affected by radiative losses, allowed a direct estimate of the injection spectrum, and thus the shock Mach numbers, yielding $\mathcal{M}_N = 2.9 \pm 0.5$ and $\mathcal{M}_S = 2.9 \pm 0.8$ for the northern and southern relics, respectively. Finally, I focused on the surface brightness morphology of the northern relic, the well-defined radio structure that made this cluster commonly known as the "Sausage" cluster. I found that, contrary to expectations, the eastern part of the northern relic shows a remarkably symmetric profile, with wings extending on either side of the peak. This is inconsistent with the standard scenario of particle acceleration at a single, sharp shock and the subsequent downstream radiative losses of accelerated electrons. To explain this, I modeled the surface brightness profile, including projection effects, magnetic field variation and shock deformation to provide more realistic description of the observed emission.

The third project focuses on the complex triple-merger system Abell 746, where I analysed multiple relic-like structures and the central radio halo using LOFAR LBA, HBA, and complementary higher-frequency data. I confirmed the presence of a classical arc-shaped relic in the northwest, with standard spectral steepening (from $\alpha_{144}^{53} \sim -0.5$ at the outer edge to $\alpha_{144}^{53} \sim -2.5$ toward the cluster centre) consistent with ageing behind a shock front with $\mathcal{M}_{\rm NW} = 2.8 \pm 0.3$. Similarly low Mach numbers are derived for the other relic-like structures (R1, R2, R3), pointing to inefficient particle acceleration and suggesting the contribution of fossil plasma as a seed population for reacceleration. Finally, I found that the central region hosts a ~ 1 Mpc ultra-steep spectrum radio halo $\alpha_{144}^{53} \sim -1.6$, characterized through surface brightness profile fitting, which also enabled to isolate it from surrounding diffuse contaminating emission. This result is consistent with predictions from the turbulent re-acceleration scenario, which expects ultra-steep halos to preferentially reside in low-mass clusters, such as A746.

The results from these works prove that the combination of low- and ultra-low frequency observations is essential to detect and characterize the population of steep-spectrum radio sources in galaxy clusters. Thanks to the synergy between LOFAR HBA (~ 150 MHz) and LBA (~ 50 MHz) used in this work, I was able to study the spectral shape of these sources, providing insights into particle ageing and re-acceleration processes, that would otherwise remain unseen at higher (~ GHz) frequencies.

List of publications

This thesis is based on (but does not include all of) the following publications:

First author publications:

- **Lusetti, G.**, F. de Gasperin, V. Cuciti, M. Brüggen, C. Spinelli, H. Edler, G. Brunetti, R. J. van Weeren, A. Botteon, G. Di Gennaro, R. Cassano, C. Tasse, and T. W. Shimwell. *Re-energisation of AGN head-tail radio galaxies in the galaxy cluster ZwCl0634.1+47474*, MNRAS 528, 141–159 (2024)
- **G. Lusetti**, M. Brüggen, H. W. Edler, F. de Gasperin, M. Hoeft, G. Di Gennaro, D. Hoang, T. Pasini, R. van Weeren, V. Cuciti, H. Rottgering, and G. Brunetti. *The view of the CIZA J2242.8+5301 galaxy cluster at very-low radio frequencies*, accepted by A&A
- **G. Lusetti**, T. Beeth, F. de Gasperin, M. Brüggen, H. W. Edler, G. Di Gennaro, W. Lee, K. HyeongHan and K. Rajpurohit. *The Complex Cluster Merger System Abell 746: insights from very-low frequencies LOFAR LBA observations*, to be submitted to A&A

Publications with major contributions (the content is not included in this thesis):

- Riseley, C. J., Biava, N., **Lusetti, G.**, Bonafede, A., Bonnassieux, E., Botteon, A., Loi, F., Brunetti, G., Cassano, R., Osinga, E., Rajpurohit, K. , Röttgering, H. J. A., Shimwell, T., Timmerman, R., van Weeren, R. J. *A MeerKAT-meets-LOFAR study of Abell 1413: a moderately disturbed non-cool-core cluster hosting a 500 kpc 'mini'-halo*, MNRAS - 6052-6070 (2023)

Co-author publications (the content is not included in this thesis):

- Bruno, L., Botteon, A., Shimwell, T., Cuciti, V., de Gasperin, F., Brunetti, G., Dallacasa, D., Gastaldello, F., Rossetti, M., van Weeren, R. J., Venturi, T., Russo, S. A., Taffoni, G., Cassano, R., Biava, N., **Lusetti, G.**, Bonafede, A., Ghizzardi, S., De Grandi, S. *A three-component giant radio halo: The puzzling case of the galaxy cluster Abell 2142*, A&A Vol. 678 d.A133, p.24 (2023)
- Bonafede, A., Gitti, M., La Bella, N., Biava, N., Ubertosi, F., Brunetti, G., **Lusetti, G.**, Brienza, M., Riseley, C. J., Stuardi, C., Botteon, A., Ignesti, A., Röttgering, H., van Weeren, R. J *Shock imprints on the radio mini halo in RBS 797*, A&A Vol. 680, id.A5, p.13 (2023)
- Rajpurohit, K., Lovisari, L., Botteon, A., Jones, C., Forman, W., O'Sullivan, E., van Weeren, R. J., HyeongHan, K., Bonafede, A., Jee, M. J., Vazza, F., Brunetti, G. ; Cho, H., Domínguez-Fernández, P., Stroe, A., Finner, K., Brüggen, M., Vrtilek, J. M., David, L. P., Schellenberger, G., Wittman, D., **Lusetti, G.**, Kraft, R., De Gasperin, F. *Abell 746: A Highly Disturbed Cluster Undergoing Multiple Mergers*, AJ Vol. 998 id.13 p.17

Contents

1 Introduction

Over the past century, astronomy evolved from an optical-dominated into a multi-wavelength science, significantly expanding our understanding of astrophysical processes. In this context, a relevant role has been played by radio astronomy, which, since the serendipitous discovery of radio emission from the Milky Way by Karl Jansky in 1933 (Jansky, 1933), has made a continuous stream of fundamental contributions to astrophysics. Proof of its impact is reflected in the Nobel Prize-winning discoveries, such as the detection of the cosmic microwave background (Penzias & Wilson, 1965; Mather et al., 1994) and the discovery of pulsars (Hewish et al., 1968). Particularly relevant for the work presented in this dissertation, is the discovery of an extended radio source with no optical counterpart in the Coma cluster (Large et al., 1959), which marked the beginning of the study of the origin and nature of extended synchrotron sources in galaxy clusters. As highlighted later in this thesis, galaxy clusters are complex astrophysical laboratories, that offer a unique opportunity to study cosmic ray acceleration and large-scale magnetic fields in extreme environments.

The Coma diffuse emission discovery, as many in the early years of radio astronomy, was performed with a single antenna and a beam of 45 arcminutes[1]. Since its birth, observing at long radio wavelengths has always posed a major challenge: radio antennas require enormous dishes to achieve meaningful angular resolution[2]. The breakthrough came in the 1950s with the development of aperture synthesis and interferometry, pioneered by Martin Ryle and his colleagues at the University of Cambridge (Ryle & Hewish, 1960). Thanks to the combination of signals from multiple antennas, this technique revolutionized radio astronomy, allowing radio observations to achieve arcsecond resolution, comparable to optical instruments. Interferometry became the backbone/foundation of modern radio astronomy and is today the standard way of producing high-resolution radio images. Another challenge of radio telescopes — particularly for interferometric arrays — is the need for extensive calibration to correct for instrumental effects, radio frequency interference (RFI) and ionospheric disturbances, the latter becoming increasingly severe at lower frequencies. Between 1970 and 2000, radio astronomy was dominated by high-frequency aperture synthesis arrays, such as the Very Large Array (VLA), Westerbork Synthesis Radio Telescope (WSRT), MERLIN, Australia Telescope Compact Array (ATCA), and the Giant Metrewave Radio Telescope (GMRT). These facilities primarily operated above a few hundred MHz, where ionospheric distortions are less severe, and achieving high angular resolution observations.

[1] In radio astronomy, the main lobe of the antenna beam pattern is equivalent to the point spread function in optical systems and defines the angular resolution used to observe the sky.

[2] The resolution of a single dish radio telescope is $\propto \lambda/\mathrm{D}$, where D is the telescope diameter and λ the observing frequency. For an interferometer, this becomes $\propto \lambda/\mathrm{B}_{\mathrm{max}}$, with B_{max} the maximum baseline, i.e. maximum distance between a couple of antennas.

In the last two decades, interest in low-frequency radio astronomy ($\lesssim$ 300 MHz) has significantly increased, driven by both scientific and technological advancements. A simple reason is that the vast majority of radio sources have steep spectra and thus they become bright, i.e. more easily detectable, at lower frequencies. Additionally, the discovery of low-surface-brigthness and ultra-steep spectrum radio sources reinforced the need for sensitive low-frequency instruments. Moreover, many astrophysical sources exhibit inverted radio spectra due to synchrotron self-absorption or free-free absorption, requiring observations in the tens to hundreds of MHz range for a complete characterization.

This dissertation focuses on the study of non-thermal phenomena in galaxy clusters observed at low radio frequencies, with a particular emphasis on the ultra-low ($\lesssim$ 100 MHz) regime. This spectral window remains relatively unexplored, yet it offers unique insights into the oldest, faintest, and lowest-energy synchrotron-emitting particles in the ICM. These observations offer important insights into particle (re-)acceleration mechanisms and the life cycle of cosmic rays in dense cluster environments. Moreover, they revealed to be crucial to detect low-surface-brightness and/or ultra-steep spectrum sources that would remain largely undetectable at conventional GHz frequencies. Only recently, with the advent of LOFAR LBA and its now-mature data processing pipeline, it has become possible to produce high-fidelity images at these ultra-low radio frequencies, enabling precise studies of low-energy and steep spectrum phenomena. The work presented in this thesis also demonstrates how the LOFAR LBA capabilities are applied to the study of galaxy clusters physics $\lesssim$ 100 MHz.

1.1 Galaxy Clusters - a general overview

In the current paradigm of large-scale structure formation, galaxy clusters form via a hierarchical process of mergers and accretion of smaller structures, driven by the gravitational collapse of dark matter overdensities (e.g., Kravtsov & Borgani, 2012, for a review). For this reason, clusters reside at the intersections of cosmic filaments, where matter flows along these large-scale structures, continuously feeding their growth. This network of filaments, sheets, nodes and voids is known as the Cosmic Web (e.g., Bond et al., 1996; Springel et al., 2006) and traces the underlying distribution of dark matter. In a macroscopic sense, galaxy clusters can be seen as fundamental markers, outlining the Universe's large-scale structure and acting as powerful cosmological probes (see e.g., Allen et al., 2011, for a review). Their abundance, spatial distribution, and scaling relations with observable properties encode information about the underlying cosmological model and, thus can probe the growth of structure over cosmic time. On the other hand, on the cluster scale, they act as unique astrophysical laboratories (see e.g., Voit, 2005, review for an extensive description of the processes involved), that can be used to study the interplay between gravitational collapse and baryonic processes, including the thermodynamics of the Intra-Cluster Medium, the role of Active Galactic Nuclei in regulating gas cooling and heating, and the microphysics of high-energy plasmas.

Clusters typically include 100-1000 galaxies, bound together by the cluster self-gravity (see **Fig. 1.1**, *top left panel*). They have a size ranging from a few to several Mpc and typical masses of 10^{14-15} $M_{\odot}$. Despite their name, galaxies constitute only a small fraction (~ 5%) of a cluster's total mass. The dominant component is the dark matter, comprising ~ 80% of the total mass. The remaining ~ 15% of the mass consists of a diffuse, hot plasma known as the Intra-Cluster Medium (ICM, **Section 1.2**). Co-spatial with the ICM, an increasing number of galaxy clusters is also observed to host diffuse non-thermal synchrotron emission, with no obvious connection to the individual cluster members (**Section 1.3**).

In this thesis, galaxy clusters are investigated as astrophysical laboratories. In particular, we will explore the non-thermal phenomena associated with relativistic particles and magnetic fields in the ICM. Special attention will be given to the study of radio emission connected to radio galaxies (**Section 1.4**) and diffuse synchrotron sources, such as radio halos (**Section 1.3.1**) and relics (**Section 1.3.2**), which trace the complex interplay between cluster dynamics and particle acceleration mechanisms. The following sections provide an overview of the ICM, diffuse synchrotron sources and radio galaxies, as they have a central role in this thesis.

1.2 The Intra-Cluster Medium

1.2.1 Thermal Emission

Galaxy clusters are luminous X-ray sources, with typical luminosity values in the range from few 10^{43} to 10^{46} erg s^{-1}. This emission originates mainly from Intra-Cluster medium (ICM), the dominant baryonic component of galaxy clusters. It consists of fully ionized hydrogen and helium plus traces of highly ionized heavier elements with a temperature T ~ $10^7 - 10^8$ K ($1 - 10$ keV) and particle number densities steeply declining from $n_e \sim 10^{-2} - 10^{-3}$ cm^{-3} near the centre to 10^{-4}cm^{-3} in the outskirts. The high temperatures are the result of gravitational heating processes taking place during cluster formation, as the gas falls into the deep potential dark matter wells and is shock-heated to the virial temperature of the cluster halo (e.g., Voit, 2005). At clusters typical temperatures (i.e., kT $\gtrsim$ 2.5 keV), the ICM X-ray emission is dominated by thermal bremsstrahlung (free-free emission), resulting from the interaction between free elections and ions, whose emissivity scales as $\epsilon \propto n_e^2 T^{-1/2} e^{-h\nu/k_B T}$, with n_e and T the electron number density and gas temperature, respectively (e.g., Forman & Jones, 1982; Sarazin, 1988). Additional contributions come from recombination (free-bound) radiation and line emission (bound-bound) processes. While line emission becomes more prominent in cooler plasma, the iron K-shell line complex at ~7 keV remains an important feature. An example of cluster ICM emission is shown in **Fig. 1.1** *(top right panel)*.

Over the past 20 years, a dichotomy between cool-core (CC) and non-cool-core (NCC) has been established. CC clusters (nomenclature proposed originally in Molendi & Pizzolato, 2001) exhibit a central surface brightness enhancement, together with an increase in metallicity and a decrease of temperature. In contrast, NCC clusters display flatter surface brightness profiles in their cores and do not exhibit the typical central temperature drop and metallicity peak. Several statistical studies have highlighted these differences concerning their thermodynamic properties, for example Cavagnolo et al. 2009; Arnaud et al. 2010; Lovisari & Reiprich 2019; Ghirardini et al. 2019. These observational differences are thought to reflect the dynamical status of the

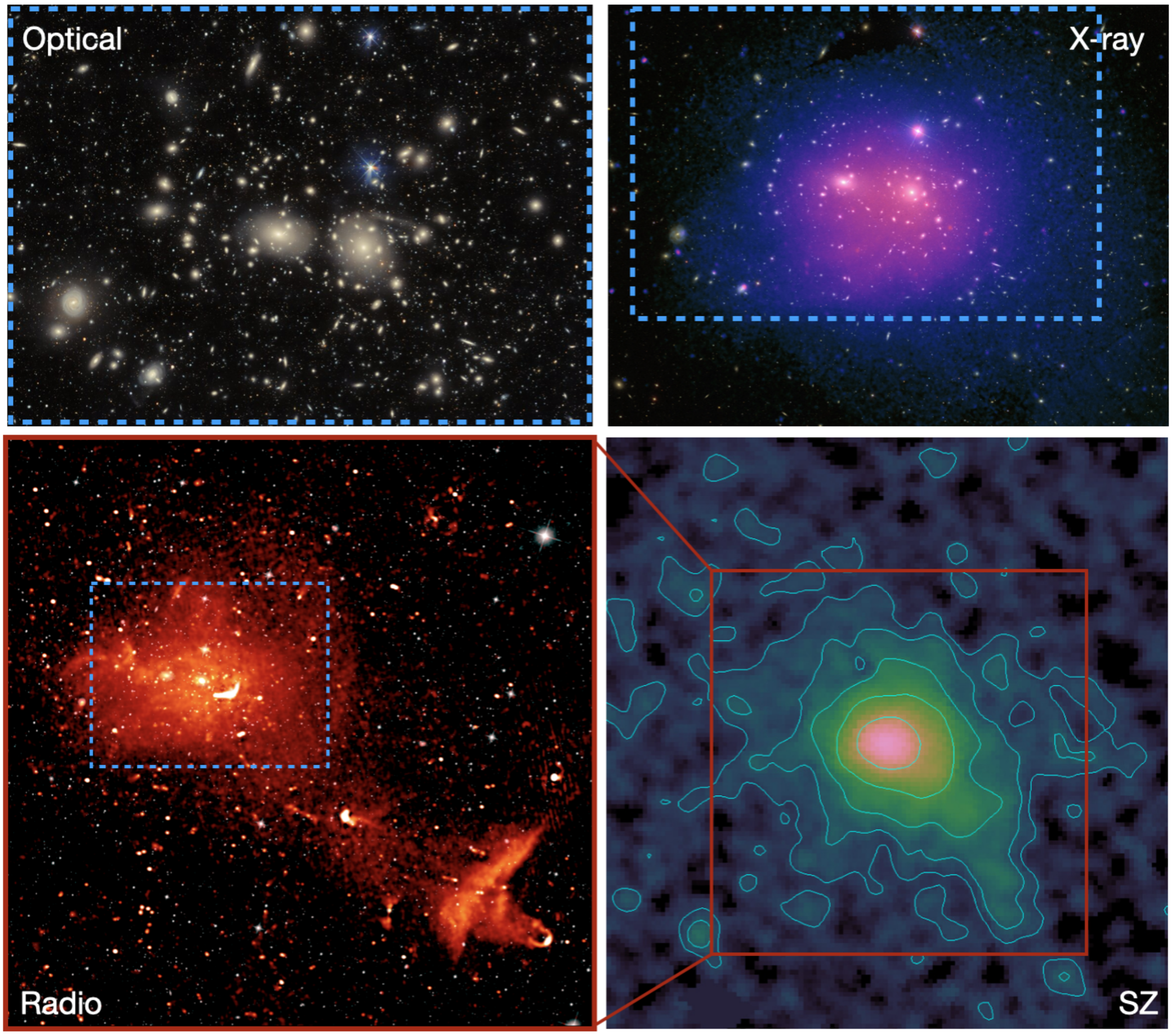

Figure 1.1: The multi-wavelength view of the Coma galaxy cluster. *Top left:* Optical image depicting the cluster member galaxies, captured with the Dark Energy Camera of the Víctor M. Blanco 4-meter Telescope at Cerro Tololo Inter-American Observatory in Chile. Credit: CTIO/NOIRLab/DOE/NSF/AURA. Image Processing: D. de Martin and M. Zamani (NSF NOIRLab). *Top right:* X-ray emission (in purple-magenta colours) that traces tha hot ICM in the cluster. This image shows the XMM-Newton superimposed on the optical image. Credits: ESA/XMM-Newton/SDSS/J. (Sanders et al., 2020). *Bottom left:* Composite IR-radio image of the Coma cluster field studied by Bonafede et al. (2022). In white the Wide-field Infrared Survey Explorer IR image. The red-orange color scale shows the synchrotron radiation coming from the diffuse emission and sources in the field. Credit: Bonafede et al. (2022). *Bottom right:* SZ images of the Coma cluster obtained with the Planck satellite by Churazov et al. (2021). The image maps the Compton parameter y, and the lowest contour corresponds $y = 2.5 \times 10^{-6}$. Credit: Churazov et al. (2021). The boxes serve as a visual aid for the reader. They approximately indicate which area each image represents.

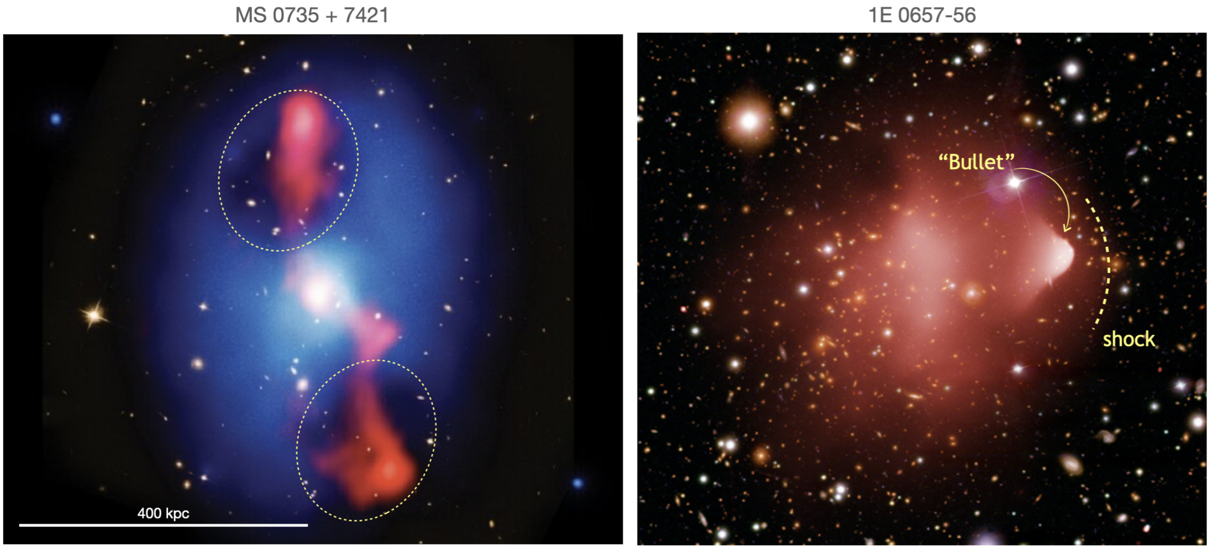

Figure 1.2: Examples of galaxy cluster's central AGN jets activity. *Left:* Chandra X-ray image (blue) and Very Large Array at 330 MHz radio image (red) superposed with the Hubble Space Telescope visual image of the galaxy cluster MS 0735 + 7421. The giant X-ray cavities, filled with radio emission, are surrounded by a cocoon shock visible in the Chandra image as an elliptical edge. Credit: Gitti et al. (2012). *Right:* The Bullet Cluster is a much-studied pair of galaxy clusters, which have collided head on. The X-ray gas shows a prominent bow shock preceding a small, cool "bullet" subcluster, whose boundary is a cold front, flying west after passing through a core of a bigger cluster and disrupting it. Credit: NASA/CXC/CfA/M.Markevitch (Markevitch, 2006).

clusters (e.g., Leccardi et al., 2010): relaxed systems, with usually regular X-ray morphologies, naturally develop a cool-core, while NCCs are generally associated with dynamically disturbed systems, where energetic merger events can have a significant impact on the core region, often resulting in its disruption or preventing the reformation of a cool-core. The link between dynamical state and core properties is further supported by statistical studies or radio emission about the connection between cluster mergers and the presence of radio halos (see discussion in **Section 2.3.4**). However, several questions have arisen regarding the classification of CC and NCC clusters. First, there has been considerable discussion about the choice of indicators used to define these categories. As shown by Hudson et al. (2010), the classification strongly depends on the parameters adopted and they concluded that the two most robust indicators are the central cooling time and the central entropy. Second, an ongoing debate concerns whether CC and NCC clusters constitute two distinct populations or instead represent the two extremes of a continuous distribution (e.g., Pratt et al., 2010). The lack of a clear-cut separation in some of their observational properties suggests the latter scenario may be more accurate. This idea is further supported by recent simulations, such as TNG-Cluster, which find that the distribution of core properties is unimodal, in which CC and NCC systems simply represent the two extremes of a single, continuous population (Lehle et al., 2024).

In cool-core clusters, the dense central regions have short radiative cooling times, theoretically leading to substantial cooling flows: a steady, subsonic inflow of hot gas toward the center, where it would cool to low temperatures and condense, potentially forming cold gas and stars (e.g., Fabian, 1994). However, high-resolution X-ray observations have revealed that the amount of thermal gas radiatively cooling was much less than predicted rates of hundreds to thousands of solar masses per year, giving rise to the classic "cooling flow problem". The implication and solution to this is the presence of some form of heating that prevents the gas from cooling. Feedback from central AGN of the dominant cD galaxies (e.g., McNamara & Nulsen, 2007), has been identified as the primary mechanism to offset cooling and regulate core thermodynamics (see Gitti et al., 2012, for an extensive review about AGN feedbacks in galaxy clusters). Signatures of its influence include radio jets and X-ray cavities in the ICM (**Fig. 1.2** *left*), which provides direct evidence of AGN-driven phenomena and allow direct measurement of the mechanical jet power of these radio sources (Bîrzan et al., 2008).

1.2.2 Shocks and Cold Fronts

The ICM is a highly dynamic environment. During hierarchical structure formation, mergers and accretion generate a variety of phenomena that significantly impact the ICM thermodynamic state (see e.g., Markevitch & Vikhlinin, 2007; Markevitch, 2010, reviews). X-ray observation, in particular the high-resolution arcsecond-imaging allowed by *Chandra*, have made it possible not only to study the global ICM distribution but also to capture the fine structure of these hydrodynamic phenomena in clusters with great details. Among these structures, we find bow shocks and cold fronts. Galaxy clusters can host three main types of shocks: accretion, merger and AGN-driven shocks.

Accretion shocks from at the outer boundaries of clusters, when the infalling gas is shock-heated. However, due to their location at very large off-center distances (∼ several Mpc), have never been observed at any wavelenghts so far. Merger shocks are generated during major cluster mergers when subclusters collide at supersonic speeds, driving shock fronts into the ICM. AGN-driven shocks, resulting from energetic outbursts of active galactic nuclei in cluster cores, which inflate cavities and drive weak shocks into the surrounding ICM. For this work, we are primarily interested in the merger shocks, which propagate outward from the merger axis and are often found in the cluster outskirts. They compress and heat the ICM and accelerate particles, thus they can be traced in both X-ray and radio observations (see **Section 1.3.2** for their radio counterparts). Cold fronts are contact discontinuities (Ghizzardi et al., 2010) that can arise in two main contexts: *(ii)* merger cold fronts - where the cool, dense core of an infalling subcluster survives the merger and creates a contact discontinuity as it flows through the hotter ICM; and *(ii)* sloshing cold fronts, mainly found in relaxed clusters, where minor mergers or perturbations displace the central cool gas, causing it to oscillate (or "slosh") in the gravitational potential well. These sloshing motions produce characteristic spiral patterns of cold fronts in X-ray images (e.g., Churazov et al., 2003; Simionescu et al., 2012; Bellomi et al., 2024). Both shocks and cold fronts appear as sharp surface brightness discontinuities, but they differ in the sign of the temperature jump across the front. Shocks create pressure discontinuities: they exhibit a density and temperature jump in the same direction, with the downstream (post-shock) region showing higher temperature and density relative to the upstream (pre-shock) gas. In contrast, cold fronts mark density and temperature jump of opposite signs: the denser side of the front is also cooler[3], but the pressure across the discontinuity remains almost continuous. Shocks and cold fronts are known to be characteristic signatures of disturbed clusters which are undergoing significant merger activity (e.g., Markevitch et al., 2000; Vikhlinin & Markevitch, 2002). One of the most extraordinary examples of cold front and shock are found in the so-called Bullet cluster (Markevitch et al., 2002), illustrated in **Fig. 1.2**, (*right*). Here, because of the geometry of the interaction, we can clearly witness the infalling subcluster (the 'Bullet') passing through a core of a bigger cluster, disrupting it, and producing a contact discontinuity between its dense and low-entropy core and the surrounding hot gas. Ahead of it, a second discontinuity accompanied by a reversed temperature jump (a shock), also arises. However, also morphologically relaxed clusters can show such surface brightness discontinuities. In this case, shocks are mostly connected to the central AGN outbursts (Nulsen et al., 2005); while cold fronts are produced by sloshing induced by minor merger events that produce a disturbance on the gas in the core, displace it from the centre of the potential well (e.g., Ascasibar & Markevitch, 2006).

1.2.3 Magnetic Fields

Despite being a high-β plasma[4], where the thermal pressure dominates over the magnetic one, magnetic fields play a critical role. They can modify heat transport by suppressing thermal conduction in the direction perpendicular to the magnetic field lines (Ruszkowski et al., 2011), stabilize front surfaces by suppressing Kelvin-Helmholtz instability (Chandrasekhar, 1961), and contribute to the total pressure budget of the ICM, providing non-thermal pressure support that can bias hydrostatic mass estimates (Lau et al., 2009). Historically speaking the strongest evidence of magnetic fields in clusters came from the detection of cluster-size synchrotron radiation observed in the radio band, making the radio observations a primary probe of cluster magnetic field studies. Several methods have been developed to obtain magnetic field estimates (see Carilli & Taylor, 2002; Brüggen, 2013, for reviews on magnetic fields in galaxy clusters).

A first method relies on minimum conditions and involves the detection of inverse Compton hard X-ray emission in clusters with diffuse synchrotron radio emission. Assuming the hard X-ray component[5] comes from IC scattering of CMB photons by the same relativistic electrons responsible for the synchrotron emission, the volume-averaged cluster magnetic field can be estimated from the ratio between the power emitted through synchrotron and IC, as this is proportional to the square of the magnetic field strength (Blumenthal & Gould, 1970). Such estimates typically resulted in volume-averaged magnetic field strength of the order $\sim 0.1 - 0.5\mu$G (e.g., Fusco-Femiano et al., 1999; Fusco-Femiano, 2004; Wik et al., 2009; Murgia et al., 2010).

The main techniques to measure cluster magnetic fields include Faraday rotation of sources located both behind and within galaxy clusters. Faraday rotation is an effect that rotates the direction of the polarization plane by an angle proportional to the square of the wavelength, the electron density (usually derived from ICM X-ray studies), and the strength of the field along

[3]For this exact reason, these types of discontinuities have been labeled "cold" (Vikhlinin et al., 2001).

[4]This parameter is defined as $\beta = P_{th}/P_B \approx 100$, i.e. the ratio between the thermal and magnetic pressures.

[5]In some cases the hard X-ray IC emission is not detected (e.g., Finoguenov et al., 2010). In such cases, upper limits on the IC flux can be used to place a lower limit on the ICM magnetic field strength.

the line-of-sight — the quantity being constrained: $\Delta\chi = \mathrm{RM} \times \lambda^2$, with $\mathrm{RM} \propto \int_{\mathrm{LOS}} \mathrm{n_e B_{\|} dl}$. The intrinsic polarisation angle of the source does not need to be known, since Faraday rotation produces a distinct wavelength-dependent rotation measure signature. While diffuse synchrotron emission traces magnetic field properties on large scales, the depolarization of the radio galaxy signals provides information on its small-scale properties. Studies based on rotation measures provided valuable insights into the ICM magnetic field morphology, including its power spectrum (e.g., Enßlin & Vogt, 2003; Murgia et al., 2004; Laing et al., 2008b), central strength and radial decline (Bonafede et al., 2010). However, recent MHD simulations (e.g., Vazza et al., 2018) suggest that, due to the dynamics of the ICM, the magnetic power spectrum in clusters is more complex than a simple power-law, as commonly assumed in RM studies.

Finally, magnetic fields have been constrained from the sharpness and stability of temperature discontinuities at cold fronts in clusters (Lyutikov, 2006; ZuHone et al., 2013), or from the thickness of radio relics produced by shock front (e.g., Markevitch et al., 2005; van Weeren et al., 2010).

Altogether, these studies found that cluster magnetic fields are of the order of $\sim 1\mu$G, with peaks of $\sim 10-40\,\mu$G in CC clusters (Enßlin & Vogt, 2003). Estimates based on the rotation measure of background sources, particularly in clusters such as Coma (Bonafede et al., 2010) and Abell 2345 (Stuardi et al., 2021), suggest that the central magnetic field strength scales with the thermal gas density, following a power-law with an index in the range 0.5–2.

The origin of cluster magnetic fields is an active and complex field of research with still many open questions. The origin of cluster magnetic fields is an active field of research with still many open questions. Two main scenarios have been proposed: a *primordial* origin (see Subramanian, 2016, for a detailed review about primordial seeding mechanisms), where seed fields were generated in the early Universe, during the inflationary phase, and an *astrophysical* origin, i.e., magnetic fields are injected into the ICM by galactic winds, AGN, or starbursts (e.g., Ensslin et al., 1997; Völk & Atoyan, 2000). Observational constraints support the existence of weak seed fields, but their strength remains uncertain. Measurements of CMB B-mode polarisation constrain primordial magnetic fields to be below $\sim 10^{-9}$G (comoving) on Mpc scales at recombination (Ade et al., 2015). While Neronov & Vovk (2010) reported a lower limit of $\sim 10^{-16}$G, derived from high-redshift blazar spectra. The astrophysical origin is further supported by the fact that galactic winds and AGN must have significantly enriched the ICM of metals (Werner et al., 2008) thus it sounds plausible that winds and jets carry magnetic fields as well. Simulations (Xu et al., 2011; Vazza et al., 2017), confirm that AGN can be efficient sources of magnetic seed fields, able to magnetize the cluster to up to μG level.

In both cases, these initial seeds are thought to be efficiently amplified from weak seed fields to reach μG-level strengths observed in galaxy clusters (see Donnert et al., 2018, for a recent review). The main mechanism is believed to be the small-scale dynamo (Kraichnan & Nagarajan, 1967), a process in which kinetic energy from merger-driven turbulence is transferred into magnetic energy. As turbulent eddies stir the plasma, they stretch, fold, and tangle existing magnetic field lines, leading to an exponential growth of magnetic energy on small scales. The amplification continues over several eddy turnover times — often spanning a few Gyr in cluster environments — until the magnetic energy saturates at levels comparable to the kinetic energy of the turbulence (Beresnyak & Miniati, 2016). Numerical simulations support this hypothesis,

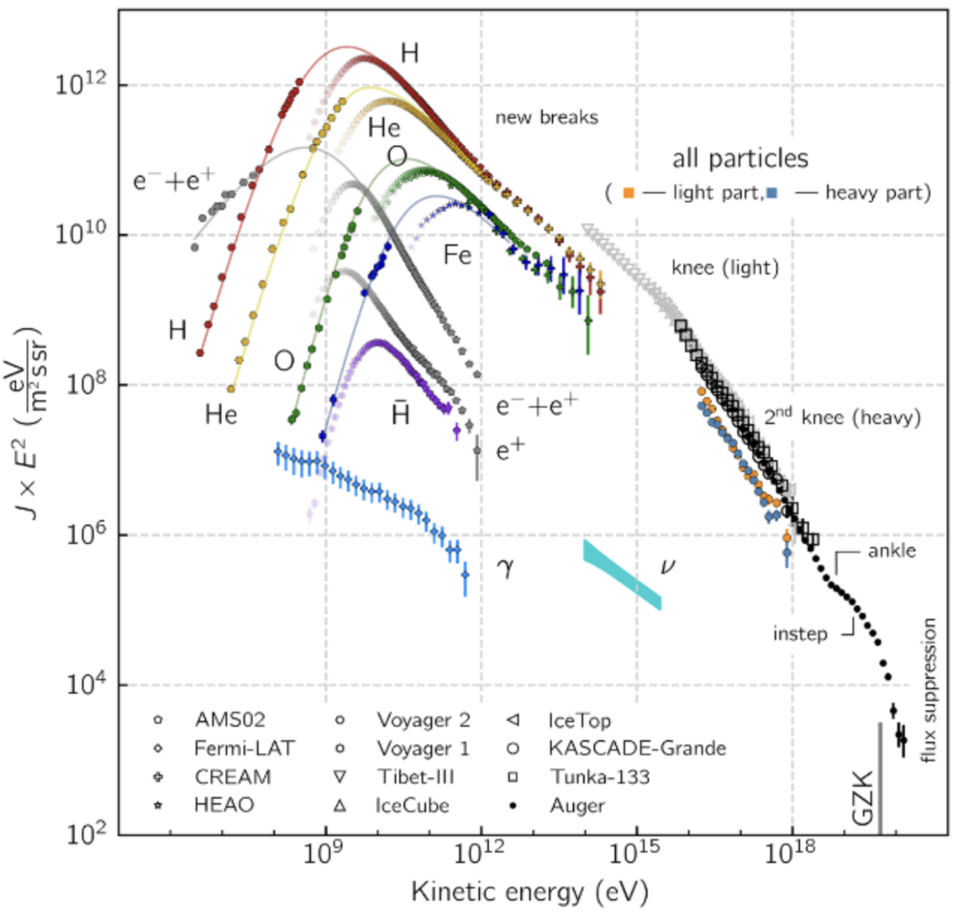

Figure 1.3: Local cosmic rays energy spectrum, highlighting contributions from the different types of nuclei, electrons, positrons, photons and neutrino. On the y-axis, the spectrum is multiplied by $\times E^2$, making it proportional to the energy density of CRs. In this way, the peak of the curve gives information about where most of the energy is stored. Credit: Lenok (2022).

showing that small-scale turbulent dynamo amplification can produce such field strengths (Vazza et al., 2018).

1.2.4 Cosmic Rays

In addition to the thermal gas and magnetic field, another important ICM component is constituted by high-energy non-thermal particles, the cosmic-rays (CRs). The CRs are particularly relevant in the context of this thesis, as they are the radio-emitting particles responsible for the emission discussed in **Section 1.4** and **Section 1.3**.

Cosmic rays are relativistic charged particles, such as protons and electrons, together with heavier nuclei and positrons, originating from astrophysical sources outside the Solar System. Thanks to the combination of data from different telescopes and ground-based air shower detectors, it was possible to determine the local CRs spectrum (see **Fig. 1.3**) across many orders of magnitudes, from $\sim 10^7$ to $\sim 10^{20}$ eV (Lenok, 2022). This is important as it encodes the information about CRs origin, acceleration and confinement, as well as mass composition. I refer to Owen et al. (2023); Ruszkowski & Pfrommer (2023) for recent reviews on the topic.

The CRs spectrum shape also clearly reveals that, unlike thermal particles, CRs follow a non-thermal distribution, typically a power law in energy $dN/dE \propto E^{-\delta}$, with δ the energy index. At low energies (below several GeV), CRs spectrum is characterized by a flat power-law ($\delta \sim 0$). The maximum contribution to the CR energy density is provided by particles with energies of a few GeV. Above a few GeV, the spectrum declines as a power-law with $\delta \sim 2.7$ index ($dN/dE \propto E^{-2.7}$). This result is attributed to the combination of CRs acceleration in supernova remnant shock waves (which inject particles with $\delta \sim 2.2$) and diffusive escape losses that steepen the spectrum by 0.5. At higher energies, the spectrum features several breaks. Around 3 Pev it steepens further ($\delta \sim 3$) forming the so-called "knee". This likely reflects the upper energy limit CRs can be accelerated by shocks waves. A second "knee" appears around 100 PeV ($\delta \sim 3.1$) and the CR composition becomes increasingly dominated by heavier nuclei, and the spectrum begins a gradual transition from being of Galactic to extragalactic origin. Above $\sim 10^{18}$ eV, the spectrum flattens again at the "ankle," marking the onset of the extragalactic CR component. At these energies, the gyroradius of CRs is comparable with the thickness of the Galactic disk, therefore they are no longer efficiently confined. Following the flattening, the spectrum exhibits a sharp cutoff at around 5×10^{19} eV, the reason for which is still being investigated by current research. Some options include the Greisen–Zatsepin–Kuzmin limit (Greisen, 1966) or it could reflect a maximum energy limit set by the acceleration mechanisms themselves (Kotera & Olinto, 2011).

Sources of CRs, i.e. sites where CRs are directly accelerated, operate across a wide range of environments. The most famous accelerators are certainly supernova explosions (Baade & Zwicky, 1934), but CRs can also be produced in pulsars and their wind nebulae (Abdo et al., 2010), stellar (Bykov et al., 2020) as well as galactic winds (Veilleux et al., 2020), active galactic nuclei with powerful relativistic jets (Hlavacek-Larrondo et al., 2022), turbulence and shock waves from structure formation (Brunetti & Jones, 2014).

Unlike the ISM in galaxies, galaxy clusters are efficient "containers" of CRs[6], able to confine CRs with energies up to 10^7 GeV. In the cluster environment, the two main contributions to the CR population are merger shocks and turbulence, generated in the ICM as a result of cluster formation[7].

The acceleration of CRs at shocks is customarily described according to the diffusive shock acceleration (DSA) theory (Blandford & Ostriker, 1978; Drury, 1983). During this process, diffusing particles are temporarily trapped across the shock, they scatter back and forth gaining energy due to the converging plasma flows on either side until they eventually escape downstream. This is a Fermi I efficient process that for strong non-relativistic shocks leads to a power-law

[6]The very large diffusion coefficient of these particles, combined with their relatively short lifetimes, also gives rise to the so-called *diffuse problem*, i.e. the fact that observed large-scale radio emission cannot be explained by the spatial diffusion of cosmic ray electrons alone, and instead requires their *in-situ* (re-)acceleration.

[7]Additional sources of CRs include AGN outflows or normal galaxies, where CRs are first accelerated by galactic SN and pulsars and then transported into the ICM.

energy spectrum of $dN/dE \propto E^{-2}$.

On the other hand, during turbulent acceleration, CRs are accelerated via second-order Fermi processes, during which they stochastically scatter with MHD irregularities in the ICM (Brunetti & Lazarian, 2007). During these interactions, particles can gain or lose energy depending on whether they encounter head-on collisions or not. However, on average there is a net energy gain, as the head-on collisions are statistically more likely. Turbulent motions in the ICM arise from a variety of processes, including galaxy motions, AGN outflows, sloshing of cluster cores, and most importantly, from the chaotic dynamics of cluster mergers. However, this mechanism is inefficient at accelerating particles directly from the thermal pool (Petrosian & East, 2008), thus it requires the presence of pre-existing (seed) CRs, potentially injected from past episodes of AGN activity. These mechanisms produce the populations of relativistic electrons that give rise to the diffuse radio emission observed in galaxy clusters. Their origin and characteristics are discussed in **Section 1.3**.

CRs are subjected to energy losses that limit their life-time in the ICM. Cosmic-ray protons (CRp) with energy 1 GeV – 1 TeV are long-living particles with life-times in the cores of galaxy clusters of several Gyrs. For relativistic protons, the main channel of energy losses is the inelastic proton-proton collisions, while at lower energies (< 1 GeV) the energy losses are dominated by ionization. Given that CR proton cooling times due to hadronic interactions can be comparable to the Hubble time, CRs can accumulate in the ICM and have sufficient time to propagate away from their production sites to fill the entire ICM volume. However, they do not radiate efficiently at observable wavelengths and are thus extremely difficult to detect directly in clusters. The main electromagnetic byproduct of hadronic reaction are γ-ray photons (Colafrancesco & Blasi, 1998). However, most attempts to detectγ-rays from clusters resulted in upper limits (e.g. Ackermann et al., 2010; Ahnen et al., 2016). On the other hand, cosmic-ray electrons (CRe) suffer much more severe energy losses and are the particles producing the observed emission at radio frequencies. At highly relativistic energies, CRe experience synchrotron interactions with the magnetic field and IC interactions with the ambient photon field (where for clusters photon energy density is dominated by the CMB), while Bremsstrahlung and Coulomb losses dominate below 100 MeV (see **Fig. 1.4**, *left*). For example, in typical ICM magnetic fields of a few μG, electrons with energies of several GeV emit synchrotron radiation at 1.4 GHz and radiative lifetimes on the order of 0.1–0.2 Gyr.

CRe with a power-law energy spectrum $N(E) = N_0 E^{-\delta}$, radiate synchrotron emission with a power-law in frequency $J_\nu \propto N_0 B^{\alpha+1} \nu^{-\alpha}$ and therefore the resulting radio spectrum is defined as:

$$S(\nu) \propto \nu^{-\alpha} \tag{1.1}$$

where $\alpha = (\delta - 1)/2$ is a direct measure of the electron distribution and is referred to as the spectral index. For instance, if electrons are injected with $\delta_{inj} = 2.2$, the synchrotron emission from the freshly accelerated population would follow a power law with $\alpha_{inj} = 0.6$. At later times, the electron population evolves from a pure power-law due to the above-mentioned synchrotron and IC energy losses for a total energy loss rate of $\dot{E}_\mathrm{e} \propto \left(B^2_\mathrm{CMB} + B^2\right)\gamma^2$, where the first term $\dot{E}_\mathrm{e} \propto B^2_\mathrm{CMB} = \left[3.25 \times (1+z)^2\right]^2$ represents the energy loss resulting from IC scattering with CMB photons and the second $\propto B^2$ the synchrotron emission.

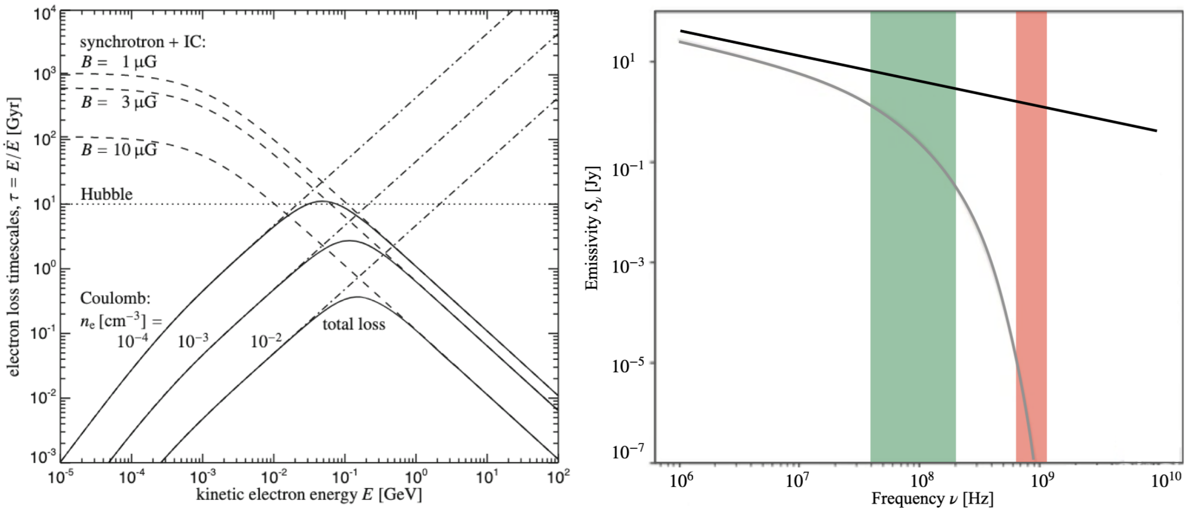

Figure 1.4: Electron cooling times and synchrotron spectrum. *Left:* CR electron cooling times resulting from Coulomb and IC/synchrotron interactions for different densities and magnetic fields. Electrons emitting radio waves at a frequency of 1.4 GHz possess an energy of approximately 5 GeV in μG magnetic fields, resulting in a lifetime of about 0.2 Gyr. *Right:* Synchrotron spectrum for a population of electrons initially accelerated as $S(\nu) \propto \nu^{-0.6}$ (black line). The high-frequency curvature (grey line) arises from radiative synchrotron and IC losses after approximately 500 Myr. The shaded areas highlight the difference between low (40-200 MHz) and high ($\sim$ 1 GHz) frequencies.

Because higher-energy electrons lose energy more rapidly, the electron energy distribution is depleted at the high-energy end (see **Fig. 1.4** *right*). This produces a steepening of the synchrotron spectrum beyond a critical frequency, known as the break frequency $\nu_{\rm break}$, which is the frequency at which the electrons have lost a significant fraction of their energy over the lifetime of the source. The corresponding radiative lifetime is given by:

$$t_{\rm rad} = 1.61 \cdot 10^3 \times \frac{B^{0.5}}{B^2 + B^2_{\rm CMB}\left[(1+z)\nu_{\rm break}\right]^{0.5}} \quad {\rm Myr} \tag{1.2}$$

where B is the magnetic field in μG and $B_{\rm CMB} = 3.25 \times (1+z)^2$ is the CMB equivalent magnetic field at redshift z, used to parametrised the IC losses. It becomes clear that the determination of the spectral index of a radio source, observationally measured by comparing the flux density at two different frequencies $\alpha_{\nu_1}^{\nu_2} \equiv \log(S_{\nu_2}/S_{\nu_1})/\log(\nu_2/\nu_1)$, is key to characterize its origin and radiative age.

1.2.5 The Sunyaev-Zel'dovich effect

Finally, the ICM also emits through the thermal[8] Sunyaev-Zel'dovich (tSZ) effect (Sunyaev & Zeldovich, 1972), which results from inverse-Compton scattering of cosmic microwave back-

[8]The SZ effect comprises a family of phenomena, including the thermal, kinematic, relativistic, non-thermal, and polarised SZ effects (see Mroczkowski et al., 2019, for a recent review).

ground (CMB) photons by hot electrons in the cluster. This scattering process transfers energy from the electrons to the photons, causing a characteristic frequency-dependent distortion in the CMB black-body spectrum (Mather et al., 1990). The tSZ effect appears as a decrease in the observed CMB intensity at frequencies below ~218 GHz (1.4 mm) and as an increase at higher frequencies. The amplitude of the distortion is proportional to the integrated thermal pressure of the electron population and it is represented by the Compton parameter $y \propto \int_{LOS} n_e k_B T dl$. Therefore, the tSZ effect offers a complementary mm-wavelengths view (see **Fig. 1.1**, *bottom right*) to X-ray observations in tracing the density and temperature of the plasma (see Carlstrom et al., 2002; Mroczkowski et al., 2019, for review on the SZ effect and its application for astrophysical studies). Beyond its utility in probing the thermal structure of the ICM, the SZ effect serves as a powerful cosmological tool. For example, its redshift independence makes SZ surveys particularly suited to detect galaxy clusters across cosmic time (e.g., Planck Collaboration et al., 2014).

1.3 Diffuse Radio Emission in Galaxy Clusters

Cluster formation is accompanied by some of the most energetic phenomena since the Big Bang. During mergers, enormous amounts of gravitational energy ($\sim 10^{63} - 10^{64}$ erg) are released in ~ 1 Gyr. A few percent of the merger energy can be channeled into non-thermal plasma components (Brunetti & Jones, 2014). Thus, in addition to the hot, X-ray-emitting ICM, galaxy clusters also host a non-thermal component that consists of relativistic (Lorentz factor $\gamma > 1000$) electrons and $\sim \mu$G magnetic fields, which produce synchrotron radiation visible at radio wavelengths. As these two ingredients are ubiquitous in galaxy clusters, a growing number of them have been found to host diffuse radio sources filling the central $\sim$ Mpc^3 region. Two main categories have been identified: *halos* and *relics* (see van Weeren et al., 2019, review).

1.3.1 Radio Halos

Radio halos are historically further classified into *mini-* and *giant-* halos (**Fig. 1.5**); however, recent observations reveal radio emissions that exceed the classical cluster scale, defining a new category of *mega*-halos (discussed separately in **Section 1.3.1.1**). They have in common the diffuse, roundish morphology, with peak intensity near the centre of galaxy clusters, but are thought to be produced by different mechanisms, thus forming distinct subclass. These sources are not localized to a specific region; instead, they occur throughout a significant volume of the cluster.

Giant and mini halos are centrally located and both exhibit steep spectrum[9] with a spectral index $\alpha \lesssim -1$. While giant radio halos are Mpc-sized radio sources which cover large parts of the cluster volume morphology roughly follows the distribution of the thermal ICM, mini-halos

[9] We bring to the reader's attention that, in **Section 1.2.4**, the derivation of **Eq. (1.1)** was based on the assumption of a positive α. However, from here on we adopt the more general convention $S(\nu) \propto \nu^{\alpha}$, where α is typically negative for synchrotron-emitting sources. While potentially confusing, this convention is more convenient as it aligns with the notation used in the following chapters.

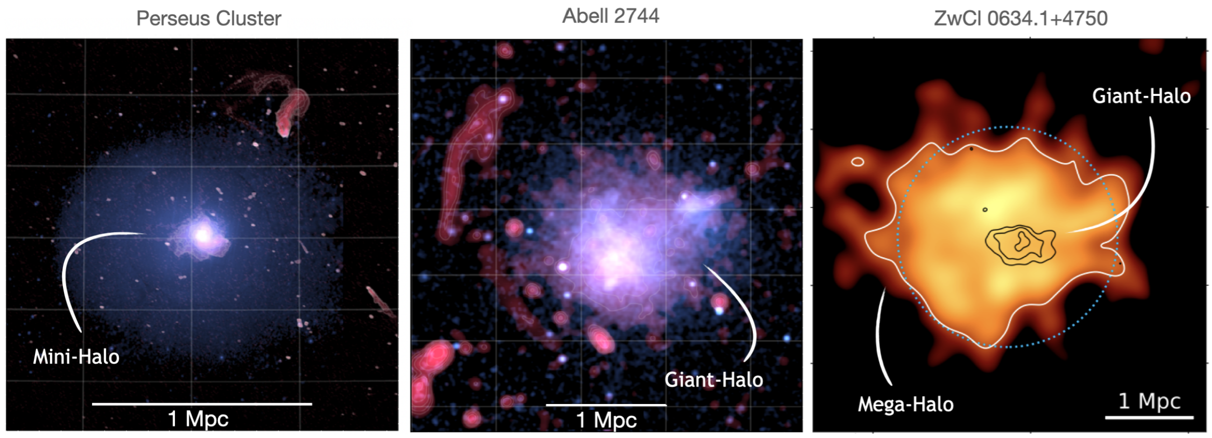

Figure 1.5: Examples of clusters hosting radio mini- giant- and mega- halos. The 1 Mpc scale bar serves to highlight the different physical scales involved. *Left panel:* Perseus cluster (Gendron-Marsolais et al., 2017): VLA 230–470 MHz (red) and XMM-Newton 0.4–1.3 keV (blue). *Central panel*: Abell 2744 cluster (Pearce et al., 2017): VLA 1–4 GHz (red) and Chandra 0.5–2.0 keV (blue). *Right panel*: ZwCl 0634.1+4750 cluster (Cuciti et al., 2022): giant halo (black contours from LOFAR 144 MHz at 30″ resolution) and mega halo (white contours from LOFAR 144 MHz at 30′ resolution). Images credit: adapted from van Weeren et al. (2019); Cuciti et al. (2022).

are typically confined within the cool-cores ($\lesssim 300 - 500$ kpc) of relaxed galaxy clusters and are characterized by higher emissivity (e.g., Cassano et al., 2008; Murgia et al., 2009).

Two emission mechanisms have been proposed to explain these non-thermal radio sources (see Brunetti & Jones, 2014, for a review): *(i)* the (re-)acceleration scenario, where CRe are (re-)accelerated by turbulence that develops during cluster mergers; *(ii)* the hadronic scenario, where secondary CRe are produced by proton-proton collisions between relativistic cosmic-ray protons (CRp) and thermal protons in the ICM. Radio halos are believed to be powered by electrons re-accelerated by merger-driven turbulence. Purely hadronic models fail to account for the observed properties of giant radio halos, as they cannot generate the required levels of γ-ray radiation, which would be among the byproducts of the hadronic decay (Brunetti et al., 2008, 2017; Adam et al., 2021; Osinga et al., 2024). However, secondary models remain a viable mechanism for mini-halos (Pfrommer & Enßlin, 2004; Jacob & Pfrommer, 2017; Adam et al., 2021), although most probably they don't play a main role.

Most radio halos are found to be unpolarized sources, with upper limits on polarization typically below a few per cent in multiple halos (e.g., Bacchi et al., 2003; Murgia et al., 2009; Govoni et al., 2013). This was generally attributed to the presence of strong turbulence in the intracluster medium (ICM), which disrupts ordered magnetic field structures and results in depolarized emission. However, it is likely that lack of polarization is due to a combination of beam depolarization and internal Faraday rotation. Beam depolarization happens when the angular scale of coherent magnetic field regions is smaller than the beam size, resulting in polarization signals cancelling out when averaged over the beam area. Moreover, even at higher resolution, Faraday depolarization can act and further suppress the observed polarized signal. Finally, the low surface brightness of radio halos - and thus the intrinsic faint nature of their polarized emission - requires higher sensitivity than current interferometers can typically provide to properly detect polarized emission. Even though cosmological MHD simulations predict that halos should be intrinsically polarized at levels of 15–35%, with values varying from cluster to cluster and increasing with the distance from the cluster centre (Govoni et al., 2013), current radio observations lack the sensitivity and resolution needed to detect this signal, making polarization studies of halos particularly challenging. Evidence of significant polarization has been reported in a few clusters: fractional linear polarization reaches levels of $\simeq 20 - 40\%$ (Govoni et al., 2005), $\simeq 8 - 17\%$ (Bonafede et al., 2009a) and $\sim 45\%$ (Murgia et al., 2024). It remains unclear whether these signals originate from the halo itself or superimposed relic emission (Pizzo et al., 2011).

As previously mentioned, the turbulent re-acceleration is currently the accepted mechanism responsible for generating radio halos (see e.g., Brunetti & Jones, 2014). During this process, part of the gravitational energy released by mergers is channeled into turbulence that, in turn, accelerate CRe and amplify magnetic fields (Brunetti & Lazarian, 2007). As a result, the occurrence of radio halos is closely linked to a cluster's dynamical state and mass, which determine the available energy budget for particle acceleration. It is generally accepted that radio halos are predominately found in merging clusters, while clusters without halo detection are generally relaxed. Observational evidence comes from the connection between the dynamical status of the cluster — obtained from X-ray studies — and the presence of radio halos (Buote, 2001; Markevitch & Vikhlinin, 2001; Cassano et al., 2010; Cuciti et al., 2015, 2021). A key prediction of turbulent re-acceleration models (e.g., Cassano & Brunetti, 2005a; Cassano et al., 2006) is that the radio particle spectrum should show a cutoff at a frequency that is proportional to the energetics of the merger event and therefore ultimately on the cluster mass $\nu_b \propto M^{4/3}$ (Cassano et al., 2010). As a result, massive clusters undergoing major mergers are expected to host radio halos with flatter spectra ($\alpha \sim -1.3$), visible up to ~ GHz frequencies. In the case of less energetic events, such as minor mergers or major mergers between low-mass clusters, the level of turbulence is too low to re-accelerate CRe at the energies required to emit synchrotron radiation at GHz frequency, which leads to the formation of steeper spectrum sources called ultra-steep spectrum radio halos with $\alpha < -1.5$ (USSRHs; Brunetti et al., 2008). The first serendipitous discoveries of USSRH have been found in Abell 521 (Brunetti et al., 2008; Dallacasa et al., 2009). After that, a number of other detections of USSRH or candidates, based on GMRT, MWA and LOFAR observations, have been reported (Bonafede et al., 2012; Shimwell et al., 2016; Wilber et al., 2018; Bruno et al., 2023a; Di Gennaro et al., 2021a; Edler et al., 2022; Pasini et al., 2022; Duchesne et al., 2022; Groeneveld et al., 2025a). A new example is studied in this thesis and reported in Chapter 4, and it is expected that more USSRH radio halos will be uncovered with sensitive observations at low frequencies (Cassano et al., 2006, 2023). Historically, the correlation between radio halos power and the mass of the host cluster was proved at GHz frequencies, which constrain the number of detected radio halos and limit the explorable mass range to $M_{500} > 5–6 \times 10^{14} M_\odot$. (Basu, 2012; Cassano et al., 2013; Cuciti et al., 2021; van Weeren et al., 2021; Duchesne et al., 2021). Recent low-frequency surveys have significantly improved this picture. In particular, Cuciti et al. (2023) confirmed the existence of a strong correlation between radio power at 150 MHz (in agreement with the previously established $P_{1.4,\mathrm{GHz}}$–M_{500} correlation) and pushed the mass limit down to $M_{500} \sim 3 \times 10^{14}\, M_\odot$.

Statistical studies show that halos are not ubiquitous, with early works reporting an average detection fraction of ~30% in massive galaxy clusters (Venturi et al., 2007; Cassano et al., 2013; Kale et al., 2015). More recently, Cassano et al. (2023) extended the investigation to lower-mass systems, including clusters down to $M_{500} \sim 2.5–3 \times 10^{14}$, $M_{\odot}$, thus building a statistical sample large enough to explore how the occurrence of radio halos depends on both cluster mass and redshift. The authors show that the occurrence rate of radio halos increases with cluster mass at fixed redshift, in line with expectations from turbulent re-acceleration models. Moreover, by comparing with previous studies in the same mass and redshift range, the fraction of clusters with RHs increases from $\sim 45\%$ in 600 MHz sample to $\sim 70\%$ in the 150 MHz sample, showing how crucial it is to go to low frequency for building statistical samples and test model predictions.

While giant radio halos are predominantly found in merging clusters; mini-halos are usually found in relaxed cool-core clusters (Gitti et al., 2004; Cassano et al., 2010; Gitti et al., 2018). Moreover, a statistical study by Giacintucci et al. (2017) on massive galaxy clusters ($M > 6 \cdot 10^{14} M_{\odot}$) found that $\sim 80\%$ of cool-core clusters host a mini-halo, indicating a strong link between mini-halo formation and cool-core gas properties.

1.3.1.1 Mega halos

Recent low-frequency LOFAR observations have led to the discovery of a new class of large-scale diffuse radio sources, called mega halos (Cuciti et al., 2022, see **Fig. 1.5** *right*) in four galaxy clusters (ZwCl 0634.1+4750, A665, A697, A2218). Although their name might suggest a direct scaling relation with classical radio halos, implying a factor of 1000 in size (as in the metric prefixes "mega" vs. "giga"), this is not the case. Instead, mega halos refer to diffuse radio sources that extend beyond the volume of classical giant radio halos, reaching distances of 2–3 Mpc and filling the cluster volume up to $\sim R_{500}$. Mega halos exhibit steep radio spectra ($\alpha < -1.6$ between 50–150 MHz) and have a much lower surface brightness than classical RHs, with an emissivity that is about 20 times lower. The galaxy clusters studied by Cuciti et al. (2022) have radial surface brightness profiles with two distinct components: a bright inner core corresponding to the classical giant halo and a more extended, low-surface-brightness outer region, separated by a clear discontinuity. All detected mega halos so far are associated with disturbed clusters. However, an attempt was made to understand whether this new emission is exclusive to peculiar systems or more common than previously assumed. To explore this, Cuciti et al. (2022) investigated the turbulent kinetic energy flux in both relaxed and disturbed clusters, comparing its distribution in the inner and outer regions where mega halos are observed. Their analysis showed that while turbulence is significantly stronger in the centers of post-merger clusters, the outer regions, where mega halos extend, exhibit similar turbulence levels in both relaxed and disturbed clusters. This suggests the presence of baseline turbulence in the outskirts, likely driven by continuous matter accretion from the large-scale structure. In this framework, Fermi-II re-acceleration could sustain mega halos even in more relaxed clusters, expanding their potential occurrence beyond merging systems. The physical origin of mega remains an open question. Subsequent ad-hoc simulations (Beduzzi et al., 2024) suggest that both classical and mega radio halos originate indeed from cosmic-ray re-acceleration by turbulence, but with key differences in the turbulence properties: the turbulence producing the expected radio emission turned out to be more solenoidal and more subsonic in the classical radio halo region, than in the mega radio halo region. The discovery of these sources highlights the need for deeper low-frequency surveys to explore how turbulence, particle acceleration, and magnetic fields shape the non-thermal properties of the ICM on large scales.

1.3.1.2 Hybrid halos

One of the major challenges is the emerging diversity of radio halos, which complicates the traditional dichotomy between giant halos in merging clusters and mini-halos in cool-core systems, as discussed in **Section 1.3.1**. In the last decade, some so-called "intermediate" or "hybrid" radio halos have been identified, with properties falling somewhere in between those of classical giant radio halos and mini-halos. In some cases, a few cool-core clusters show the presence of a fainter diffuse synchrotron halo or halo-like emission that extends quite far from the central mini-halo (Bonafede et al., 2014; Venturi et al., 2017; Sommer et al., 2017; Savini et al., 2018, 2019; Kale et al., 2019; Raja et al., 2020; Biava et al., 2021; Riseley et al., 2022b; Bruno et al., 2023a; Lusetti et al., 2024; Biava et al., 2024; van Weeren et al., 2024). This implies that giant radio halos might be relatively widespread, possibly even present in most massive cool-core clusters, rather than being found exclusively in merging systems. These peculiar galaxy clusters, either present giant halos (Bonafede et al., 2014; Savini et al., 2018), or show a hybrid morphology in the radio emission (Biava et al., 2021; Lusetti et al., 2024; van Weeren et al., 2024), even though being classified as relaxed systems based on their thermal X-ray properties. Even the Perseus cluster, one of the most famous prototypical examples of relaxed systems hosting a clear mini-halo, has been very recently found to host a 1.1 Mpc diffuse giant-halo emission around the central famous mini-halo van Weeren et al. (2024). An even more complex morphology has been found in Abell 2142, a galaxy cluster with an intermediate dynamical state, already known to host a hybrid radio halo with two distinct components (Venturi et al., 2017), revealing a third ultra-steep spectrum and wider component when observed at low-frequency by Bruno et al. (2023a).

The detection of extended radio emission beyond the cluster core suggests that sufficient turbulent energy exists in the outskirts to sustain particle re-acceleration. The origin of this turbulence remains uncertain but could be linked to past off-axis mergers, where large-scale ICM motions persist even in systems that appear thermally relaxed. In such cases, it has been suggested that a minor or off-axis merger could trigger large-scale turbulent re-acceleration while leaving the cluster core undisturbed, allowing the simultaneous presence of a radio mini-halo in the cooling core and a more extended giant halo component tracing the minor merger-induced turbulence.

An alternative scenario is an evolutionary link between mini- and giant- radio halos, where merger-driven turbulent motions, or diffusion and advective transport, redistribute cosmic-ray electrons from the disrupted cool core to larger scales, where they can undergo re-acceleration. In this framework, a once-active mini-halo could fade, giving way to the formation of a giant radio halo as the cluster evolves. This candidate scenario (Brunetti & Jones, 2014) suggests the potential existence of intermediate transitional phases, where both components are present simultaneously.

All this evidence suggests that the simple merger versus relaxed classification may be an

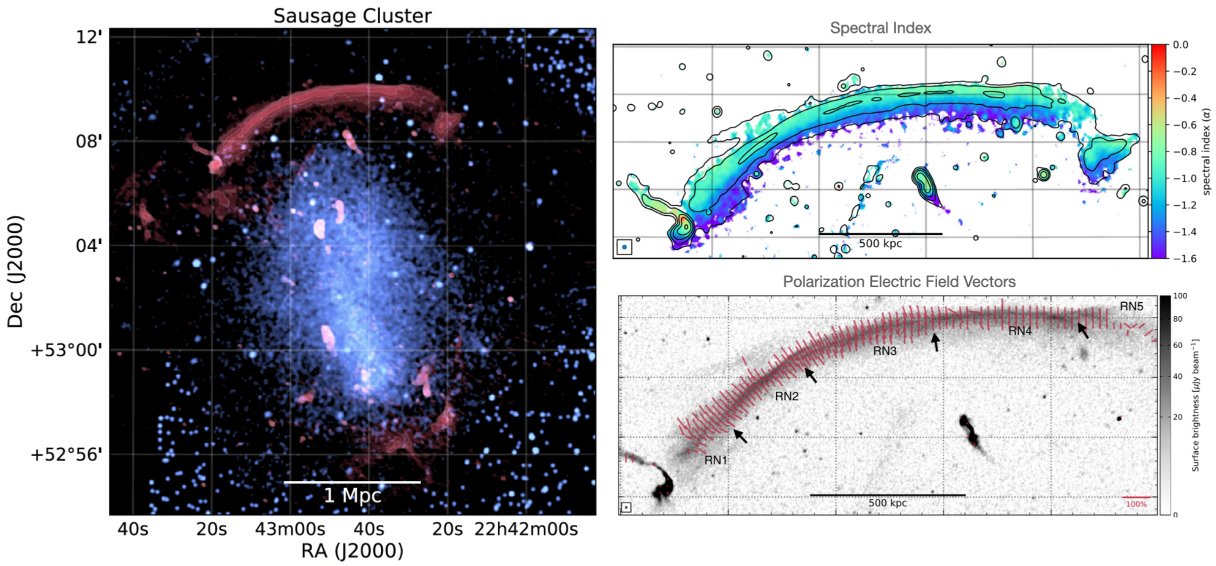

Figure 1.6: The textbook example of a radio relic: CIZA J2242.8+5301 galaxy cluster. *Left* The radio emission is shown in red (GMRT 610 MHz, van Weeren et al. (2010)) and the X-ray emission in blue (Chandra 0.5–2.0 keV, Ogrean et al. (2014)). *Right*: Spectral index distribution between 0.15 and 3.0 GHz at 5″ resolution (Di Gennaro et al., 2021b) across the northern cluster radio shock (top); Stokes I observation in the 1–2 GHz band with the polarization electric field vectors at 2.7″ resolution, corrected for Faraday rotation, displayed in red from Di Gennaro et al. (2021b); the length of the vectors is proportional to the intrinsic polarization fraction (scale in the lower right corner). White and black arrows in the two panels indicate the points where the relic breaks into separate laments, following Figure 7 in Di Gennaro et al. (2018) (bottom).

oversimplification, highlighting the role of weaker dynamical interactions in shaping the non-thermal properties of galaxy clusters.

1.3.2 Radio Relics

Radio relics are diffuse, elongated, steep-spectrum synchrotron emission ($\alpha < -1.1$) (see Wittor, 2023, for a recent review). Differently from other forms of diffuse emission, they are very localized sources, predominantly in the outskirts of merging galaxy clusters. The leading formation scenario attributes radio relics to the shock acceleration of cosmic-ray electrons via the Diffusive Shock Acceleration (DSA) mechanism (Blandford & Ostriker, 1978; Drury, 1983; Blandford & Eichler, 1987; Ensslin et al., 1998). DSA is a Fermi I (Fermi, 1949) process, where particles are scattered up and downstream of the shock by plasma irregularities, gaining energy with each shock crossing. These shocks arise during major cluster mergers, where the infall of massive substructures generates strong compressions in the ICM, leading to shock heating, compression, and particle acceleration.

Ideally, every shock front should be visible both in the radio (as synchrotron emission) and X-ray (as temperature and density discontinuities) band. X-rays observations with Chandra, XMM-Newton or Suzaku led to a great number of shock detections in clusters (e.g., Markevitch & Vikhlinin, 2007; Botteon et al., 2018a). However, the confirmation of radio relics with their X-ray counterparts is not always possible. This is partly due to the limited resolution of some X-ray satellites, such as Suzaku and XMM-Newton, and partly because relics often reside in low signal-to-noise regions of the instrumental field of view (e.g., Akamatsu & Kawahara, 2013). Until recently, a long-standing issue was related to the discrepancy between X-ray and radio estimate of the shock strength, namely its Mach number $\mathcal{M}$. In general, Mach numbers from radio observations, derived from the radio spectrum[10], tend to be larger than those obtained from X-ray measurements, derived from Rankine-Hugoniot jump conditions at the shock discontinuities[11]: $\mathcal{M}_R > \mathcal{M}_X$. Theoretical studies (Wittor et al., 2021; Whittingham et al., 2024) show instead that these discrepancies in Mach number estimates arise from the fact that different observational techniques probe different aspects of the underlying Mach number distribution. Radio observations are particularly sensitive to the highest Mach numbers, which occur in localized regions along the shock surface, whereas X-ray measurements capture a broader, averaged Mach number across the entire shock. Additionally, X-ray-derived Mach numbers are highly dependent on the viewing angle of the relic, while radio measurements are less affected by orientation, making them a more robust proxy.

The standard DSA theory, involves the thermal electrons being directly accelerated (sometimes referred to as *fresh injection*). However, a major challenge is that the observed low shock Mach numbers ($\mathcal{M} \lesssim 3$) would imply unrealistically large particle acceleration efficiencies, which DSA from the thermal pool alone hardly explains. In other words, considering an acceleration efficient, i.e. the ratio between the shock kinetic power and the energy flux of accelerated CRs, $\lesssim$ few% (as predicted by current models, e.g., Vazza et al., 2016; Ryu et al., 2019), it would be difficult to explain the observed high radio luminosities of most relics (Botteon et al., 2020a). Only a few systems (e.g., Locatelli et al., 2020) are known where the DSA from the thermal pool works.

To solve this tension, models have invoked the presence of a pre-existing population of mildly-relativistic electrons (e.g., Markevitch et al., 2005; Kang & Ryu, 2011; Pinzke et al., 2013) either pre-accelerated by previous shock passages (e.g., Kang, 2021; Inchingolo et al., 2022) or coming from fossil plasma from radio galaxies, often observed in the proximity or radio relics (e.g., van Weeren et al., 2017). The latter scenario is supported by observational evidence of radio galaxies in the proximity of many radio relics (e.g., Bonafede et al., 2014; van Weeren et al., 2017; Di Gennaro et al., 2018), which can supply seed electrons that are subsequently re-accelerated by shocks. A case study is the work of van Weeren et al. (2017), who found the relic in Abell 3411-3412 morphologically connected to the tail of a cluster-member radio galaxy. They also showed that the energy spectrum steepens along the tail, consistent with standard radiative losses, and subsequently flattens again at the inner boundary of the relic, implying re-acceleration.

Historically, relics have been detected in edge-on orientations, exhibiting arc-like morpholo-

[10] DSA mechanism predicts that the volume-integrated spectrum of accelerated electrons depends solely on the shock Mach numbers as $\alpha_{\rm int} = (\mathcal{M}^2 + 1)/(\mathcal{M}^2 - 1)$.

[11] The temperature and density jumps detected in X-ray images lead to $\frac{\mathrm{T_{post}}}{\mathrm{T_{pre}}} = \frac{5\mathcal{M}^4+14\mathcal{M}^2-3}{16\mathcal{M}^2}$ and $\frac{\mathrm{n_{post}}}{\mathrm{n_{pre}}} = \frac{4\mathcal{M}^2}{\mathcal{M}^2+3}$.

gies that resemble the shock fronts believed to generate them (see example in **Fig. 1.6**). They generally show a bright outer rim in radio emission, which fades toward the cluster centre. This gradient in radio intensity is often accompanied by a steepening spectral index: from a relatively flat value at the edge of the relic, indicating freshly accelerated electrons, to a steeper value closer to the cluster core, where the electrons lose energy through synchrotron and inverse compton radiative processes (see **Fig. 1.6**, top right panel). However, high-sensitivity observations have recently revealed a diverse range of relic shapes, including filamentary structures (e.g., de Gasperin et al., 2022), inverted morphologies (e.g., Riseley et al., 2022a), and even face-on relics that lack the expected arc-like appearance(e.g., Rajpurohit et al., 2022). These complex morphologies challenge the classical understanding of relics as uniform structures, suggesting instead that they are intrinsically composed of multiple filaments and shaped by turbulent ICM dynamics. Recent TNG-Cluster simulations (Lee et al., 2024) further support this view, indicating that relics are not simple smooth arcs but rather fragmented and dynamically evolving features within the cluster environment.

A distinguishing feature of radio relics is that they often have a high fractional polarisation, i.e. $\gtrsim 20\%$-60%, at GHz frequencies (e.g., Bonafede et al., 2009b; Kale et al., 2012; de Gasperin et al., 2015a). Moreover, the polarisation angle orientation is remarkably uniform across the entire relic (e.g., van Weeren et al., 2010; Pearce et al., 2017, (see **Fig. 1.6**, bottom right panel)). The strong polarization results from the compression of the magnetic field frozen into the ICM, aligning unordered magnetic fields with the shock plane.

This characteristic is consistent with theoretical expectations for magnetic field alignment along the shock surface (Ensslin et al., 1998). Recent simulation showed that ICM shocks are indeed able to align a turbulent magnetic field, producing the observed degree of polarisation at the shock front. Moreover, they found that the post-shock region still hosts enough turbulent motions to cause the degree of polarisation to rapidly decrease.

In certain cases, diffuse radio emission appears to connect radio halos and relics within the same cluster. In some systems, the radio relic overlaps with the halo emissions, (e.g., Dallacasa et al., 2009; Carretti et al., 2013; van Weeren et al., 2016; Pasini et al., 2022); while in others (e.g., Bonafede et al., 2012; Hoang et al., 2017; Di Gennaro et al., 2018) the halo emission covers the entire area between double radio shocks. The physical origin of these bridges remains unclear. One possible explanation is that they represent a transition between different particle acceleration mechanisms—from first-order Fermi acceleration at the shock front to second-order turbulent re-acceleration in the post-shock region (e.g., Markevitch et al., 2005; Markevitch, 2012). Electrons could be re-accelerated downstream of the shock as they enter an extended turbulent region, where conditions favour the formation of a radio halo. However, projection effects must also be considered. As discussed in Rajpurohit et al. (2020); de Gasperin et al. (2020a), the observed connection between relics and halos may not always be physical but instead arise from line-of-sight superposition of two distinct plasma populations: the aging tail of the relic and the flatter, faint emission from the radio halo. This raises the need for deeper spectral and polarization studies to determine whether these features are truly connected or merely coincidental alignments.

Theoretically speaking, during a binary merger scenario, two opposed axial[12] shocks are expected to form, propagating outward along the merger axis. However, in the majority of cases, only one axial radio relic is observed. Double relics are, instead, relatively rare and typically associated with the "lucky" configuration of the mergers occurring on the plane of the sky. Thanks to this privileged point of view, double relics systems can be used to constrain the merger geometry and timescales involved (e.g. Roettiger et al., 1999; van Weeren et al., 2011a), as well as the efficiency of electron acceleration (e.g., Bonafede et al., 2012). One of the most prominent examples of a double radio relic system is CIZA J2242.8 + 5301, also known as the Sausage cluster, which will be the focus of this dissertation. In Chapter 3, we will explore this system in detail, examining its radio morphology, spectral properties, and implications for the understanding cluster magnetic fields.

Unlike radio halos (**Section 2.3.4**), statistical studies of relics have been comparatively limited. This is primarily due to their lower abundance: only $\lesssim 10\%$ of clusters are found to host radio relics (Kale et al., 2019; Zhou et al., 2022; Jones et al., 2023a). Additionally, their certain identification is challenging because of the difficulty of confirming them in the X-rays and other observational limitations related to projection effects, their irregular morphology and interactions with other sources. Initial statistical studies (van Weeren et al., 2009a; Bonafede et al., 2012; de Gasperin et al., 2015b) studied the correlation between merger properties and relics characteristics, such as the relic's linear size, their radio power, the double relic projected distance and the spectral index. However, the number of double radio relics of these samples was limited and therefore the statistical significance of the correlations is not sufficient to put loose constraints on models.

Recent low-frequency surveys (e.g., Kale et al., 2015; Jones et al., 2023a) have significantly expanded the known relic population, allowing for statistical studies of their properties. Jones et al. (2023a) confirmed and refined the previous foundings, showing that (i) the relic linear size correlates with their projected distance from the cluster center, and (ii) relic radio power scales steeply with the cluster mass. The first correlation indicates a tendency for larger relics to be located at greater distances from the cluster centre. This can be explained by the fact that the larger shock waves occur mainly in lower-density and lower-temperature regions, further from the centres. The second indicates that more powerful relics are generally found in higher-mass clusters. This phenomenon may be explained by considering that relics are generated by shock waves during galaxy cluster mergers, where the energy budget is determined by the total of the merging clusters. Jones et al. (2023a) also interestingly noticed that the occurrences at high and low mass are compatible, suggesting that there is no dependence on the cluster mass, unlike for RHs (Cassano & Brunetti, 2005a; Cuciti et al., 2015).

Radio relics not only provide insight into the origin of cosmic rays in galaxy clusters but also serve as key tracers of magnetic field properties in the ICM outskirts, as they are often found at distances reaching a significant fraction of the cluster's virial radius. However, key

[12] We specify *axial* as opposed to the so-called *equatorial* shocks. These shock are predicted by numerical simulation (e.g., Ha et al., 2018; Zhang et al., 2021), although they have not yet been observed. They form in an early stage, as the two dark matter clumps are approaching one another, propagating outward in the equatorial plane perpendicular to the merger axis.

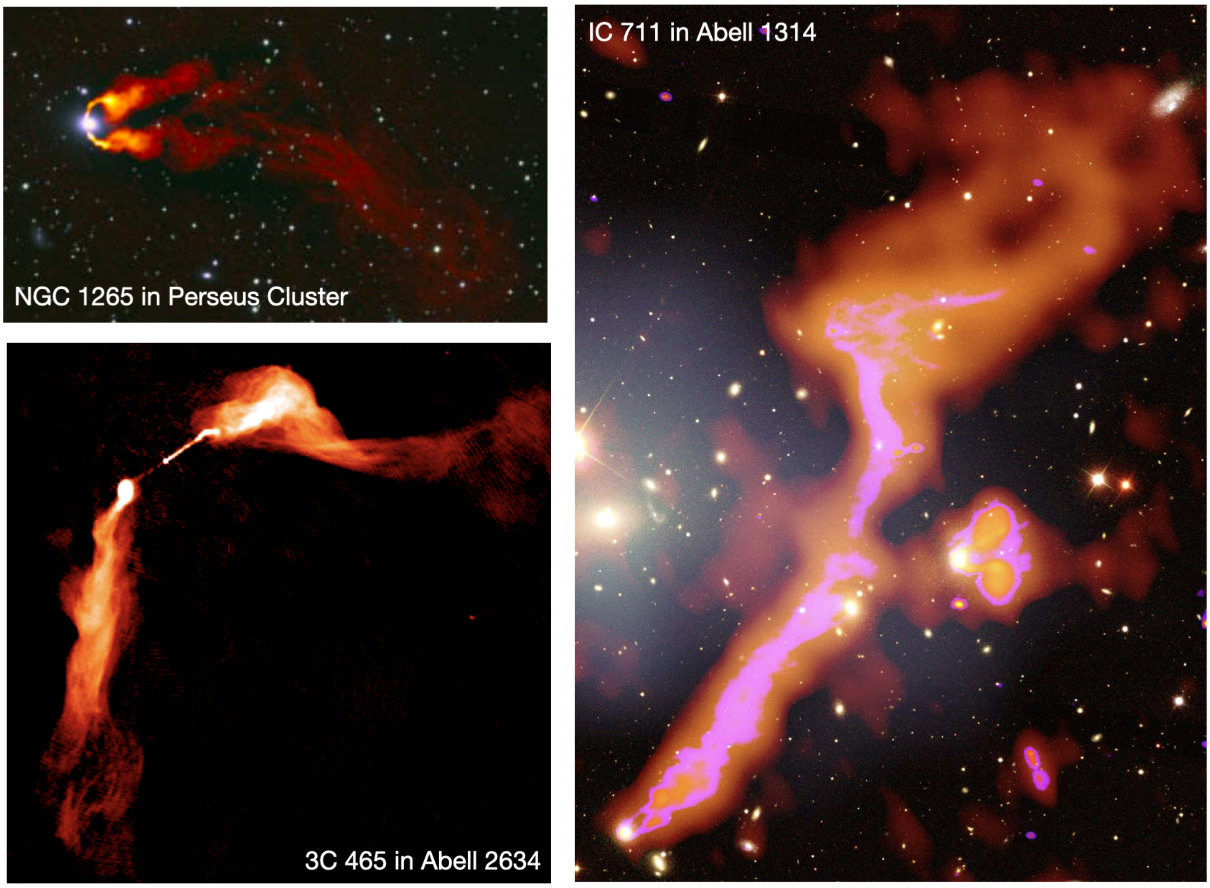

Figure 1.7: Examples of radio galaxies with disturbed morphologies. The NAT NCG 1255 member galaxy in the Perseus galaxy cluster (*top left*); the 3C 465 WAT radio galaxy, associated with the central dominant galaxy in Abell 2634 (*bottom left*) and the HT radio galaxy IC 711, found in Abell 1314 galaxy cluster. Credit: Gendron-Marsolais et al. (2021), NRAO/AUI/NSF; Hardcastle & Croston (2020), courtesy of Emmanuel Bempong-Manful; Wilber et al. (2019), LOFAR Surveys Team/NASA/CXC.

open questions remain regarding the efficiency of particle acceleration at cluster shocks, the role of fossil plasma from past AGN activity, and the impact of magnetic field amplification on relic formation and evolution.

1.4 Radio Galaxies in Galaxy Clusters

While baryonic matter in the form of galaxies constitutes only a few % of the total cluster mass, galaxies play a crucial role in shaping cluster evolution through their interactions with the ICM and feedback processes. Rich galaxy clusters host a diverse population of galaxies, including passively evolving ellipticals, star-forming spirals, and merger remnants resulting from dynamical galaxy-galaxy interactions or mergers (see e.g., Dressler, 1980; Boselli & Gavazzi, 2014). In fact, it is known that the cluster environment plays an important role in shaping the properties and evolution of the member galaxies, leading to a higher fraction of early-type systems compared to the field population, which is more likely to be composed by late-type galaxies (e.g. Alpaslan et al., 2015). Within this diverse galaxy population, a particularly significant role is played by radio galaxies, active galaxies characterized by radio emission originating from jets on scales from pc to Mpc (see Hardcastle & Croston, 2020, for a recent review on AGN). They act as sources of cosmic ray electrons and magnetic fields, while also injecting energy into the ICM via AGN feedback (see e.g., Gitti et al., 2012, review). Their interaction with the surrounding gas influences both the thermodynamic properties of clusters and the formation of large-scale diffuse radio structures, such as halos and relics (**Section 1.3**). AGN-driven jets structures are observed across a vast range of radio luminosity ($\sim$ 10 order of magnitude) and sizes ($\sim$ 6 orders of magnitude), see Fig. 2 of Hardcastle & Croston (2020). One of the classical yet widely used classification schemes is the Fanaroff-Riley (FR, Fanaroff & Riley (1974)) classification distinction which is based on the morphology and radio brightness distribution of their jets and lobes. Radio galaxies are divided into two main categories: center-brightened FRI, with initially relativistic jets that quickly decelerate on kpc scale (e.g., Laing et al., 2008a); and edge-brightness FRII, where the jets remain relativistic over large distances before terminating in bright hotspots at the edges of their lobes (Pyrzas et al., 2015, e.g.,). The division between FR I and FR II occurs at a critical radio luminosity threshold of ($\sim 10^{25}\mathrm{W\,Hz^{-1}}$) at 1.4 GHz, with FR I sources generally lying below this threshold and FR II sources above it (Ledlow & Owen, 1996). However, this transition is not purely determined by jet power alone, but it also depends on external environmental factors, such as the density and pressure of the surrounding medium, which influence jet stability and morphology. It is generally accepted that this structural difference results from the interplay of jet power and environmental density. At a given jet power, jets in low-density environments remain relativistic and well-collimated over large distances, leading to the formation of FR II sources. Conversely, in denser environments, such as galaxy clusters, jets are more prone to deceleration, gas entrainment, and turbulence, resulting in the plume-like morphology characteristic of FR I sources. It is important to note that most historical studies of FR classification have been conducted at ~GHz frequencies. However, since GHz observations are more sensitive to flatter-spectrum emission (such as the one of the core or hot-spots), the morphological and luminosity-based separation between FR I and FR II may not fully hold at lower frequencies, where steep-spectrum emission from diffuse lobes dominates. As a matter of fact, thanks to the increasing sensitivity of recent low-frequency radio surveys, an unexpected population of low-luminosity, edge-brightened FR II radio galaxies (FR II-low) has been identified (e.g., Capetti et al., 2017; Mingo et al., 2019). The study by Mingo et al. (2019) found that FR II-low sources constitute a substantial fraction of the FR II population at $z < 0.8$. However, this discovery remains consistent with the Fanaroff-Riley paradigm, as FR II-low sources tend to reside in sparsely populated environments, allowing their jets to remain undisrupted despite their lower power.

The majority of radio galaxies do not live in rich cluster environments; however, when they do, they usually show distorted morphologies (see **Fig. 1.7**). These distortions are caused by the dynamical interaction between the radio jets and the surrounding dense ICM (Garon et al., 2019; Vardoulaki et al., 2025). It is widely accepted that the bending of the jets or tails is due to the radio-emitting plasma being deflected by the ICM via ram pressure P_{ram} while the host galaxy is moving through the cluster. This effect (originally proposed by Gunn & Gott 1972) is equal to:

$$P_{ram} = \rho \upsilon^2 \tag{1.3}$$

where ρ is the density of the ICM, and υ is the relative velocity between the galaxy and the ICM. However, it is very likely that other effects (known under the label of "cluster weather") are playing along in the formation of these types of radio galaxies (Burns, 1998). Dynamical interactions, such as cluster–cluster mergers or group accretion onto clusters, are thought to influence the bending of the jets in the ICM. (Rickel et al., 2025) found that merging cluster environments have a statistically significant higher proportion of disturbed radio sources, proving that such merging environments can affect the morphology of cluster AGN.

As mentioned before, FR I sources are typically found in dense environments, such as galaxy clusters, where external pressure helps confine and disrupt the jets (see Fig. 3 of Hardcastle & Croston 2020; Croston et al. 2019, and also the works of Hill & Lilly 1991; Rodman et al. 2019). In this context, FR I radio galaxies exhibit a variety of morphology and have been further divided (see examples illustrated in **Fig. 1.7**). The first morphological classification by Owen & Rudnick (1976) is based on the angle between the radio tails and the core of the galaxy (see also Miley, 1980, for a review). Narrow-angle tails (NATs; Venkatesan et al., 1994; Feretti et al., 1998) have angles between the two jets smaller than 90°, because of the high ram pressure they experience that leads to the narrow V- or L-shape they assume. NAT morphologies are typically found to be hosted byhigher-velocity host galaxies, often moving through the ICM at several hundred km s^{-1}.

Wide-angle tails (WATs; Burns et al., 1986; O'Donoghue et al., 1993; Klamer et al., 2004; Mao et al., 2010; Gómez & Calderón, 2020) show C-type morphologies with angles between the two tails greater than 90° but smaller than 180°. They are usually thought to experience weaker ram pressure, caused by low velocities relative to ICM and/or lower density of the surrounding ICM. Since WAT are typically associated with a dominant galaxy in a cluster of galaxies (e.g. 3C 465 Riley & Branson, 1973, also shown in **Fig. 1.7**), they were initially assumed to move slowly with respect to the ICM (e.g., Quintana & Lawrie, 1982), thus posing a problem due to the insufficient dynamical pressure to create the observed disrupted morphologies. However, later radial velocities studies (e.g., Oegerle & Hill, 2001) revealed that a significant fraction of BCGs actually exhibit larger velocities with respect to their host clusters (~200–400 km s^{-1}). Moreover, because sloshing gas motions have been observed in several clusters with WATs (e.g., Douglass et al., 2018; Tiwari & Singh, 2022), it is possible that even in the absence of high-velocity host galaxy, large-scale ICM motions can provide enough ram pressure to account for WAT morphologies.

Lastly, the head-tail (HT) radio galaxies (Ryle & Windram, 1968; Hill & Longair, 1971; Miley, 1973; Sebastian et al., 2017; Cuciti et al., 2018; Wilber et al., 2018; Srivastava & Singal, 2020; Lal, 2020; Müller et al., 2021; Botteon et al., 2021b; Bruno et al., 2024; Koribalski et al., 2024), are NATs whose distinctive feature is a very elongated structure formed by the radio jets. In HT radio galaxies, both jets are bent in the same direction and threfore it is not always possible to resolve them. FR I sources in clusters — including WATs, NATs and HTs — represent a crucial component in understanding the interplay between radio galaxies and their surrounding environment. Interestingly, they have increased dramatically thanks to the recent LOFAR surveys Pal & Kumari (2023b); Mingo et al. (2019). In this thesis, HT galaxies in clusters are studied in detail in Chapter 2, with insights derived from ultra-low-frequency observations.

1.4.1 Remnants, Phoenixes and GreET sources

Radio galaxies deposit relativistic plasma into the ICM, and over time, the synchrotron-emitting electrons lose energy due to radiative losses. As discussed in **Section 1.2.4**, in addition to synchrotron losses, electrons further radiate through Inverse Compton scattering of CMB photons with a characteristic radiative time given by **Eq. (1.2)**.

As a result of these processes, AGN's radio lobes can fade into so-called remnant radio galaxies: relic lobes of past AGN activity no longer fueled by a central engine (see Morganti et al., 2021, review). Remnant radio galaxies are difficult to identify due to their low surface brightness (requiring sensitive instruments) and steep spectrum (as they are expected to be intrinsically aged plasma). Once again, observations at 50-200 MHz frequencies are ideal for detecting lobes of remnant galaxies and reconstructing their past activity (e.g., Brienza et al., 2017; Mahatma et al., 2018; Shulevski et al., 2024; Nair et al., 2024). In this regard, spectacular is the case of the Nest200047 galaxy group (Brienza et al., 2021, 2025) where the authors, thanks to LOFAR observations, were able to identify multiple cycles of radio activities. This study further demonstrates that radio bubbles from past AGN outbursts can be ejected in the ICM up to the virial radius, providing a population of relativistic electrons that can act as seeds for the formation of the large-scale diffuse emission, described in **Section 1.3**.

In certain conditions, these fossil plasma sources can be revived, giving rise to the so-called radio phoenixes and Gently Re-Energised Tails (GReETs). The re-energization happens in situ - that is, at the location of the aged plasma - via mechanisms unrelated to the AGN activity itself. Their study is crucial to understanding the interplay between the ICM, radio galaxies, and particle re-acceleration mechanisms. Despite being usually discussed in the context of diffuse cluster emission (**Section 1.3**), these sources have a natural and clear connection to AGN activity and for this reason are presented in this section.

Radio Phoenixes Radio phoenixes are steep-spectrum sources ($\alpha \sim 1.5 - 2$) typically extending up to $\sim$ 500 kpc and exhibiting a variety of irregular morphologies, from roundish to filamentary (Kempner et al., 2004; Clarke et al., 2013; de Gasperin et al., 2015b; Mandal et al., 2019). They sometimes resemble radio relics, but their orientation is often parallel to the merger axis. Moreover, when a polarization study was possible, it showed generally lower polarization and larger variations than for cluster radio shocks (e.g., Slee et al., 2001). In many cases, their spectra are curved, with high-frequency spectral steepening (e.g., van Weeren et al., 2009b). Lastly, the resolved spectral index distribution across these sources is oftentimes irregular without clear trends (e.g., Cohen & Clarke, 2011; Kale et al., 2012; Mandal et al., 2020; Raja et al., 2024a). These sources are thought to be the result of old radio lobes from AGN undergoing adi-

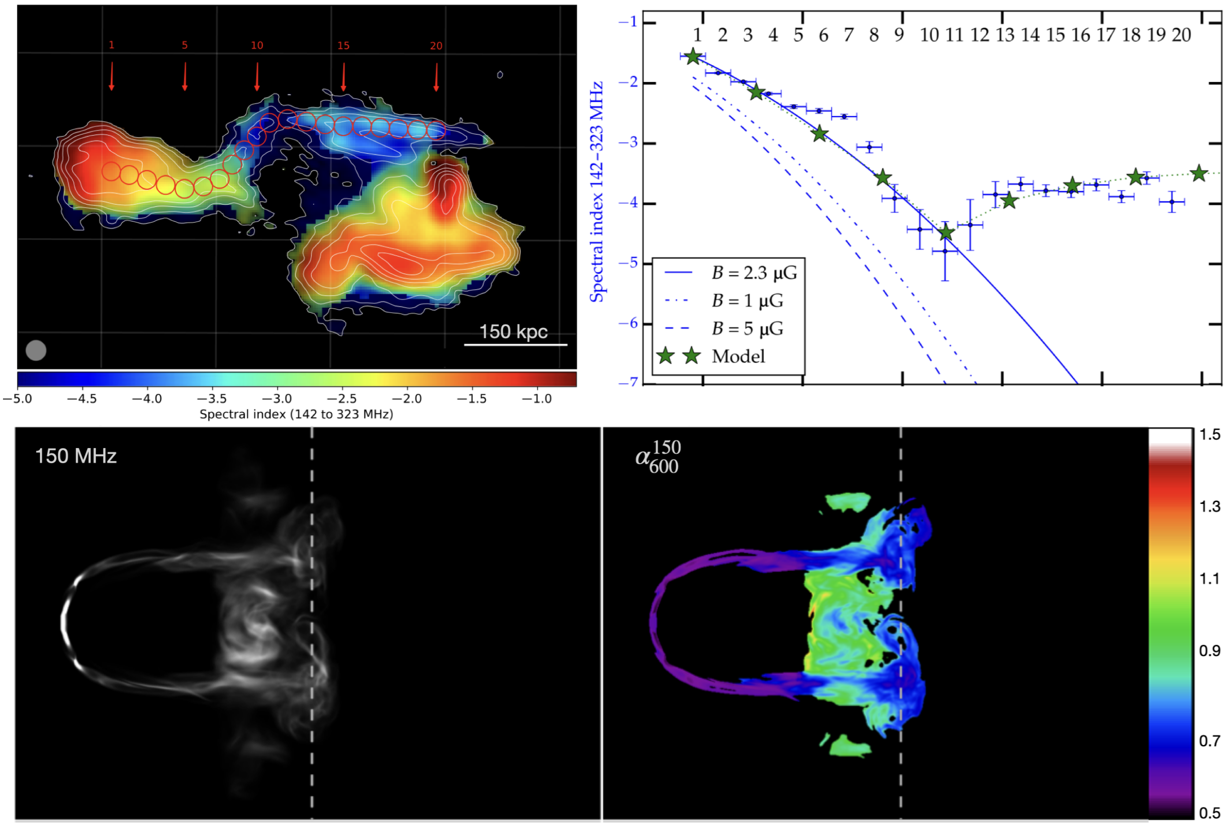

Figure 1.8: *Top panels*: Spectral index map of the GReET emission in Abell 1033. Spectral index values are calculated between 142 to 323 MHz and the contours are from LOFAR observation at 142 MHz (left). The spectral index profile is calculated in 20 regions along the tail (right). Credit: de Gasperin et al. (2017). *Bottom panels:* Result of a simulated interaction between a shock and a radio galaxy giving rise to a radio phonexi emission. For this simulation, the jet axes are orthogonal to the shock normal. This snapshot is taken after 104 Myr. On the left, the total intensity at 150 MHz with arbitrary units. On the right, the spectral index α_{600}^{150} between 150 and 600 MHz. The location of the shock is outlined in dashed gray lines. Credit: adapted from Nolting et al. (2019b).

abatic compression by shocks passing through the ICM (Enßlin & Gopal-Krishna, 2001; Ensslin & Brüggen, 2001; Enßlin & Brüggen, 2002; Nolting et al., 2019b,a). The relativistic nature of the plasma within old radio lobes results in a high sound velocity, which prevents the shock in the ambient medium from penetrating into the radio plasma when these lobes encounter shock waves in the ICM. Instead, the fossil radio plasma would get adiabatically compressed, and the energy gain of the electrons is expected to be mainly due to adiabatic heating. This compression increases the energy of relativistic electrons and amplifies magnetic fields within the plasma, leading to a temporary revival of synchrotron emission, observable as radio phoenixes. Enßlin & Gopal-Krishna (2001) demonstrates that fossil radio plasma, even up to 2 Gyr old, can be revived by such compression mechanisms. This formation mechanism has not only the potential to reproduce the observed properties of phoenixes (as shown by recent simulations Nolting et al., 2019a,b, also reported in **Fig. 1.8**), but is also physically plausible as shock waves are ubiquitous in the clusters dynamic environment (as discussed in **Section 1.2.2**). However, this scenario still lacks robust observational evidence, confirming the spatial coincidence between shock waves and phoenixes. To date, Abell 2443 (Whyley et al., 2024) is the only case where a shock front is reported at the precise phoenixe location. In other cases, shock features are reported near the phoenix emission (Schellenberger et al., 2022; Rahaman et al., 2022; Raja et al., 2024a).

Gently Re-Energised Tails (GReETs) Unlike radio phoenixes, GReETs are found in fossil tails of radio galaxies, where a characteristic flattening of the spectral index occurs in regions far from the AGN core (see **Fig. 1.8** from de Gasperin et al., 2017; Edler et al., 2022). Standard tailed-sources (such WATs, NATs and HTs) typically exhibit progressive spectral steepening due to ageing, while in GReETs, this trend is suddenly reversed or flattened. The prototype case is in A1033 (de Gasperin et al., 2017) where after an initial standard ageing, the spectral index maintains with a steep value over large distances. This would imply a scenario where the particle acceleration time scale is comparable to the radiative time below 100 MHz. This spectral behaviour suggests a gentle, extended re-acceleration process, likely induced by ICM turbulence. The proposed mechanism involves Rayleigh-Taylor and Kelvin-Helmholtz instabilities arising in the radio tails, which generate turbulent waves that re-accelerate electrons via second-order Fermi processes. This turbulence would need to be continuously forced in the tail by the interaction between perturbations in the surrounding medium with the tail itself. Additional candidates identified in Cuciti et al. 2018; Wilber et al. 2018; Ignesti et al. 2022; Pasini et al. 2022. An example of GReETs is discussed in Chapter 2.

1.5 Low-Frequency Radio Astronomy with LOFAR

The opening of the low-frequency window (< 300 MHz) that happened in the last 10 years has revolutionized radio astronomy — with incredible results in particular for galaxy clusters. This was possible thanks to the significant improvement in instrumental sensitivity of modern instruments, advanced calibration and imaging techniques and the development of successful large surveys. Among the various low-frequency instruments currently available, a leading role has been played by the LOFAR interferometer, which has not only achieved successful radio observation

Figure 1.9: The LOFAR antennas and configuration. *Left:* Distribution of LOFAR stations in Europe. Image credit: ASTRON. *Right:* Low Band Antenna (top) and High Band Antenna tile (bottom). The inset shows the LBA amplifier that is cast in resin to keep the mice out. The HBA picture shows a zoom-in into the styrofoam support antenna structure and the 15 cm space between HBA tiles to allow for water draining and access to the cover anchors. Image credit: van Haarlem et al. (2013a).

down to ~ 20 MHz but has also played a key role as Square Kilometre Array (SKA) pathfinder. Its innovative use of phased array technology, early-stage signal digitization, and advanced calibration techniques has provided invaluable insights into the challenges and methodologies required for the next-generation SKA-Low, being the most advanced sub-100 MHz facility. Some of the astonishing results reached by LOFAR in its first 10 years of activity in the context of the diffuse radio sources and radio galaxies in galaxy clusters are outlined in **Section 1.3** and **Section 1.4**. Together with that, the results presented in this dissertation Chapter 2, Chapter 3, Chapter 4 are a valuable showcase of LOFAR LBA results.

The LOw-Frequency ARray (LOFAR, van Haarlem et al. (2013a)) is currently the largest radio telescope operating at frequencies from 10 to 240 MHz (wavelengths of 30–1.2 m), the lowest rage that can be observed from Earth. The core of the array was built in the Netherlands but it has expanded across Europe **Fig. 1.9** (*left*). Currently, LOFAR consists of 24 Core stations around Exloo (a city located in the Netherlands), 14 Remote stations distributed over the Netherlands and 14 International stations distributed over Europe. These stations have no moving parts and, due to the effectively all-sky coverage of the component dipoles, give LOFAR a large field-of-view (FoV) - from $3°$ to $10°$ depending on the ised antennas. LOFAR antenna stations operate as phased arrays, where signals are aligned by applying phase shifts to ensure that waves arriving from the desired direction are coherently summed. For example, as an incoming wavefront reaches the array, it first encounters the leftmost antenna and reaches the rightmost antenna last. To compensate for this delay, the signal from the leftmost antenna is artificially delayed by the same amount before being combined with the signal from the rightmost antenna, ensuring constructive interference in the target direction. Electronic beam-forming techniques are crucial to make the system agile, able to rapidly repoint the telescope and observe multiple targets simultaneously.

LOFAR consists of two types of antennas (**Fig. 1.9**, *right*):

- **Low Band Antennas (LBAs)**: Designed to operate from 10–90 MHz, though due to strong radio frequency interference (RFI) at the lower and upper ends, observations are typically conducted between 30–80 MHz. Each LBA element is a simple dipole, sensitive to two orthogonal linear polarizations (X and Y), placed above a conducting ground plane.
- **High Band Antennas (HBAs)**: Operating in the 120–240 MHz range, where sky noise no longer dominates system noise. Each HBA tile consists of 16 bow-tie-shaped dipole antennas arranged in a 4×4 grid. To minimize system noise, a different design from LBAs was required.

LOFAR antennas are grouped into stations, which function similarly to the dishes in traditional radio interferometers. However, unlike conventional telescopes, LOFAR's antennas are fixed and do not physically move. Instead, pointing and tracking are achieved through beamforming, where signals from multiple antennas are combined electronically. There are three types of LOFAR stations, classified by their distance from the array core:

- **Core stations (CS)**: Densely clustered in the Netherlands, providing short baselines and high sensitivity to extended emission.
- **Remote stations (RS)**: Located farther from the core, extending LOFAR's resolution and imaging capabilities.
- **International stations (IS)**: Spread across Europe, contributing to the longest baselines (up to 2000 km) and enabling sub-arcsecond resolution. Next to the Netherlands (38 stations), these are Germany (6 stations), Poland (3 stations), France, Ireland, Latvia, Sweden, and the United Kingdom (one station each); stations in Italy and Bulgaria are funded to be built soon.

LOFAR's beamforming flexibility enables multiple simultaneous observations and rapid repointing, making it ideal for studying transient sources, pulsars, cosmic rays, and large-scale diffuse emission. With baselines spanning 50 m to 2000 km, LOFAR achieves a resolution ranging from a few degrees to sub-arcsecond scales, making it a powerful tool for low-frequency radio astronomy.

1.5.1 Science with LOFAR

LOFAR's multi-beaming capabilities enable astronomers to conduct research in multiple and diverse range of astrophysical phenomena, from probing the early Universe before the first stars and galaxies (the Dark Ages) to surveying vast regions of the low-frequency radio sky and monitoring for radio transients from the most energetic cosmic explosions. One of their most compelling applications is the detection of highly redshifted 21 cm line emission from the Epoch of Reionization (from $z = 6$ to $z = 20$, e.g. Zaroubi et al. 2012). As neutral hydrogen at these redshifts emits at 21 cm (1420 MHz), cosmic expansion shifts this signal into the 70–200 MHz range, perfectly aligning with LOFAR's observing capabilities.

While solar activity significantly impacts the Earth's ionosphere -introducing signal fluctuations that degrade the quality of radio observations and therefore challenge low-frequency astronomy - this same activity can also represent a valuable scientific opportunity. For this reason, LOFAR can be used for solar science and space weather studies, as many solar phenomena, such as flares and coronal mass ejections (CMEs), produce strong radio signatures within this frequency range (e.g., Zucca et al., 2018; Maguire et al., 2021).

LOFAR can provide new opportunities to probe magnetic fields across different environments. Through observations of synchrotron emission and Faraday rotation, LOFAR contributes to the study of magnetic fields in the Milky Way, galaxy clusters, and large-scale cosmic filaments (e.g., O'Sullivan et al. 2018; Stuardi et al. 2020; Piras et al. 2024).

One of the most exciting capabilities of LOFAR resides in its international stations, that allow for Very Long Baseline Interferometry (VLBI)). HBA-VLBI has already achieved subarcsecond imaging at frequencies around 150 MHz, an unprecedented result at such low frequencies (Morabito et al., 2025). Early works started about ten years ago (e.g. Varenius et al., 2015, 2016) leading to the development of a more standardized and partially automated calibration workflow by (Morabito et al., 2022). Even if a fully automated pipeline is still in progress, the quality of HBA-VLBI results is remarkable (e.g., Sweijen et al., 2022; de Jong et al., 2024) This has opened new frontiers for detailed studies of compact radio sources, such as AGN cores and for testing jet physics, which would otherwise remain unresolved at standard LOFAR resolutions (e.g., Harwood et al., 2022; Timmerman et al., 2022). LBA-VLBI imaging still lags behind HBA in terms of routine application and reliability, with only a few successful observation to date (Morabito et al., 2016; Groeneveld et al., 2022). Because ionoshperic phase effects scale inversely with frequency, LBA-VLBI is affected three times more than HBA, increasing the difficulty of the calibration, which becomes highly dependent on excellent ionospheric conditions. Nevertheless, these studies have proven that using LBA international antennas is feasible, and this is an exciting development for the future.

Finally, a big role is played by the extensive surveys across the entire Northern Sky, which are producing unprecedently large catalogues of radio sources (see next **Section 1.5.2**).

1.5.2 LOFAR Surveys

Large-are radio continuum surveys became fundamental in radio astronomy, as they offer homogeneous, statistically robust datasets that can be used for statistical studies of large samples of objects, as well as for the discovery of new classes of sources (see Norris, 2017, for an overview of continuum surveys).

At the moment, LOFAR is surveying the whole Northern Sky with unprecedented sensitivity, resolution, and sky coverage. There are three ongoing surveys, namely the LOFAR Two-metre Sky Survey (LoTSS; Shimwell et al., 2017), the LOFAR LBA Sky Survey (LoLSS; de Gasperin et al., 2021) and LOFAR Decameter Sky Survey (LoDeSS, Groeneveld et al. in prep.).

LoTSS is performed using HBA at frequencies between 120 and 168 MHz, reaching a sensitivity of $\sim 100\,\mu$Jy/beam at an angular resolution of $6''$ (Shimwell et al., 2019, 2022). It is an ongoing project, which started in 2017, had its second data released in 2022 (completing 27% of the northern sky) and it is now approaching its third data release. Its success is not only visible from the high-fidelity imaging (being almost an order of magnitude more sensitive than the current best high-resolution sky survey, such as FIRST (Becker et al., 1994)) but also from the resulting high-quality catalogues, are expected to detect over 10 million radio sources, predominantly star-forming galaxies, with a large proportion of active galactic nuclei. Among LoTSS data products, the most relevant for this thesis are Hoang et al. (2022); Botteon et al. (2022a) - for the detection of diffuse radio sources - the latter of which, worked as a starting point for statistical studies such as Bruno et al. (2023b); Zhang et al. (2023); Cassano et al. (2023); Cuciti et al. (2023); Jones et al. (2023b). Moreover, LoTSS has proven successfull in assembling large samples of AGN jet-related emission, Pal & Kumari (2023a); Gopal-Krishna et al. (2024).

Complementing LoTSS, LoLSS covers instead the low-end of the LOFAR frequency range, the one from 42 to 66 MHz at a resolution of $15''$ and achieving a noise of $1-2\,$mJy/beam, depending on the declination and observing conditions (de Gasperin et al., 2023). Together with the studies presented in this dissertation, the first data release of LoLSS proves that LOFAR LBA is the best instrument to date in terms of performance to observed at the lowest energy end of the radio window.

Lastly, LoDeSS is designed to explore the sky at even lower frequencies, between 14 and 30 MHz, pushing the boundaries of low-frequency radio astronomy and probing the largely unexplored decameter wavelength regime. Some preliminary results are presented in Groeneveld et al. (2025b).

Looking ahead, the future for LOFAR is bright as the next LOFAR2.0 upgrade promises to further improve the telescope's capabilities. In fact, LOFAR 2.0 will introduce several key improvements, including the possibility of simultaneous low- and high-band observations, increased FoV and improvement in sensitivity and automated data processing. Significant for this works and its future developments, the parallel LBA and HBA observing is expected to improve the LBA sensitivity by a factor of five.

1.6 Scope of this Thesis

This thesis aims to investigate the origin and properties of non-thermal radio emission in galaxy clusters, in the low- ($\lesssim 300\,$MHz) and ultra-low- ($\lesssim 100\,$MHz) radio frequency regime. This regime is particularly powerful for two main reasons. First, because of the characteristic steep synchrotron spectra, radio sources are intrinsically brighter at lower frequencies, making them detectable above the noise level. Also, as relativistic electrons age, their emission fade rapidly at GHz frequencies, while remaining detectable in the $\sim 50-200$ MHz range. Second, at higher frequencies only the most energetic cosmic-ray acceleration processes are visible - sometimes referred to as the "tip of the iceberg". This metaphor refers to our potentially incomplete knowledge of non-thermal phenomena. In fact, a "silent" majority of sources, powered by less-energetic phenomena - such as ultra-steep spectrum radio halos, radio phoenixes, and gently re-energised sources - becomes visible only at ultra-low frequencies (< 100 MHz), representing the (so-far) unseen, submerged part of the iceberg. By using radio observations at the lowest radio frequencies currently accessible with LOFAR, I also aim to study these phenomena while also investigate the life cycle of cosmic-ray electrons in galaxy clusters: from their injection and consequent spectral ageing to re-acceleration.

The main scientific questions addressed in this thesis are:

i. How does the interaction between AGN jets and the surrounding ICM affect the morphology and spectral evolution of radio galaxies jets?

ii. Which processes are responsible for re-acceleration of radio galaxies-connected plasma in clusters of galaxies?

iii. How can the combination of low- and ultra-low- frequency observations constrain the injection spectrum of radio relics and the strength of cluster merger shocks?

iv. Can the standard diffusive acceleration model fully explain shock's radio emission at galaxy clusters' outskirts?

In **Chapter 2**, I focused on the three head-tail radio galaxies in ZwCl 0634.1+4747. I present a multi-frequency study combining LOFAR LBA 53 MHz with LOFAR HBA 144 MHz, GMRT 323 MHz, VLA 1.5 GHz and X-ray XMM-Newton data. The radio data reduction was performed and described in Cuciti et al. (2018, 2022), while the X-ray data reduction was carried out by C. Spinelli. I took care of the scientific analysis, including flux and spectral index profiles, model fitting and interpretation. The low-frequency observations allowed to detect and study the radio galaxies jets up to a projected size of $\sim$ 1 Mpc, showing that radio galaxies can enrich the ICM with fossil electrons also on a cluster-size level. I also show that the observed spectral flattening and surface brightness enhancements in the tails' profiles suggest the presence of a turbulence-induced, gentle re-acceleration mechanism acting during the interaction of the tail with the surrounding ICM.

In **Chapter 3**, I present for the first time the LOFAR LBA observations at 45 MHz of the well-known merging galaxy cluster CIZA J2242.8+5301. In this project, I carried out the full calibration and imaging of the LOFAR LBA observation at 45 MHz, achieving a therml-noise-limited image at ultra-low radio frequencies. These data were combined with HBA (145 MHz), GMRT (325, 610 MHz), WSRT (1.2, 1.4 GHz); and VLA (1.5, 3 GHz). Thanks to the wealth of available data, I derived the integrated and spatially resolved spectral index and curvature maps. I extracted and modelled the surface brightness profiles of the northern relic, including projection effects and shock deformation. This allowed to provide a more realistic description of the observed emission and test the ability of the standard diffusive shock acceleration to reproduce the observed data. The toy model was developed by M. Hoeft, with my assistance in both its development and testing. I contributed to the observational constraints and provided the necessary radio measurements to integrate into the model, thereby enabling a direct ad-hoc comparison with the data of this specific galaxy cluster.

In **Chapter 4**, I investigated the merger scenario and diffuse radio emission in the dynamically disturbed cluster Abell 746. The multi-frequency analysis included LOFAR LBA (53 MHz), LOFAR HBA (144 MHz), uGMRT (650 MHz), and VLA (1.4 GHz) data. I produced spectral index maps and computed the integrated spectra of the diffuse radio sources. I performed an exponential profile fitting to disentangle the central halo emission from overlapping relic-like features. This allowed me to classify the central source as an ultra-steep spectrum radio halo and place it within the framework of turbulent re-acceleration models.

For all the outlined projects, I was the lead author and I was responsible for the scientific analysis, as well as the manuscript writing. The other coauthors assisted with the preparation of the manuscript, acted as scientific consultants and provided complementary radio and X-ray data that enabled the multi-frequency analysis presented in this work. These contributions are explicitly acknowledged throughout each chapter in more detail, as they are part of previously published works.

Lastly, in **Chapter 5** I summarize my results and discuss how they fit in the broader context of galaxy cluster's physics. Furthermore, I outline possible directions for future research works in the context of upcoming radio surveys and advanced technical capabilities.

2 Re-energisation of AGN head-tail radio galaxies in the galaxy cluster ZwCl0634.1+47474

G. Lusetti, F. de Gasperin, V. Cuciti, M. Brüggen, C. Spinelli, H. Edler, G. Brunetti, R. J. van Weeren, A. Botteon, G. Di Gennaro, R. Cassano, C. Tasse, and T. W. Shimwell. **MNRAS 528, 141–159 (2024)**

Abstract

Low-frequency radio observations show an increasing number of radio galaxies located in galaxy clusters that display peculiar morphologies and spectral profiles. This is the result of the dynamical interaction of the galaxy with the surrounding medium. Studying this phenomenon is key to understanding the evolution of low-energy relativistic particles in the intracluster medium. We present a multi-frequency study of the three head-tail (HT) radio galaxies and the radio halo in the galaxy cluster ZwCl0634.1+4747. We make use of observations at four frequencies performed with LOFAR LBA (53 MHz), HBA (144 MHz), GMRT (323 MHz) and VLA (1518 MHz) data. The use of extremely low radio frequency observations, such as LOFAR at 53 and 144 MHz, allowed us to detect the extension of the tails up to a distance of ∼ 1 Mpc. We extracted spectral profiles along the tails in order to identify possible departures from a pure ageing model, such as the Jaffe-Perola (JP) model, which only involves synchrotron and inverse-Compton losses. We found clear evidence of departures from this simple ageing model, such as surface brightness enhancement and spectral flattening along all of the tails. This can be interpreted as the consequence of particle re-acceleration along the tails. Possible explanations for this behaviour include the interaction between a shock and the radio tails or a turbulence-driven re-acceleration mechanism. We show that the latter scenario is able to reproduce the characteristic features that we observed in our profiles.

2.1 Introduction

Galaxy clusters host a large variety of radio emission, generally divided between diffuse radio sources van Weeren et al. (2019) (van Weeren et al., 2019) and radio galaxies (Hardcastle & Croston, 2020). These non-thermal emissions are the results of relativistic cosmic-ray electrons (CRe) interacting with the cluster or galactic magnetic field.

Radio galaxies in clusters of galaxies usually show distorted morphologies (O'Dea & Owen, 1985; Feretti & Giovannini, 2008; Garon et al., 2019), because of the dynamical interaction between the radio jets and the surrounding dense ($n_e \sim 10^{-2} - 10^{-4}\,\mathrm{cm}^{-3}$), hot ($10^7 - 10^9\,\mathrm{K}$) intra-cluster medium (ICM). The first morphological classification by Owen & Rudnick (1976) is based on the angle between the radio tails and the core of the galaxy (see also Miley, 1980, for a review). Narrow-angle tails (NATs; Venkatesan et al., 1994; Feretti et al., 1998) have angles between the two jets smaller than 90°, because of the high ram pressure they experience that leads to the narrow V- or L-shape they assume. Wide-angle tails (WATs; Klamer et al., 2004; Mao et al., 2010) show C-type morphologies with angles between the two tails greater than 90° but smaller than 180°. They are usually thought to experience weaker ram pressure, caused by low velocities relative to the cluster centre and/or lower density of the surrounding ICM. Among these types, we focus on the head-tail (HT) radio galaxies (Ryle & Windram, 1968; Hill & Longair, 1971; Miley, 1973; Sebastian et al., 2017; Cuciti et al., 2018; Srivastava & Singal, 2020; Lal, 2020; Müller et al., 2021; Botteon et al., 2021b), NATs whose distinctive feature is a very elongated structure formed by the radio jets. In HT radio galaxies, both jets are bent in the same direction and thus it is not always possible to resolve them. Their radio surface brightness usually peaks close to the host (optical) galaxy and gradually decreases along the tail that can reach up to hundreds of kiloparsecs (e.g., Srivastava & Singal, 2020; Botteon et al., 2021b). Their spectral index becomes steeper, moving from the core towards the tail (e.g., Cuciti et al., 2018; Wilber et al., 2018), while the fractional polarisation increases along the jets (Feretti et al., 1998; Müller et al., 2021), reflecting an increase of the degree of ordering of the magnetic field. However, after the jets are launched into the ICM, relativistic electrons are visible only for tens of Myrs at GHz frequencies because of their energy losses, owing to synchrotron and Inverse-Compton (IC) emission. Thus, these tails left behind by the galaxy moving within the cluster are expected to fade quickly, becoming invisible at high frequencies. Because of the longer cooling times of low-energy CRe, low-frequency observations are crucial for identifying and tracing CRe for much longer.

In fact, with the advent of low-frequency (< 1 GHz) radio astronomy, tails extending to very long distances have become more common and can be studied in detail (Sebastian et al., 2017; Wilber et al., 2018; Botteon et al., 2021b; de Gasperin, 2017; Edler et al., 2022). In this context, the LOw-Frequency Array (LOFAR; van Haarlem et al., 2013a), being the largest and most sensitive radio-interferometer in the 10-240 MHz regime, has made many recent contributions to the field (e.g. Mandal et al., 2020; Pal & Kumari, 2023a).

Moreover, in some cases the tails show peculiar properties, such as an increase in surface brightness and flattening of the spectral index along the tail (e.g., Sijbring & de Bruyn, 1998; Parma et al., 1999; Giacintucci et al., 2007; de Gasperin, 2017). To explain such behaviours far from the host galaxy, the presence of re-energetization processes has been proposed. In fact, re-acceleration of CRe would be able to power the population of aged electrons initially injected by the AGN, making them visible at larger distances, where they would be expected to disappear owing to radiative losses. For example, de Gasperin (2017) proposed a re-acceleration mechanism invoking turbulence driven into the tail by interactions with the ICM. This would create the so-called gently re-energized tail (GReET; de Gasperin, 2017; Edler et al., 2022) sources. Müller et al. (2021) suggest the transition from laminar to turbulent flow as the cause of gentle re-acceleration of the electrons along the tail. They also point out that for complex morphologies, more than one AGN cycle, i.e. a change in the injection rate, must be taken into account to explain the entire appearance of the jets. In other cases, adiabatic compression (Enßlin & Gopal-Krishna, 2001; Enßlin & Brüggen, 2002) would be able to form radio phoenices, revived fossil plasma from old radio lobes. Radio phoenices usually show an irregular morphology, steep spectral index ($\alpha \sim < -1.5$ with the $S_\nu \propto \nu^\alpha$ for the synchrotron emission) and curved integrated spectra (Kempner et al., 2004; van Weeren et al., 2009a, 2011e; de Gasperin et al., 2015b; Mandal et al., 2019; Duchesne et al., 2021; Pasini et al., 2022). A first attempt to systematically study radio phoenices was performed by Mandal et al. (2020). They found a non-uniform spectral index across the sources, suggesting a possible mix of cosmic-ray populations with different ages, losses, and re-acceleration efficiencies. Regardless of the type of mechanism that generates them, sources that trace re-energised AGN radio plasma are characterized by very steep spectra. Thus, low-frequency facilities, such as LOFAR, are ideal to study these phenomena.

An increasing number of galaxy clusters is also observed to host diffuse Mpc-scale sources, called radio halos (see van Weeren et al., 2019, for a review). Radio halos are steep spectrum ($\alpha < -1.1$), centrally located sources, whose morphology roughly follows the distribution of the thermal ICM. Turbulent re-acceleration is thought to be the main mechanism responsible for generating radio halos (see e.g., Brunetti & Jones, 2014). In this scenario, a population of seed particles are re-accelerated by turbulence generated in the ICM during cluster mergers. Thus, the presence of radio halos is connected to the merging history of the systems and the cluster mass, which sets the available energy budget during mergers. Observational evidences for this scenario are the connection between the dynamical status of the cluster and the presence of radio halos (Buote, 2001; Cassano et al., 2010; Cuciti et al., 2015, 2021) and the correlation between radio halos power and the mass of the host cluster (Cassano et al., 2013; Cuciti et al., 2021; van Weeren et al., 2021; Duchesne et al., 2021; **?**). A key prediction of the turbulent re-acceleration model is that the cutoff in the synchrotron spectrum scales with the energetics of the merger (e.g., Cassano & Brunetti, 2005a; Cassano et al., 2006). This means that more massive systems suffering major mergers, host radio halos visible up to ~GHz frequencies, while less massive systems and/or minor mergers produce radio halos with steeper spectra ($\alpha < -1.5$), preferentially detectable at lower frequencies. These are generally referred to as Ultra-Steep Spectrum radio halos (USSRH; Brunetti et al., 2008).

2.1.1 ZwCl 0634.1+4747

ZwCl 0634.1+4747 is a massive ($M_{500} = (6.65 \pm 0.33) \times 10^{14}\,\mathrm{M}_\odot$, Planck Collaboration et al. (2016a)) nearby ($z = 0.174$, Rossetti et al. (2017)) galaxy cluster located at R.A. (J2000) = $06^{\mathrm{h}}38^{\mathrm{m}}02.5^{\mathrm{s}}$, DEC. (J2000) = $+47°47'23.8''$, also known as PSZ1 G167.64+17.63/ PSZ2 G167.67+17.63, CIZA J0638.1+4747, MCXC J0638.1+4747 or RXC J0638.1+4747. Chandra X-ray observations show evidence of a non-relaxed dynamical state, such as the presence of substructures in the X-ray surface brightness distribution (Cuciti et al., 2015). The morphology of the cluster is elongated in the east-west direction (see **Fig. 2.1**).

ZwCl 0634.1+4747 hosts a variety of peculiar radio sources. A radio halo was already detected at 323 and 1518 MHz by Cuciti et al. (2018). It extends over ~600 kpc in the E-W direction following the morphology of the X-ray emission of the cluster. More recently, a radio megahalo has been discovered in this system using LOFAR 144 MHz observations (Cuciti et al., 2022). The megahalo covers the whole cluster volume, with a linear size of 2.8 Mpc and an integrated spectral index between 53 and 144 MHz of $\alpha = -1.62 \pm 0.25$. In addition, LOFAR observations clearly revealed the presence of three head-tail (HT) radio galaxies in the cluster field, with $\sim 0.6 - 1$ Mpc linear size, labelled HT-A HT-B and HT-C in **Fig. 2.2**, which are the focus of this paper. The HT-B has been studied at high frequency (323 and 1518 MHz) by Cuciti et al. (2018). Possible signs of re-energetisation have been found through the analysis of the spectral index and surface brightness along the tail. In that case, the interaction between the tail and a shock has been proposed to explain the emission.

In this paper we present a multi-wavelength radio study of the galaxy cluster ZwCl 0634.1+4747, combining data from 53 MHz to 1.5 GHz. First, we focus our analysis on the three extended HT radio galaxies residing in ZwCl 0634.1+4747 (**Section 2.3.1**). We produce flux density and spectral index profiles along the tails of the HT radio galaxies (**Section 2.3.1**), comparing them with a standard ageing model (**Section 2.3.2**). In **Section 2.3.3** we complement the analysis of the cluster with X-ray information using XMM-Newton data. Additionally, we present a new study of the radio halo down to the very-low frequencies in **Section 2.3.4**. In **Section 4.4**, we discuss possible scenarios that involve the interaction of HT radio galaxies with the external ICM. We summarize our results in **Section 4.5**.

Throughout the paper we adopt a ΛCDM cosmology with $H_0 = 70\,\mathrm{km\,s^{-1}Mpc^{-1}}$, $\Omega_\Lambda = 0.7$ and $\Omega_m = 0.3$. Thus, $1''$ corresponds to a physical scale of 2.95 kpc at the redshift of ZwCl 0634.1+4747. We use the convention $S_\nu \propto \nu^\alpha$ for the radio synchrotron emission, with $\alpha < 0$.

2.2 Observations and data reduction

The data used in this work cover a broad range of frequencies, including The LOFAR Low Band Antennas (LBA) at 53 MHz, High Band Antennas (HBA) at 144 MHz, Giant Meterwave Radio Telescope (GMRT) at 323 MHz and Karl G. Jansky Very Large Array (VLA) at 1.5 GHz data. A summary of the observations used is listed in **Tab. 2.1**. GMRT and VLA data of this cluster were already analysed by Cuciti et al. (2018), while LOFAR LBA and HBA data are extensively described is Cuciti et al. (2022). Thus, we briefly summarize the data reduction procedure in next sections.

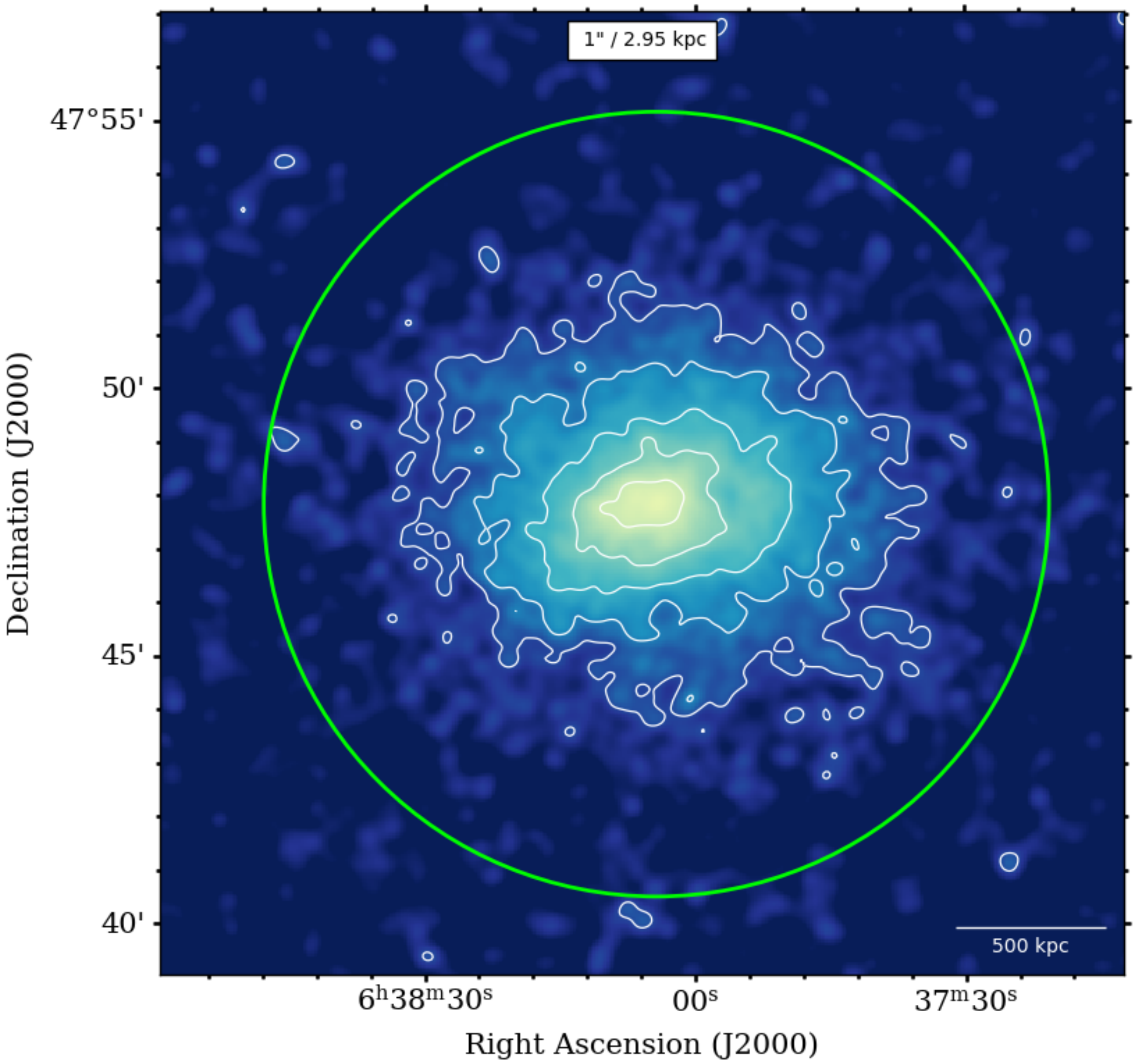

Figure 2.1: Background-subtracted exposure-corrected XMM image of ZwCl 0634.1+4747, in [0.5-2] keV band. The contour levels start at $3 \cdot$ rms where rms $= 5 \cdot 10^{-6}\,\mathrm{cts\,s^{-1}}$. As a size reference, green circle indicates $R_{500} = 1299$ kpc (Lovisari et al., 2017), namely the radius within which the mean mass over-density of the cluster is 500 times the cosmic critical density at the cluster redshift.

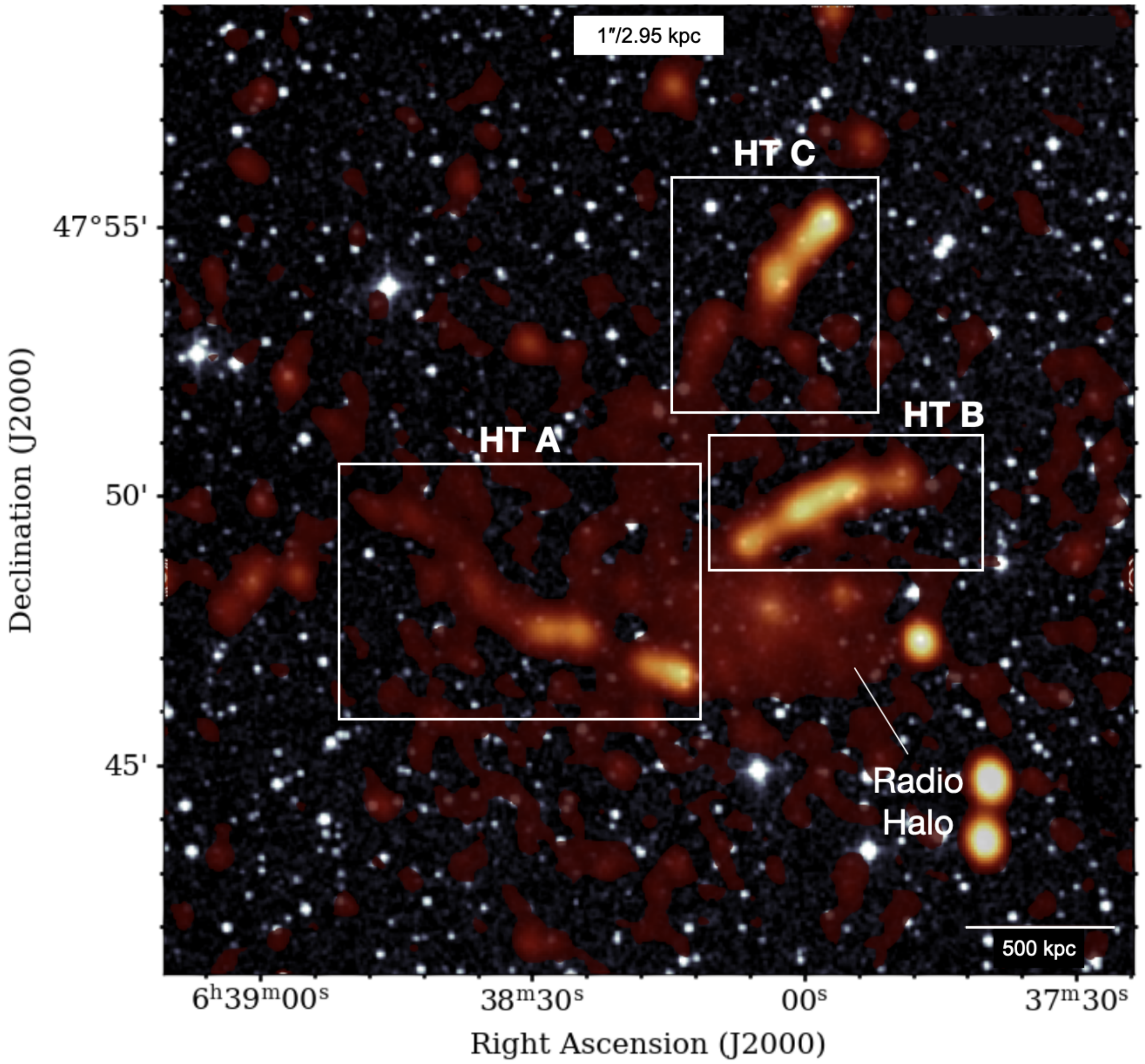

Figure 2.2: Composite radio-optical image of ZwCl 0634.1+4747. LOFAR HBA at 144 MHz superimposed on the DSS image (Pâris et al., 2014).

Table 2.1: Observational overview: LOFAR LBA, HBA, GMRT and VLA observation. References: (1) Cuciti et al. (2022), (2) Cuciti et al. (2018)

Telescope	Frequency MHz	Bandwidth MHz	Configuration	Time	Observation Date	Ref.
LOFAR LBA	53	47	LBA_OUTER	8 h	2018 Sep 28	(1)
LOFAR HBA	144	48	HBA_DUAL	8+8 h	2019 Oct 27, 2021 Mar 10	(1)
GMRT	320	32	-	5 h	2015 Dec 19	(2)
VLA L-band	1518	48	D array	45 m	2015 Oct 19	(2)
VLA L-band	1518	48	B array	40 m	2015 Feb 22	(2)

2.2.1 LOFAR LBA data

This cluster was observed at ultra-low frequencies using LOFAR LBA for a total of 8 hours integration time in the frequency range 30 - 77 MHz, using the LBA_OUTER antenna configuration. Observations were conducted using the multi-beam mode, with one beam continuously pointed at the calibrator and one beam at the target. First, following de Gasperin et al. (2019), the calibrator solutions are derived and applied to the target field together with the primary beam correction. The data of the target field were self-calibrated first for direction-independent, and then for direction-dependent effects (de Gasperin et al., 2020a). Finally, the image quality was improved via extraction and self-calibration of a small region around the target, adapting the procedure used for HBA analysis of van Weeren et al. (2021) for LBA data. The final model and solutions from the direction-dependent calibration are used to subtract sources outside a circular region of 23′ centered on the target. Then, the dataset is phase-shifted to the centre of this region, corrected for the primary beam in this direction and additional rounds of self-calibration on the target are performed to further improve the image quality. For more details on the data used, we refer the reader to Cuciti et al. (2022), where the observations used in this work were first presented.

2.2.2 LOFAR HBA data

The LOFAR HBA data used in this work are part of the LOFAR Two-metre Sky Survey (LoTSS; Shimwell et al., 2017, 2019, 2022), a low-frequency (120-168 MHz) radio survey of the northern sky. Data were processed through the Survey Key Science Project reduction pipeline v2.2 presented in Tasse et al. (2021); Shimwell et al. (2022), which includes direction-independent and direction-dependent calibration (prefactor (de Gasperin et al., 2019); killMS (Smirnov & Tasse, 2015); DDFacet (Tasse et al., 2018)). Finally, the data sets have undergone the extraction procedure generally used for HBA observations to enhance the quality of the image (van Weeren et al., 2021; Botteon et al., 2022a). For more details, we refer again to Cuciti et al. (2022), where the observations used in this work were firstly used.

A flux-scale correction factor $f = 0.992$ has been applied to the nominal LOFAR HBA map values to align the images with the flux density scale of the LOFAR Two-Metre Sky Survey (Hardcastle et al., 2021; Shimwell et al., 2022).

2.2.3 GMRT data

ZwCl 0634.1+4747 has been observed with the GMRT at 320 MHz for a total time on source of ~5 h (Cuciti et al., 2018). First, amplitude and gain corrections were calculated for the calibrator sources and then transferred to the target. Radio frequency interference (RFI) has been removed automatically using Common Astronomy Software Applications package (`CASA` McMullin et al., 2007) and the central 220 channels were averaged to 22 to reduce the size of the data-set. Finally, a few steps of phase-only self-calibration were performed to reduce phase variations. Moreover, similarly to the extraction procedure, bright sources in the field of view were subtracted from the *uv*-data using the peeling method (see Cuciti et al., 2018, for more details on the data reduction of this dataset).

2.2.4 VLA data

VLA L-band observations of ZwCl 0634.1+4747 include D and B array configuration with a total time on source of ~45 and 40 mins respectively (Cuciti et al., 2018). First, the complex gain solutions for the calibrator sources (and the phase calibrator when present) on the full bandwidth were obtained, applying the bandpass and delay solution beforehand. Then, the calibration tables were applied to the target and an automatic radio frequency interference (RFI) removal was made using CASA. The 48 central channels of each spectral window were averaged to 6 to reduce the size of the data-set. All images were corrected for the primary beam attenuation.

After cycles of calibration and self-calibration on each array configuration, the B and D array observations were combined. Since the two pointings did not coincide perfectly, bright sources far from the phase center are subtracted separately for each spectral window from the *uv*-data before combining the data-set. The combined B+D array image is used for the HT analysis (**Section 2.3.1**), while the D array only is used for imaging the extended radio halo (**Section 2.3.4**).

2.2.5 Source subtraction

Discrete sources embedded in the extended radio halo, contaminate the diffuse emission and thus, we proceeded to remove them. This allows to properly study the low surface brightness emission from the radio halo. Previous work (Cuciti et al., 2018, 2022) presented the source subtraction for the low frequency (53 and 144 MHz) and high frequency (323 and 1518 MHz) data set separately. To be consistent through our analysis, we apply the same source subtraction procedure for all four data sets. We describe here briefly the general process. First, we produced high ($4'' \times 5''$) resolution images, to identify the compact sources. Then, we selected the corresponding components in the model image and we proceeded to remove them, subtracting these clean components directly from the $uv-$data. Finally, we imaged the source-subtracted data sets at low angular resolution (see **Fig. 2.3**), maintaining a negative Briggs weighting with robust parameter −0.25, using a common inner *uv*-cut of 135λ (equivalent to an angular scale of $\sim 25'$), which corresponds to the shortest baseline of the VLA data set. Moreover, we taper down the long baselines (i.e., using Gaussian taper with a FWHM of $30''$) to gain sensitivity towards the diffuse emission.

Throughout the paper, the images were created with WSClean software (Offringa et al., 2014). The uncertainty Δ_S associated with a flux density measurement S is estimated as

$$\Delta_S = \sqrt{(\sigma_c \cdot S)^2 + N_{\rm beam} \cdot \sigma^2_{\rm rms}}, \tag{2.1}$$

where $N_{\rm beam} = N_{\rm pixel}/A_{\rm beam}$ is the number of independent beams in the source area, and σ_c indicates the systematic calibration error on the flux density. Typical values of σ_c are within 10% for LOFAR LBA (de Gasperin et al., 2021), HBA (Shimwell et al., 2022) and GMRT (e.g. Chandra et al., 2004), while 2.5% is used for VLA (Perley & Butler, 2013).

2.2.6 XMM-Newton data

X-ray data for ZwCl 0634.1+4747 are available in the *XMM-Newton* Science Archive (XSA), OBSID 0692932601. The data reduction of the *XMM-Newton* data is performed using HEASoft version 6.29 (Nasa High Energy Astrophysics Science Archive Research Center (Heasarc), 2014) and the Science Analysis Software (SAS[1]) version 20.0.0. Hereafter, we provide a summary of the procedure. For a more extended description of the steps, the reader can refer to Veronica et al. (2022).

The first step consists of identifying Good Time Intervals (GTI), filtering out those that are affected by the presence of soft proton flares (SPF) (De Luca & Molendi, 2004; Kuntz & Snowden, 2008). This is achieved by creating a light curve for each of the three instruments of EPIC on board of XMM-Newton, namely MOS1, MOS2 and pn. For all instruments, we also generate count histograms. In the absence of SPF contamination the histogram is well fitted by a Poisson distribution. This allows us to estimate a mean value for the counts and apply a $\pm 3\sigma$ cut to discard the time intervals affected by flares and, for this reason, falling outside this range. Additionally, the IN/OUT ratio test (De Luca & Molendi, 2004; Leccardi & Molendi, 2008) allows us to further check the quality of our flare filtering procedure by comparing the count rates within the FoV (IN) to those of the unexposed region of the detectors (OUT). An IN/OUT ratio close to 1 for each detector indicates that the contamination by SPF was successfully removed. After the SPF filtering procedure the exposure time is reduced from $\sim$ 21 ks to $\sim$ 13 ks for the MOS cameras and from $\sim$ 18 ks to $\sim$ 10 ks for pn. Note that MOS1-3 and MOS1-6 were not in use at the time of this observation. Moreover we model and rescale the instrumental background, eventually we subtract it to the observation of ZwCl 0634.1+4747 and obtain background subtracted and exposure corrected images (**Fig. 2.1**). The procedure for this step is extensively described in Ramos-Ceja et al. (2019) and Migkas et al. (2020).

Since we are interested in the diffuse X-ray emission associated with the ICM in ZwCl 0634.1+4747, we mask the point sources that contaminate the field of view. First, we apply an automated procedure described in Pacaud et al. (2006) which detects point sources and stores them in a catalog. Afterwards, we manually remove any further sources by looking at images in the soft (0.5-2 keV) and hard (2-10 keV) X-ray bands. The surface brightness analysis, described in Sec. 2.3.3, is performed on the masked images.

2.3 Results

2.3.1 Head-tail galaxies

The three HT galaxies in ZwCl 0634.1+4747 are all very extended and bright at lower frequencies (reaching up to $\sim$ 1 Mpc projected size at 144 MHz). They are spread over the cluster volume and show peculiar spectral properties. We named them HT-A, HT-B and HT-C (see **Fig. 2.2**). Their properties, including the position and redshift of the optical counterpart, the projected distance from the cluster centre and their maximum extension measured from the $3\sigma_{\rm rms}$ contours

[1]https://www.cosmos.esa.int/web/xmm-newton/sas

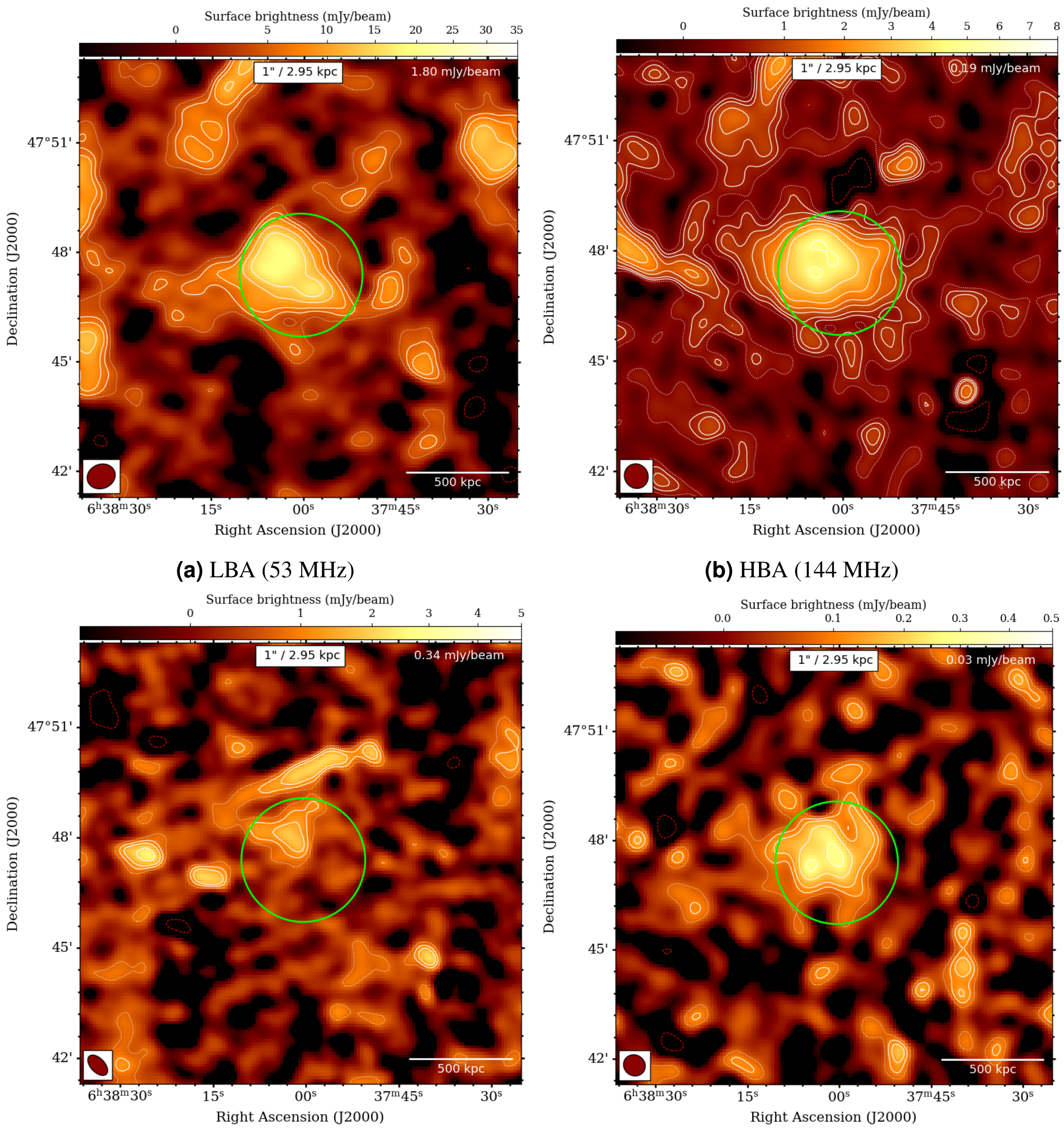

(a) LBA (53 MHz)

(b) HBA (144 MHz)

(c) GMRT (323 MHz)

(d) VLA (1518 MHz)

Figure 2.3: Low-resolution source-subtracted images of the radio halo hosted by ZwCl 0634.1+4747. The beam is shown in the bottom left corner of each image. The contour levels start at $2\sigma_{\rm rms}$ (where $\sigma_{\rm rms}$ is shown in the top right area of the images) and are spaced with a factor of $\sqrt{2}$. The $2\sigma_{\rm rms}$ contours are dotted in white. The $-3\sigma_{\rm rms}$ contours are dashed in red colour. The green circle indicates the region with R = 300 kpc used to extract the flux densities (**Tab. 2.4**).

Table 2.2: Images used in this work

Source	Telescope	Frequency [MHz]	Briggs weighting	Taper FWHM [″]	Resolution [″×″]	$\sigma_{\rm rms}$ [mJy/beam]	Reference
Halo	LBA	53	-0.25	30	47×40	1.80	**Fig. 2.3a**
	HBA	144	-0.25	30	41×38	0.19	**Fig. 2.3b**
	GMRT	323	0	30	40×23	0.34	**Fig. 2.3c**
	VLA	1518	-0.25	30	37×34	0.03	**Fig. 2.3d**
Head-tails	LBA	53	-0.25	15	20×20	1.22	**Fig. 2.4a**
	HBA	144	-0.25	15	20×20	0.12	**Fig. 2.4b**
	GMRT	323	0	15	20×20	0.13	**Fig. 2.4c**
	VLA	1518	-0.25	15	20×20	0.04	**Fig. 2.4d**

of the LOFAR HBA image, are listed in **Tab. 2.3**. The cluster-centric distances are projected, and are thus lower limits. Wide-field, medium-resolution images are shown in **Fig. 2.4** while zoomed-in images in **Fig. 2.5**. The locations of the optical counterparts are shown in **Fig. 2.4**. Photometric redshift are taken from the DESI DR9 photometric redshift catalogue (Zhou et al., 2021).

Every tail shows a bright head, followed by a lower surface brightness tail, which shows ripples in the radio brightness. The presence of multiple radio bumps could be interpreted as other radio-galaxies within the cluster volume rather than a continuation of the tails. In order to exclude the possibility of a sequence of multiple radio galaxies, we produced spectral index map between 53 MHz and 144 MHz (**Fig. 3.5**, *left*) and 144-320 MHz (**Fig. 3.5**, *right*). To this end, we re-imaged LBA and HBA data, using Briggs weighting with Robust parameter $R = -0.25$, common uv-range and convolved to the same beam size. In each map, we measured spectral index values for pixels with flux density $\geq 2\sigma_{\rm rms}$ in both frequencies. We find that $\alpha_{53\,{\rm MHz}}^{144\,{\rm MHz}}$ has flatter values where the heads of the AGN are located (consistent with values **Fig. 2.7**) and steepens along the tails. Hence, the bright bumps are unlike other AGN which are expected to have $\alpha \sim -0.5$. Moreover, no other optical counterparts at the cluster redshift are present in the DESI DR9 photometric redshift catalogue (Zhou et al., 2021).

In order to identify possible departures from a pure-ageing model (see **Section 2.3.2** for details), we extracted flux densities and spectral index profiles (**Fig. 2.8**). The flux densities are extracted using beam-size sliding regions from the nucleus until the end of the tail, based on their largest linear extent at 144 MHz (**Fig. 2.8**, *first row*). The sliding regions are separated by a few kpc from each other. In this way, we relaxed the requirement of independent measurements, which is not relevant in this case, as we do not use those values for fitting purposes. We then calculated the spectral index profiles between 54-144, 144-323 and 54-1518 MHz, considering only the regions with fluxes $\geq 3\sigma_{\rm rms}$ for each pair of frequencies (**Fig. 2.8**, *second and third row*). Another common method to analyse synchrotron spectra is through colour-colour plots (e.g. Katz-Stone et al., 1993; Stroe et al., 2013a; Edler et al., 2022; Rudnick et al., 2022). This method employs two, two-point power laws to characterize the curved shape of a source spectrum. For these plots, we use measurements made over beam-size separated regions of the source. The results are then compared to the expected trajectories in the color-color space, predicted by the

Table 2.3: Summary of the properties of the head-tail galaxies

Source	R.A.; DEC	z_{phot}	d	LLS	α_{inj}	$v_{\perp}$
			kpc	Mpc		km/s
HT-A	6 : 38 : 13.22, +47 : 46 : 40.44	0.19 ± 0.01	350	1.2	0.43	225
HT-B	6 : 38 : 06.81, +47 : 49 : 05.88	0.16 ± 0.01	300	0.6	0.60	274
HT-C	6 : 37 : 57.52, +47 : 55 : 09.48	0.18 ± 0.01	870	0.8	0.37	196

Columns: (1) Tail name; (2) Coordinate of the optical counterpart; (3) Photometric redshift from (Zhou et al., 2021); (4) Projected distance from the cluster centre; (5) Largest linear extension above $3\sigma_{\text{rms}}$ at 144 MHz; (6) Injection index $\alpha_{\text{inj}} = \alpha^{144\text{ MHz}}_{53\text{ MHz}}$, shown in **Fig. 2.7**; (7) Tails' projected velocity.

standard model of spectral ageing (**Fig. 2.8**, *fourth row*). This method is useful to identify points that still follow the same spectral curvature even though they are spatially distant from each other. In the next section, we describe our model and we study their behaviour separately.

2.3.2 Spectral ageing

Once injected in the ICM from the AGN, the relativistic plasma starts loosing energy due to synchrotron and inverse Compton losses. At the point of the initial acceleration, the energy distribution of the electron population is assumed to be a power law in the form $N(E) = N_0 E^{-\delta}$, where δ is the power-law index. At later times $t > 0$, we expect the energy distribution of the electron population to have a characteristic form depending on t. Since the characteristic time-scale for synchrotron losses is $\propto 1/E$, the electron energy distribution at $t > 0$ will be characterized by a depletion of the highest-energy electrons. The same reasoning applies to the synchrotron spectrum, which steepens with time away from the initial power law shape $S \propto \nu^{-\alpha}$ with $\alpha = (\delta - 1)/2$. In the case of HT radio galaxies, this results in a spatial evolution of the spectrum from the head down to the tail. Specifically, the further from the nucleus, the older the electrons, i.e. they were accelerated at earlier times, and the more curved the spectrum is expected to be. In the absence of re-acceleration mechanisms, we expect to see the aged synchrotron spectrum assuming a characteristic curved shape.

Here we first consider a pure-ageing scenario to describe the flux and spectral index evolution. One of the most commonly used models to describe ageing of radio galaxies is the Jaffe-Perola (JP; Jaffe & Perola, 1973) model. It accounts for ageing of plasma assuming: (*i*) negligible adiabatic losses, in line with models where the tail flow is contained and channeled along magnetic field lines; (*ii*) a single initial injection event with given injection index $\alpha_{\rm inj}$, that represent the plasma spectral index when it is first injected in the ICM by the AGN, i.e. before any ageing; (*iii*) a given uniform magnetic field that we decide to keep fixed at the minimum aging value $B = B_{\rm min}$. This choice means maximizing the lifetime of the emitting electrons by minimizing their losses due to synchrotron and IC: higher or lower values of the magnetic field would cause the radio source to fade faster. This equals to $B_{\rm min} = B_{\rm CMB}/\sqrt{3}$, where $B_{\rm CMB} = 3.2\times(1+z)^2\,\mu$G is the equivalent magnetic field of the Cosmic Microwave Background at the source redshift, which for ZwCl 0634.1+4747 corresponds to $B_{\rm min} = 2.55\,\mu$G. We calculated the spectra of each head in a region 1.5 times bigger than the beam, centered on the head (**Fig. 2.7**). We fix the injection index using the lowest frequencies available in this work $\alpha_{\rm inj} = \alpha_{53\,\rm MHz}^{144\,\rm MHz}$, since they are the less affected by ageing (**Tab. 2.3**).

In order to obtain the JP profiles we used the PYSINCH[2] libraries (presented in Hardcastle et al., 1998, and subsequent work). Through these libraries, we built an initial electron spectrum (with the injection energy index $\delta_{\rm inj}$ derived from the observed $\alpha_{53\,\rm MHz}^{144\,\rm MHz}$) and let it age in the minimum magnetic field condition, following the JP model. We then evolved the JP spectrum at 53, 144, 323, 1518 MHz and obtained the flux density (together with the spectral-index). We normalized the initial JP flux density to the first data point, which corresponds to the head of the tail. The time-ageing of the JP model spectra can be converted to space-ageing along the tail, considering a given constant velocity. We thus obtain a rough estimation of the projected velocity on the plane of the sky $v_\perp$ which is of the order of $200-300\,\rm km\,s^{-1}$ (**Tab. 2.3**). We point out that this is a lower limit for multiple reasons. First, magnetic field and velocity are strongly

[2] https://github.com/mhardcastle/pysynch

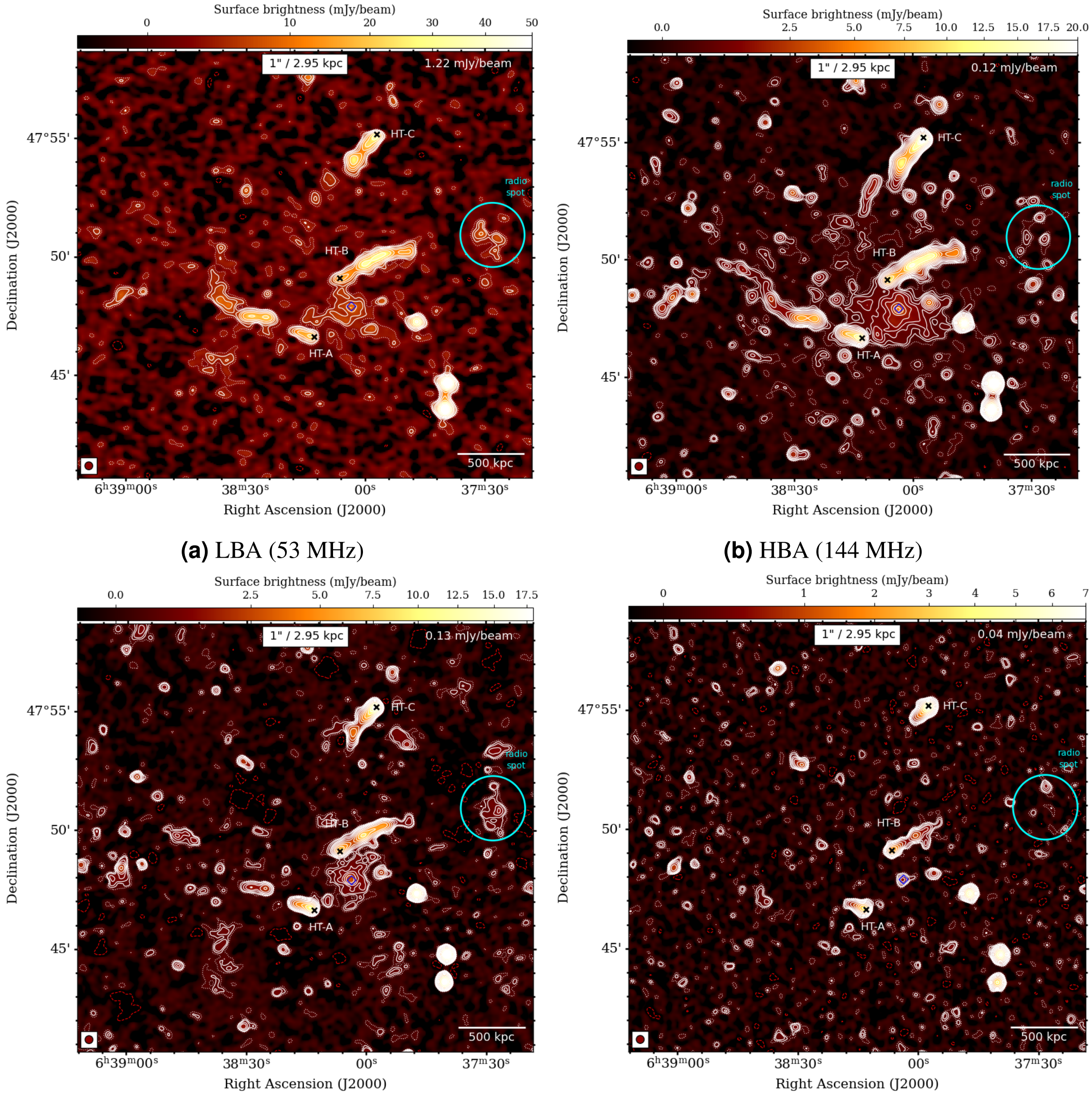

(a) LBA (53 MHz)

(b) HBA (144 MHz)

(c) GMRT (323 MHz)

(d) VLA (1518 MHz)

Figure 2.4: Images of the head-tail galaxies hosted in ZwCl 0634.1+4747 at different frequencies. In each image, the contour levels start at $2\sigma_{\rm rms}$, where $\sigma_{\rm rms}$ shown in the top right area of the images, and are spaced with a factor of $\sqrt{2}$. The $2\sigma_{\rm rms}$ are dotted white coloured and $-3\sigma_{\rm rms}$ contours are dashed red coloured. The beam is shown in the bottom left corner of each image and has a FWHM of 20″. Black crosses indicate the optical counterparts of the HT radio galaxies (**Tab. 2.3**). The blue diamond is the location of the Brightest Cluster Galaxy (BCG) (Cutri et al., 2003).

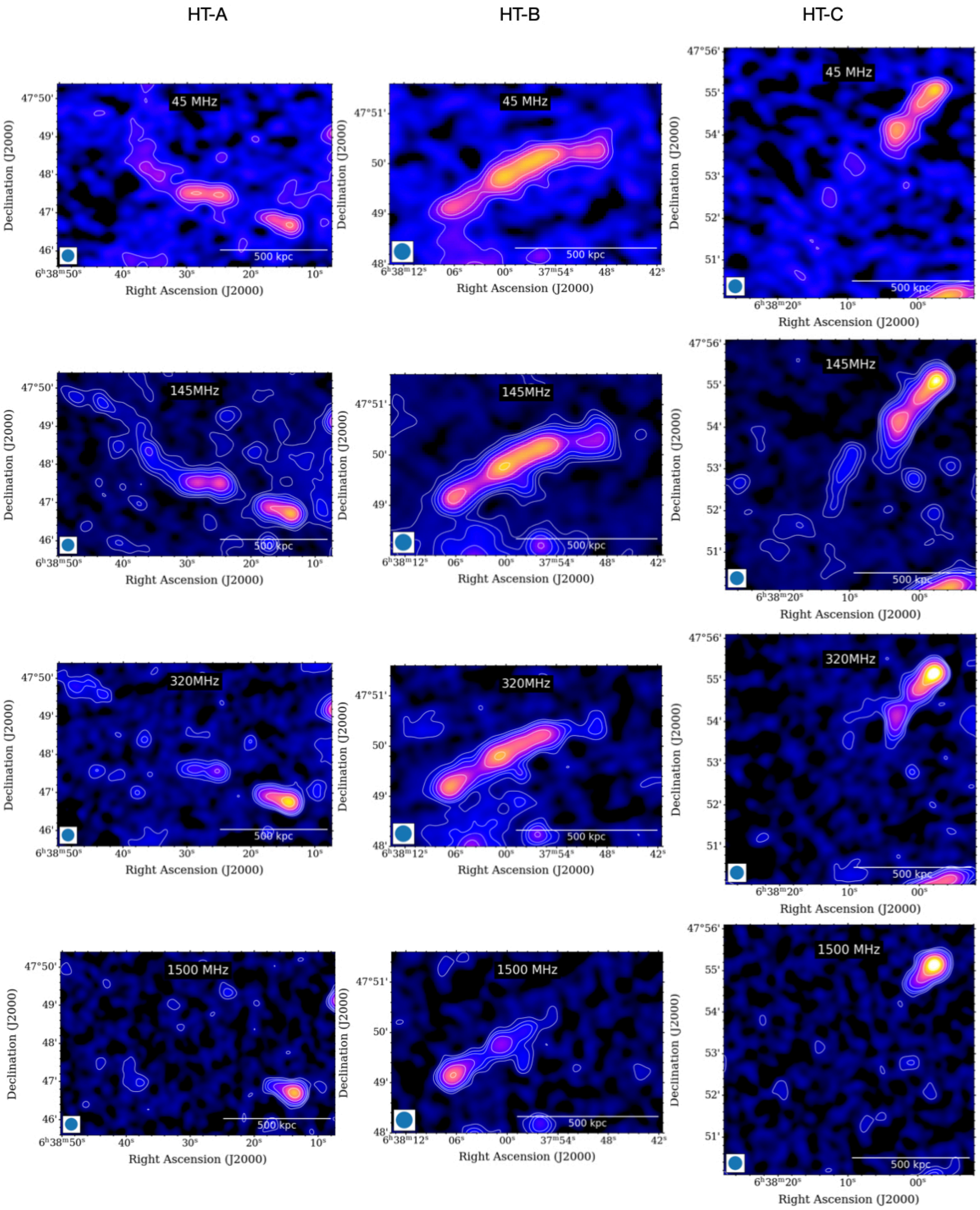

Figure 2.5: Zoom-in on the source HT-A *(first column)*, HT-B *(second column)* and HT-C *(third column)* at all frequencies, from 53 MHz *(top)* to 1518 MHz *(bottom)*. For each cut-out, the resolution and $\sigma_{\rm rms}$ are the same as **Fig. 2.4**, listed in **Tab. 2.2**.

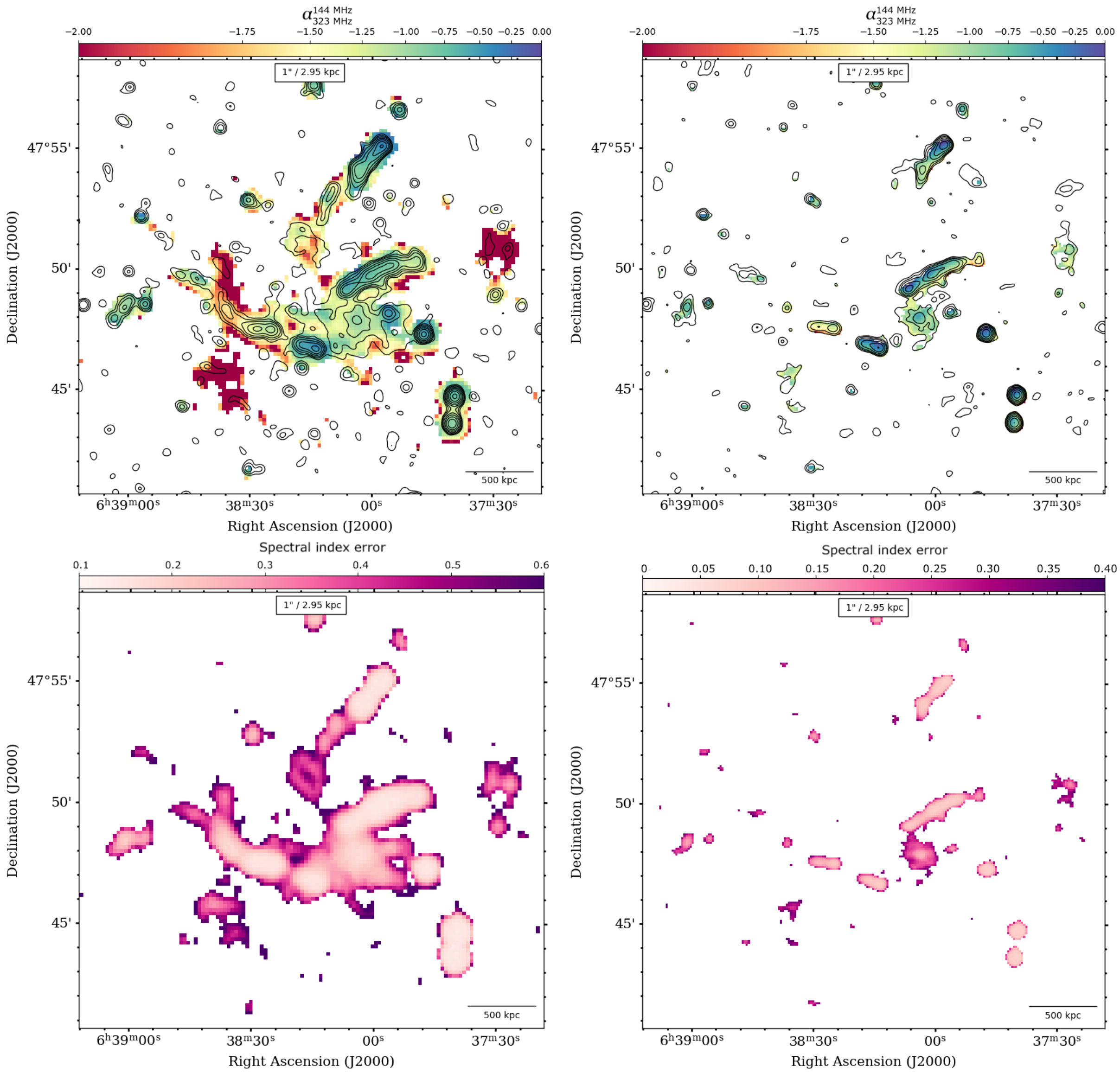

Figure 2.6: *Left panel*: Spectral index map between 53 MHz and 144 MHz at a spatial resolution of $36'' \times 36''$ *(top)* and relative spectral index error $\Delta\alpha^{53\,\mathrm{MHz}}_{144\,\mathrm{MHz}}$ *(bottom)*. Pixels with surface brightness values below $2\sigma_{\mathrm{rms}}$ in the two images were blanked. Black contours start at $3\sigma^{145\,\mathrm{MHz}}_{\mathrm{rms}}$ and are spaced by a factor of 2. *Right panel*: Spectral index map between 144 MHz and 320 MHz at a spatial resolution of $20'' \times 20''$ *(top)* and relative spectral index error $\Delta\alpha^{144\,\mathrm{MHz}}_{320\,\mathrm{MHz}}$ *(bottom)*. Pixels with surface brightness values below $2\sigma_{\mathrm{rms}}$ in the two images were blanked. Black contours start at $3\sigma^{320\,\mathrm{MHz}}_{\mathrm{rms}}$ and are spaced by a factor of 2.

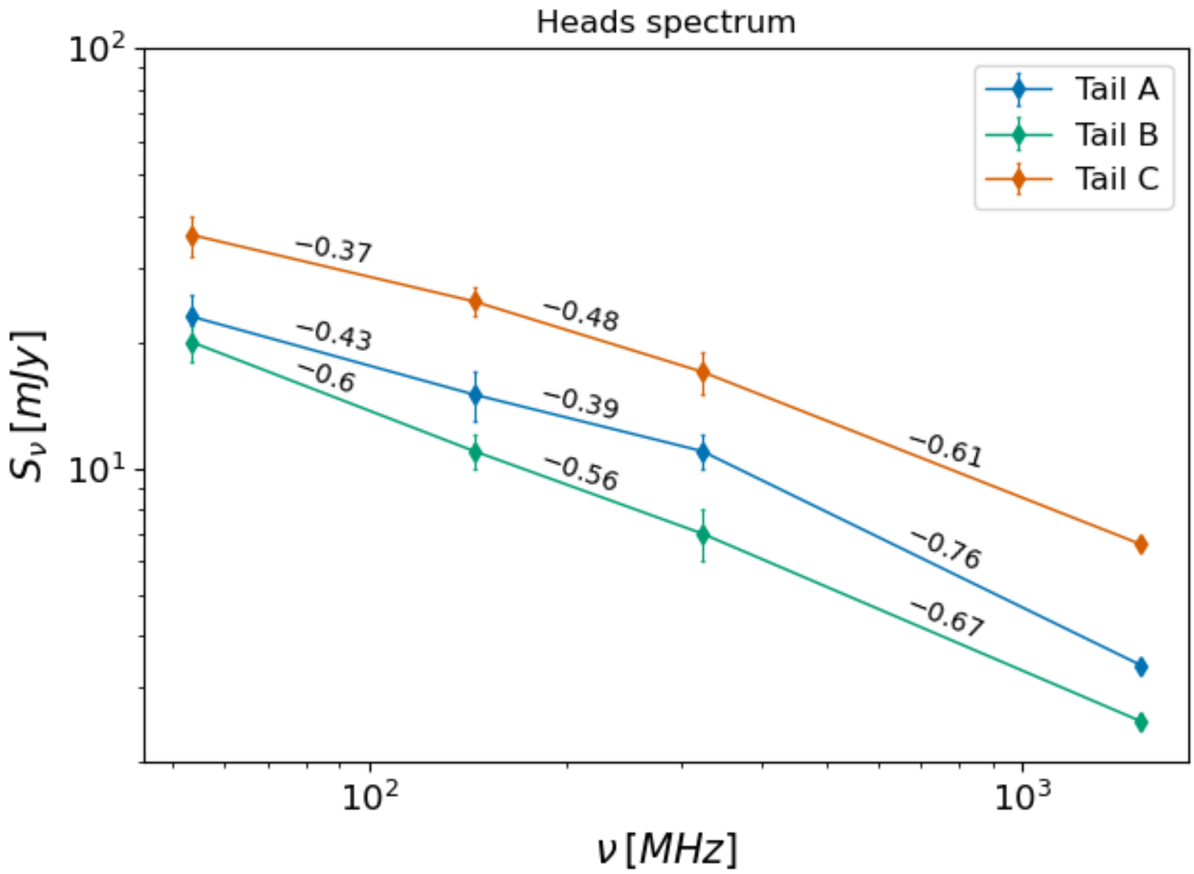

Figure 2.7: Integrated flux densities of the HTs nuclei, extracted from **Fig. 2.4** in regions with ∼ 1.5 beam area size.

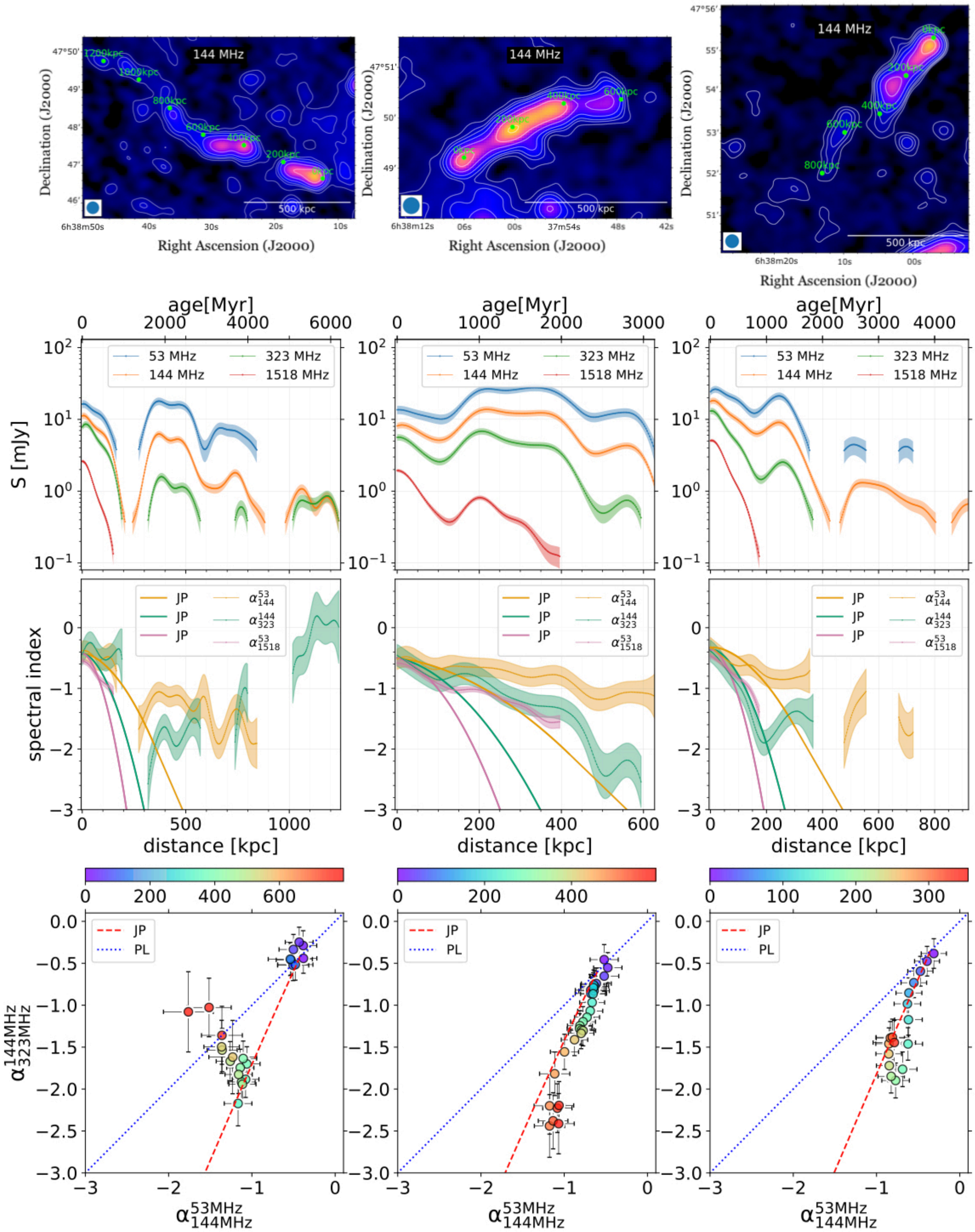

Figure 2.8: *First row:* HT extension at 144 MHz, where the tails are more visible. Reference points are shown to help the reader in matching the profiles with images; *Second row:* flux profile; *Third row:* spectral index profile considering regions with flux above $3\sigma_{\rm rms}$; *Fourth row:* three frequency (53, 144, 323 MHz) color-color plot with the bisector indicating the set of point where $\alpha^{53}_{144} = \alpha^{144}_{323}$, which means that the spectrum resembles a power-law (PL). The dashed red line represents the curved spectrum ($\alpha^{53}_{144} > \alpha^{144}_{323}$) of the JP model. The colorbar reflects the distance from the head of each point. The profiles are shown for HT-A (first column), HT-B (second column) and HT-C (third column).

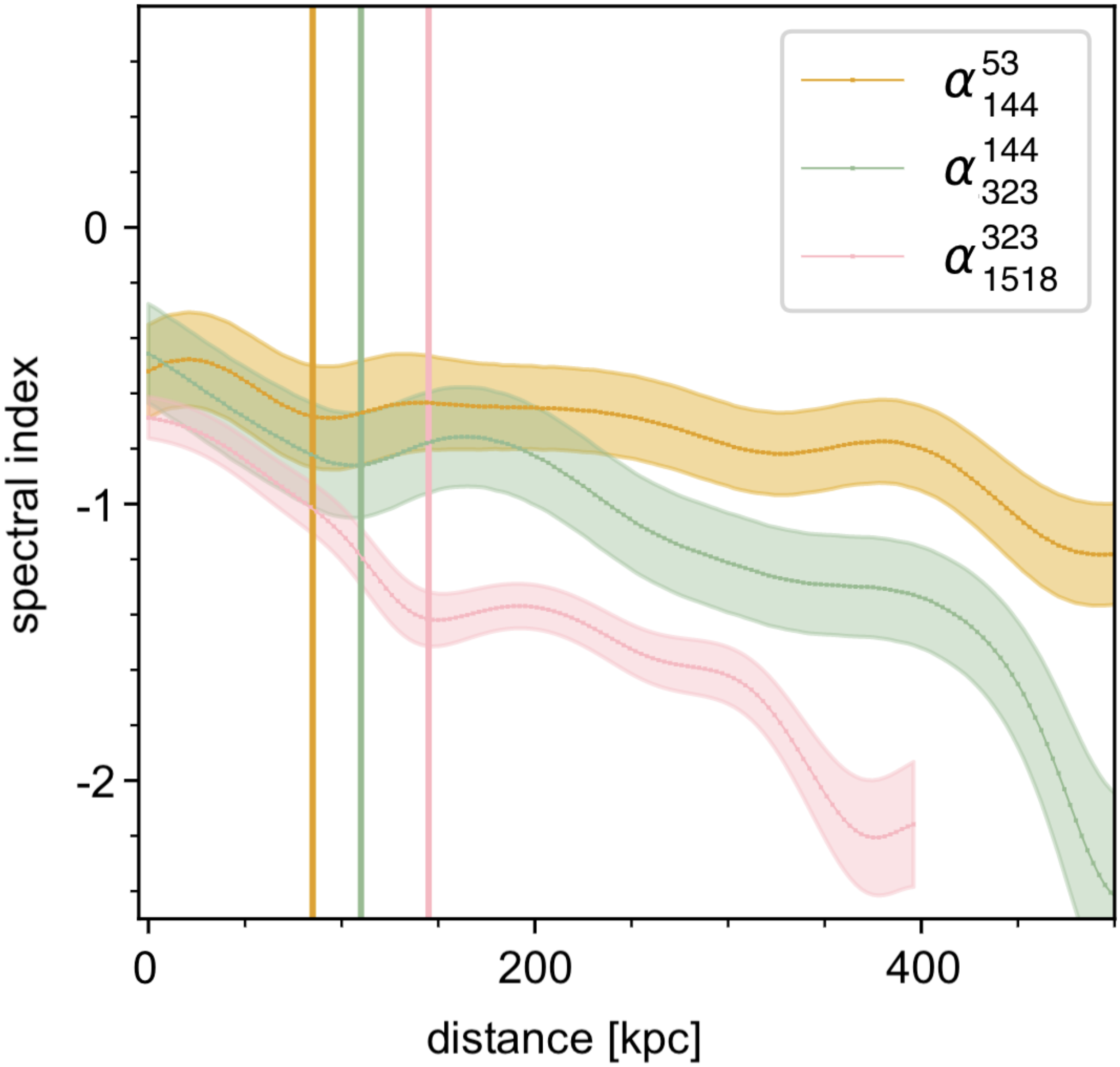

Figure 2.9: Spectral index profile for HT-B: comparison between α^{53}_{144}, α^{144}_{323} and α^{323}_{1518}. Vertical lines trace the shift of the flattening point from $\sim$ 150 to $\sim$ 110 and $\sim$ 80 kpc.

correlated, which means that it is not possible to discern between the minimum ageing scenario and any other value of the magnetic field B, far from $B_{\rm min}$, combined with higher velocities of the tail. Secondly, this velocity is projected, meaning that there could be a non-negligible component along the line of sight.

HT A The radio galaxy HT A shows unusual properties: after the bright nucleus (the head), we note another bright peak in the surface brightness at $\sim$ 380 kpc (**Fig. 2.8**, *second rows*). Correspondingly, the spectral index profile shows a flattening, jumping from ~ -0.5 of the head to ~ -1.5 and then stabilizing at ~ -1.3 in both α_{53}^{144} and α_{144}^{320}. The flattening extends to $\sim$ 550 kpc (**Fig. 2.8**, *third rows*). We overplot the JP model (solid lines) for all frequencies. Up to 200 kpc, the spectral index profile decline as expected due to radiative losses of the electron population accelerated by the radio galaxy. In this first part, the JP model is able to reproduce the profiles. At larger distances, it is not trivial to account for the bump in the flux density profile and the flattening of the spectral index, using this pure-ageing scenario. Moreover, the color-color plot shows that points corresponding to 380-550 kpc are progressively moving from the expected curved JP towards the power-law line. That means the shape of the spectrum is getting flatter instead of continuing the steepening due to ageing. Thus, we conclude a mechanism able to re-energise the relativistic population of CRe, initially injected by the AGN, must have occurred. We also note that there are few points in the range 740 - 800 kpc from the head that surprisingly cross the power-law line, lying in the area where $\alpha_{144}^{323} > \alpha_{53}^{144}$. We argue this is an effect due to mixing of the electrons along the line of sight. Such an effect is common at very large distances from the AGN.

HT B Using GMRT and VLA observations, Cuciti et al. (2018) found a surface brightness jump at $\sim$ 150 kpc from the head of the tail, in correspondence with a flattening (150 – 300 kpc) of the spectral index. This was interpreted as evidence for electron re-energisation and they suggested that an interaction with a shock can explain the brightness and spectral index properties. The proposed scenario included the presence of a weak shock (Mach number $\mathcal{M} \lesssim 2$), moving from the back end of the tail until the point of the brightness bump $\sim$ 200 kpc. The geometry of this scenario includes the tail travelling outward from the cluster centre with an angle $\theta_0 = 60°$ to the line of sight. This model was able to explain the high-frequency radio observations for reasonable choices of the model parameters, as for example the velocity of the tail of the order of $\sigma_{\rm v} \sim 1400\,{\rm km\,s^{-1}}$. Nonetheless, they did not detect any shock at the jump position in the X-ray image. Thus they concluded that, if the shock is present, it should be moving with a significant inclination with respect to the plane of the sky (see Fig. 13 in Cuciti et al., 2018).

Our results at high frequencies are consistent with the brightening starting at $\sim$ 150 kpc, and the subsequent spectral flattening. As a reference with the analysis of Cuciti et al. (2018), in **Fig. 2.9** we show α_{53}^{144} compared to α_{323}^{1518}. The spectral profile shows a peculiar feature: the flattening starts at different distances depending of the frequencies used. To better appreciate this feature, we zoom in the first 400 kpc of HT-B and performed spectral index profiles comparing α_{144}^{53}, α_{323}^{144} and α_{1518}^{323}. In **Fig. 2.9**, the flattening point appears to be spatially shifted from 150 kpc (α_{1518}^{323}) to 110 kpc (α_{323}^{144}) and 80 kpc (α_{144}^{53}). This frequency-dependent feature would discourage the shock scenario, since the latter would create re-energisation feature happening simultaneously at the same point of the tail. We discuss and test possible scenarios in **Section 4.4**. Interestingly, we also find a residual emission with $\alpha_{144}^{53} < -2.5$ at the very end of the HT B (**Fig. 2.4**). This is clearly visible only in the LOFAR low-frequencies images and after a region where there is no emission. If this steep spot is part of the tail, the total extent of the HT galaxy would be of 1.2 Mpc. However, we cannot rule out that it may be a residual emission, also present in other parts of the image. In addition, given the large distance and the significant spectral index uncertainty associated with it, we exclude the radio spot from further analysis.

HT-B is the tail with the most extended frequency coverage. This means we can follow the flux density and spectral index evolution up to ~ 400 kpc at all the available frequencies in this work. Therefore, in addition to the profiles shown in **Section 2.3.2**, we performed local spectral fitting along HT-B. This allows us to study possible variations of the synchrotron spectrum along the tail. To do that, we extracted the spectra in eight circular beam-size independent regions along the source and fitted each local spectrum with a JP model using SYNCHROFIT[3] package. The result of the local JP fitting is shown in **Fig. 2.10**. The model has three free parameters: the energy injection index $\delta_{\rm inj}$, the break frequency $\nu_{\rm break}$ and the normalisation factor N for correct scaling. From the syncrhotron theory (see e.g., Longair, 2011), the break frequency is related to the spectral age t_s as

$$t_s = 1.61 \times 10^3 \frac{B^{0.5}}{(\mathbf{B}^2 + \mathbf{B}^2_{\rm CMB})(\nu_{\rm break}(1+z))^{0.5}} \quad \text{Myr} \tag{2.2}$$

where the magnetic field B and the equivalent magnetic field of the CMB $B_{\rm CMB}$ are in μG, while $\nu_{\rm break}$ in GHz. The initial energy spectrum spectrum undergoes a gradual transformation, with an exponential decline emerging beyond the point $\nu_{\rm break}$. If no source of re-acceleration is present, the measured break frequency decreases systematically along the tail as $\nu_{\rm break} \propto t_s^{-2}$. In the approximation of constant velocity that leads to $\nu_{\rm break} \propto d^{-2}$, in agreement with the scenario in which the oldest particles are those at a larger distance from the AGN. We first fitted the spectra with the injection index free to vary in the range $[1.5, 3.5]$ (purple, **Fig. 2.11**). We noticed that the injection index does not show a clear trend but fluctuates around 2.2 ± 0.2. Thus we fitted again the same regions fixing the energy injection index to 2.2 (i.e. $\alpha_{\rm inj} = 0.6$), which is also in agreement with the low-frequency power-law index of synchrotron emission, $\alpha_{53\,\rm MHz}^{144\,\rm MHz}$, observed of HT-B (**Fig. 2.7**). Thus we can limit the number of free parameters and we show the trend of the best-fit parameters $\nu_{\rm break}$ and $\delta_{\rm inj}$ in **Fig. 2.11** (teal). Keeping $\delta_{\rm inj}$ fixed or free to vary, does not influence the overall trend of the frequency break along the tail. Interestingly, we notice that after an initial decrease (up to region 3), the break frequency remains fairly constant. The distance at which this happens coincides with the distance of the spectral index flattening at ~ 150 kpc. This confirms that at some point along the tail, there must be a mechanism that stops the natural ageing (spectral index flattens and the break frequency stops decreasing).

To quantitatively assess the slowdown of the break frequency steepening, we employed a general power-law model of the form $f(d) \propto d^{-a}$ to fit the data points spanning from Region 2 to 8 (**Fig. 2.11**, *left*), where d is the distance from the core and a the power-law index. We excluded

[3] https://github.com/synchrofit/synchrofit

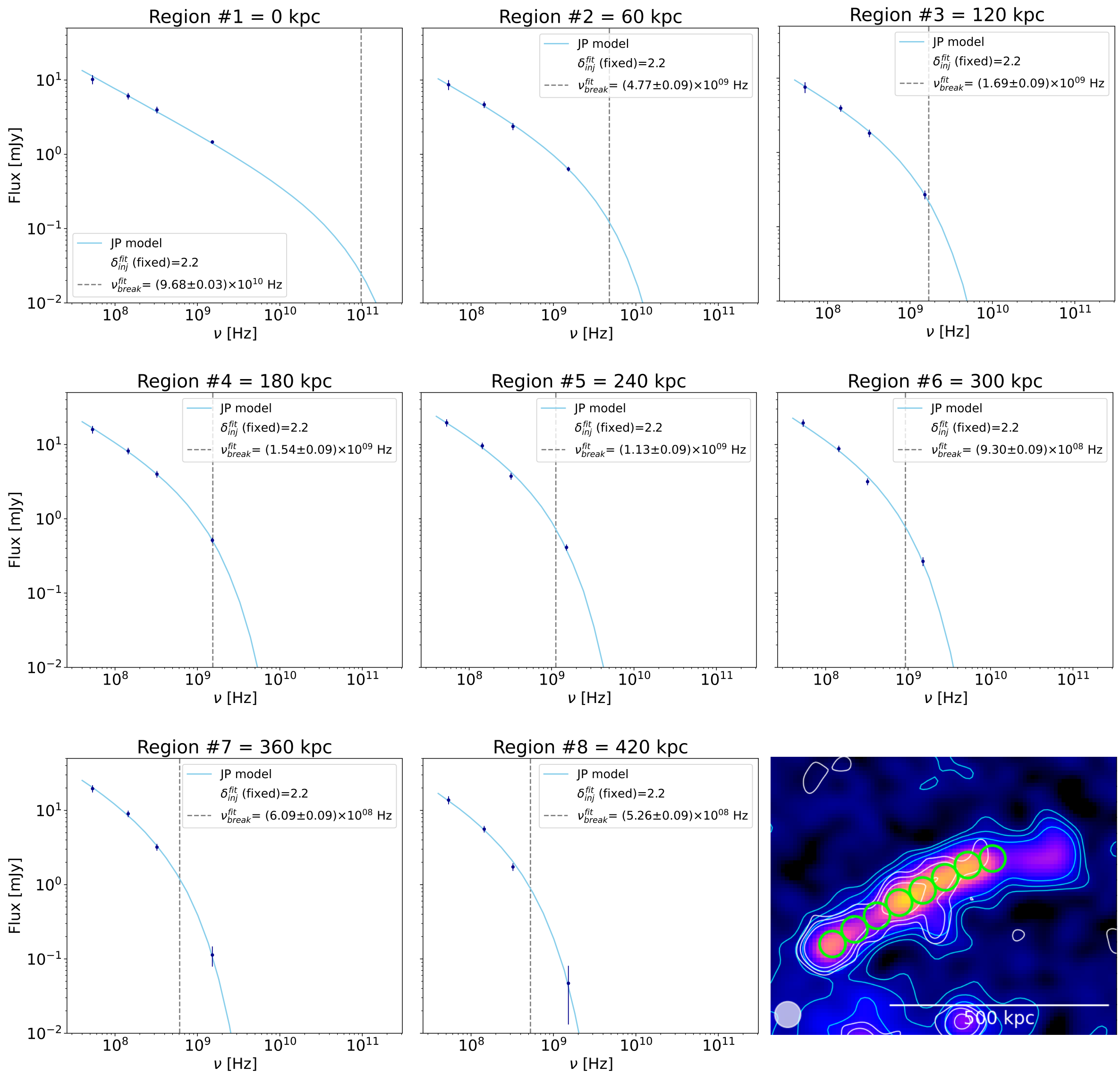

Figure 2.10: Spectra extracted in 8 circular beam-sized independent regions along the HT-B. The light blue line represent the best fit of the JP model and the model parameters ($\delta_{\rm inj}$, $\nu_{\rm break}$) are listed in the legend of each plot. The image of HT-B at 144 MHz is shown in the bottom right panel with the 8 regions overlapped. We plot the 3-, 6- and 12$\sigma_{\rm rms}$ contours at 144 (cyan) and 1518 (white) MHz, as a reference of the tail extension at different frequencies.

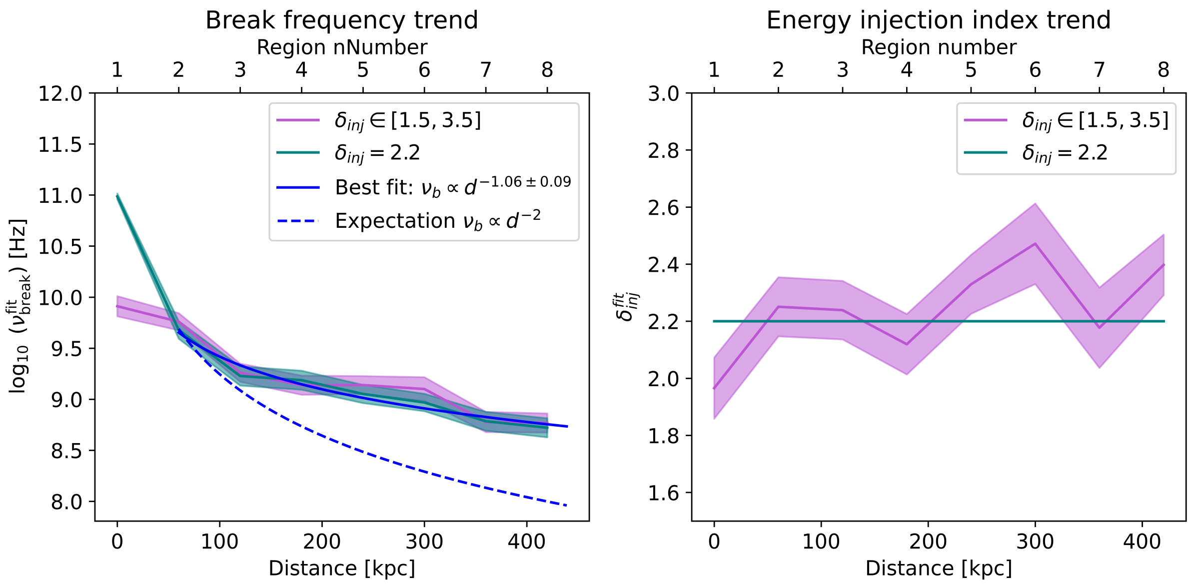

Figure 2.11: Best-fit break frequency and energy spectral index trend along HT-B. In purple the result with energy injection index free to vary, $\delta_{\rm inj} \in [1.5, 3.5]$; in teal it is kept fixed $\delta_{\rm inj} = 2.2$ (i.e. $\alpha_{\rm inj} = 0.6$, in agreement with the HT-B head spectrum of **Fig. 2.7**). *Left panel:* A power-law function was fitted to $\nu_{\rm break}^{\rm fit}$ corresponding to regions number 2 to 8. The best fit power-law index results to be $a = -1.06 \pm 0.09$ (blue solid line). The break frequency trend expectation from a pure ageing scenario $\nu_{\rm break} \propto d^{-2}$ is plotted as a reference (blue dashed line).

the break frequency value in Region 1, as is strongly vary among the two JP fitting models, and it can be considered as a lower limit since it is much higher than the highest spectral point in the case $\delta_{\rm inj} = 2.2$. The best fit (blue solid) shows a power-law index $a = 1.06 \pm 0.09$. Notably, this value indicates a slower rate of change compared to expected law based on the relationship between spectral age and break frequency (see **Eq. (2.2)**) and assuming a constant tail speed, $\nu_{\rm break} \propto d^{-2}$ (dashed blue line for comparison).

Similar evidence has been found in (Parma et al., 1999), who claimed re-acceleration processes for four of the radio galaxies in their sample.

HT C Analysing HT C is difficult because of its morphology and extension. In fact, the radio galaxy is more compact at $\sim$ GHz frequency (see also **Fig. 2.5**), while revealing a longer structure only in LOFAR images. Nevertheless, also in this case a pure-ageing JP model cannot account for the emission observed at distances larger than 200 kpc. Again, we see evidence for re-energised CRe left behind the AGN. These CRe do not age as expected by the considered model: the flattening of the spectral index implies that the energy distribution of the CRe is boosted toward higher energies.

2.3.2.1 Other ageing models

Another widely used model for spectral ageing is the Kardashev (1962) and Pacholczyk (1970) model (KP). The JP and KP models differ in the treatment of the emitting electrons' pitch angles, i.e. the angle between the magnetic field **B** and velocity **v** of the charged particle. In the KP model, the pitch angles of the electrons are fixed over their radiative lifetime, while in the JP model, pitch angle scattering takes place. This difference influences the way CRe lose energy, and thus, affects the resulting synchrotron spectra (Harwood et al., 2013). The pitch angle scattering of the JP model is a more likely scenario than that of the fixed pitch angles of the KP model (Tribble, 1993). The reason for this is that for a turbulent magnetic field configuration, the expected resonant scattering of the particles is effective on scales comparable to the Larmor radius of CRe, and thus smaller than the resolution of observations (Carilli et al., 1991; Hardcastle, 2013). Finding the best model for radiative ageing is beyond the scope of this work (see **Section 4.4**). We note that the differences between JP and KP model spectra would not change our conclusion, i.e. standard ageing cannot account for the observed profile and thus other re-acceleration mechanisms need to operate in this system.

2.3.3 X-ray properties

We use XMM-Newton observations to study the environment of the HT galaxies, i.e. the ICM that deflects their jets. From previous studies, it is known that this cluster appears to be in a non-relaxed state (Cuciti et al., 2015).

2.3.3.1 Surface brightness profile

We first studied the X-ray surface brightness to check for jumps in the azimuthal profile. We used `pyproffit`[4] (Eckert et al., 2020) to compute and model the surface brightness with a single, spherically symmetric β-model (Cavaliere & Fusco-Femiano, 1976) of the form:

$$I(r) = I_0\left[1 + \left(\frac{r}{r_c}\right)^2\right]^{-3\beta+0.5} + b, \tag{2.3}$$

where I_0 is the central surface brightness, r_c the core radius, β describes the ratio between thermal and gravitational energy of the plasma and one additional parameter b to describe the background (Eckert et al., 2020). We extracted a profile in circular annuli centered on the X-ray peak, with a bin size of 15″ until R_{500}. The azimuthal fit shows that a smooth β-model accounts for the emission, which does not show bumps or discontinuities (**Fig. 2.12**).

2.3.3.2 Gaussian Gradient Magnitude Filter

In order to look for features in the ICM that can be connected to the HT galaxies, we used standard X-ray image processing techniques. When studying galaxy clusters, particularly relaxed objects, the bright core of ICM emission gives rise to steeply peaked surface brightness profiles, where it can be difficult to detect variations such as edges, filaments, cavities or ripples. Thus, filtering techniques are frequently used to see and enhance variations in the surface brightness distribution. Among the different techniques, we used the adaptive version of the Gaussian Gradient Magnitude[5] (GGM; Sanders et al., 2016b,a) filter. In standard GGM filter, the image is convolved with a function that is the gradient of a Gaussian with a particular scale, measuring the gradients on this scale. This is a useful method to detect edge-like structures, such as shocks and cold fronts, which lead to strong gradients (Sanders et al., 2018). Since the accuracy of the gradient depends on the number of counts within the scale probed, this standard GGM filtering becomes noisier in regions where the count rate is lower, i.e. the outskirts of galaxy clusters. Therefore, we used the adaptively smoothed GGM described in Sanders et al. (2022) that dynamically choses the appropriate scale that reduces this effect. The main input parameter of this software is the signal-to-noise ratio, which is used to calculate the smoothing scale from the input counts. Following Sanders et al. (2022) we set it to 32, and we used the image counts in the energy band from 0.5 to 2 keV. We note the presence of bright regions, i.e., high gradient values, in the central left part of the GGM-filtered image (**Fig. 2.13**) but this region does not intersect any of the tails. Hence, we conclude that the ICM does not show features that appear to interact with the radio tails.

2.3.4 Radio halo morphology

Based on the $3\sigma_{\rm rms}$-contours, the radio halo in ZwCl 0634.1+4747 has a diameter of ∼ 400-800 kpc in the E-W direction, depending on the frequency (see **Tab. 2.4**).

[4] https://github.com/domeckert/pyproffit
[5] https://github.com/jeremysanders/ggm

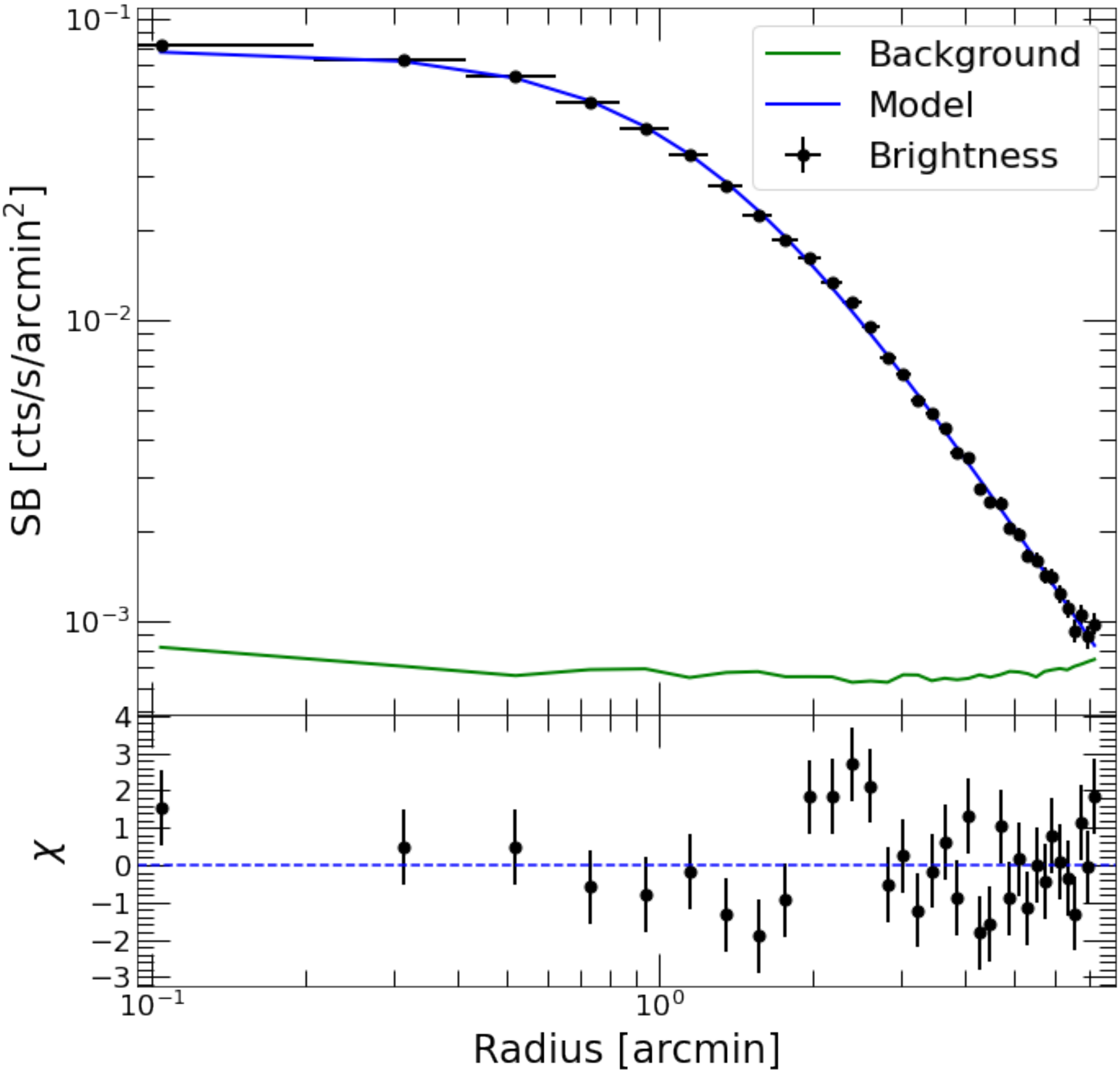

Figure 2.12: Surface brightness profile with the fitted single β-model. The best fit parameters are β = 0.59 ± 0.05, r_c = 1.24 ± 0.02 arcmin, I_0 = 0.079 ± 0.006 cts/s/arcmin^2, with a reduced χ^2 = 1.2.

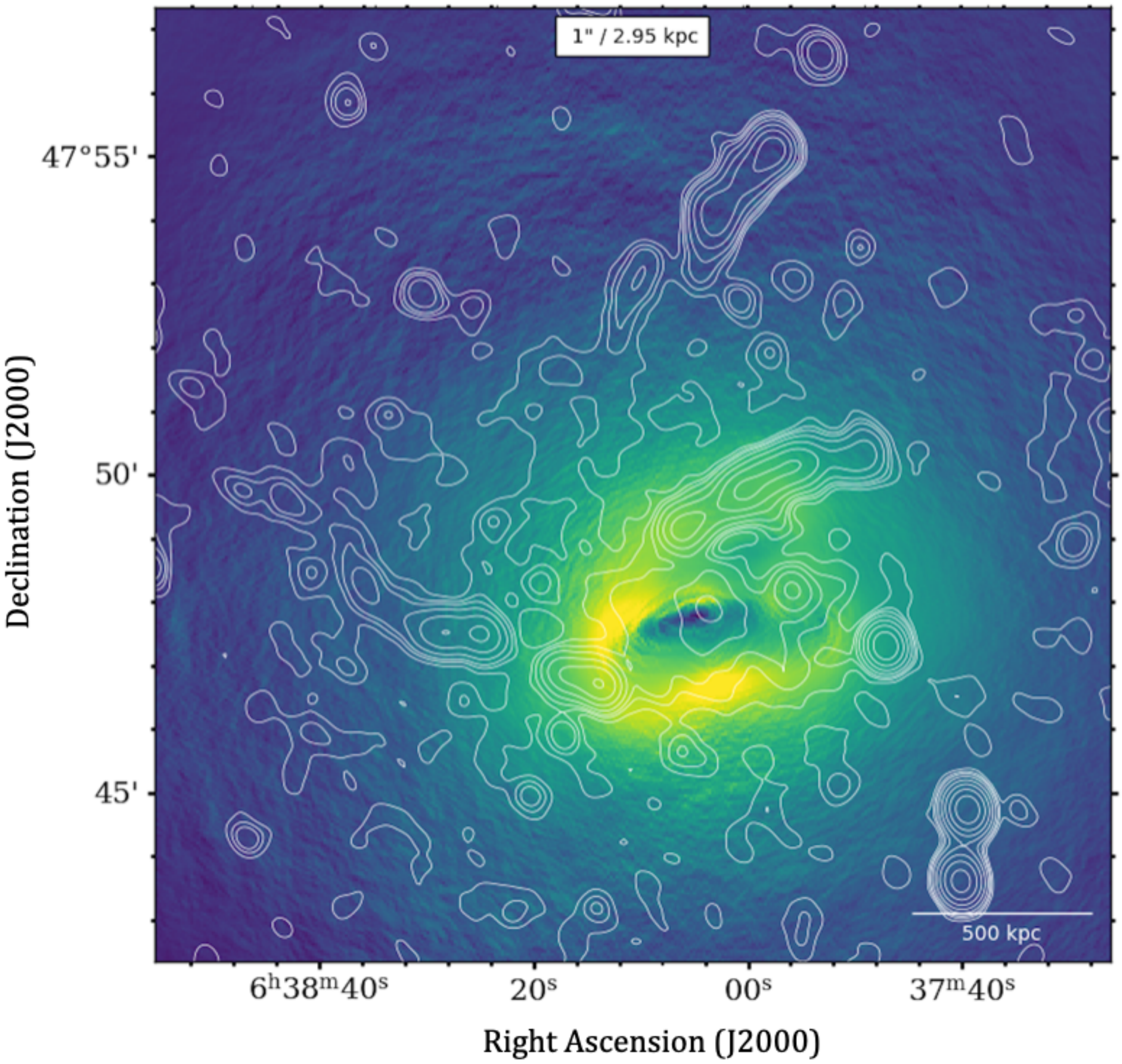

Figure 2.13: X-ray 0.5 - 2 keV image filtered with an adaptive GGM filter, using a signal-to-noise ratio of 32. Radio contours from **Fig. 2.4b** are overplotted.

Following the procedure of Cuciti et al. (2018), we measure the flux density within a circular area of ∼ 600 kpc diameter, which roughly follows the $3\sigma_{\rm rms}$-contours of the images (see **Fig. 2.3**), using the source-subtracted tapered images described in **Section 2.2.5**. This region avoids the two HT-A and HT-B radio galaxies, which are extended sources, and thus cannot be subtracted from the *uv*-data with the same procedure used for the compact sources in **Section 2.2.5**. The results are listed in **Tab. 2.4**. We point out that we find high-frequency flux densities that are slightly different from Cuciti et al. (2018). Our values of $S_{1.5\rm GHz} = 2.5 \pm 0.2$ mJy and $S_{320\ \rm MHz} = 14 \pm 2$ mJy are nevertheless still consistent with measurements reported in Cuciti et al. (2018). The difference could be due to different sources subtraction methods. Cuciti et al. (2018) measured the compact-sources flux density from the high-resolution images and subtracted that from the measurement on the radio halo region of the low resolution images, while here we subtracted the compact sources directly from the *uv*-data.

In order to obtain a size and flux estimate that is independent of the signal-to-noise ratio of the radio images (i.e., that does not rely on the $3\sigma_{\rm rms}$−contours), we fit the the same low-resolution source-subtracted images of **Fig. 2.3** with Flux Density CAlculator software[6] (`FDCA-Halo`; Boxelaar et al., 2021). This method fits the surface brightness profile of halos to a 2D-model using Bayesian inference. The general exponential model used is

$$I(\mathbf{r}) = I_0 e^{-G(\mathbf{r})}, \tag{2.4}$$

where $I(\mathbf{r})$ is the surface brightness and $G(\mathbf{r})$ the function that takes different forms depending on the complexity of the model (see Boxelaar et al., 2021, for details). In the circular model case, $G(\mathbf{r}) = |\mathbf{r}|/r_{\rm e}$, where the e-folding radius $r_{\rm e}$ is the length-scale at which the surface brightness drops to I_0/e. To avoid contaminating sources, we first masked the regions corresponding to extended radio sources other than the radio halo. Masked regions, model and residuals can be found in **Section A.1**, while the fitting results in **Tab. 2.4**.

The fitted $r_{\rm e}$ values are more uniform across the frequency range (120 – 145 kpc) compared to the size based on the $3\sigma_{\rm rms}$-contours ($D \sim 480 - 850$ kpc) and consistent with each other because they are less affected by the noise. Flux densities with `FDCA-Halo` are integrated up to a radius $R = 3r_{\rm e}$ that contains 80% of the total flux $S_\nu(< 3r_{\rm e}) = 0.8S_\nu^\infty$ (Murgia et al. (2009)).

To date, this is one of the few radio halos where we can study the radio spectrum from 1.5 GHz down to 50 MHz. In the near future, observations by the LOFAR LBA Sky Survey (LoLSS; de Gasperin et al., 2021, 2023), combined with archival data from other telescopes (such as uGMRT and VLA), will increase the number of systems with such a large frequency coverage (Pasini et al., in prep.).

The spectrum of the radio halo in ZwCl 0634.1+4747 is shown in **Fig. 2.14**: green points represent flux densities extracted within a radius of 300 kpc $S_\nu(< 300\,\rm kpc)$, while purple points are values obtained via `FDCA-Halo` procedure $S_\nu^{\rm FDCA}(< 3r_{\rm e})$. We note that the fitted size of the halo, i.e. $3r_{\rm e}$, is wider than the circular extraction region with $R = 300$ kpc (based on the $3\sigma_{\rm rms}$−contours), and thus the `FDCA-Halo` flux is higher. Despite of this, the spectral shape remains unchanged (**Fig. 2.14**). We fit the spectrum using a power law, finding a best-fit spectral index between 53 Hz and 1518 Hz of $\alpha = -1.18 \pm 0.04$ and $\alpha^{\rm FDCA} = -1.24 \pm 0.03$, respectively.

[6] https://github.com/JortBox/Halo-FDCA

Table 2.4: Summary of the main radio halo properties

ν	D	$S_\nu(< 300\,\text{kpc})$	P_ν	I_0	r_e	$S_\nu^{\text{FDCA}}(< 3\text{r}_\text{e})$	P_ν^{FDCA}
MHz	kpc	mJy	W/Hz	μJy/arcsec^2	kpc	mJy	W/Hz
53	770	138 ± 16	$(1.2 \pm 1) \times 10^{25}$	16 ± 2	141 ± 14	184 ± 27	$(1.6 \pm 0.2) \times 10^{25}$
144	850	40 ± 4	$(3.5 \pm 0.3) \times 10^{24}$	4.5 ± 0.3	145 ± 7	54 ± 6	$(4.7 \pm 0.2) \times 10^{24}$
320	480	14 ± 2	$(1.2 \pm 0.2) \times 10^{24}$	2.1 ± 0.5	130 ± 28	20 ± 6	$(1.8 \pm 0.5) \times 10^{24}$
1518	530	2.5 ± 0.2	$(2.2 \pm 0.2) \times 10^{23}$	0.36 ± 0.04	120 ± 12	3.0 ± 0.3	$(2.6 \pm 0.3) \times 10^{23}$

Col. 1: Frequency; Col. 2: Linear extension corresponding to the $3\sigma_{\text{rms}}$ contour in the E-W direction as a size reference; Col. 3: Flux density measured within a circular region with R = 300 kpc (see **Fig. 2.3**); Col. 4: Radio power calculated from $S_\nu(< 300\,\text{kpc})$ with the K-correction applied, assuming $\alpha = -1.2$; Col. 5: Central surface brightness from `FDCA-Halo` fitting, using a circular halo model; Col. 6: e-folding radius from `FDCA-Halo` fitting, using a circular halo model; Col. 7: Flux density measured within the $3r_e$ calculated by `FDCA-Halo`; Col. 8: Radio power calculated by `FDCA-Halo` corresponding to $P_\nu^{\text{FDCA}}(< 3\text{r}_\text{e})$, assuming $\alpha = -1.2$.

These values are consistent with previous high-frequency (Cuciti et al., 2018) and low-frequency (Cuciti et al., 2022) studies. Spectral indices $\alpha < -1.1$ are expected for the radio halos and are in agreement with other radio halos studied over the whole radio spectrum (e.g., A1758 Botteon et al. (2018b, 2020b), Coma Bonafede et al. (2022)). Moreover, this halo is under-luminous in the power-mass correlation in both $P_{1.5\text{GHz}} - M_{500}$ (Cuciti et al., 2021) and $P_{150\text{MHz}} - M_{500}$ (Cuciti et al., submitted); and has an emissivity $J_{1.4\text{GHz}} = (3.2 \pm 0.2) \times 10^{-43}$ erg/(s cm^{3}Hz) slightly lower compared to the emissivity of classical radio halos at 1.4 GHz in the range of [$5{\times}10^{-43}$; $4{\times}10^{-42}$] erg/(s cm^{3}Hz) (Cuciti et al., 2022). Statistical studies showed that halos not lying on the $P_{1.5\text{GHz}} - M_{500}$ correlation are usually associated with non-merging clusters or with USSRHs. In the framework of the turbulent re-acceleration scenario, this means that either the radio halo is not present at all, or the system is less massive and has experienced minor mergers, thus producing radio halos with steeper spectra.

2.4 Discussion

In this work, we studied HT radio galaxies that show ripples in the surface brightness profiles and spectral index flattening along the tail. In order to assess whether this is in line with pure radiative ageing due to IC and syncrotron losses, we compared the data to the JP model. This is a standard and widely used spectral ageing model, that assumes electrons are injected with a constant power-law energy spectrum. Moreover, in this analysis, we work under the assumptions of uniform minimum magnetic field, constant velocity and fixed inclination of the radio galaxy (see **Section 2.3.2**). Though simple, these are reasonable hypotheses given, for example, that the tails do not show sudden changes in direction. More complex models that include variations of the magnetic field etc. would require more data. Our results show that the jet emission deviates from the pure radiative ageing due to IC and syncrotron losses. We conclude that this is evidence

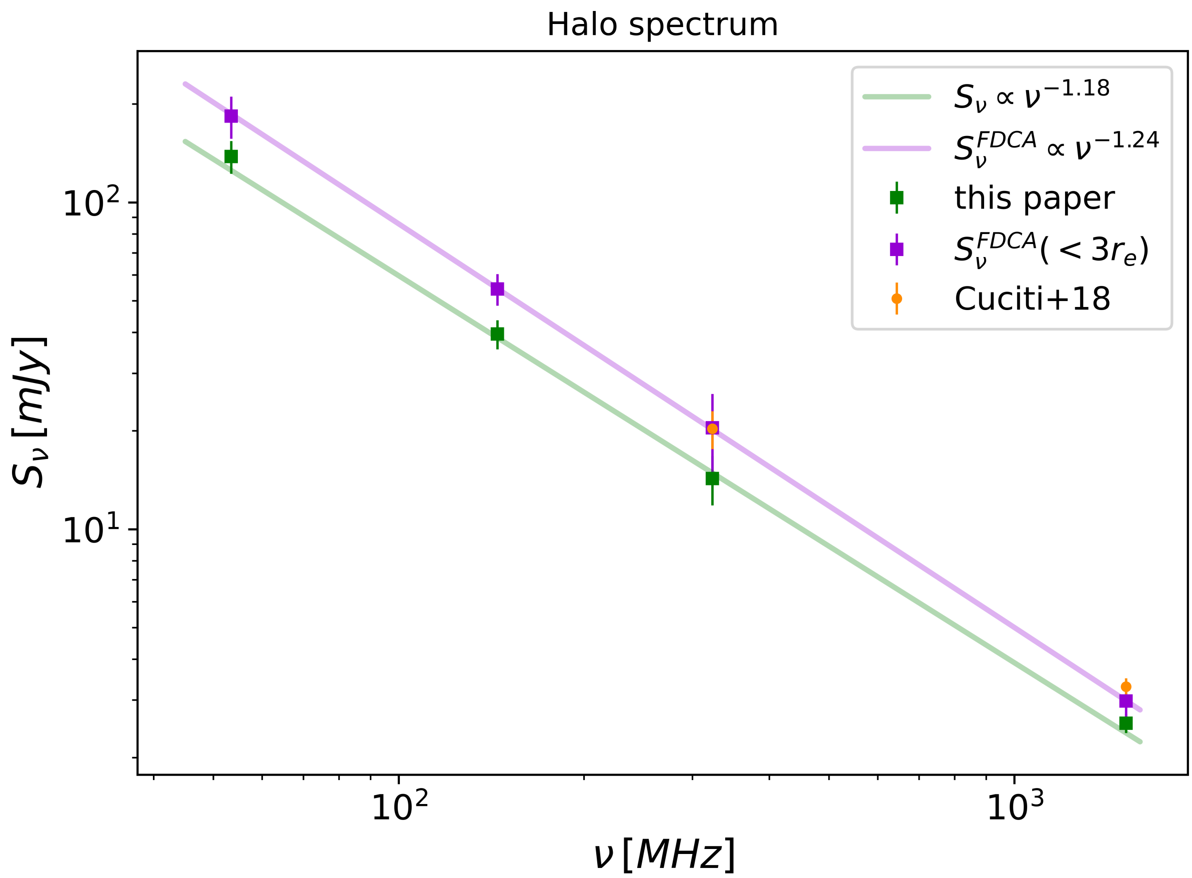

Figure 2.14: Integrated spectrum of the radio halo from 1.5 GHz down to 53 MHz. Green points indicate the integrated flux values measured in a circular region with $R = 300$ kpc. Purple points represent $S_\nu^{\mathrm{FDCA}}(< 3\mathrm{r_e})$, the flux calculated via `FDCA-Halo` fitting procedure within three e-folding radii. Values at 320 MHz and 1.5 GHz from Cuciti et al. (2018) are displayed in blue.

for re-acceleration. In this section we discuss possible scenarios that can affect the tail's spectral behaviour and morphology. Particular focus is on the long flattening of the spectral index and a frequency-dependent feature, only clearly visible in HT B (**Fig. 2.9**). This is due to the lack of high frequency information to use for measuring the spectral index α_{323}^{1518} at distances $> 150-200$ kpc from the head for HT A and HT C.

A first simple explanation for ripples in the brightness profile can be a varying output of the AGN. The standard JP model (**Section 2.3.2**) uses a single injection event. Thus, we are assuming that the AGN injection rate remains constant with time. A varying AGN would reproduce the ripples in the surface brightness profiles but not the flattening in the spectral index that we see in **Fig. 2.8**. Thus, although a varying AGN is still a plausible mechanism that contributes to the observed profiles, we exclude it as the main mechanism creating the observed features. We point out that possible changes of inclination during the motion through the cluster can also alter the observed surface brightness and spectral index profiles, causing deviations from the expected JP profile. However, we argue that this scenario is very unlikely for two main reasons. First, the morphology of the tails does not show sharp bends that could suggest such a scenario of varying direction of motion. Secondly, even if projection effects happened along the tail, in those regions we would be summing younger "foreground" electrons with older "background" ones. The result would be a spectral index decreasing faster with respect to the standard ageing, not slower, as we observe.

2.4.1 Shock - tail interaction

The interaction between shocks and tails is a possible scenario that can alter the tail morphology and physical properties. It is well known that when a shock encounters a population of aged electrons, it can re-energize particles, leading to observable synchrotron emission. However, the expected very high sound speed of the relativistic plasma does not allow the shock to penetrate into the radio tail (Enßlin & Gopal-Krishna, 2001).

However, a shock can adiabatically compress the fossil plasma and increase the magnetic field (Enßlin & Gopal-Krishna, 2001; Enßlin & Brüggen, 2002). In fact, adiabatic compression is able to re-energize an electron population, inducing brightening and spectral flattening. This kind of interaction was already investigated in the past, either in combination with the presence of a shock (van Weeren et al., 2017; Botteon et al., 2019; Wilber et al., 2019), or a cold front (Botteon et al., 2021b; Giacintucci et al., 2022). The shock scenario was also proposed by Cuciti et al. (2018) as a possible explanation to the HT-B observed radio properties. There are very few examples of HT-radio galaxies formation (O'Neill et al., 2019a) or shock-radio galaxy interaction (Nolting et al., 2019a,b; O'Neill et al., 2019b) simulations in the literature that can shed light on this complicated scenario. Although none of these simulations are tuned to reproduce the geometrical configuration proposed by Cuciti et al. (2018), we can use them for a general comparison. In particular, Nolting et al. (2019a) studied the interaction between a shock and an active radio galaxy, in the case where jets are aligned with the shock normal. They show that, as the shock travels along the jets, vortices are generated behind it (see Fig. 5 of Nolting et al. (2019a)). This toroidal vortex was found also in other simulations of a shock wave interacting and adiabatically compressing a radio plasma cocoon (Enßlin & Brüggen, 2002; Pfrommer &

Jones, 2011). The fact that we do not observe this morphological feature suggests that there is no shock travelling through the tail. However, we cannot completely rule out this option since signs of jets disruption might be present on scales smaller than our resolution. Moreover, we point out the need of tailored simulations, where a shock crosses a head-tail radio galaxy whose morphology has been already modified by the interaction with the ICM. As mentioned in **Section 2.3.2**, a shock interacting with the tail in the same configuration proposed by Cuciti et al. (2018) would create re-acceleration features at the same point of the tail (i.e., simultaneous brightness jumps and flattening of the spectra in correspondence of the shock location), while in HT-B we observe a shift of the point where the spectrum flattens (**Fig. 2.9**). This will be discussed in detail in **Section 2.4.2**. Finally, we point out that the XMM-Newton observation does not show any shocks at or near the radio tails, (see **Section 2.3.3**). For all the arguments mentioned above, we consider the presence of a shock as an unlikely scenario to explain the data.

2.4.2 Turbulence

Turbulence within the tail can arise from hydrodynamic instabilities that result from the interaction between the relativistic plasma and the surrounding medium. (Mignone et al., 2004; Jones et al., 2017; Mukherjee et al., 2021; Kundu et al., 2021; Ohmura et al., 2023). This turbulence can trigger several mechanisms of stochastic acceleration of particles, such as gentle acceleration, which has been suggested as a possible explanation for the GReET in Abell 1033 (de Gasperin, 2017; Edler et al., 2022).

As mentioned in **Section 2.3.2**, data for HT-B suggest that the spectral index flattens at different distances, depending on the frequency. In particular, the spectrum measured at higher frequencies flattens at greater distances from the head. Considering the kinematics of the tails, this corresponds to a situation in which the spectrum at higher frequencies flattens over longer times. This scenario agrees with the fact that spectral flattening is more evident at higher frequencies: α_{53}^{144} remains almost constant in the first 400 kpc around a value of $-0.6, -0.8$, while α_{323}^{1518} shows a well-defined decrease up to ~ -1.4 before flattening (see **Fig. 2.9**). This evidence allows us to understand something more about the mechanisms of particle re-acceleration. In practical terms, the flattening of the spectrum at higher frequencies over longer times indicates a gradual shift of the particles towards high energies. This, in turn, places constraints on the re-acceleration times. **Fig. 2.9** suggests that the energy of the emitting electrons essentially doubles in about 80 kpc, corresponding to about 260 Myr (considering a speed of the tail $\sim 300\,\mathrm{km/s}$).

We can conceive of two scenarios. In the first scenario, the electrons cool due to losses for a time t_{start} without being re-accelerated. After a time t_{start}, necessary for the development of the instabilities in the head tail and possibly also necessary for the turbulence to cascade to resonant scales, the same particles are re-accelerated on a time scale, τ_{acc}. This causes the spectrum to increase again at higher energies if τ_{acc} ¡ t_{start} ($\tau_{\mathrm{acc}} \geq t_{\mathrm{start}}$ would otherwise simply balance cooling on time scales τ_{acc}). In this case, $\tau_{\mathrm{acc}} \sim 260$ Myr and $t_{\mathrm{start}} \sim 500$ Myr (from kinematics ~ distance spectral flattening/velocity). A second option could be that a second component of (relativistic) particles is re-accelerated starting at t_{start} with $\tau_{\mathrm{acc}} \sim 200 - 300$ Myr. These particles might be present in the tail at lower energies and potentially filling a different volume with respect to the other component. This second scenario could explain the strong brightness increase observed in the re-acceleration phase and might also suggest that volume is not uniformly filled with CR particles. Discriminating between the two possibilities and constraining model parameters by fitting the data is beyond the scope of the current work and will deserve a future study. Finally, we point out that galaxies in clusters are expected to move with a velocity of the order of the velocity dispersion ($\sim 10^3$ km/s), which is not compatible with the value of a few hundreds km/s, derived from our modelling in **Section 2.3.2**. This suggests deficits in the JP model, even in the first kpc from the AGN. This means that no part of the tail is ageing subject to pure radiative synchrotron and IC losses, and we are facing a mechanism that acts broadly along the tail and starts as soon as the jets interact with the external medium. Recent simulations by Ohmura et al. (2023) show the effect of turbulent reacceleration on HT galaxies. They simulated AGN jets in an ICM wind and computed the evolution of CRe, considering both energy losses and stochastic acceleration. Their work clearly shows that in the presence of re-acceleration, the spectral index does not decrease substantially along the tail but remains fairly flat ($\alpha_{600}^{150} \sim -0.8, -1$) for about 150 Myrs. This is in agreement with our observations at low frequencies. At higher frequencies, we find a decrease of the spectral index in the first kpc from the head, which we attribute to the factors described above.

2.5 Conclusions

In this work, we have studied the radio halo and three HT radio galaxies of the same cluster ZwCl 0634.1+4747 (z=0.174). We make use of LOFAR LBA 53 MHz, LOFAR HBA 144 MHz, GMRT 323 MHz, VLA 1.5 GHz and X-ray XMM-Newton data. The cluster has already been studied at higher frequencies (Cuciti et al., 2018). However, the addition of low-frequency LOFAR observations has enabled us to study low brightness emission on large scales, both, in terms of diffuse halo emission and radio galaxies.
Our main results can be summarized as follows:

- We studied three HT radio galaxies, spread over the whole cluster volume. Their properties are listed in **Tab. 2.3**. This is the first time where multiple tails belonging to the same cluster can be studied over a frequency range from 53 to 1518 MHz. The use of very low frequency observations allowed us to observe them up to ~ 1 Mpc projected size and study the spectra at very large distances from the head.
- We investigated the properties of the HT galaxies by extracting surface brightness and spectral index profiles, revealing an increase of surface brightness and flattening of the spectral index. These characteristics together with their considerable lengths point towards a process that involves the re-acceleration of the initial electron population, which otherwise would cool below energies capable of radiating at our reference radio frequencies.
- We have proposed a scenario that could explain the morphological and spectral properties of the HT galaxies. This scenario involves a turbulence-induced, gentle re-acceleration mechanism that could explain the long flattening of the spectral profiles and the frequency-dependent feature of **Fig. 2.9**. We propose two scenarios: one involving a standard single population of electrons which initially cools down and then starts to be re-accelerated after $t_{\rm start}$; a second one, including multiple components of relativistic particles that are activated

at different times. Regardless of the scenario, the re-acceleration mechanism would act on a characteristic time scale $\tau_{\rm acc} \sim 200 - 300$ Myr or shorter, derived by comparing the distances at which the spectrum at different frequencies flattens.
- ZwCl 0634.1+4747 also hosts a radio halo with a linear size varying from ~400 to 800 kpc, depending on the frequency. We find that the spectrum is well represented by a power law with a spectral index between 53 and 1518 MHz of $\alpha^{\rm FDCA} = -1.24 \pm 0.03$ (**Fig. 2.14**). In previous studies, this halo was found to be under-luminous in both the power-mass correlation at 1.5 GHz and 150 MHz. Together with the relatively flat spectrum and the small size, we suggest that minor mergers can cause the extended radio emission.

Our results show that low-frequency observations are key to observe phenomena producing low brightness and steep spectrum emission. The presence of multiple HT radio galaxies with extreme lengths suggest that radio galaxies in clusters can enrich the ICM with fossil electrons. Moreover, if the proposed gentle turbulent scenario is a common process for radio galaxies in clusters, then this would imply that large amounts of electrons released into the ICM by AGN would be able to survive with high energies producing a seed population of energetic particles. These seed electrons have been invoked to explain cluster-scale radio emission, such as radio halos and relics.

Acknowledgements

MB acknowledges support from the Deutsche Forschungsgemeinschaft under Germany's Excellence Strategy - EXC 2121 "Quantum Universe" - 390833306. CS acknowledge support from the German Federal Ministry of Economics and Technology (BMWi) provided through the German Space Agency (DLR) under project 50 OR 2112. RJvW acknowledges support from the ERC Starting Grant ClusterWeb 804208. GDG acknowledges support from the Alexander von Humboldt Foundation. AB acknowledges financial support from the European Union - Next Generation EU. LOFAR (van Haarlem et al., 2013b) is the Low Frequency Array designed and constructed by ASTRON. It has observing, data processing, and data storage facilities in several countries, which are owned by various parties (each with their own funding sources), and that are collectively operated by the ILT foundation under a joint scientific policy. The ILT resources have benefited from the following recent major funding sources: CNRS-INSU, Observatoire de Paris and Université d'Orléans, France; BMBF, MIWF-NRW, MPG, Germany; Science Foundation Ireland (SFI), Department of Business, Enterprise and Innovation (DBEI), Ireland; NWO, The Netherlands; The Science and Technology Facilities Council, UK; Ministry of Science and Higher Education, Poland; The Istituto Nazionale di Astrofisica (INAF), Italy. This research made use of the Dutch national e-infrastructure with support of the SURF Cooperative (e-infra 180169) and the LOFAR e-infra group. The Jülich LOFAR Long Term Archive and the German LOFAR network are both coordinated and operated by the Jülich Supercomputing Centre (JSC), and computing resources on the supercomputer JUWELS at JSC were provided by the Gauss Centre for Supercomputing e.V. (grant CHTB00) through the John von Neumann Institute for Computing (NIC). This research made use of the University of Hertfordshire high-performance computing facility and the LOFAR-UK computing facility located at the University of Hertfordshire and supported by STFC [ST/P000096/1], and of the Italian LOFAR IT computing infrastructure supported and operated by INAF, and by the Physics Department of Turin university (under an agreement with Consorzio Interuniversitario per la Fisica Spaziale) at the C3S Supercomputing Centre, Italy.

Data Availability

Raw data are publicly available in the archives. FITS files of LOFAR HBA can be found at https://lofar-surveys.org/. Processed data used in this work will be made available upon reasonable request.

A.1 Flux Density CAlculator results

Flux Density CAlculator (`FDCA`) results for the 2D surface brightness fitting to study the central radio halo (see **Section 2.3.4**). The first column refers to the original source-subtracted images shown in **Fig. 2.3**.

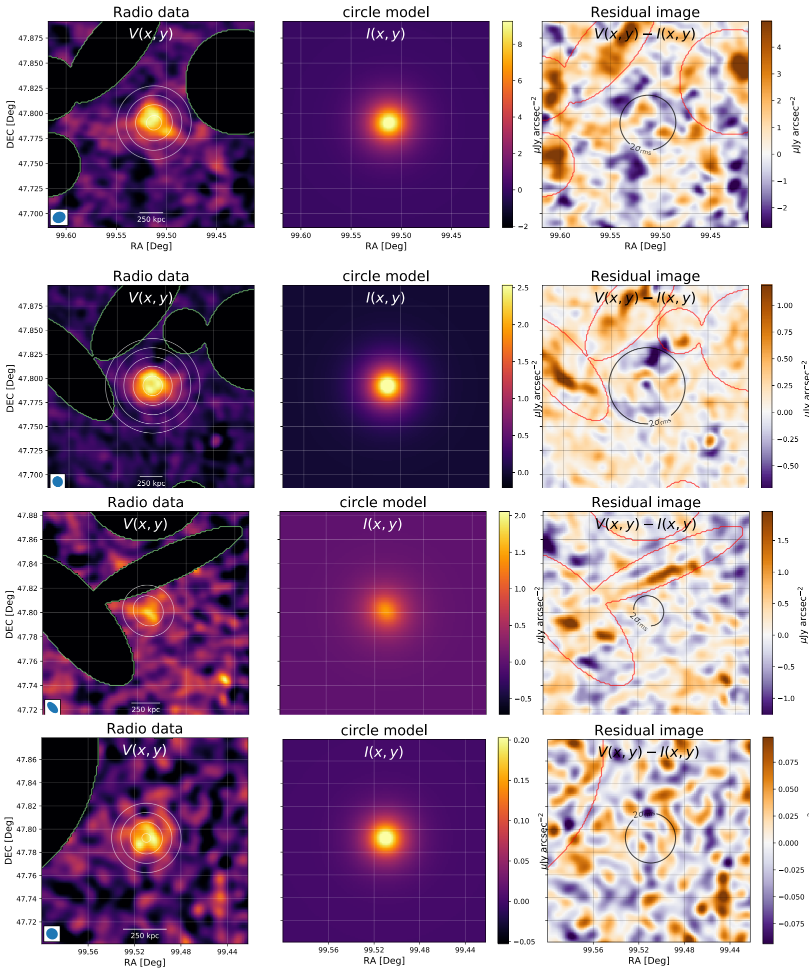

Figure A1: `FDCA-Halo` results for the radio halo in ZwCl 0634.1+4747 at LBA *(first row)*, HBA *(second row)*, GMRT *(third row)*, VLA *(fourth row)* frequency. *Left panel:* Original image with the contaminating regions masked out. *Middle panel:* Circular model map. *Right panel:* Residual image. The contour shows the $2\sigma_{\rm rms}$ level of the model. The red contours show the masked regions, the contamination sources are visible.

3 The view of the CIZA J2242.8+5301 galaxy cluster at very-low radio frequencies

G. Lusetti, M. Brüggen, H. W. Edler, F. de Gasperin, M. Hoeft, G. Di Gennaro, D. Hoang, T. Pasini, R. van Weeren, V. Cuciti, H. Rottgering, and G. Brunetti - accepted by A&A

Abstract

Context. *The galaxy cluster CIZA J2242.8+5301 is a well-studied merging galaxy cluster which hosts prominent double radio relics including the famous sausage relic, as well as other diffuse radio sources. Observations at frequencies below 100 MHz are essential for investigating the physics of radio relics as they provide unique access to the low-energy population of cosmic-ray electrons.*
Aims. *We aim to study the morphology, spectral characteristics and physical processes producing relics.*
Methods. *We present the first observations of the Sausage cluster at 45 MHz, the lowest radio frequency at which this cluster has been studied to date, using the Low Band Antenna (LBA) of the LOFAR radio interferometer. We made use of 10 hours of LOFAR LBA observations, from which we achieved a thermal-noise limited radio image with a noise level of* $1.5\,mJy/beam$ *at a resolution of* $15''$. *These data were combined with exhisting multi-frequency measurements at higher frequencies: LOFAR High Band Antenna (HBA: 145 MHz); Giant Metrewave Radio Telescope (GMRT: 325, 610 MHz); Westerbork Synthesis Radio Telescope (WSRT: 1.2, 1.4 GHz); Karl G. Jansky Very Large Array (VLA: 1.5, 3 GHz). This broad frequency coverage allowed us to derive integrated spectral indices, spectral index and curvature maps, and Mach number distributions across the relics.*
Results. *We derived Mach numbers from the local injection index measure using low-frequency data with* $\mathcal{M}_N = 2.9 \pm 0.5$ *for the northern relic and* $\mathcal{M}_S = 2.9 \pm 0.8$ *for the southern relic. LOFAR LBA observations reveal a remarkably symmetric surface brightness profile across the eastern part of the northern relic, with wings extending on either side of the peak. This discovery is contrary to the expectation of particle acceleration at a single, sharp shock and the subsequent downstream advection of accelerated electrons. We model the surface brightness profile, including effects of projection, magnetic field variation and shock deformation.*

3.1 Introduction

During the formation of the large-scale structure, galaxy clusters emerge through hierarchical merging and accretion processes. These events release vast amounts of energy into the intra-cluster medium (ICM), generating shocks and turbulence that can accelerate particles to relativistic energies (Brunetti & Jones, 2014). When relativistic electrons interact with the cluster's μG magnetic field, they emit synchrotron radiation, making these processes observable at radio wavelengths. Evidence of these processes is widely observed in the form of Mpc-scale diffuse radio sources, such as *radio halos* and *relics* (van Weeren et al., 2019). Radio halos are diffuse, centrally located steep spectrum sources that roughly follow the ICM distribution. They are believed to be powered by turbulence induced by cluster mergers, which re-accelerates a pre-existing population of relativistic electrons (Brunetti & Jones, 2014). Radio relics are elongated synchrotron sources located at the outskirts of galaxy clusters (see Wittor, 2023, for a recent review). They generally exhibit a bright outer rim in radio emission, which fades toward the cluster centre. This gradient in radio intensity is often accompanied by a steepening spectral index: from a relatively flat value at the edge of the relic, indicating freshly accelerated electrons, to a steeper value closer to the cluster core, where the electrons lose energy through synchrotron and inverse compton (IC) radiative processes. When observed edge-on, these structures often display an arc-like shape, resembling the shocks believed to produce them. However, high-sensitivity radio observations have revealed that radio relics can adopt a variety of morphologies, complicating our understanding of their origins and evolution. An increasing number of studies show relics with filamentary structures (e.g., de Gasperin et al., 2022), inverted morphology (e.g., Riseley et al., 2022a), or almost completely face-on (e.g., Rajpurohit et al., 2022). This diversity in shape is also supported by the latest simulations (**?**), which show that relics are not smooth structures, but intrinsically made of filaments and display a variety of morphologies driven by the complex dynamics of the ICM.

The prevailing theory is that radio relics form through the shock acceleration of cosmic-ray electrons via the Diffusive Shock Acceleration (DSA) process (Blandford & Ostriker, 1978; Drury, 1983; Blandford & Eichler, 1987; Ensslin et al., 1998; Hoeft & Brüggen, 2007). These shocks arise during cluster mergers, as large substructures collide and pass through one another, compressing and heating the ICM. The standard DSA theory involves the thermal electrons being directly accelerated (sometimes referred to as *fresh injection*). However, a major challenge is that the observed low Mach numbers ($\mathcal{M} \lesssim 3$) would imply unrealistically large particle injection efficiencies, which DSA from the thermal pool alone hardly explains (e.g., **?**). To solve this tension, models have invoked the presence of a pre-existing population of mildly-relativistic electrons (e.g., Markevitch et al., 2005; Kang & Ryu, 2011; Pinzke et al., 2013) either pre-accelerated by previous shock passages (Inchingolo et al., 2022) or coming from fossil plasma from radio galaxies, often observed in the proximity or radio relics (e.g., van Weeren et al., 2017). However, it is not straightforward that injection of fossil electrons by one or more radio galaxies would automatically produce a uniform population of electrons, able to produce the highly coherent radio emission observed in some giant relics (e.g., van Weeren et al., 2010; **?**). Another observational challenge has been the Mach number discrepancy. The shock Mach number can be inferred from both X-ray (via shock jump conditions) and radio (via the spectral slope of synchrotron emission) observations. In principle, these two independent methods should be consistent, as they measure the same shock. However, they rarely agree, with $\mathcal{M}_{\rm radio} > \mathcal{M}_{\rm X-ray}$. Recent simulations (Wittor et al., 2021; Whittingham et al., 2024) resolved this inconsistency, showing that the discrepancy naturally arises from the differences in how the two methods sample the underlying Mach number distribution (**?**). Radio observations are more sensitive to localized regions of high Mach numbers, which characterize only a small fraction of the shock's surface. While X-ray observations measure an averaged of the Mach number distribution across the entire shock front, leading to lower inferred values.

Studying individual relics in detail is crucial for testing and refining current models. One of the most studied systems in this regard is CIZA J2242.8+5301, which has become an ideal benchmark system, due to its well-defined relic structures and wealth of multi-wavelength data. CIZA J2242.8+5301 is a dissociative major merging galaxy cluster located at redshift $z = 0.1921$. It was first identified in X-rays by Kocevski et al. (2007) using *ROSAT*, but became widely known for hosting one of the most striking examples of a double radio relic. In particular, the distinctive morphology of the northern relic led to its designation as the 'Sausage cluster' (van Weeren et al., 2010). Due to its high brightness and morphological simplicity, the Sausage galaxy cluster quickly became a preferred target for the study of shock acceleration in the ICM.

Over the last decade, it has been extensively studied in the radio band across a wide frequency range, from 150 MHz to 30 GHz (van Weeren et al., 2010, 2011d; Stroe et al., 2013b, 2014b, 2016; Hoang et al., 2017; Loi et al., 2017; Di Gennaro et al., 2018; Loi et al., 2020; Di Gennaro et al., 2021c; Raja et al., 2024b). However, deeper observations have revealed that the radio emission in CIZA J2242.8+5301 is more complex than initially thought. While the cluster host a seemingly simple double-relic system, at approximately 1.5 Mpc north and south from the cluster centre, additional relic-like sources are detected in the downstream region of the main relics, as well as on the adjacent eastern and western sides of the radio shocks. This observationally proves that the merger environment is more intricate than a straightforward binary collision scenario, with multiple shock interactions and possible re-accelerated plasma components shaping the observed radio structures. In order to better characterize the shape of the relic spectrum, observations at frequencies up to 30 GHz have been performed. These observations aimed to investigate whether the integrated spectrum follows a single power-law, as predicted by the DSA model. Initially, Stroe et al. (2016) found a significant steepening of the spectrum from ~ -1.0 to ~ -1.6, above 2 GHz using interferometric data, invoking possible contributions from the Sunyaev-Zel'dovich (SZ) effect or the presence of a non-uniform magnetic field. However, subsequent single-dish observations with the Effelsberg Telescope (Kierdorf et al., 2017), as well as combined single-dish and interferometric measurements from the Sardinia Radio Telescope (Loi et al., 2017), found no evidence of spectral steepening at high frequencies. The cluster also contains a low surface brightness radio halo $\bar{\alpha}^{145\rm MHZ}_{2.3\rm GHz} = -1.01 \pm 0.10$; Hoang et al. 2017), previously reported in van Weeren et al. 2010; Stroe et al. 2013c; Hoang et al. 2017; Di Gennaro et al. 2018). Its characterization proved to be difficult, due to the substantial contamination from tailed radio galaxies and its connection to the relics.

Many efforts have been devoted to studying CIZA J2242.8+5301 also in the X-ray band

(Ogrean et al., 2013; Akamatsu & Kawahara, 2013; Ogrean et al., 2014; Akamatsu et al., 2015), which is crucial for confirming the presence of shocks and investigating the dynamics of the merger scenario. Analyses by Ogrean et al. (2013) with *XMM-Newton* and by Akamatsu & Kawahara (2013) with *Suzaku* reveal an elongated X-ray morphology aligned with the merger axis indicated by the radio relics. However, detecting an unambiguous cluster merger shock (exhibiting both a sharp gas density edge and a temperature jump), in connection with the relics has proven challenging. This is partly due to the low resolution of Suzaku and XMM-Newton, and partly because the relics reside in low signal-to-noise regions of the instrumental field of view. Akamatsu & Kawahara (2013) observed a temperature jump at the northern relic corresponding to a Mach number of 3.15, but no surface brightness jump in the X-ray profiles. These authors show that this is due to the limited spatial resolution of Suzaku, which is larger than the length of the shock, causing the discontinuity to be diluted and thus undetectable. Also Ogrean et al. (2013) found no evidence of shock compression near the northern relic while identifying a surface brightness jump by a factor of $\sim 2-3$, corresponding to a weak shock with a Mach number of 1.2-1.3 near the southern one (approximately 1 Mpc from the centre). However, due to the size of XMM-Newton FOV, even in this case, it was not possible to get data immediately beyond the southern relic to better constrain the gas properties at the exact relic position. In a consequential study, Ogrean et al. (2014) found multiple density discontinuities spread throughout the cluster volume but not a clear, strong shock signature at the northern relic location. While they confirm the detection of a temperature jump (consistent with a Mach number of 2.54), they only find a hint ($< 2\sigma$ detection) of a density jump at the northern relic location using Chandra data. Finally, Akamatsu et al. (2015) managed to detect two clear temperature drops at the location of the northern and southern relic, finding Mach values of 2.7 and 1.7, respectively.

Optical studies confirmed that the dynamics of the merger is dominated by two sub-clusters with comparable masses, leading to a near 1:1 mass ratio. In particular, spectroscopic velocity-dispersion analysis (Dawson et al., 2015) derived $M_1 = 16.1^{+4.6}_{-3.3} \times 10^{14} M_\odot$ and $M_2 = 13.0^{+4.0}_{-2.5} \times 10^{14} M_\odot$ for the northern and southern sub-clusters respectively, while weak-lensing inferred masses (Jee et al., 2015) were $M_{200} = 11.0^{+3.7}_{-3.2} \times 10^{14} M_\odot$ and $9.8^{+3.8}_{-2.5} \times 10^{14} M_\odot$ for the northern and southern halos, respectively. Furthermore, the low, relative line-of-sight velocity $69 \pm 190\,\mathrm{km/s}$ (Dawson et al., 2015) supports the scenario of a merger occurring close to the plane of the sky. The excellent agreement between the merger axis inferred from radio relics, ICM and bi-modal galaxy distribution strongly suggests that the merger is occurring close to the plane of the sky.

Being one of the brightest and most widely studied galaxy cluster, the Sausage cluster offers a unique opportunity to study properties of radio relics at very low radio frequencies ($\lesssim 100$ MHz) and to prove the technical capability of the LOw Frequency ARray (LOFAR; van Haarlem et al., 2013b) telescope and its related data calibration. Moreover, the small projection effect, clear shock feature and the large amount of observational data available made, this object a perfect reference target in simulation and for testing analytical models (Donnert et al., 2016; Kierdorf et al., 2017; Kang, 2016).

In this paper, we present for the first time 45 MHz observation of CIZA J2242.8+530, conducted using the LOFAR Low Band Antennas (LBA). We complement our study including higher frequency data from Hoang et al. (2017); Stroe et al. (2013c); van Weeren et al. (2010); Di Gennaro et al. (2018). The paper is organised as follows: we describe the radio observations and the data reduction in **Section 3.2**. In **Section 4.3**, we present our results for the Sausage galaxy cluster, including its morphology, spectral index and curvature analysis. The discussion appears in **Section 4.4**, including a thorough study of the shock Mach number and surface brightness profile modelling of the northern relic. Finally, we summarize our conclusions in **Section 4.5**.

Throughout this paper, we adopt a ΛCDM cosmology with $H_0 = 70\,\mathrm{km\,s^{-1}\,Mpc^{-1}}$, $\Omega_\mathrm{m} = 0.3$, and $\Omega_\Lambda = 0.7$. At the redshift of the Sausage cluster ($z \approx 0.19$), we have $1'' = 3.169$ kpc. The spectral index is defined as: $S_\nu \propto \nu^\alpha$, where S_ν is the flux density. The uncertainty Δ_S associated with a flux density measurement S is estimated as

$$\Delta_S = \sqrt{(\sigma_\mathrm{c} \cdot S)^2 + N_\mathrm{beam} \cdot \sigma_\mathrm{rms}^2}, \tag{3.1}$$

where $N_\mathrm{beam} = N_\mathrm{pixel}/A_\mathrm{beam}$ is the number of independent beams in the source area, and σ_c indicates the systematic calibration error on the flux density, with a typical value of 10% for LOFAR LBA (de Gasperin et al., 2021).

3.2 Observation and data reduction

In this section, we describe the data reduction for the LOFAR LBA data. In **Tab. 3.1**, we summarize the details of the observations.

Table 3.1: Observation details

Target	CIZA J2242.8+5301
Calibrator	3C380
Observing time	5th July 2022, 5h
	7th July 2022, 5h
Frequency range	20-68MHz
Time resolution*	4 s
Frequency resolution*	8 ch/SB
Antenna-set	LBA_SPARSE
Project	LC18_13
Obs. ID	2005118
	2005123

*: after initial averaging. SubBand bandwidth: 0.195 MHz.

3.2.1 Demixing

The target lies about 8 and 30 deg away from CasA ($\sim$ 27 000 Jy at 50 MHz) and CygA ($\sim$ 22 000 Jy at 50 MHz). Being among the brightest radio sources on the sky, it is necessary to carefully remove these sources from the data to avoid strong contamination by their emission spilling into LOFAR sidelobes. For this, we employ the *demixing* algorithm (Van der Tol, 2009), a technique specifically designed to remove the contribution of ultra-bright off-axis sources. This allows us to calibrate and subtract the bright sources from the visibilities. The model used for CasA and CygA is obtain from $\sim 10''$ resolution images (de Gasperin et al., 2020c) and contains over 1600 and 300 components, respectively. To accurately subtract the sources, we found that it is critically important to also take into account the sky model of the sources in the target field during demixing. This is currently not routinely done in pre-processing of LOFAR observations at the level of the LOFAR Observatory. Our model of the target field was constructed from the Global Sky Model which is built from radio surveys such as TGSS (TIFR GMRT Sky Survey, Intema et al. (2017)), NVSS (NRAO VLA Sky Survey, Condon et al. (1998)), WENSS (Westerbork Northern Sky Survey, Condon et al. (1998)) and VLSSr (Very Large Array Low-frequency Sky Survey Redux, Lane et al. (2014)). We show the impact of the demixing process with and without a target field sky model in **Fig. 3.1**.

3.2.2 Cross- and Self-calibration

The LBA observations were performed in observation mode LBA_SPARSE and using the multi-beam capability of LOFAR, which allows to continuously point one beam towards the calibrator source 3C380.

For calibration of the LBA data, we employ the standard routines implemented in the Library for Low-Frequencies (`LiLF` [1]). The initial step involves computing the solutions for the calibrator as described in de Gasperin et al. (2019). The calibration solutions were then applied to the target field data together with an analytic model of the dipole beam effect.

Next, the direction-independent (DI) self calibration of the target field was performed, as presented in de Gasperin et al. (2020a). This step aims at finding the solutions for the average ionospheric effects. From an initial sky model derived from the LOFAR Global Sky Model, solutions for the total electron content (TEC), Faraday rotation and second-order beam effects are derived and applied.

The last step consists of direction-dependent (DD) calibration, following de Gasperin et al. (2020a); Edler et al. (2022). This step addressed the remaining direction-dependent errors caused by the ionosphere. Firstly, the Python blob detector and source finder (`PyBDSF`; Mohan & Rafferty, 2015) was used to select bright and compact sources, which are then used as direction-dependent calibrators. Then, all sources of the source model found after direction-independent calibration were subtracted from the *uv*-data to create an empty data set. One at a time starting with the brightest source, the calibrators were re-added to the empty data, the data was phase-shifted to the calibrator direction and averaged in time and frequency, corrected for the primary beam in the new phase centre and self-calibrated in several cycles. If the rms noise level of

[1] `https://github.com/revoltek/LiLF`

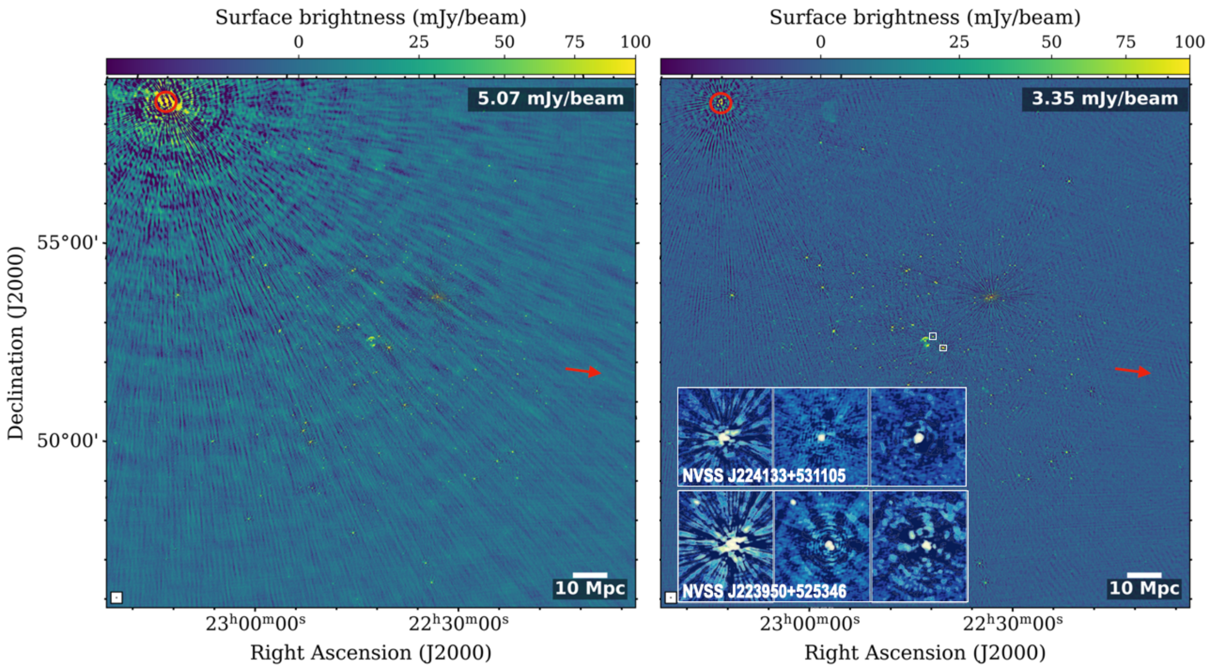

Figure 3.1: Results of the demix without (*left*) and with (*right*) considering the target field sky model. The red circle indicates the location of Cassiopeia A while the arrow points towards the location of Cygnus A outside of field-of-view (FoV). The sausage cluster resides at the centre of the image, the two bright radio galaxies NVSS J224133+531105 and NVSS J223950+525346 are highlighted with white squares. The insets show zoom-in images on these two radio galaxies after DI, DD and extraction calibration steps, from left to right respectively.

the image did not improve by more than 1% during a self-calibration cycle, the corresponding calibrator direction was considered converged, the calibrator was re-subtracted from the data set using the improved source model and solutions and the calibration for the next calibrator started. We performed a single DD cycle, that allowed us to obtain a high-fidelity image with well-recovered compact and extended emission.

3.2.3 Extraction

To further improve the quality of the image at the target position, in particular to reduce the artifacts in the vicinity of the strong sources, we employed the extraction technique. This was originally developed by van Weeren et al. (2021) for LOFAR HBA data. Here we use and describe the LOFAR-LBA adapted approach described by Pasini et al. (2022).

The first step consists of subtracting all sources outside the region of interest, i.e. circle of 20′ around the Sausage cluster, from the visibilities. For this, we take into account the DD calibration solutions of the sources to be subtracted using the facet-mode prediction in `WSClean` (v 3.4; Offringa et al. 2014). We then shift the phase centre of the observation to the centre of the region, and we average the data to a resolution of 0.2 MHz in frequency and 32 s in time. Finally, we perform a few additional self-calibration cycles to further refine the image quality. The final product shows improvement in terms of the image artifacts and also allows flexible re-imaging because of the smaller dataset size. Using `WSClean`, we produced the final images at high (15″, **Fig. 3.2**) mid (30″) and low (45″) resolution (**Fig. 3.3**). We reached a final rms noise of 1.5 mJy/beam, in line with the expected sensitivity of $\sim 1-1.5$ mJy/beam for an 8-hour observation (de Gasperin et al., 2023).

The data reduction of this cluster is made difficult by the two A-Team sources (CasA, CygA) degrees away from the target centre as well as by two strong radio galaxies (NVSS J224133+531105 and NVSS J223950+52534, see insets in **Fig. 3.1**) in the very proximity of the diffuse radio emission. With our calibration strategy, we reached thermal-noise, showing the capability of the `LiLF` pipeline.

3.3 Results

3.3.1 Radio morphology

In **Fig. 3.2** we show the 45 MHz image at LBA 15″ nominal resolution, together with zoomed-in parts showing relevant sub-regions of the radio emission at different frequencies (1.4 GHz, from Di Gennaro et al. 2018 and 145 MHz from Hoang et al. 2017). In line with previous work, we detect the two main relics (north and south, RN and RS), and three other regions of diffuse emission (R1-R3) above the $3\sigma_{\rm rms}$ level. While the LOFAR LBA system provides excellent sensitivity for detecting large-scale features, its nominal 15″-resolution limits the ability to resolve finer filamentary substructures. To address this, we complement **Fig. 3.2** with higher-frequency

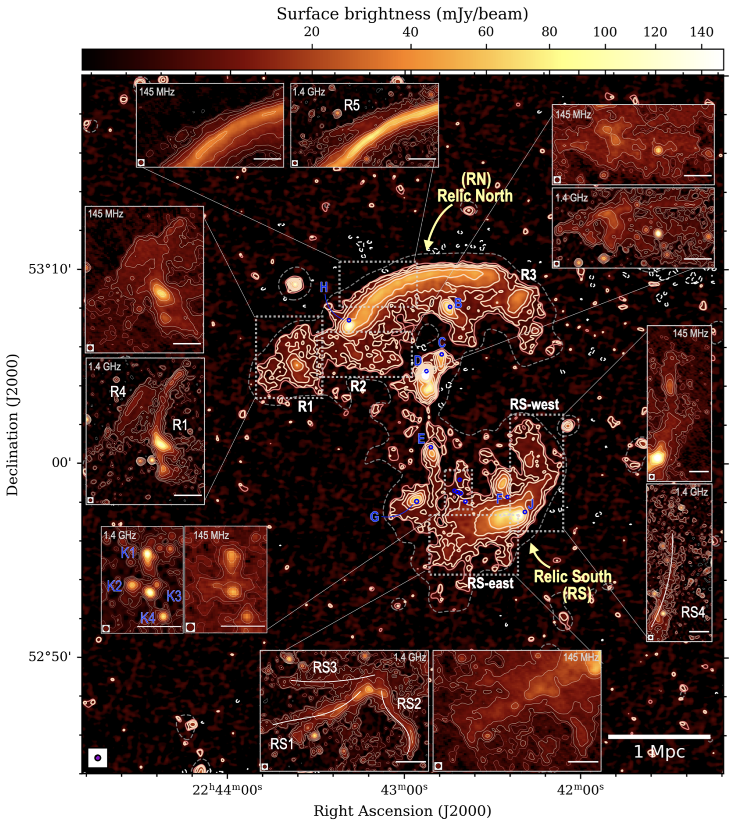

Figure 3.2: Image of CIZA J2242.8+5301 at 45 MHz, shown at the LBA nominal resolution (15″ beam). The contour levels are $[-3, 2, 3, 6, 12, 24, 48, 96] \times \sigma^{45}_{\rm rms}$, where $\sigma^{45}_{\rm rms} = 1.5$ mJy/beam, with additional dashed $3\sigma_{\rm rms}$ level from 45″ image (**Fig. 3.3**). Insets show zoomed-in views at different frequencies (1.4 GHz, Di Gennaro et al. 2018 and 145 MHz, Hoang et al. 2017) and comparable resolution (6″ and 7.5″, respectively) of the main substructures of the galaxy cluster. Contour levels in all panels are drawn at $[-3, 2, 3, 6, 12, 24, 48, 96] \times \sigma_{\rm rms}$, with $\sigma^{1.4}_{\rm rms} = 3.05\,\mu$Jy/beam and $\sigma^{145}_{\rm rms} = 0.11$ mJy/beam. The scale bar at the bottom right of each sub-plot corresponds to 150 kpc. Source labels are adapted from previous studies (e.g., Stroe et al., 2013c; Hoang et al., 2017; Di Gennaro et al., 2018).

and high-resolution images.

The northern relic (RN) shows the famous sausage-like morphology, with a projected linear size of ∼ 2 Mpc × 450 kpc based on the $3\sigma_{\rm rms}$ of the 15″-resolution image (**Fig. 3.3**, *left*). It increases to a linear size of ∼ 2.2 Mpc × 760 kpc when measured from the 30″-resolution image (**Fig. 3.3**, *centre*).

Blended with the source RN itself, at its eastern end, we find the double-radio source H, with one jet engulfed in the downstream region of RN and the other which gives rise to the radial tail-like emission in front of the relic. Further east, about 630 kpc from source H, we find an extended, patchy source (R1), with a north-south extension of 570 kpc. R1 displays an irregular arc-like morphology and has a bright peak in the southern part. South from source H and tightly connected to RN, lies another radial-like source (R2), which extends for 760 kpc. We note that, unlike in higher-frequency observations where these substructures appear fragmented

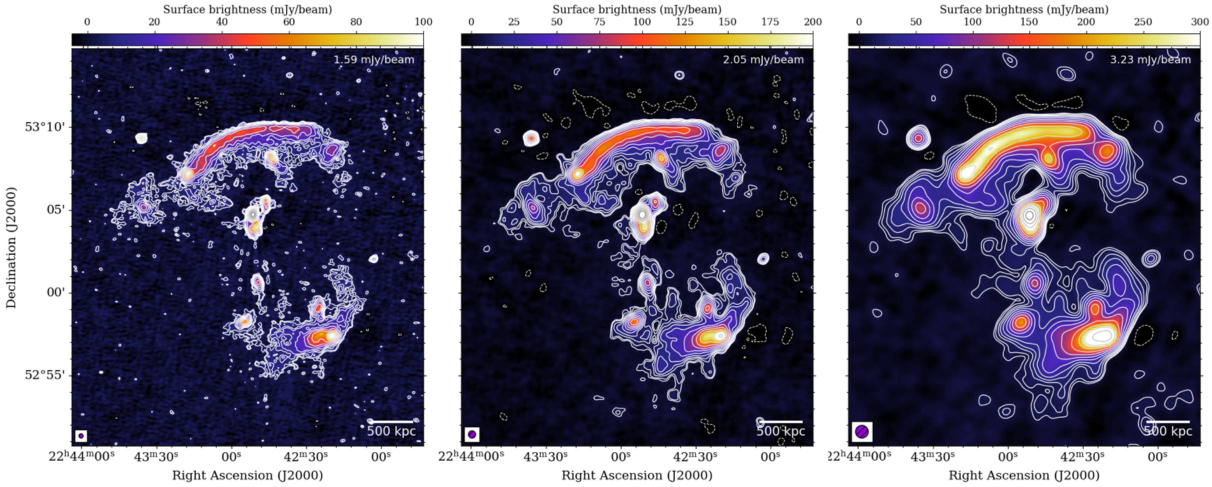

Figure 3.3: Final images at different resolutions. Left: 15″−beam, $\sigma_{\rm rms}$ = 1.59 mJy/beam; Centre: 30″−beam, $\sigma_{\rm rms}$ = 2.05 mJy/beam; Right: 45″−beam, $\sigma_{\rm rms}$ = 3.23 mJy/beam; Contours are drawn at [-3,3,...]×$\sigma_{\rm rms}$ with $\sqrt{2}$ steps.

and disconnected from each other —even when compared at similar resolution—, R1, R2 and RN appear interconnected by a homogeneous low-brightness emission that envelops and links these features. Moreover, in studies at higher-resolution and higher-frequencies (Di Gennaro et al., 2018; Raja et al., 2024b), both, R1 and R2 sources exhibit substructures and appear to consist of multiple components. Specifically, R1 is further resolved into R4 and R1 (see left panels of **Fig. 3.2**); while R2 shows arms-like structures that follow the radial direction. While the western half of RN shows a sharp edge, which closely coincides with the bright shock rim, we detect emission along the complete length of the eastern half, for a total size of ~ 700 kpc (see further discussion in **Section 3.4.3**). Originally reported by Di Gennaro et al. (2018), and recently confirmed by Raja et al. (2024b), faint diffuse radio emission, labelled as R5, is located north of the eastern edge of RN. This feature is more clearly defined at higher frequencies and appears more diffuse at LOFAR frequencies (see top panels of **Fig. 3.2**). On the western side of RN, we detect a patchy box-like source labelled as R3. It is elongated towards the radial direction, with a size of 380 kpc. The source R3 is blended with the main relic and further extends towards the southern direction by up to 430 kpc and it is also detected in Raja et al. (2024b) work as R3S.

The southern relic (RS) exhibits an irregular morphology, far thicker and much more contaminated by radio galaxies than the northern one. Moreover, its morphology changes significantly with frequency, showing filamentary arms at high frequencies (see RS1, RS2, RS3, RS4 in the bottom and left sub-panels of **Fig. 3.2**) while remaining smoother and more diffuse at lower frequencies. Overall, RS extends for ~ 1.5 Mpc×520 kpc (linear size based on the $3\sigma_{\rm rms}$-contours of the 15″-resolution image (**Fig. 3.3**, *left*) and ~ 1.9 Mpc × 900 kpc when in the 30″-resolution image (**Fig. 3.3**, *centre*).

For all the sources (R1, R2, RS1, RS2, RS3, RS4), we find an overall increase in the degree of patchiness with frequency, based on visual inspection. While for the 45 MHz data, part of this effect may be attributed to the relatively low 15″ resolution achievable, which smooths out substructures with characteristic widths smaller than this scale, this trend also persists when comparing the morphology at similar $\sim 7''$ resolution (see insets at 145 and 1400 MHz in **Fig. 3.2**). Previous studies have shown that a turbulent pre-shock medium can naturally reproduce the small-scale substructures in relics (Dominguez-Fernandez et al., 2021). Interestingly, recent simulations by **?** showed that an increase in patchiness at higher frequencies would mainly depend on the Mach number distribution of the shock. Specifically, they find that a Mach number distribution with a spread greater than 0.3–0.4 is required to produce observational differences between low- and high-frequencies emission at $5''$.

CIZA J2242.8+5301 hosts a variety of radio sources, many of which have a head-tail morphology and show interactions with the extended emission (see labelled radio galaxies in **Fig. 3.2**). Radio sources, such as sources H and B, are found close to source RN, while radio sources J and F are connected to RS. We find sources C, D, E, and G between the two relics. The proximity of these radio galaxies to the diffuse emission regions may play a significant role in shaping relic morphologies and contributing to the overall cluster extended radio emission. In fact, radio galaxies are possible sources of seed electrons dispersed into the ICM (van Weeren et al., 2017), which can be re-energized by propagating shocks and turbulence commonly present in galaxy clusters (Brunetti & Jones, 2014; Vazza & Botteon, 2024). The role of radio galaxies hosted in CIZA J2242.8+5301 is discussed throughout this paper when relevant, while more details about them and their optical counterparts can be found in Stroe et al. (2013c); Di Gennaro et al. (2018).

3.3.2 Integrated spectral index

Using 45 MHz LOFAR observations together with additional frequencies from Hoang et al. (2017) (LOFAR HBA: 145 MHz), Stroe et al. (2013c) (GMRT: 325), van Weeren et al. (2010) (GMRT: 610 MHz; WSRT: 1230, 1382 MHz) and Di Gennaro et al. (2018) (JVLA: 1.5, 3 GHz), we measured the volume-integrated spectral indices for the main extended sources: RN, RS, R1, R2 and R3.

In order to minimise biases in measured emission - and resulting spectral shapes - due to differences in the interferometers used to acquire the data and their respective uv-coverages, we used images with a common $0.2\,\mathrm{k}\lambda$ (corresponding to 0.3 deg) inner uv-cut and uniform weighting scheme. The integrated flux densities for all sources were calculated within regions defined by the $3\sigma_{\rm rms}$-contours of the LOFAR LBA $15''$ image (see inset of **Fig. 3.4**). The RN area is large enough to capture diffuse emission in the downstream region of the shock while avoiding contamination from radio galaxies (such as sources H and B). Being more extended and irregular, RS embeds a few point sources that were masked during the flux extraction procedure. We note that while the majority of them are compact and well-defined, source J appears to have a tail that steepens and becomes well-mixed with the relic emission (see **Fig. 3.5**), potentially playing a role in the formation of RS itself and affecting its morphology. As no clear distinction between the two sources could be made, we decided to not subtract it. Therefore, we point out that the overall RS spectrum might be artificially slightly steepened because of that. The spectral index is obtained by a weighted least-square fitting a single power-law function. The integrated spectra of both relics follow a close power law with a slope of $\alpha_{\rm int}^{N} = -1.09 \pm 0.03$ for RN and

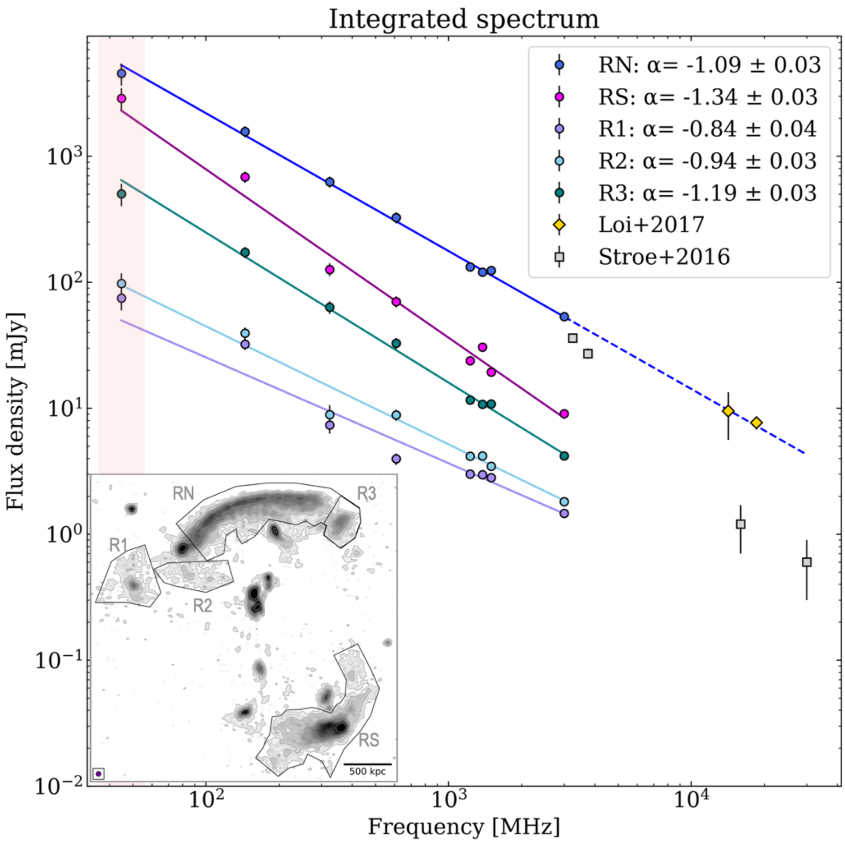

Figure 3.4: Integrated radio spectrum of RN, RS, R1, R2 and R2 from 45 MHz to 3 GHz. Extraction regions are shown in the bottom left corner. Values obtained in this work at 45 MHz are highlighted in red, while extra points are at 145, 323, 608, 1230, 1380 MHz (Hoang et al., 2017) and 1.5, 3 GHz Di Gennaro et al. (2018). Above 3 GHz values from high-frequencies from Stroe et al. (2016) (grey squares) and Loi et al. (2017) (yellow diamonds) studies are reported.

Table 3.2: Flux densities for the radio relics in CIZA J2242.8+5301. The integrated fluxes were measured from 15″ images described in **Section 3.3.2**. Extraction regions and integrated spectra are shown in **Fig. 3.4**.

Freq MHz	RN mJy	RS mJy	R1 mJy	R2 mJy	R3 R3
45	4535 ± 907	2886 ± 578	449 ± 91	293 ± 60	502 ± 101
145	1570 ± 157	684 ± 68	194 ± 20	119 ± 12	173 ± 17
325	625 ± 63	126 ± 15	44.2 ± 6.6	26.7 ± 4.9	63.2 ± 7.2
610	326 ± 33	70 ± 7	4 ± 2	27 ± 3	32.8 ± 3.3
1230	132 ± 7	23.9 ± 1.4	18.0 ± 1.0	12.5 ± 0.7	11.6 ± 0.7
1382	120 ± 6	30.5 ± 1.6	17.8 ± 0.9	12.5 ± 0.6	10.8 ± 0.6
1500	124 ± 6	19.3 ± 1.1	16.9 ± 0.9	10.4 ± 0.6	10.8 ± 0.6
3000	53.3 ± 2.7	9.0 ± 0.5	8.8 ± 0.5	5.4 ± 0.3	4.2 ± 0.2

$\alpha^{S}_{\rm int} = -1.34 \pm 0.03$ for RS (see **Fig. 3.4**). The power-law spectrum obtained for both relics is consistent with the standard scenario for the relic formation, where DSA acceleration occurs from the thermal pool electrons. These integrated spectral index values are in line with previous studies (see **Tab. 3.3**) and are in agreement with other relics studied across a wide frequency range (e.g., Rajpurohit et al., 2020). At higher frequencies, a discrepancy exists between Stroe et al. (2016), who found evidence of spectral steepening for $\nu > 2.5$ GHz, and a subsequent study by Loi et al. (2017), which reported no steepening up to 18.6 GHz, attributing the difference to missing diffuse flux in interferometric data. Our new values, focused on the low-frequency end of the spectrum, reveal a spectral behaviour still in line the high-frequency points of Loi et al. (2017) (see **Fig. 3.4**). We notice a significant scatter around the best-fit lines for sources R1 and R2 (compared with RN RS and R3). This may result from the low signal-to-noise ratio of the detections and the challenges associated with accurately imaging large, faint and diffuse sources. However, the resulting best-fit spectral index values ($\alpha^{R1}_{int} = -0.84 \pm 0.04$, $\alpha^{R2}_{int} = -0.94 \pm 0.03$) are in agreement with higher-frequency studies, such as Stroe et al. (2013c); Hoang et al. (2017); Raja et al. (2024b). The variety of spectral indices highlights the complexity of the merger, which cannot be simply attributed to the emission from a primary shock and its counter-shock, and suggests the presence of a combination of processes, perhaps including multiple shocks on different scales. If these substructures are interpreted as additional relic-like regions or smaller-scale shock structures, their relatively flatter integrated spectral indices would imply strong Mach numbers, suggesting the presence of more energetic shocks (see **Section 3.4.1** for further details).

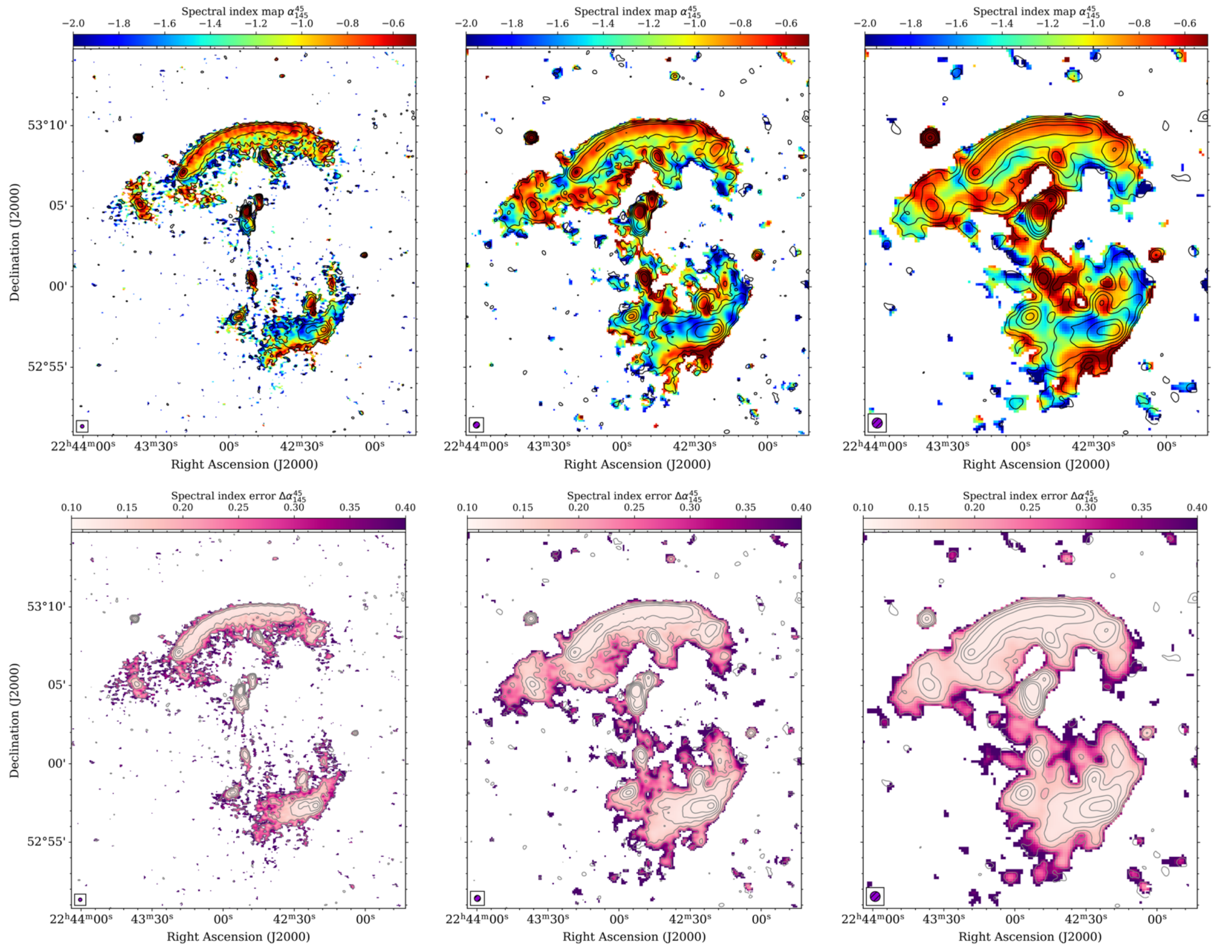

Figure 3.5: *Top panel*: Spectral index map between 45 and 145 MHz at a spatial resolution of $13'' \times 13''$ *(left)*, $23'' \times 23''$ *(middle)* and $37'' \times 37''$ *(right)*. *Bottom panel*: relative spectral index error $\Delta\alpha^{45\,\mathrm{MHz}}_{145\,\mathrm{MHz}}$. Pixels with surface brightness values below $2\sigma_{\mathrm{rms}}$ in the two images were blanked and $[3, 6, 12, 24, 48, 96] \times \sigma^{45\,\mathrm{MHz}}_{\mathrm{rms}}$ contours are overplotted.

Table 3.3: Integrated spectral index estimates for the northern (RN) and southern (RS) radio relics in CIZA J2242.8+5301.

	Source		
	RN	RS	Ref.
$\alpha_{0.153}^{2.7}$	-1.06 ± 0.04	-1.29 ± 0.04	Stroe et al. (2013c)
$\alpha_{0.145}^{2.3}$	-1.11 ± 0.04	-1.41 ± 0.05	Hoang et al. (2017)
$\alpha_{0.145}^{18.6}$	-1.12 ± 0.03	-	Loi et al. (2020)
$\alpha_{1.5}^{3}$	-1.19 ± 0.05	-1.12 ± 0.07	Di Gennaro et al. (2018)
$\alpha_{0.045}^{2.3}$	-1.09 ± 0.03	-1.34 ± 0.04	this work

3.3.3 Spectral index maps

We produced spectral index maps between 53 MHz and 144 MHz (**Fig. 3.5**). To this end, we re-imaged LBA and HBA data, using Briggs weighting with Robust parameter $R = -0.25$, common *uv*-range (80 λ inner *uv*-cut, corresponding to 0.7 deg) and convolved to the common beam size. In each map, we measured spectral indices for pixels with a flux density $\geq 2\sigma_{\rm rms}$ in both frequencies.

Both relics exhibit a spectral index gradient that decreases from the outskirts toward the cluster centre. In the 13″-resolution map (**Fig. 3.5**, *left*), the RN shows a spectral index gradient from the outskirts toward the centre of the cluster, from $\alpha_{45}^{145} \sim -0.7$ to ~ -1.8; while the RS goes from ~ -0.5 to ~ -2 across its width. In the mid-resolution 23″-map (**Fig. 3.5**, *centre*) the northern relic shows the spectral index gradient followed by a re-flattening. These flat $\alpha_{45}^{145} \sim -0.7$ values correspond to sources I and R2, two radial structures in the downstream region of the shock (see **Fig. 3.3**). The patchy source R3 appears to have a similar gradient to the main relic RN, but appears more diffuse and less pronounced. While morphologically we could not detect a clear distinction in R1 (**Section 3.3.1**), the spectral index maps allow us to identify two areas. R1-east, with values -0.8 ± 0.1, and R1-west (spatially corresponding to R4) show more values around -1.3 ± 0.2. This clear difference in terms of the spectral index implies that there are two distinct sources. Source R2 shows fluctuations of α_{45}^{145} from -0.8 to -1.2 and no clear gradient or trend. This patchy nature in terms of morphology and spectral index (both in this work and at a higher frequency - see Fig. 4 in Di Gennaro et al. 2018) might indicate a scenario where this relic emission is seen with a larger inclination, i.e. more face-on. This behaviour with mixed values of spectral index is for example seen in Abell 2256 (Rajpurohit et al., 2022), one of the most famous face-on radio relics.

The southern relic, RS, shows an irregular morphology, which is reflected in the variance of spectral indices and their spatial distribution. In fact, despite showing a gradient reaching even to steeper values ($\alpha_{45}^{145} \sim -2$) with respect to RN, only the south-east part of the relic shows

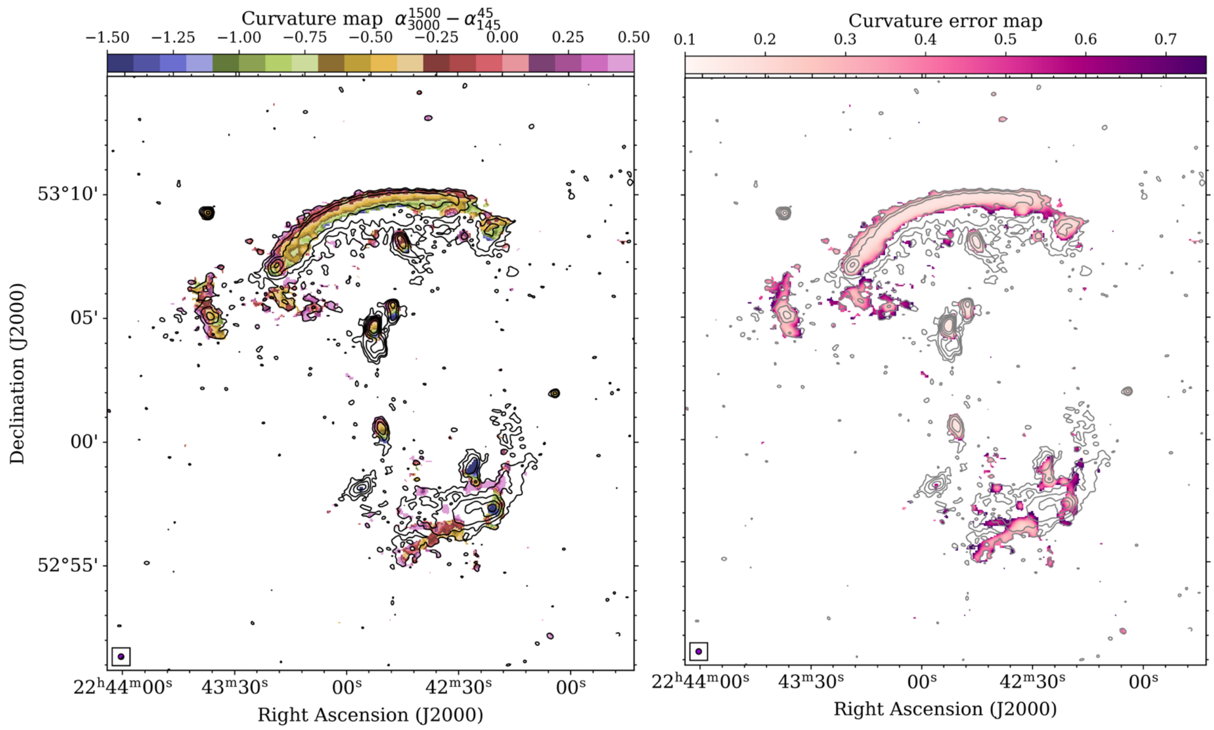

Figure 3.6: Four-frequency (45, 145, 1500, 3000 MHz) spectral curvature map. Pixels with surface brightness values below $2\sigma_{\rm rms}$ in the two images were blanked and $[3, 6, 12, 24, 48, 96] \times \sigma_{\rm rms}^{45\,\rm MHz}$ contours are overplotted.

the expected flat rim followed by a decrease. On the other hand, the western part of RS shows already steep values at the furthest edge ($\sim -1.8 \pm 0.2$) and no inward steepening. These broad steep-spectrum areas explain why RS fade quickly at higher frequencies ($\nu \gtrsim 600$ MHz), where primarily the southern edge remains bright.

3.3.4 Curvature maps

The LOFAR LBA 45 MHz data represents the lowest frequency observation available for this target and it offers a unique opportunity to study the spectral curvature across an unprecedentedly wide frequency range.

We produced curvature maps using images at 45, 145, 1500 and 3000 MHz convolved to the same 15″ resolution. As discussed in **Section 3.3.3**, we only considered pixels above the 2σ threshold. In agreement with previous work (Stroe et al., 2013c; Di Gennaro et al., 2018), we define the four-frequency spectral curvature as

$$C = \alpha_{\rm high} - \alpha_{\rm low}, \tag{3.2}$$

where $\alpha_{\rm high} = \alpha_{3000}^{1500}$ and $\alpha_{\rm low} = \alpha_{145}^{45}$. **Eq. (3.2)** is consistent with the three-frequency definition used Leahy & Roger (1998). In this framework, C < 0 for $|\alpha_{\rm high}| > |\alpha_{\rm low}|$, which is the case of a concave spectrum affected by standard spectral ageing. Conversely, $C < 0$ corresponds to an inverted spectrum, where $|\alpha_{\text{high}}| < |\alpha_{\text{low}}|$, i.e. the spectrum is steeper at lower frequencies. The resulting spectral curvature maps are shown in **Fig. 3.6**. The curvature at source RN increases from $C = 0$ in the outer part to values of ~ -1.5 in the downstream area. This is expected from the DSA theory which predicts a power-law energy distribution at the front of the travelling shock, where the electron population is freshly accelerated, leading to a relatively flat and constant spectral index across frequencies. The ranges of values obtained by this analysis agree with the previous curvature analysis by Stroe et al. (2013c). However, while Stroe et al. (2013c) reported small-scale variations along the source with a size of $\sim$ 64 kpc, we observe fewer pronounced variations in our data. Along the shock rim, the spectral curvature appears patchy and discontinuous. R1 shows a slight change in curvature from $\sim$ 0.2 to ~ -1.25 curvature. However, the large uncertainties at the edges ($\Delta C \sim 0.50$) prevent meaningful conclusions about this gradient, as within these uncertainties, the curvature values remain consistent with a power-law spectrum. In the same way, also source R2 shows a rather small curvature with values ~ -0.3. Source R3 shows a gradient similar to the one of the main relic, going from ~ -0.45 to ~ -1.25. The southern relic, RS, does not show areas with zero curvature with constant values of $C \sim -0.2$ to -0.5 in the RS-south area. Finally, point sources such as B, C, D, E, F show a canonical aged spectrum with increasing curvature the furthest away from the AGN reaching values of $C \sim -1.5$ at the ends of the jets.

3.4 Discussion

3.4.1 Mach number from radio data

Based on the assumption of standard DSA theory, the shock's Mach number, $\mathcal{M}$, can be estimated from the radio spectrum via (Drury, 1983; Blandford & Eichler, 1987):

$$\delta_{\text{inj}} = 2\frac{\mathcal{M}^2 + 1}{\mathcal{M}^2 - 1}, \tag{3.3}$$

where δ_{inj} is the index of the electrons power-law energy distribution injected by the shock ($\mathrm{dN(p)/dp} \propto \mathrm{p}^{-\delta_{\text{inj}}}$). This is related to the injection spectral index as $\alpha_{\text{inj}} = -(\delta_{\text{inj}} - 1)/2$. The volume-integrated spectral index on a radio relic, where there is a balance between acceleration and energy losses, is related to the injection index as (Kardashev, 1962)

$$\alpha_{\text{int}} = \alpha_{\text{inj}} + 0.5. \tag{3.4}$$

Thus **Eq. (4.4)** can be re-written as

$$\mathcal{M} = \sqrt{\frac{2\alpha_{\text{inj}} - 3}{2\alpha_{\text{inj}} + 1}}, \tag{3.5}$$

so that $\mathcal{M}$ can be derived directly from radio flux density measurements.

Table 3.4: Mach number estimates for the northern (RN) and southern (RS) radio relics in CIZA J2242.8+5301.

	Source		
	RN	RS	Ref.
$\mathcal{M}_{\rm R}^{\star}$	$4.6^{+1.3}_{-0.9}$	–	van Weeren et al. (2011d)
$\mathcal{M}_{\rm R}^{\star}$	4.58 ± 1.09	2.81 ± 0.19	Stroe et al. (2013c)
$\mathcal{M}_{\rm R}^{\star}$	$4.4^{+1.1}_{-0.6}$	2.4 ± 0.1	Hoang et al. (2017)
$\mathcal{M}_{\rm R}^{\star}$	$4.2^{+0.4}_{-0.6}$	–	Loi et al. (2020)
$\mathcal{M}_{\rm R}^{\star}$	4.8 ± 0.8	2.6 ± 0.1	this work
$\mathcal{M}_{\rm R}^{\dagger}$	$2.90^{+0.10}_{-0.13}$	–	Stroe et al. (2014a)
$\mathcal{M}_{\rm R}^{\bullet}$	$2.9^{+0.3}_{-0.2}$	$2.2^{+2.1}_{-0.4}$	Raja et al. (2024b)
$\mathcal{M}_{\rm R}^{\bullet}$	2.58 ± 0.17	2.10 ± 0.08	Di Gennaro et al. (2018)
$\mathcal{M}_{\rm R}^{\bullet}$	$2.7^{+0.6}_{-0.3}$	$1.9^{+0.3}_{-0.2}$	Hoang et al. (2017)
$\mathcal{M}_{\rm R}^{\bullet}$	2.9 ± 0.4	2.9 ± 0.8	this work
$\mathcal{M}_{\rm X}$	$2.7^{+0.7}_{-0.4}$	$1.7^{+0.4}_{-0.3}$	Akamatsu et al. (2015)
$\mathcal{M}_{\rm X}$	$2.54^{+0.64}_{-0.43}$	-	Ogrean et al. (2014)
$\mathcal{M}_{\rm X}$	3.15 ± 0.52	-	Akamatsu & Kawahara (2013)
$\mathcal{M}_{\rm X}$	-	1.2 – 1.3	Ogrean et al. (2013)

*: derived from volume-integrated spectral index via **Eq. (3.4)**;
†: derived from spectral ageing modelling;
$^{\bullet}$: derived from local spectral index measurement at the relic edge from images or maps.

From integrated spectral index values of **Section 3.3.2**, we derived injection indices between 45 and 145 MHz of $\alpha^N_{\rm inj} = -0.59 \pm 0.03$ and $\alpha^S_{\rm inj} = -0.84 \pm 0.03$ and Mach numbers of $\mathcal{M}_N = 4.8 \pm 0.8$ and $\mathcal{M}_S = 2.6 \pm 0.1$.

These results are consistent with previous work (see also **Tab. 3.4**): van Weeren et al. (2010) found $\mathcal{M}_N = 4.6^{+1.3}_{-0.9}$, from spectral index map, Stroe et al. (2013c) measured $\mathcal{M}_N = 4.58 \pm 1.09$ and $\mathcal{M}_N = 4.58 \pm 1.09$, from spectral index maps and colour-colour analysis, Hoang et al. (2017) ($\mathcal{M}_N = 4.4^{+1.1}_{-0.6}$) and Loi et al. (2020) ($\mathcal{M}_N = 4.2^{+0.4}_{-0.6}$) derived it from the integrated spectrum. Although consistent with one another, these estimates are considerably higher than the Mach numbers derived from X-ray data, reflecting the known trend $\mathcal{M}_{\rm R} > \mathcal{M}_{\rm X-ray}$, as also expected from simulations (Wittor et al., 2021; Whittingham et al., 2024). Deriving the Mach number from integrated spectral properties relies on the assumption of constant shock properties (such

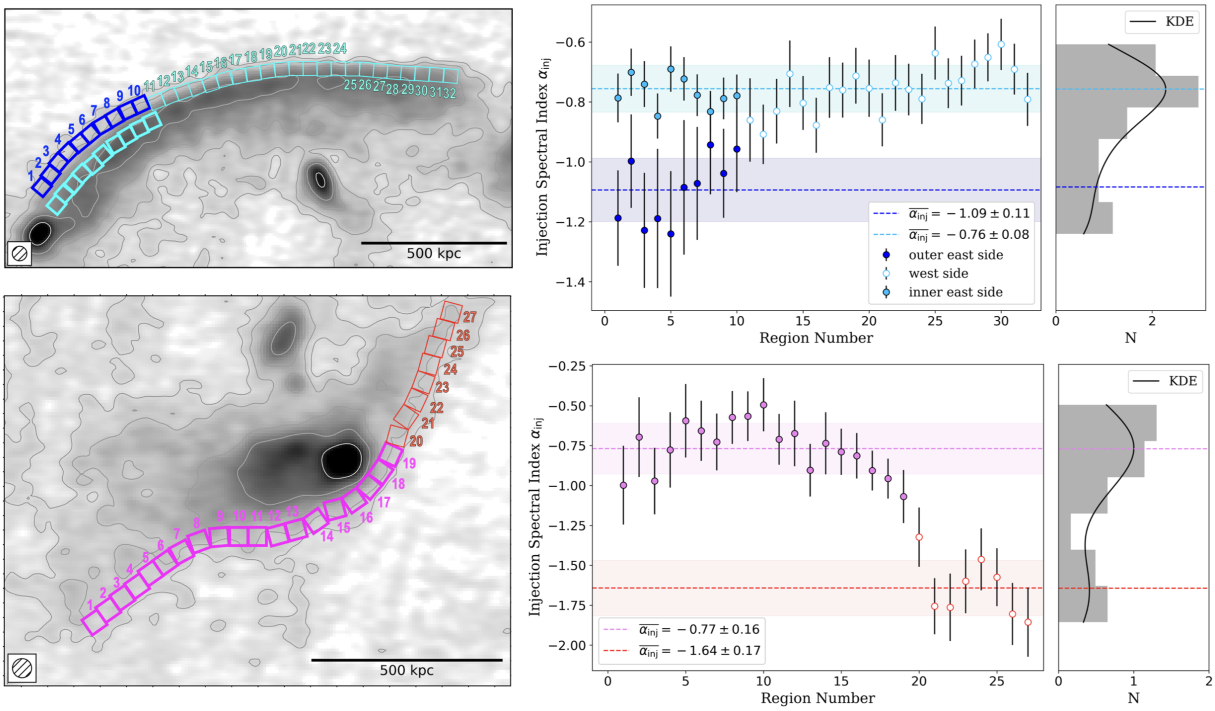

Figure 3.7: Injection spectral index calculated in 15″-box (~ 48 kpc separation) along the relics' edges. *Left:* zoom-in over the RN (top) and RS (bottom). *Right:* Injection spectral index profiles extracted from 45-145 MHz 15″-resolution images. The right panels display the density-normalized histograms together with a Kernel Density Estimation (KDE) curve for a smooth and continuous representation of the data distribution. For each relic, the data are colour-coded by the different clusters/groups identified by the GMM. The GMM means are plotted as horizontal dashed lines.

as velocity, compression ratio and magnetic field) and that the downstream ageing gas maintains steady conditions over time, with a balance between particle injection, acceleration, and radiative losses. However, several studies (Wittor et al., 2019a; Domínguez-Fernández et al., 2024; Whittingham et al., 2024) using cosmological MHD simulations showed that shocks in radio relics are complex structures, with significant spatial variation in both Mach numbers and magnetic fields.

A more accurate method to calculate the Mach number from the radio spectral index involves directly measuring the injected spectral index $\alpha_{\rm inj}$, by identifying α at the shock front - presumed to be injection region - rather than relying on $\alpha_{\rm int}$ via **Eq. (3.4)** and **Eq. (4.5)**. This is because, at the shock front, where particles have been recently (re-)accelerated, the injection spectral index is expected to be flat, while it steepens downstream due to synchrotron and IC energy losses. Low-frequency observations are particularly well-suited for this analysis, as they are less affected by these energy losses, providing a more reliable proxy for the injection spectral index.

The highest achievable resolution with LOFAR LBA is 15″. As this sets the minimum size of the regions over which we calculate the flux and corresponding spectral index, we need to ensure that these regions correspond to the physical thickness of the shock, thus minimizing the risk of mixing different electron populations. Considering a downstream velocity of $\sim 1000\,\mathrm{km/s}$ van Weeren et al. (2010), the travel time for the electrons to cross a distance equivalent to the $15''$ beam-size is ~ 50 Myr. This is about 5 times shorter than the typical electron cooling time (~ 360 Myr, for relativistic electrons in $\sim \mu$G magnetic field and detected at 45 MHz). Thus, we can assume that the energy losses due to synchrotron and IC process are negligible over the sampled distance, ensuring the measured spectral index is an accurate measure of the injection spectral index at the shock front.

To measure α_{inj}, we used the $15''$−resolution images at 45 and 145 MHz as done for spectral maps (**Section 3.3.3**) and estimated the injection spectral index in different beam-size regions along the relic edges (**Fig. 3.7**, *left*). In an ideal scenario with no projection effects and an edge-on view, the shock front coincides with the furthest contour of the relic emission and a common approach is to draw these regions along the furthest $3\sigma_{\mathrm{rms}}$-contour. However, from the spectral maps of **Fig. 3.5**, we note that the furthest edge of the northern relic RN (in particular the eastern half) does not correspond to the brightest rim or the region with the flattest spectral index. The picture is even more complex for the southern relic RS, due to its very irregular morphology and lack of a well-defined shock-like edge. Given these complexities, we first measured the spectral index in regions along the furthest edge of both relics, as this would be the expected location of the shock front (**Fig. 3.7**, *left*). This initial choice was made to avoid bias from prior knowledge of the relics morphology and ensure a systematic approach. To assess whether the spectral index values across the edges of the relics represent distinct populations, we employed a Gaussian Mixture Model (GMM) to classify the data into clusters. We then used information criteria, such as Akaike Information Criterion (AIC, Akaike (1974)) and Bayesian Information Criterion (BIC, Schwarz (1978)) to validate the GMM results by evaluating model fit. We applied a 2-sample Kolmogorov-Smirnov (KS, Massey (1951)) test to independently verify that the identified clusters represent statistically distinct populations. The results are shown in (**Fig. 3.7**, *right*).

For the southern relic, RS, the GMM analysis identified two distinct clusters with mean spectral index values of $\bar{\alpha}_{\mathrm{inj}} = -0.77 \pm 0.16$ and $\bar{\alpha}_{\mathrm{inj}} = -1.64 \pm 0.17$. Both the BIC and AIC confirmed that two Gaussian components ($k = 2$) best describe the data. The KS test further supported this finding, yielding a test statistic of 1 and a highly significant p-value 1.9×10^{-7}. The two distinct statistical populations also correspond to two separated locations of the relic (see **Fig. 3.7**): the flatter one corresponds to the south-east section of the relic (RS-east of **Fig. 3.2**), while the steeper is the top right edge (RS-west of **Fig. 3.2**). This indicates that the source RS contains two statistically distinct populations of spectral index values along the outer edge, potentially reflecting spatial variations in shock properties or a combination of different effects given the more complex RS dynamics and the potential interaction with source J. One possible explanation for the spectral difference is the effect of slow compression, i.e. acting on a time scale longer than the radiative losses, enacted by source J. Compression generally increases both the particle energy and magnetic field strength, but its impact can differ based on the time scale it happens. If compression occurs rapidly, the energy gained can effectively accelerate particles before significant losses occur. On the other hand, if compression occurs over a timescale comparable to or longer than the cooling time, it will increase the magnetic field strength, but at the same time, radiative losses ($\propto \gamma^2 B^2$) will become dominant, causing high-energy particles to lose energy faster than they gain from compression. This might explain why the northwest extension of source RS is drastically reduced at high frequencies (see **Fig. 3.2**).

We performed the same analysis also for RN, finding two statistically distinct populations (KS test statistic 1 and p-value 3×10^{-8}) with mean spectral index values of $\bar{\alpha}_{\rm inj} = -0.76 \pm 0.08$ and $\bar{\alpha}_{\rm inj} = -1.09 \pm 0.11$. Our measured $\bar{\alpha}_{\rm inj}$ is also in perfect agreement with the value obtained by Stroe et al. (2014a) ($0.77^{0.03}_{0.02}$), which was instead inferred by modelling emission with different ageing models. We note that the steepening of the spectral index in the eastern part of RN (blue boxes and points of **Fig. 3.7**) coincides with the source R5, which is located in front of RN. However, if we follow the morphology of the main shock - traced by the cyan bold regions and cyan-filled points in **Fig. 3.7** - we find values consistent with those in the western part of RN. Notably, these cyan regions align with the brightest rim of the relic, the location where, based on visual inspection, one would expect the shock front to be. The R5 region is interesting because, on one hand, it exhibits a significantly steeper spectral index, with $\bar{\alpha}^{45}_{145} \sim -1.09$; on the other hand, if considered part of the main relic, it affects the overall morphology of RN, broadening its width. The characterization of this region will be discussed in **Section 3.4.2** and **Section 3.4.3**.

These results show that even when small projection effects are present (as in the case of CIZA J2242.8+5301) the edges of the relic present significant spectral index variation across their length. Variation of $\alpha_{\rm inj}$ might imply variations of Mach numbers. This is consistent with previous studies that show how shocks producing radio relics often exhibit Mach number variations across the shock fronts, due to the interaction with a turbulent medium. In particular, numerical simulations (**?**Wittor et al., 2016; Dominguez-Fernandez et al., 2021) have proven that the distribution of Mach numbers naturally arises when a uniform shock propagates through a turbulent medium. Observational evidence supporting this scenario was reported by de Gasperin et al. (2015b), who found a gradient in the Mach number along the shock front of the radio relic in PSZ1 G108.18-11.53. Moreover, this demonstrates that estimating $\alpha_{\rm inj}$ by simply measuring values across the full relic following the $3\sigma_{\rm rms}$-contour can result in misleading averages. Since the resulting $\bar{\alpha}$ values would appear artificially steeper without distinguishing between different regions, such an approach risks underestimating the shock acceleration efficiency and the corresponding Mach number, possibly leading to oversimplified interpretations of the underlying physics.

Considering the results above, we define the injection indices of $\bar{\alpha}^{N}_{\rm inj} = -0.76 \pm 0.08$ and $\bar{\alpha}^{S}_{\rm inj} = -0.77 \pm 0.16$. This corresponds to Mach numbers $\mathcal{M}_N = 2.9 \pm 0.4$ and $\mathcal{M}_S = 2.9 \pm 0.8$. The derived Mach number for RN is consistent with previous literature estimates based on local spectral index measurements (see $\mathcal{M}^{\bullet}_{R}$ listed in **Tab. 3.4**). In contrast, the Mach number obtained for RS is significantly higher than in previous studies, though still within agreement given the large associated uncertainty. So far the Mach numbers derived for CIZA J2242.8+5301 double-relic system are found to be quite different from each other with $\mathcal{M}_N$ almost double $\mathcal{M}_S$ when measured from the volume-integrated spectral index (see $\mathcal{M}^{\star}$ values in **Tab. 3.4**). The discrepancy is reduced when Mach numbers are derived from $\alpha_{\rm inj}$ at the shock location (see $\mathcal{M}^{\bullet}$ values in **Tab. 3.4**), yet $\mathcal{M}_N > \mathcal{M}_S$. The results from our analysis instead, suggest that the two main shocks have comparable strengths. The overall distribution of Mach number estimates from

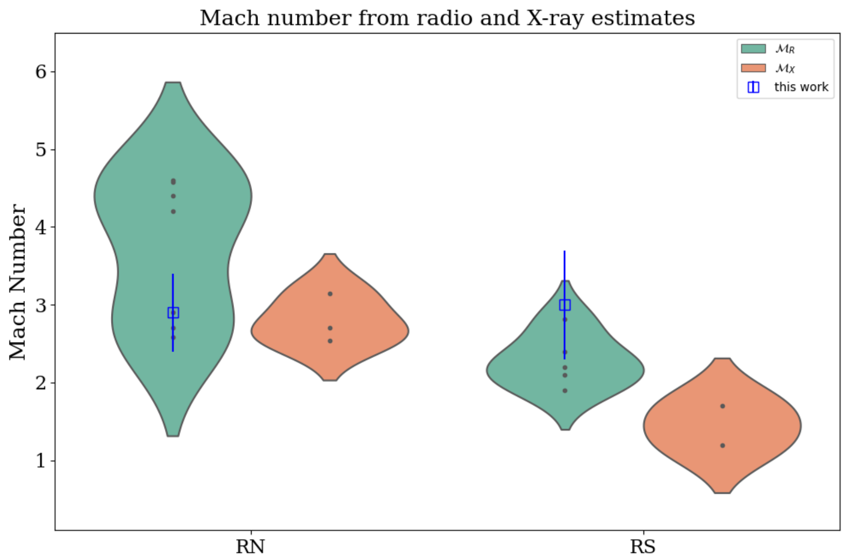

Figure 3.8: Mach numbers estimates for northern (RN) and southern (RS) radio shocks in CIZA J2242.8+5301, derived from the radio spectral index ($\mathcal{M}_R$, teal) and the ICM X-ray analysis ($\mathcal{M}_X$, orange). The violin plots illustrate the distribution of Mach number estimates from the literature (listed in **Tab. 3.4**), highlighting the range and density of measured values. Overlaid points represent individual measurements, while the blue empty squares are the values derived in this work (see **Section 3.4.1**).

both radio and X-ray studies is visually shown in **Fig. 3.8**, together with the newly derived values from this work. This is not unexpected, as in nearly equal-mass mergers (mass ratio $\sim 1:1$) such as CIZA J2242.8+5301, both shocks are often similar in strength, though local variations in pre-shock conditions and magnetic fields can introduce asymmetries. High consistency in Mach number couples is also observed in other well-studied double relic systems, where both relics have been characterized in detail. That is the case of Abell 1240 (Hoang et al., 2018, $\mathcal{M}_1 = 2.4$, $\mathcal{M}_2 = 2.3$), PSZ1 G108.18-11.53 (de Gasperin et al., 2015b, $\mathcal{M}_1 = 2.33$, $\mathcal{M}_2 = 2.20$), Abell 2345 (Bonafede et al., 2009b, $\mathcal{M}_1 = 2.8$, $\mathcal{M}_2 = 2.2$), and ZwCl 0008.8+5215 (van Weeren et al., 2011c, $\mathcal{M}_1 = 2.2$, $\mathcal{M}_2 = 2.4$), where the Mach numbers of the opposing relics are found to be very similar.

It is important to note the significant discrepancy between the two methods used to derive the Mach numbers. In the standard DSA framework, we can apply **Eq. (3.4)**, **Eq. (4.5)**. That means that ideally, the injection spectral index calculated at the shock from $\alpha_{\rm inj}$ should be 0.5 flatter than the integrated value $\alpha_{\rm int}$ derived in **Section 3.3.2**. However, for this and other clusters (**?**), this relation does not hold exactly. A simple explanation might be related to projection effects. In case of projection, the observed radio emission possibly contain a mixture of emission from different regions along the line of sight. Thus, it becomes difficult to isolate the pure injection spectrum. In this scenario, the measured local $\alpha_{\rm inj}$ will appear steeper than the one obtained via **Eq. (3.4)** from the integrated spectrum, due to mixing of emission with slightly different spectral ages. Alternatively, the Mach number discrepancy would mean that the standard DSA from thermal pool electrons fails to explain the origin of a fraction of radio relics and other mechanisms, either the presence of seed electrons or a modification of the standard DSA, are required. Possible explanations include injection intermittency, where particle acceleration is not continuous but varies over time due to the fact that weak shocks ($\mathcal{M}_{cr} \sim 2-3$) may become not efficient in accelerating particles if super-critical conditions are not generated at these shocks (e.g, **?**). In this case, continuous injection may not be established, affecting the overall downstream spectrum. Another contributing factor could be Alfvénic drift at the shock, which is expected to modify the spectrum of the accelerated particles (e.g, **?**). While a detailed investigation of these effects is beyond the scope of this work, the Mach number discrepancy highlights the complexity of low-Mach number shocks in galaxy clusters and the need for more refined models of shock acceleration.

3.4.2 Surface brightness profile across the northern relic

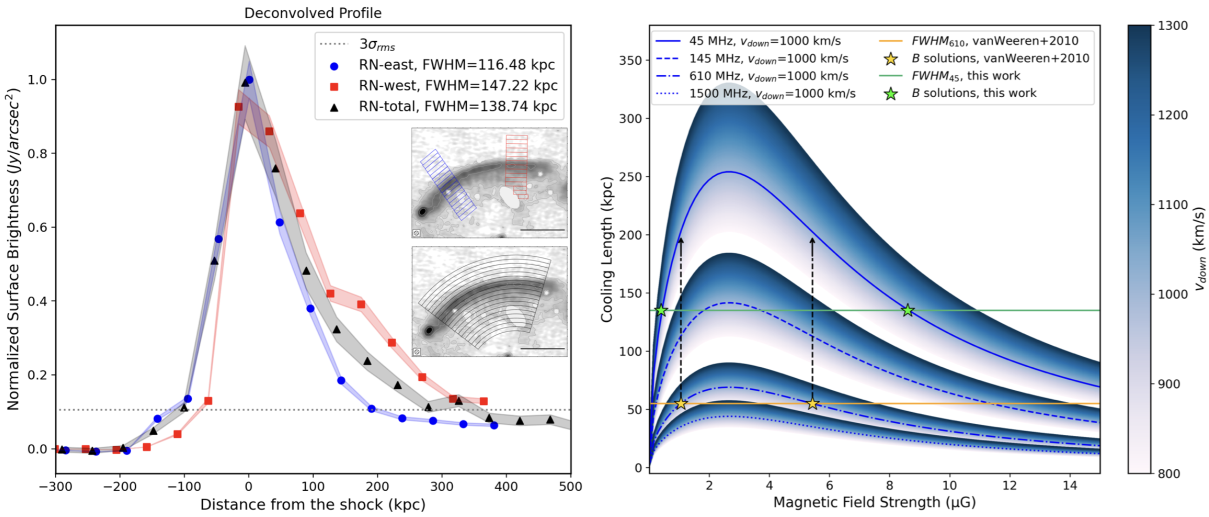

Figure 3.9: Deconvolved surface brightness profile of RN compared with theoretical relic cooling lengths. *Left:* Normalized surface brightness versus distance from the shock. Negative values correspond to the upstream region, while positive ones correspond to the downstream. Data points represent measurements extracted from the LOFAR model-image at 45 MHz along the eastern half (blue), western half (red) and full length (black) of the main relic RN. The dotted horizontal line indicates the image noise level of $3\sigma_{\rm rms} = 1.70 \times 10^{-5}$Jy/arcsec^2. The insets show the 15″-spaced extraction regions, with black 500 kpc scale bar in the bottom right corner. *Right*: Relationship between the cooling length (i.e., the relic thickness under ideal conditions of no projection effects and pure radiative losses), magnetic field strength and varying downstream velocity. Yellow stars represent the B solutions from van Weeren et al. (2010), while the green stars are the values from the analysis at 45 MHz. As a comparison, the vertical dashed arrows indicate the expected $\mathrm{FWHM}_{45\,\mathrm{MHz}}$ at low frequency, i.e. the extrapolated values from the relic B solutions derived from $\mathrm{FWHM}_{610\,\mathrm{MHz}}$.

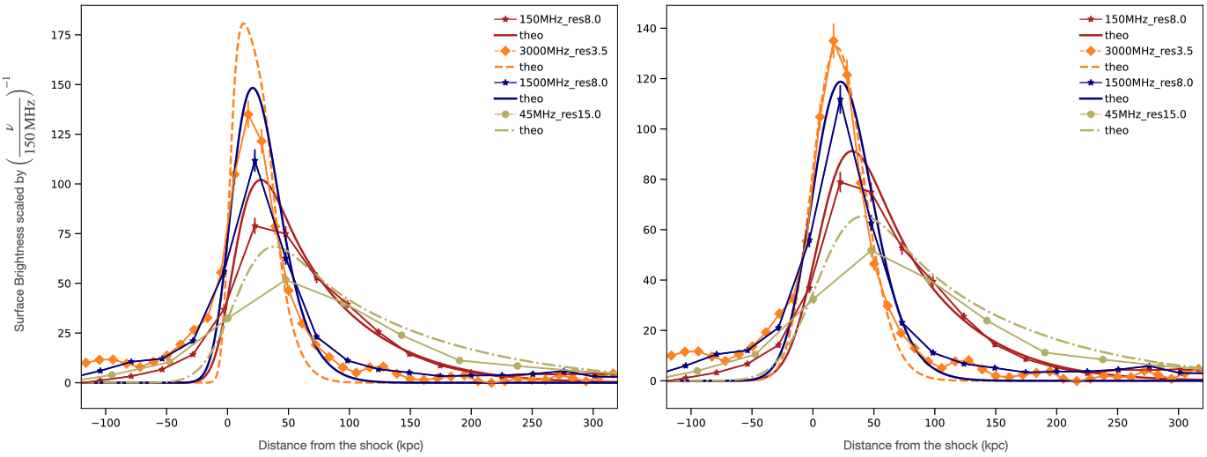

Figure 3.10: Surface brightness profile across the western half of RN. We applied the model to different frequencies at different resolutions: 3 GHz at 3.5″ (orange), 1.5 GHz at 8″ (blue), 150 MHz at 8″ (red) and 45 MHz at 15″. *Left*: Log-normal magnetic field distribution ($B_0 = 0.3\,\mu$G, $\log(\sigma) = 1.65$) and $\Psi = 12°$ projection. *Right:* Log-normal magnetic field distribution ($B_0 = 0.3\,\mu$G, $\log(\sigma) = 1.65$), $\Psi = 12°$ projection and additional wiggle-effect with $\sigma = 15$ kpc.

Due to its simple morphology and minimal projection effects, the modelling of RN has been extensively studied to infer the physical properties of the shock dynamics. Low-frequency observations are particularly sensitive to re-acceleration mechanisms and variations in the magnetic field, making them crucial for understanding the relic physics. In this section, we analyze the surface brightness (SB) profile of RN, focusing on 45 MHz data, and compare it with results at higher frequencies and theoretical models.

In the simple and idealized scenario of a planar shock observed perfectly edge-on (i.e., without projection effects) and assuming a uniform magnetic field, the width of the relic can be estimated based on spectral ageing principles. If no additional acceleration mechanisms are present in the downstream region, the width of the radio shock is entirely determined by spectral ageing due to synchrotron and IC losses at a given frequency ν as $\tau_{\rm loss} \propto B^{0.5} / \left[(B^2 + B^2_{CMB}) \times (\nu(1+z))^{0.5}\right]$, where B is the magnetic field strength and $B_{CMB} \propto (1+z)^2$ is the Cosmic Microwave Background equivalent magnetic field strength. From dynamical considerations, the relic's cooling length can be derived as $l_{\rm cool} = \tau_{\rm loss} \times \upsilon_d$, where the shock's downstream velocity is $\upsilon_{\rm d} = c_{\rm s}(\mathcal{M}^2+3)/(4\mathcal{M}) \propto \sqrt{\gamma T}(\mathcal{M}^2+3)/(4\mathcal{M})$. The relationship between $l_{\rm cool}$ and B shows that the magnetic field can be estimated from the relic width (Markevitch et al., 2005). Conversely, from independent measurements of the magnetic field, the expected width of the relic can be predicted and compared with observations. **Fig. 3.9** (*right panel*) shows the dependence of the cooling length $l_{\rm cool}$ on the magnetic field for varying $\upsilon_{\rm d} \in [800, 1300]$ km/s. This range keeps into account all possible combinations of the lowest and highest Mach numbers literature values derived from radio observations (**Tab. 3.4**), combined with pre-shock temperatures from X-ray study: ~ 2.7 keV (Akamatsu et al., 2015) and ~ 3.35 keV (Ogrean et al., 2014). This is then calculated at fixed cluster redshift and for four reference frequencies (45, 145, 610, and 1500 MHz, from top to bottom, respectively). Using the LOFAR LBA 15 arcsec image, we extracted surface brightness profiles along the main relic to estimate its width. To measure the intrinsic width of the relic and mitigate the effects of beam convolution, we used the clean component model image. This approach allows us to directly obtain the deconvolved SB profiles, leading to a reliable estimate of the relic intrinsic width. In **Fig. 3.9** (*left*) we show the deconvolved profiles, extracted in $70 \times 15''$ boxes, along the west (red) and east (blue) part of the relic. Additionally, we employed circular annuli to obtain an average SB measure along the full relic size ~ 1.1 Mpc (black). We normalized the values and shifted them so that the shock position aligns with the zero: negative values correspond to the upstream region, while positive ones correspond to the downstream part. We blank the compact sources that might contaminate the profiles with the help of higher frequency and higher resolution images, where these sources are more clearly visible. We immediately notice that while the RN-west profile shows a rapid increase followed by a gradual decrease, the RN-east profile appears remarkably symmetrical. The asymmetry in the western profile (red) is consistent with expectations for an edge-on relic moving outward: a sharp rise in radio luminosity at the shock location, followed by a frequency-dependent decline that becomes steeper at higher frequencies due to radiative cooling $t \propto 1/E^2$. On the other hand, the symmetry and relatively smooth profile of the eastern side, with wings extending on either side of the peak, is a strong deviation from this expected model. This duality of the east- and west- sides corresponds to the morphological difference discussed in **Section 3.4.1** and **Section 3.3.1**. The overall profile (black) maintains the broader upstream profile while representing an average of the east (blue) and west (red) curves in the downstream area. While we have masked sources that could affect the profile, it is important to note that source B is very extended and likely interacts with the downstream emission on the west side. Therefore, the red curve might be influenced by this interaction, meaning it does not purely represent the relic downstream emission. The deconvolved overall profile has an FWHM of 138 kpc at 45 MHz. This width would imply magnetic field values of $0.4\,\mu G$ or $8.5\,\mu G$, as each curve of **Fig. 3.9** has two solutions for a given width value. If projection effects play a significant role, the intrinsic profile would be narrower, implying magnetic field values of $B < 0.4\,\mu G$ or $B > 8.5\,\mu G$. Based on constraints from IC emission, equipartition arguments and Faraday rotation measurements (Stroe et al., 2014a; van Weeren et al., 2010), we can exclude the lower solution. Despite being based on ideal assumptions, these theoretical estimates are useful to constrain the possible range of magnetic field strengths at the relic location, at approximately 1.5 Mpc away from the cluster centre. Only a few other studies provide magnetic field estimates for this galaxy cluster (van Weeren et al., 2010; Donnert et al., 2016; Di Gennaro et al., 2021c). Similar considerations were put forward in van Weeren et al. (2010) who found a deconvolved FWHM of 55 kpc at 610 MHz, leading to $B \lesssim 1.2\,\mu G$ or $B \gtrsim 5\,\mu$G. Extrapolating these magnetic field values to lower frequencies, such as 45 MHz, we would expect the FWHM to broaden significantly, resulting in width estimates of approximately $l_{\rm cool,45} \lesssim 200\,{\rm kpc} \gg {\rm FMHW}_{\rm deconv,45} \sim 138\,{\rm kpc}$. It is important to note that the FWHM is only an indicator of the cooling length. In the case of the 610 MHz data, the relic width remains relatively constant across the entire profile. Thus, the FWHM is a reliable estimator. Conversely, at 45 MHz, we observe a more pronounced broadening downstream (see **Section A.1** for an appropriate discussion about the shape of the profile). If we consider only the downstream extension (from the shock front to the location where the intensity drops to 10% of its peak), we obtain a width of approximately 200 kpc, which is more in line with the extrapolation/expectations from van Weeren et al. (2010). The 10% intensity level also roughly corresponds to the $3\sigma_{\rm rms}$ threshold, which defines the limit for a reliable measurement. If we consider this and the maximum downstream extent, it provides a lower limit on B, confirming that B $> 5\mu$G is in agreement with van Weeren et al. (2010). Another independent measure of the magnetic field strength was obtained by Di Gennaro et al. (2021c), who used Faraday depolarization to estimate the turbulent magnetic field component $B_{\rm turb} \sim 6\,\mu$G. Given the assumptions and uncertainties related to these measurements, we can conclude that our estimates are broadly consistent with previous studies. We can constrain the magnetic field at the relic in the range of 5 to 10 μG.

Despite the well-defined morphology that is characteristic of the northern relic, RN, in CIZA J2242.8+5301, the shock geometry in a merging system is inherently more complex. For example, higher-resolution and frequency observations reveal a fragmented and irregular shock surface on smaller scales (see Fig. 7 in Di Gennaro et al., 2018), which suggests a more complex shock structure. Additionally, we observe a broadening in the upstream region of the profile (see **Fig. 3.9**, *left*). This raises the question of whether this is the result of projection effects or an intrinsic shock property. For these reasons, we devised a model that incorporates projection effects, possible downstream magnetic field variation and shock surface irregularities.

We model the surface brightness profile of the main relic RN, using a framework that considers, both, the physics of particle acceleration and the effects of geometry and magnetic field variations. We assume the shock front is a spherically shaped cap with a uniform Mach number. Each surface element of this spherical cap acts as the origin of a downstream emission profile, computed based on an injection spectrum for the relativistic electron population and downstream conditions parameterized by the Mach number and post-shock gas temperature (k_BT). The cosmic-ray electrons follow a power-law momentum distribution at the shock front, with their synchrotron emission decreasing with downstream distance due to radiative losses. With minor modifications, we follow the formalism of Hoeft & Brüggen (2007). Projection effects are accounted for by integrating along the line of sight for a given curvature radius (R = 1.5 kpc) and maximum opening angle Ψ of the spherical cap, resulting in a realistic surface brightness distribution. We extend the model by Di Gennaro et al. (2018) by incorporating additional data at 45 MHz, the lowest frequency available, which enables us to better constrain the model parameters and test its applicability in the extreme low-frequency regime.

It has been shown (e.g., **??**) that shock surfaces in galaxy clusters are not smooth, but exhibit small-scale irregularities. This is also observed in other clusters (e.g., de Gasperin et al., 2022; Rajpurohit et al., 2020). The deviations from a smooth shock surface are poorly constrained. To mimic them as part of our model, we assume that the radius in the spherical cap model has a Gaussian scatter. The width of this scatter, which we will refer to as 'wiggles', becomes an additional free parameter in our model. In contrast the wiggles cause a symmetric broadening in the projected shock surface profile. We extracted surface brightness profiles in $70'' \times 15''$ boxes along the eastern half of the RN, using 45, 145, 1550 and 3000 MHz images. We exploit the multi-frequency dataset to take advantage of different achievable resolutions.

We start by considering the effects of projection alone. Primarily, we relied on the highest $3''$-resolution image at 3 GHz to constrain the maximum possible projection allowed. At lower resolutions, the broader and smoother surface brightness profiles would allow the opening angle

Ψ to vary more freely in the parameter space. The opening angle that best fits the data is $\Psi = 12°$, which implies an injection up to about 33 kpc (projected size) in the downstream direction, keeping the magnetic field constant at $B = 3\,\mu G$. We demonstrate that even with a slightly different opening angle $\Psi = 18°$, the profile would strongly deviate from observations, creating a prominent downstream tail (**Fig. A2**). After fixing the opening angle, we applied the model to different frequencies at different resolutions to assess its consistency across the dataset. In **Fig. 3.10**, we compare 3 GHz at 3.5″ (orange), 1.5 GHz at 8″ (blue), 150 MHz at 8″ (red) and 45 MHz at 15″. In order to test the standard DSA scenario, we fix the Mach number to $\mathcal{M} = 4.8$, as derived from the $\alpha_{\rm int}$ in this work (**Section 3.4.1**).

Moreover, in such a complex environment as the one of the clusters undergoing mergers, it is reasonable to believe that the magnetic fields do not remain uniform across Mpc-scale shock fronts. To capture the turbulent nature of the ICM, the magnetic field is modelled as a log-normal distribution, introducing variability in the downstream emission profiles originating from each surface element. We find that the best-fit model has a mean magnetic field strength of $B_0 = 0.3\,\mu G$ and scatter $log(\sigma) = 1.65$. (**Fig. 3.10**, left). This implies that the magnetic field varies in a range from approximately 3×10^{-3} to $16\,\mu G$. This model is able to match the observed profiles in the downstream area reasonably well, while it substantially fails to reproduce the part of the profile ahead of the peak, which shows excess respect for all the modeled profiles **Fig. 3.10**. For this reason, we added wiggles with a Gaussian broadening to the original spherical cap model to test its impact on the fit. The results are shown in **Fig. 3.10** (*right*), where we applied a Gaussian broadening characterized by $\sigma = 15\,$kpc to match the width of the 3.5 arcsec profile. This helps in smoothing the models in the upstream region, however a significant discrepancy is still present. Notably, all profiles exhibit a systematic excess in the upstream region extending for approximately 100 kpc, consistent with the average profile shown in **Fig. 3.9** (*left*, black line). Overall, our modelling efforts successfully reproduce the general shape of the observed surface brightness profiles, particularly in the downstream region. However, some discrepancies remain, particularly in the upstream region, where all modelled profiles show a systematic excess compared to observations.

3.4.3 R5

As mentioned in **Section 3.3.1**, in the north-west part of the northern relic, we find an excess of emission that extends for 716 kpc and has an average width of $\sim$ 100 kpc (see **Fig. 3.11**). R5 was first identified at GHz frequencies by Di Gennaro et al. (2018) and recently confirmed at 400 and 675 MHz by Raja et al. (2024b). In our LOFAR LBA images, R5 appears irregular and less confined compared to the distinct spike structure seen at higher frequencies. A similar diffuse appearance is observed in LOFAR HBA images, suggesting intrinsic differences in the emission at low frequencies rather than being solely a consequence of resolution limitations, although resolution likely contributes to the smoothing of finer substructures. This is further demonstrated in **Fig. 3.11** (second panel), where a comparison between the 15″-beam smoothed image (with corresponding red contours) and the 5″ contours (green) at higher frequencies shows that the spiked feature remains visible even after smoothing. Moreover, we note that the width of R5 corresponds to $\sim$ 2.5 times the beam size (i.e., 15″ nominal resolution at 45 MHz), thus we

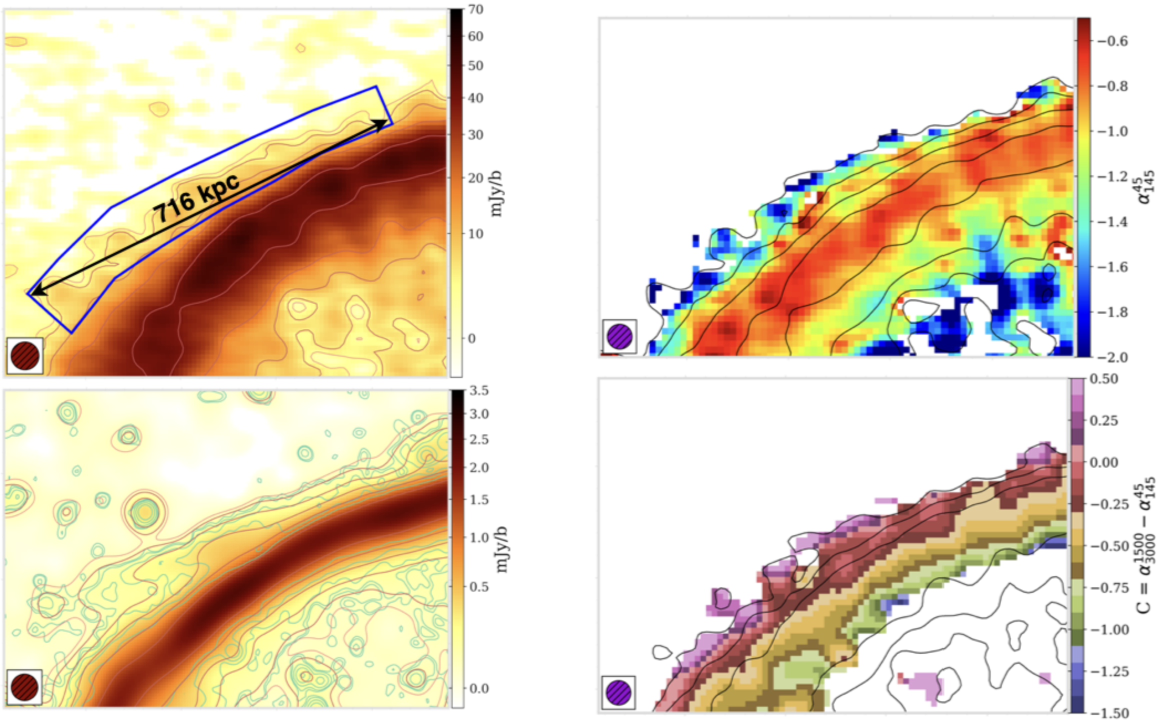

Figure 3.11: Zoom-in on the R5 emission regio. From top to bottom: 45 MHz image at 15″ resolution; 1.5 GHz image convolved to the same 15″ resolution and green contours indicating the 5″ higher resolution data; spectral index map between 45 and 145 MHz from **Fig. 3.5**, 4-frequency (45, 145, 1500, 3000 MHz) curvature map from **Fig. 3.6**

exclude the possibility of it purely being the result of the low resolution of the telescope. This area has steep spectral spectral index values $\alpha_{45}^{145} \in [-1.2, -0.9]$ range (see spectral index map in **Fig. 3.11**). Even if the relative errors are higher at the edges of the emission, with $\Delta\alpha_{45}^{145} \sim 0.2 - 0.3$ there is a clear distinction between R5 area and the main shock front area. This is also confirmed by the local spectral index analysis along the RN outer edge of **Section 3.4.1** (**Fig. 3.7**). We calculated the integrated spectral index within the R5 region (blue box of **Fig. 3.11**, top panel) by fitting a single power-law to the data and obtaining a best-fit value of $\alpha_{int}^{R5} = -0.90 \pm 0.03$. Due to the extremely low surface brightness of R5 we used only the 45, 145, 1500 and 3000 MHz images, where a clear detection above $3\sigma_{\rm rms}$ threshold was visible. The resulting power-law fit is consistent with the two-frequency spectral index reported by Di Gennaro et al. (2018) and aligns with the curvature map (**Fig. 3.11**, bottom panel), which shows $C = 0$ in the R5 region, supporting the absence of significant spectral curvature. Hints of polarized emission have been detected for R5, with a degree of polarization of $\sim 35\%$ (at 3 GHz) and $\sim 30\%$ at 1.5 GHz (Di Gennaro et al., 2021c). This level of polarization is consistent with what is typically expected for radio relics, supporting the idea that R5 is associated with a shock-related structure. However, its polarization fraction is lower than that of the main relic, suggesting potential differences in shock strength. The nature of R5 remains unclear, with two primary interpretations: either it is separate relic seen in projection, or it represents broader upstream substructure of the main northern relic, extending the shock surface in that direction.

3.5 Conclusions

We presented the first ultra-low frequency observations of the Sausage relic at 45 MHz using the LOFAR telescope, achieving a thermal-noise limited image with a noise level of 1.5 mJy/beam at 15″ resolution. These observations mark the lowest radio frequency at which this cluster has been studied to date and demonstrate the capabilities of the LOFAR LBA calibration pipeline for producing high-fidelity images of diffuse radio sources.

- The 45 MHz observations reveal a complex system of diffuse, relic-like sources, extending beyond the well-known northern and southern relics. The northern relic shows a characteristic arc-like morphology with a projected linear size of $\sim 2.2\,\mathrm{Mpc} \times 760\,\mathrm{kpc}$, while the southern relic exhibits a more irregular shape for a total extent of $\sim 1.5\,\mathrm{Mpc} \times 520\,\mathrm{kpc}$. The morphology of the relics not only appears larger but reveals connections between substructures that would appear disconnected at higher frequencies. Most sources (R1, R2, RS1, RS2, RS3, RS4), appear more fragmented with increasing frequency.
- Spectral index maps between 45 MHz and 144 MHz reveal a clear spectral gradient in both relics, where the spectral index steepens from the outer edge toward the cluster centre. RN shows a gradient from $\alpha \sim -0.7$ to ~ -1.8, while RS exhibits a broader variation, with the southeast region (RS-east) showing the expected steepening (from $\alpha \sim -0.5$ to ~ -2) while the north-western part (RS-west) remaining consistently steep (~ -1.8) even at the outermost edge, with no inward steepening. These broad steep-spectrum north-western areas of RS explain why RS-west fades quickly at higher frequencies ($\nu \gtrsim 600\,\mathrm{MHz}$), where primarily the southern edge remains bright and highlights the importance of low frequencies

in tracing these faint parts of relics. Additionally, the spectral index maps provide evidence that R1 consists of two distinct regions: (i) R1-east with a flatter spectrum ($\alpha \sim -0.8$) and (ii) R1-west which is aligned with R4 ($\alpha \sim -1.3$). The patchy morphology and mixed spectral indices of R2 indicate that this source may be seen at a larger inclination.

- The integrated spectral index of the northern relic is $\alpha^{N}_{\rm int} = -1.09 \pm 0.03$, while the southern relic has a steeper integrated index of $\alpha^{S}_{\rm int} = -1.34 \pm 0.03$. Using these indices, Mach numbers were derived as $\mathcal{M}_N = 4.8 \pm 0.8$ for the northern relic and $\mathcal{M}_S = 2.6 \pm 0.1$ for the southern relic.
- Access to ultra-low radio frequencies, which are less affected by radiative losses, allow us to measure the injection spectral index along the relic edges. By applying statistical methods to identify distinct spectral index populations, we determined injection indices of $\bar{\alpha}^{N}_{\rm inj} = -0.76 \pm 0.08$ and $\bar{\alpha}^{S}_{\rm inj} = -0.77 \pm 0.16$, corresponding to Mach numbers of $\mathcal{M}_N = 2.9 \pm 0.4$ and $\mathcal{M}_S = 2.9 \pm 0.8$. The close agreement of these Mach numbers suggests that the shocks causing both relics have comparable strengths, despite their differing morphologies.
- Using multi-frequency observations, we produced 4-frequency spectral curvature map from 45 MHz to 3 GHz. The curvature analysis of the northern relic reveals a perfectly flat spectrum with $C \sim 0$ at the outer edge, and a gradient up to $C \sim -1.5$ in the downstream region, in agreement with expectations from Diffusive Shock Acceleration (DSA). The southern relic instead shows a smaller gradient with values $C \sim -0.2$ to -0.5, suggesting it might be influenced by additional effects, such as turbulence or projection effects.
- Finally, we used a toy model to simulate the surface brightness profile of RN to gain insights into cluster dynamics, projection effects, and the magnetic field strength at the shock location. Our modelling indicates that RN is best represented by a scenario with minimal projection effects (low opening angle $\Psi = 12°$), spatial variations in the downstream magnetic field, modelled as a log-normal distribution with characteristic strength of $B_0 = 0.3\,\mu$G and scatter $\log(\sigma) = 1.65$ and Gaussian broadening of the shock surface with $\sigma = 15$ kpc. Even if the additional broadening helps in smoothing the upstream profile, some discrepancies remain, especially in the upstream region, where an excess of emission systematically persists at all frequencies. Moreover, we stress that the toy model proposed in this section serves to explore the fundamental dependencies of the surface brightness profile on the geometry of the system, projection and magnetic field variations. A fully accurate theoretical representation would require dedicated tailored simulations which is beyond the scope of this work.

Acknowledgements

MB acknowledges funding by the Deutsche Forschungsgemeinschaft (DFG, German Research Foundation) under Germany's Excellence Strategy – EXC 2121 "Quantum Universe" – 390833306. FdG and GDG acknowledges support from the ERC Consolidator Grant ULU 101086378. LOFAR (van Haarlem et al., 2013b) is the Low Frequency Array designed and constructed by ASTRON. It has observing, data processing, and data storage facilities in several countries, which are owned by various parties (each with their own funding sources), and that are collectively operated by the ILT foundation under a joint scientific policy. The ILT resources have benefited from the following recent major funding sources: CNRS-INSU, Observatoire de Paris and Université d'Orléans, France; BMBF, MIWF-NRW, MPG, Germany; Science Foundation Ireland (SFI), Department of Business, Enterprise and Innovation (DBEI), Ireland; NWO, The Netherlands; The Science and Technology Facilities Council, UK; Ministry of Science and Higher Education, Poland; The Istituto Nazionale di Astrofisica (INAF), Italy. This research made use of the Dutch national e-infrastructure with support of the SURF Cooperative (e-infra 180169) and the LOFAR e-infra group. The Jülich LOFAR Long Term Archive and the German LOFAR network are both coordinated and operated by the Jülich Supercomputing Centre (JSC), and computing resources on the supercomputer JUWELS at JSC were provided by the Gauss Centre for Supercomputing e.V. (grant CHTB00) through the John von Neumann Institute for Computing (NIC). This research made use of the University of Hertfordshire high-performance computing facility and the LOFAR-UK computing facility located at the University of Hertfordshire and supported by STFC [ST/P000096/1], and of the Italian LOFAR IT computing infrastructure supported and operated by INAF, and by the Physics Department of Turin university (under an agreement with Consorzio Interuniversitario per la Fisica Spaziale) at the C3S Supercomputing Centre, Italy.

A.1 Deconvolved profile shape comparison

We compared the shape of the deconvolved profiles at 45 MHz (RN-full from **Section 3.4.2**) and 610 MHz (van Weeren et al., 2010) by computing some statistical metrics, such as the skewness and the 10-to-50 ratio. For normally distributed data, the skewness should be about zero. A skewness value greater than zero means that there is more weight in the right tail of the distribution and vice versa. This 10-to-50 ratio quantifies the relative extent of the wings compared to the core of the profile. It is calculated as the ratio of the profile width at 10% of the maximum intensity to its full width at half maximum. A perfectly Gaussian profile has a value of 4.29. Ratios larger than 4.29 indicate broader wings, while smaller ratios suggest a steeper fall-off outside the core. We also calculate the skewness test to determine if the skewness is close enough to zero. To do this, we test the null hypothesis that the skewness of the population that the sample was drawn from is the same as that of a corresponding normal distribution. The null hypothesis is rejected when the p-value is low ($p < 0.05$), indicating that the distribution is significantly skewed and deviates from normality. Conversely, a high p-value would indicate a more symmetric form and that the skewness is not statistically different from that of a normal distribution. The metrics results for the two curves shown in **Fig. A1** are reported in **Tab. A1**.

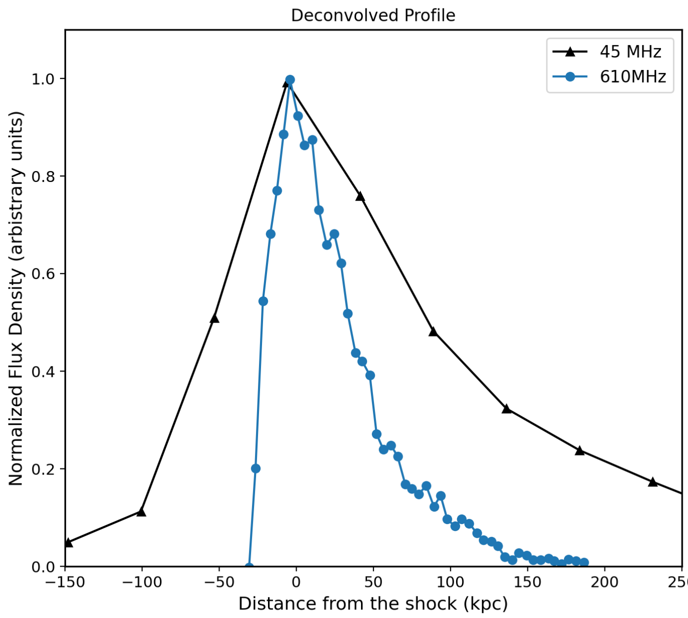

Figure A1: Comparison between full SB profile at 45 MHz (this work) and 610 MHz (van Weeren et al., 2010). Data are shifted so that the peak of each curve corresponds to zero. We highlight that this is intended purely as a qualitative shape comparison.

Both profiles show a moderate (between 0.5 and 1) positive skewness. The 45 MHz profile is closer to a symmetrical value, as a skewness between -0.5 and 0.5 is generally considered indicative of a fairly symmetric distribution. Despite this, according to the skewness test, both

Table A1: Comparison of RN deconvolved profiles shapes at 45 MHz and 610 MHz (van Weeren et al., 2010).

Metric	45 MHz	610 MHz
Skewness	0.63	0.91
p-value*	3.25×10^{-14}	0.0097
10-to-50 Ratio	2.73	2.18

*The p-value for the skewness-hypothesis test.

profiles show significant evidence of deviations from Gaussianity (p-value $\ll 0.05$). We conclude that the 45 MHz profile is broader (larger 10-to-50 ratio) and more symmetric (lower skewness) than the 610 MHz profile. On the other hand, the 610 MHz profile is more peaked, has steeper wings, and is more asymmetric.

A.2 Profile modelling

In this section, we show the effect of a bigger opening angle Ψ. Even just a slight change (from 12° to 18°) drastically changes the downstream profile, making the model unfeasible (see **Fig. A2**). The effect is particularly visible in the high-frequency high-resolution profiles (1.5 and 3 GHz, blu and orange respectively).

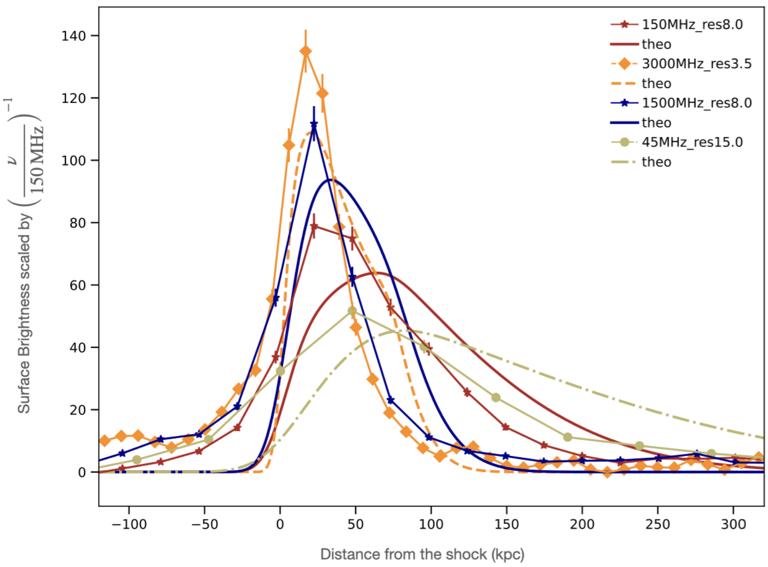

Figure A2: Surface brightness profile across the eastern half of RN. Same as **Fig. 3.10** but with constant B = 3 μG and Ψ = 18° projection.

4 The Complex Cluster Merger System Abell 746: insights from very-low frequencies LOFAR LBA observations

G. Lusetti, T. Beeth, F. de Gasperin, M. Brüggen, H. W. Edler, G. Di Gennaro, W. Lee, K. HyeongHan, K. Rajpurohit - to be submitted to A&A

Abstract

Context. *We present a detailed low-frequency radio analysis of the merging galaxy cluster Abell 746, combining new LOFAR LBA observations with existing HBA data from LoTSS DR2, and higher frequencies published data at 650 and 1500 MHz.*
Aims. *We aim to study the morphology, spectral characteristics and physical processes producing the complex radio emission hosted by A746, including its multiple relic-like structures and central radio halo.*
Methods. *We combined radio data ranging from 53 to 1500 MHz, in order to derive integrated spectral indices, spectral index maps, and Mach number estimates. We also perform a radial brightness profile fitting to the halo emission to disentangle it from surrounding diffuse features.*
Results. *The NW relic displays the typical properties of classical relics, with an arc-like morphology and well-defined spectral steepening from* $\alpha_{144}^{53} \sim -0.5$ *at the outer edge to* $\alpha_{144}^{53} \sim -2.5$ *toward the cluster centre. In contrast, R1, R2, and R3 lack the expected radial spectral index gradients. The integrated spectral index of* $\alpha_{\mathrm{int}} = -1.30 \pm 0.04$ *corresponds to a low-efficiency shock with Mach number* $\mathcal{M}_{\mathrm{NW}} = 2.8 \pm 0.3$. *Similarly low Mach numbers are derived for the other relic-like structures (R1, R2, R3), pointing to inefficient shock particle acceleration and suggesting the contribution of fossil plasma as a seed population for reacceleration. Via exponential surface brightness profile fitting, we derive a characteristic halo size, with e-folding radii of* $r_{e,53,\mathrm{MHz}} = 159 \pm 22$ *kpc and* $r_{e,144,\mathrm{MHz}} = 179 \pm 14$ *kpc. Integrated flux densities within* $3r_e$ *yield an ultra-steep spectral index of* $\alpha^{53} - 144 = -1.6 \pm 0.2$. *The corresponding 144 MHz radio power,* $P_{<3r_e}^{144} = (8.7 \pm 0.9) \times 10^{24}$ *W Hz*$^{-1}$*, is in excellent agreement with expectations from the* $P_{150,\mathrm{MHz}} - M_{500}$ *relation for low-mass cluster at 150 MHz.*

4.1 Introduction

It is well established that throughout the history of the universe, galaxy clusters form and evolve through a hierarchical process via the accretion of smaller systems and mergers with other clusters. These mergers dissipate energy via shock waves and turbulence within the intracluster medium (ICM), which can in turn (re-)accelerate cosmic rays (CRs), and, in the presence of μG magnetic fields, produce extended synchrotron sources, observed in the radio band. The resulting Mpc-scale radio sources observed in clusters are classified into two main categories: radio halos and relics, each tracing different aspects of the merger-driven processes (see van Weeren et al. (2019), for a review). Radio halos are centrally-located, diffuse radio sources, usually with a smooth and regular morphology that generally follows the thermal distribution of the ICM. These halos, often spanning up to megaparsec scales, are typically found in massive, dynamically disturbed galaxy clusters. The prevailing theory is that turbulent re-acceleration is responsible for the generation of radio halos (Brunetti & Jones, 2014). In this model, seed electrons are re-accelerated via Fermi-II mechanisms during periods of intense ICM turbulence, usually connected to cluster merger events. According to this turbulent re-acceleration model, the radio spectrum of a halo is expected to develop a high-frequency cutoff that depends on the amount of energy injected into the ICM during a merger event (Cassano & Brunetti, 2005b). Since the available energy scales with cluster mass, massive systems undergoing major mergers are predicted to host radio halos with typical spectral indices of $\alpha \sim -1.3$, observable up to GHz frequencies before steepening. In contrast, less massive clusters or those experiencing minor mergers are expected to host ultra-steep spectrum radio halos with $\alpha < 1.5$ (USSRHs; Brunetti et al., 2008), which becomes detectable at lower frequencies, i.e., < 200 MHz (Basu, 2012; Cassano et al., 2012; Cuciti et al., 2021; Duchesne et al., 2021). Historically, studies investigating the correlation between the radio power of halos and the mass of their host clusters have been performed at ~ 1 GHz, exploring the mass range $M_{500} \gtrsim 6 \times 10^{14}\, M_{\odot}$ (e.g., Cassano et al., 2013). This relation implies a physical connection between the energy budget of a merger and the resulting diffuse radio emission. The upper limits for non-detections of radio halos lie about a factor of 4 below the correlation. Recent low-frequency observations have extended this correlation to 150 MHz using LOFAR data. In particular, Cuciti et al. (2023) found that the $P_{150,\mathrm{MHz}} - M_{500}$ relation holds down to masses as low as $3 \times 10^{14}, M_{\odot}$. This opens the possibility of detecting USSRHs in lower-mass systems that would remain undetected at GHz frequencies, providing key observational support for turbulent re-acceleration models and the predicted spectral steepening in less energetic mergers.

Radio relics are elongated structures, found in the cluster periphery with sizes up to a few Mpc scales (see Wittor, 2023, for a recent review) and are instead associated with cluster merger shocks. It is widely accepted that radio relics trace the acceleration of cosmic-ray electrons at these shocks via the Diffusive Shock Acceleration (DSA) mechanism (Blandford & Ostriker, 1978; Drury, 1983; Blandford & Eichler, 1987; Ensslin et al., 1998; Hoeft & Brüggen, 2007). A long-standing challenge for this mechanism is that many observed radio relics are associated with low-Mach-number shocks ($\mathcal{M} \lesssim 3$). Such weak cluster shocks are expected to be inefficient at accelerating thermal electrons to relativistic energies. Therefore, in order to explain the observed radio power of such relics, it is often necessary to invoke the presence of pre-accelerated seed populations, possibly provided by past AGN activity or earlier merger events (e.g., van Weeren et al., 2017). The origin of radio relics is reflected in their observational properties. When viewed face-on they show an arc-shaped morphology, resembling the underlying shock front and are found to be highly polarized 30-60% (e.g., Bonafede et al., 2009b; Kale et al., 2012; Wittor et al., 2019b). This is a consequence of the magnetic field alignment happening in the shock plane due to the compression by the shock wave (Ensslin et al., 1998; Domínguez-Fernández et al., 2021). Typically, they exhibit a bright radio rim at their outer edge, with radio emission fading towards the cluster centre. This reduction in radio emission coincides with a steepening of the spectral index, i.e., from a relatively flat value at the relic edge to steeper values towards the cluster centre. This suggests that particles are being accelerated at the relic's outer edge and subsequently age as they move towards the cluster centre due to synchrotron and IC energy losses. However, in the last decades though, radio observation with unprecedented sensitivity showed a much wider variety of radio morphologies. First, in a few cases, high-resolution radio observations (Di Gennaro et al., 2018; Rajpurohit et al., 2020) revealed that even what looks like a coherent Mpc shock can the resolved into substructures and filaments. Second, when observed face-on they often lose their standard characteristic features, appearing as broad, sheets of emission constituted by filamentary substructures (de Gasperin et al., 2022; Rajpurohit et al., 2022; Wittor et al., 2023). Additionally, some dynamically complicated systems showed the presence of "inverted" radio relics (HyeongHan et al., 2020; Botteon et al., 2021a; Riseley et al., 2022a), where the curvature or the relic appears flipped with respect to the expected convex shock geometry. Böss et al. (2023) simulations showed that infalling sub-structures can deform the outward travelling shocks, resulting in a concave or inverted appearance of the relic. This extreme variety of observational differences is reproduced by the last TNGcluster simulation, illustrating a broad range of relic morphologies depending on merger geometry and line-of-sight projection Lee et al. (2024). These authors also highlight how, with upcoming sensitive radio surveys, such as SKA, low-surface brightness face-on radio relics might become more frequently detected. They also stress the risk of misclassification as the face-on relics features might even appear similar to the radio halos, and the need of combining them with data from other frequencies to avoid this. These peculiar cases challenge the standard relic formation theory and offer a starting point for investigating other effects that participate in shaping the observed relics.

4.1.1 A 746

Abell 746 (hereafter A746) is a PSZ2 cluster at $z_{phot} = 0.23 \pm 0.01$ (Koester et al., 2007) with $M_{500} = (5.34 \pm 0.40) \times 10^{14}\,M_\odot$ (Planck Collaboration et al., 2016b) located at RA:09h09m37.3603s, DEC:+51d32m47.594s. It is a spectacular system hosting multiple diffuse radio sources and substructures.

It was first studied at radio frequencies by van Weeren et al. (2011b), who identified a radio relic candidate in NVSS and confirmed it with deeper WSRT image at 1382 MHz. They found that the northwest relic is located 1.7 Mpc from the cluster center with a physical extent of 1.1×0.3 Mpc. They also measured a large polarization fraction up to 50%, suggesting the merger axis is close to the plane of the sky. Moreover they found multiple patches of radio emission near the cluster center and classified it as a radio halo with an estimated size exceeding

850 kpc. A746 is also part of the PSZ2 clusters in LOFAR Two-Metre Sky Survey data release 2 (LoTSS-DR2; Botteon et al., 2022a) at 144 MHz. It was classified as a disturbed galaxy cluster based on its X-ray morphological parameters, such as the concentration parameter c (Santos et al., 2008) and the centroid shift w (Poole et al., 2006; Mohr et al., 1995). With measured values of $c = (6.85 \pm 0.6) \times 10^2$ and $w = 3.5 \pm 0.3$, it lies in the region ($c < 0.2$ and $w > 0.012$) of dynamically disturbed systems (see bi-modal behavior in Cassano et al. (2010); Cuciti et al. (2021)). Botteon et al. (2022a) also confirmed the presence of halo and reported the primary relic in the west, as well as two smaller relics in the east and north-east direction. Additionally, they report the presence of an elongated bright structure in the south, overlapping with the central halo. However, disentangling the halo extended emission from the southern elongated structure, and thus providing accurate flux density measurements, remained not trivial. A deeper, targeted study on A746 was recently carried out by Rajpurohit et al. (2024), combining radio multiple datasets - VLA Lband (1–2 GHz), uGMRT in Band 4 (550-750 MHz) and LOFAR HBA (144 MHz) - to the X-Ray observations from XMM-Netwon satellite (with a total of 184 ks exposure time). They classified 3 out of 4 relic-like structures as radio relics for their morphology and spectral properties. However, the nature of the arc-shaped southern structure remains unclear. The morphology of the X-ray gas also points toward a very disturbed scenario, with the presence of multiple substructures. The study of the ICM surface brightness distribution led to the discovery of three discontinuities marked as merger-driven shock fronts and one density jump. Interestingly, no shock front is found in proximity of the primary and more prominent relic. Additionally, HyeongHan et al. (2024) presented a weak-lensing analysis of the cluster, using data from Subaru/Hyper Suprime-Cam observation. They found the mass distribution main peak coinciding with the geometric center of the disturbed X-ray emission. From this peak, they identified 2 elongations in both north-south and east-west directions. They confirmed the non-bimodal galaxy distribution also found by Golovich et al. (2019), detecting 3 sub-structures. Both the mass and galaxy density distribution exhibit a triangular morphology that approximately follows the ICM distribution. HyeongHan et al. (2024) found the total mass of the cluster is $M_{200} = 6.3 \pm 1.5 \times 10^{14}\, M_\odot$, and a later weak-lensing work by Finner et al. (2025) fitted a three-halo model to the cluster mass distribution, finding $M_{200,S} = 2.0 \pm 0.8 \times 10^{14}\, M_\odot$, $M_{200,N} = 2.1 \pm 0.8 \times 10^{14}\, M_\odot$, and $M_{200,W} = 1.7 \pm 0.7 \times 10^{14}\, M_\odot$.

Overall, the cluster displays a high level of complexity, that makes it challenging to reconstruct a convincing merging scenario, able to take into account the multi-wavelength view offered by optical, X-ray and radio data.

Here we present a detailed analysis of the extended radio sources up to very low frequency, adding to the picture, new information from LOFAR LBA at 54 MHz and uGMRT band 3 at 330 MHz data. Complementing the existing HBA data, where the diffuse radio structures are more prominent, with adjacent low-frequency observations allow us to achieve a more complete spectral characterization of the radio structures, particularly those that fade under the noise lever or are less extended at GHz frequencies. Only a handful of observations of clusters hosting radio relics below 100 MHz are available (van Weeren et al., 2011e; de Gasperin et al., 2015b; Botteon et al., 2022b), making these observations a valuable addition for probing radio shocks in the lowest end of the radio spectrum.

4.2 Observation and data reduction

For this study, we combined data from multiple radio telescopes, from the ultra-low frequency to the GHz regime. We present new data from LOFAR Low Band Antennas (LBA van Haarlem et al., 2013b) at 53 MHz. We then complement our analysis with exhisting LOFAR High Band Antennas (HBA van Haarlem et al., 2013b) at 145 MHz, uGMRT Band 4 (550 – 750 MHz) and the Very Large Array (VLA) at 1.4 GHz (Rajpurohit et al., 2024). In the following, the main steps of the newly calibrated data are explained. The HBA data of A746 is part of the LOFAR Two-metre Sky Survey second data release (Shimwell et al., 2022) and presented in Botteon et al. (2022a). We refer to those authors (Botteon et al., 2022a; Raja et al., 2024b) for the details on data reductions.

4.2.1 LBA

The LBA data of A746 was obtained during observations targeting the giant planet HD 80606 (de Gasperin et al., 2020b) in August and October of 2015. Abell 746 is located near the northwestern edge of these observations and was therefore particularly hard to calibrate. The calibration steps are extensively described in de Gasperin et al. (2020b) and summarized in this section.

The LBA observations were performed in observation mode LBA_OUTER and using the multi-beam capability of LOFAR, which allows to continuously point one beam towards the calibrator source 3C196. The initial step in LBA data processing involves computing the solutions for calibrators, as described in de Gasperin et al. (2019). The calibration solutions were then applied to the target field data set together with an analytic estimation of the dipole beam effect on both amplitudes and phases. Next, the direction-independent self-calibration of the target field was performed, as presented in de Gasperin et al. (2020a). This step aims at finding the solutions for the average ionospheric effects. Using the radio surveys TGSS (TIFR GMRT Sky Survey, Intema et al. (2017)), NVSS (NRAO VLA Sky Survey, Condon et al. (1998)), WENSS (Westerbork Northern Sky Survey, Condon et al. (1998)) and VLSSr (Very Large Array Low-frequency Sky Survey Redux, Lane et al. (2014)) an initial sky model is calculated. From this model solutions for the total electron content (TEC), Faraday rotation and second-order beam effects are derived and applied. The last step consists of the direction-dependent calibration, following Edler et al. (2022). This step addressed the remaining direction-dependent ionospheric errors. Firstly, the Python blob detector and source finder (PyBDSF, Mohan & Rafferty (2015)) was used to select bright and compact sources, which are then used as direction-dependent calibrators. Then, all sources of the source model found after direction-independent calibration were subtracted from the uv-data to create an empty data set. One at a time, the calibrators were re-added to the empty data, the data was phase shifted to the calibrator direction and averaged in time and frequency, corrected for the primary beam in the new phase center and self-calibrated in several cycles. If the rms noise level of the image did not improve by more than 1% during a self-calibration cycle, the corresponding calibrator direction was considered converged and the calibration for the next calibrator started.

The calibration pipeline described above creates an image of the entire field of view, out to the first null at 15″ resolution. This image is not focused on the target of interest Abell 746 and it covers a much larger region. As a result, re-imaging with different settings results laborius and less efficient. Moreover, the direction-dependent calibration splits up the image in multiple facets, assuming that the direction-dependent effects within the facets are constant. For a smaller target region, the direction-dependent effects can be calculated within smaller facets and further improve the quality of the DDE calibration. This is the so called extraction procedure (van Weeren et al., 2021), recently re-implemented for LBA (see Biava et al. (2021), Pasini et al. (2022), Edler et al. (2022)). The first step of the extraction removed all sources outside a specific user-defined region from the visibilities after applying their DDE calibration solutions. In this case, we used a circle with a radius of 22″ around Abell 746. Subsequently, the uv-data were phase shifted to the centre of the target region and then averaged over time and frequency to reduce the size of the data set and smear residual flux coming from poorly subtracted distant sources. The LOFAR station beam response in the new phase centre was corrected and the visibility weights were updated. The next step is the self-calibration of the data in the smaller target region. The self-calibration begins with *tecandphase* calibrations, somewhat mimicking the facet-calibration, followed by diagonal gain calibration. These solutions were converging towards the lowest noise level after 5 iterations.

4.2.2 Source subtraction

The cluster contains numerous compact sources embedded in the extended radio emission, particularly in the central region (see **Fig. 4.1**), which need to be subtracted to obtain reliable flux densities and related spectral index measurements (**Section 4.3.1**). The high number of contaminating sources complicates their uniform subtraction from *uv*-data, generally considered a standard method, and that would differentially affects spectrum at different frequencies. First, they are not unambiguously detected across all frequencies used for the analysis (from 53 to 1500 MHz), precluding the establishment of a reference frequency from which all sources can be identified and selected. Moreover, the majorities are fainter at GHz frequencies, and thus hard to model and subtract. To address these challenges, we decided to subtract the compact source contributions via manual flux subtraction. The details of subtracted sources are listed in **Tab. A1** and shown as red circles in **Fig. 4.1** and **Fig. 4.2** (left). This approach ensures that the spectral index value remains unaffected, as the manual subtraction was uniformly conducted across the entire frequency range.

On the other hand, for the surface brightness profile analysis at 54 and 144 MHz (**Section 4.3.3**), we opted for source subtraction directly in the *uv*-data. In this case, the proximity of the two frequencies allowed for the confident identification of all compact sources in both images, thus reliable subtraction. The process was as follows: we first produced high-resolution images using a Briggs weighting of -1 with `WSClean` (Offringa et al., 2014; Offringa & Smirnov, 2017), to identify compact sources across the field. The corresponding clean-components were then selected from the model image by creating a mask using `PyBDSF`, and subtracted from the visibilities. The source-subtracted data sets were subsequently re-imaged at low angular resolution, using a Briggs weighting with a robust parameter of -0.25, A common inner *uv*-cut of 20λ to ensure a common uv-coverage. The resulting images at different resolutions are presented in **Fig. A1**.

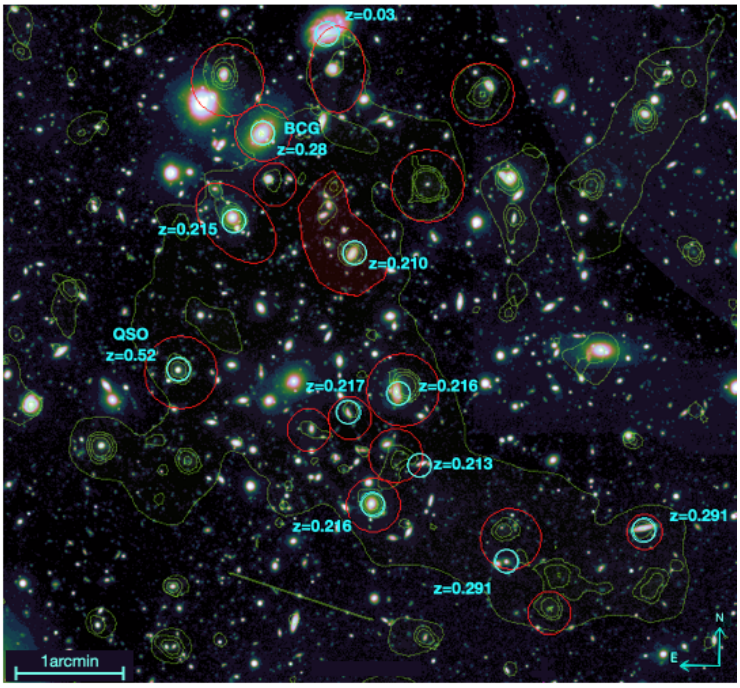

Figure 4.1: Zoom in on central $6.7' \times 6.7'$ to show in detail the sources overlapping with radio emission of the halo and R3. The green contour represents the $3\sigma_{\rm rms}^{144\,\rm MHz}$ and $3, 10 - \sigma_{\rm rms}^{1.5\,\rm GHz}$. Red circles are the subtracted sources. Cyan circles represent the optical identified sources with available redshift.

Throughout the paper we adopt a ΛCDM cosmology with $\rm H_0 = 70\,km\,s^{-1}Mpc^{-1}$, $\Omega_\Lambda = 0.7$ and $\Omega_m = 0.3$. Thus, $1''$ corresponds to a physical scale of 3.70 kpc at the redshift of A746. We use the convention $S_\nu \propto \nu^\alpha$ for the radio synchrotron emission and we calculated the error Δ_S associated with a flux density measurement S as

$$\Delta_S = \sqrt{(\sigma_c \cdot S)^2 + N_{\rm beam} \cdot \sigma_{\rm rms}^2}, \tag{4.1}$$

where $\rm N_{beam} = N_{pixel}/A_{beam}$ is the number of independent beams in the source area, and $\sigma_{\rm c}$ indicates the systematic calibration error on the flux density. We assume σ_c equal to 20% for LOFAR LBA , 10%HBA (following de Gasperin et al., 2021; Shimwell et al., 2022) and uGMRT Band 3, 5% Band 4 (e.g. Chandra et al., 2004). A flux scale correction factor $f = 0.93$ has been applied to the nominal LOFAR HBA map values to fix the uncertainty in the LOFAR flux scales.

4.3 Results

4.3.1 Radio morphology and integrated spectrum

Abell 746 is a merging galaxy cluster with multiple interesting diffuse radio structures. Here we list their characteristics in terms of morphology, extension and spectral properties (see **Tab. 4.1**).

Table 4.1: Summary of the main properties of the radio structures in A746

Source	HBA size	$S_{53,MHz}$	$S_{144,MHz}$	$S_{650,MHz}$	$S_{1500,MHz}$	α_{53MHz}^{144MHz}	$\alpha_{53MHz}^{1500MHz}$
	[arcmin × arcmin]	[mJy]	[mJy]	[mJy]	[mJy]	(Toby's)	
NW	8.3×2.3	1396 ± 280	511 ± 51	71 ± 7	21 ± 1	-1.11 ± 0.14	-1.30 ± 0.04
R1	3×1.8	116 ± 26	29 ± 3	3.1 ± 0.4	1.2 ± 0.1	-1.41 ± 0.16	-1.35 ± 0.05
R2	3.2×0.9	70 ± 17	17 ± 2	-	-	-1.26 ± 0.20	-1.25
R3[a]	4×1.3	276 ± 56	71 ± 7	6.5 ± 0.7	2.1 ± 0.2	-1.58 ± 0.19	-1.47 ± 0.03
Halo[b]	3.5	211 ± 47	34 ± 4	2.9 ± 0.3	1.9 ± 0.2	-1.84 ± 0.16	-1.39 ± 0.27

Col. 1: Name of the radio source; Col. 2: Length and width based on $3\sigma_{rms}$ contours of HBA image (cref) at 35″ resolution; Col. 3: Flux density at 144 MHz (measured in **Fig. 4.2** regions); Col. 4: integrated spectral index between 144 and 53 MHz. Col. 5: integrated spectral index between 1500 and 53 MHz. [a]: Regions have been cut off near the halo due to overlap, therefore the sizes are just an estimate. [b]: Due to the overlap with the southern radio structures, the halo size and the corresponding flux S_ν are calculated based on the e-folding radius r_e calculated in **Section 4.3.3**.

Sizes are based on the $3\sigma_{rms}$ contours of the LOFAR image at 144 MHz (which offer the best signal-to-noise ratio and reveals the most extended emission), while for the flux and integrated spectral index calculation, we used common regions shown in **Fig. 4.2** (left). High and low-resolution images are displayed in **Fig. 4.3**. For all the radio sources, the spectral index is obtained by a weighted least-square fitting a single power-law function. The results of the fitting procedure reported in this section are also shown in **Fig. 4.2** (right).

Western relic *NW*

The western relic shows a prominent arc-like structure. It is located $\sim 1531 \pm 200$ kpc (6.9′) from the X-ray centroid of the cluster (RA=137.3948, DEC=51.5489 Botteon et al., 2022a), with a size of $\sim 8.1 \times 0.5$ Mpc. The relic shows a clear filamentary inner substructure, not coincident with its outer edge and that becomes more prominent in the 20″-resolution images (**Fig. 4.3**). The integrated spectral index between 53 and 1500 MHz is $\alpha_{53}^{1500} = 1.30 \pm 0.04$.

Radio structures *R*1 **and** *R*2

Already detected in Botteon et al. (2022a), we see two elongated radio structures in the north (R1) and east (R2) direction. The diffuse radio emission $R1$ lies about $\sim$ 1800 kpc north of the X-ray centroid with a size of $665\,kpc \times 400\,kpc$ at $144\,MHz$. The integrated spectral index is $\alpha_{53}^{1500} = 1.35 \pm 0.05$. The arc-like diffuse emission in the east $R2$ is about $\sim$ 1100 kpc west of the X-ray centroid, has a size of 710×200 kpc and seems to align morphologically with the R1 emission. In the LBA 20″ resolution images of **Fig. 4.3**, it is very patchy with few pixels even inside the 3σ contours, but it can be seen in the 40″ resolution images. The integrated spectral index is ~ -1.49.

Despite their visual alignment, we find no morphological or spectral evidence supporting a physical connection. Their combined projected length would be approximately 2 Mpc, and

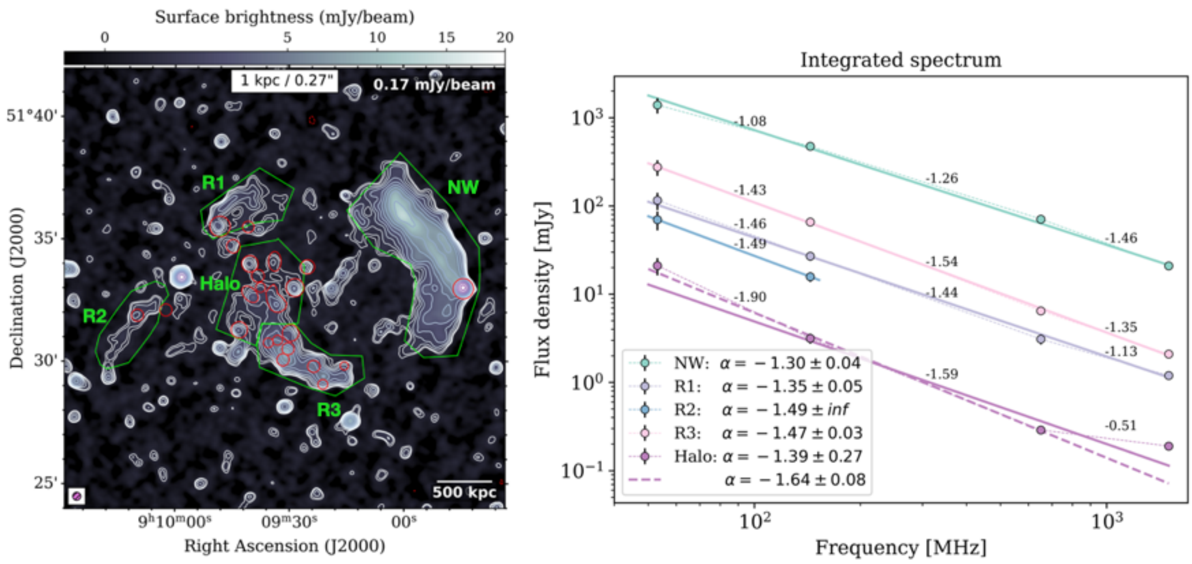

Figure 4.2: Integrated spectrum of diffuse radio sources. *Left:* HBA image with regions used for flux extraction and subtracted sources. Contours starting $2\sigma_{\rm rms}$, with $\sigma_{\rm rms}$ = 0.17 mJy/beam. *Right*: Integrated spectrum and best-fit single power-law function. Halo flux density values are scaled by a factor of $\times 10^{-1}$ for clarity purposes. Additionally, we show the $\alpha^{\rm int}_{\rm halo} = -1.64 \pm 0.08$ calculated using only three frequencies (53, 144, 650 MHz).

while such length is not uncommon for relics - see for example the famous Toothbursh, which also present a characteristic straight morphology - the absence of a bridge emission or common spectral features (see spectral index map in **Section 4.3.2**) argues against a common origin. Additionally, we rule out the possibility that R1 is a tail of the radio galaxy to the north (source A in **??**), since there is no visible connection in the high-resolution images and no spectral index gradient is observed (see **Section 4.3.2**). Therefore we conclude that R1 and R2 are not part of the same radio structure.

Halo emission and southern source *R*3

At the location of the previously detected halo (van Weeren et al., 2011e), we find diffuse emission that appears blended with a southern structure, labeled ($R3$). The structure is hard to disentangle and seems to consist of the halo region and a relic in the south $R3$. We tried to visually distinguish these regions to derive estimates on the sizes and flux densities of the structures (see regions in **Fig. 4.2**). We determined the size of the southern relic S to be of about 887 kpc×288 kpc with integrated spectral index $\alpha_S = -1.47 \pm 0.03$. The halo has roughly an extension of 775 kpc. The integrated spectral index results to be $\alpha^{1500}_{53} = 1.39 \pm 0.27$, with a not negligible steepening at low frequencies $\alpha^{144}_{53} = 1.92$. We show that, if only the lowest frequencies are considered, it results equal to ~ -1.64.

This spectral upturn, i.e., steep at low frequencies but flattening at high frequencies, has been previously observed in for example A2256 (Kale & Dwarakanath, 2010; van Weeren et al., 2012). Interestingly this feature was more prominent exactly when using LOFAR LBA data at

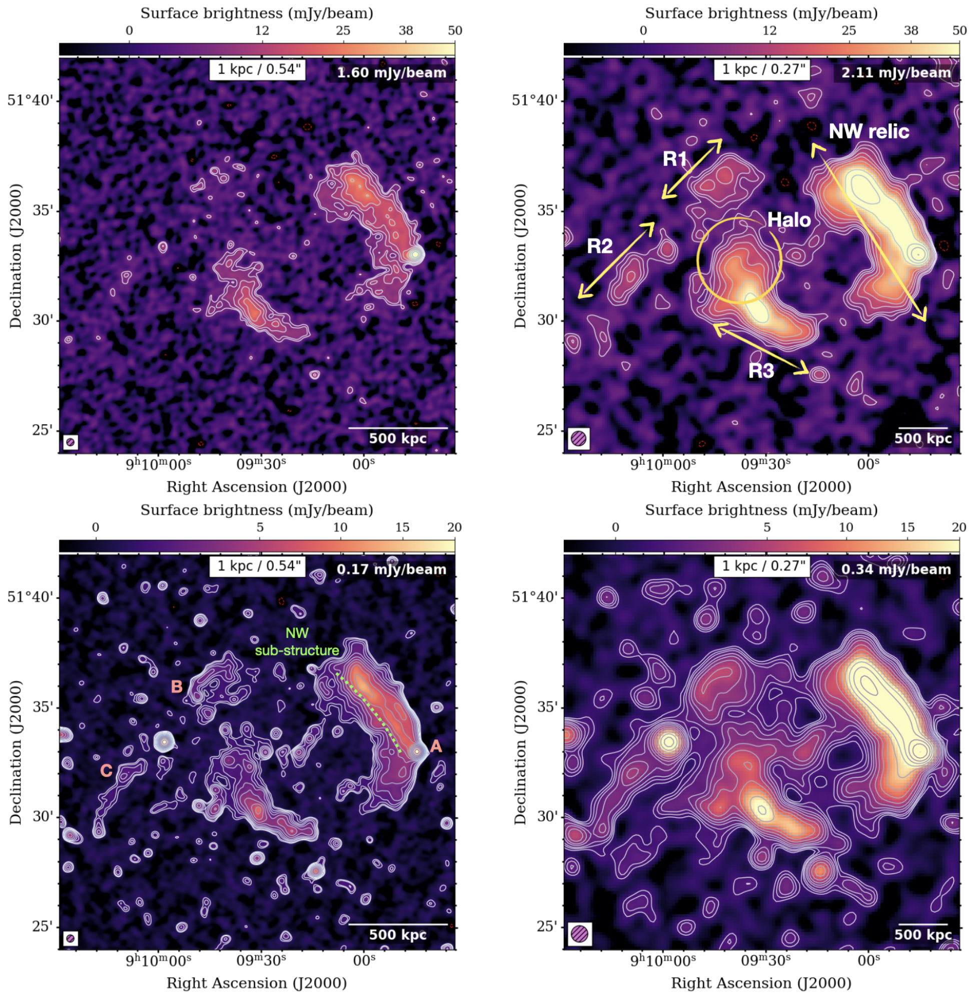

Figure 4.3: Radio images at 53 MHz (top row) and 144 MHz (bottom row). The left column shows the 20″ resolution images, while the right column shows the 40″ resolution images. Contours start at $2\sigma_{\rm rms}$ and increase by factors of 2. The noise level ($\sigma_{\rm rms}$) for each image is indicated in the top-right corner of the respective panel. Source A (FIRST J090844.3+513300), source B (FIRST J090948.5+513529) and source C (WISE J090945.06+513439.8), from **Tab. A1**.

63 MHz (van Weeren et al., 2012). These authors suggest that the complex spectral shape may result from the superposition of two (or more) emission components. In particular, projection of relic emission onto the central halo region could artificially flatten the high-frequency end of the spectrum. Such a scenario appears highly plausible in A746, where the influence of the southern structure R3, partially overlapping with the halo despite our efforts to differentiate the two components, likely contributes to the observed spectral behavior. Given the difficulty to disentangle the halo region in both images, we used a fitting procedure to estimate its size and flux, described in **Section 4.3.3**.

4.3.2 Spectral index maps

Edge-on relics are known to show a spectral index gradient, steepening from the outer to the inner part toward the cluster centre (e.g., Di Gennaro et al., 2018). To investigate such features in the radio emission and discriminate among the different sources, we performed spatially resolved spectral index maps to trace the spectral index variation. For this purpose we created spectral index maps in the 53 MHz to 144 MHz (**Fig. 4.4**) range at different resolutions (26.7″ and 50.6″). The images are convoluted to the same circular beam, the pixel size and the *uv*-coverage has been harmonized by cutting the minimum *uv*-range of the LBA image to the minimum *uv* range of HBA (20λ). Finally, all pixels with a surface brightness below $2\sigma_{rms}$ at both frequencies are discarded. We compare our data, with higher frequencies spectral index maps (**Fig. 4.5**), from Rajpurohit et al. (2024).

In the α_{144}^{53} maps, a gradient across NW relic is clearly visible, with spectral index values steepening from roughly −0.5 to −2.5 at the inner edge. The low-frequency maps (53–144 MHz) allow us to probe the outermost, flatter-spectrum regions of the relic, theoretically corresponding to the shock front injection site. At higher frequencies (**Fig. 4.5**), however, the same regions do not show such clear gradient, with steeper values ($\alpha_{650}^{144} \sim -1.1$ and $\alpha_{1500}^{650} \sim -1.4$), suggesting the presence of an already curved spectrum. Such curvature is typically expected downstream of the shock due to radiative losses, not at the acceleration site itself (Stroe et al., 2013c). This may imply there are non-negligible projection effects, playing a role in shaping the observed spectrum. On the other hand, this relic shows a high degree of polarization, reaching up to 65% at the relic's edge and decreasing in the downstream regions (van Weeren et al., 2011b; Rajpurohit et al., 2024). This would normally suggest a merger axis close to the plane of the sky and argue against strong projection effects, adding complexity to the interpretation.

Morphologically, the southern relic R3 appears to be the counter relic to the NW relic, as expected in a binary merger scenario producing double-relics. However, the spectral information does not seem to align with this picture. While the R3 gradient has roughly the same lower and upper limits as for α_{144}^{53} in the western relic, with ~ -0.5 in the southwest to less than −2 near the cluster centre, the gradient does not follow the expected radial direction. The steepening in this case occurs along the main axis of the structure, towards the cluster centre. The same behavior can be noticed in **Fig. 4.5** (*left*) with steeper spectral index values $\alpha_{144}^{650} \in [-2, -0.7]$ Moreover, also the relative positioning of the two relics with respect to the central halo does not support the standard scenario of double relics formed during a binary merger. In such case two outgoing shocks propagating in opposite directions from the centre of mass. If a radio halo is present, it would expected to be approximately at the centre, generated by the merger-driven turbulence in the core region. Examples of this dynamic are systems studied by (e.g., van Weeren et al., 2012; Lindner et al., 2014; Hoang et al., 2017). Even without considering the non-standard spectral index behaviour, NW and R3 are not symmetrically positioned around the halo, with R3 overlapping at least partially to the central radio halo, although the exact fraction is difficult to determine.

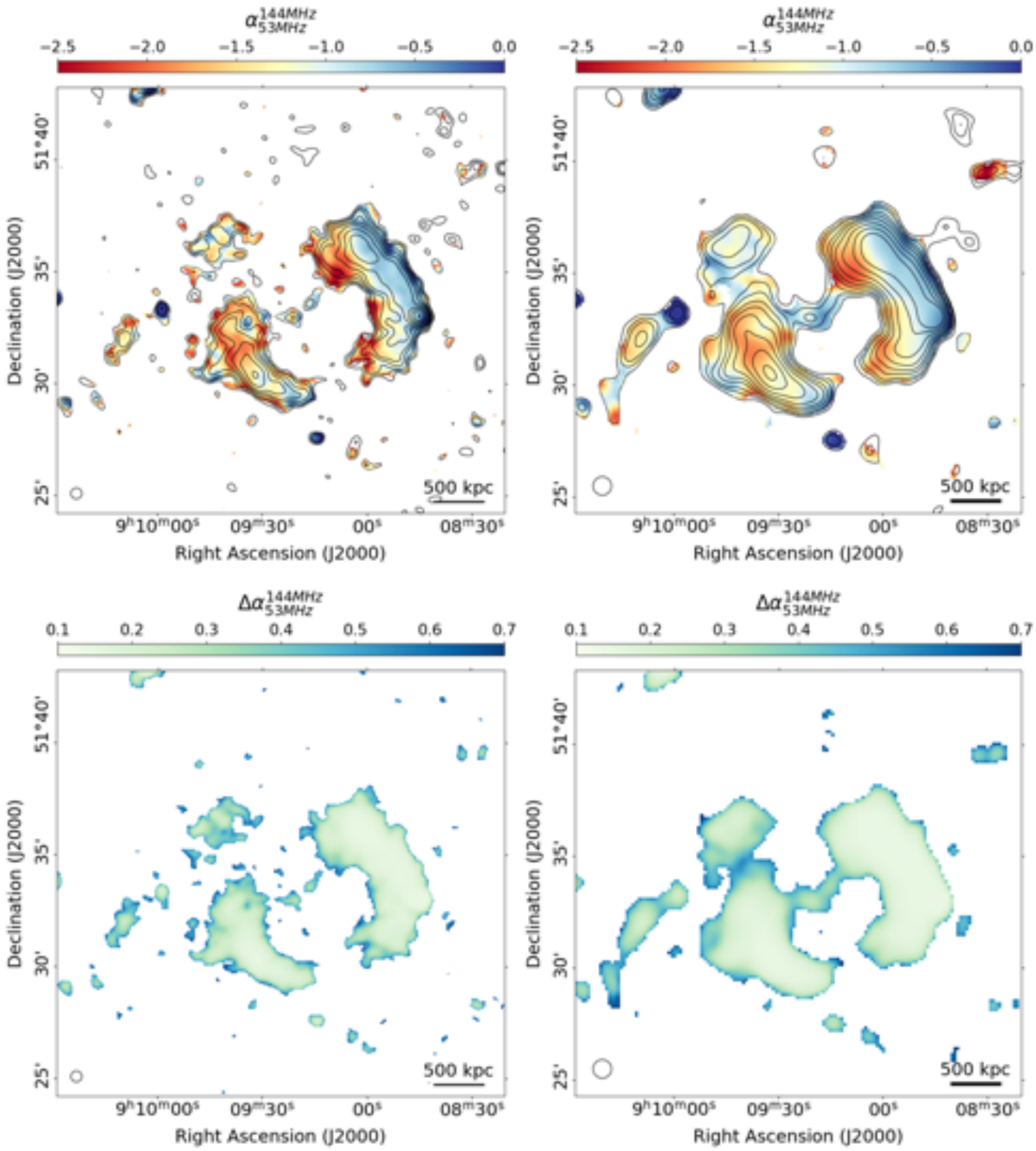

Figure 4.4: Spectral index maps between LOFAR LBA and HBA for two resolutions: 20″ (left) and 40″ (right), without compact source subtraction. The overlaid contours are from the corresponding LBA at the same resolutions (**Fig. 4.3**), starting from 2σ and increasing by factors of 2.

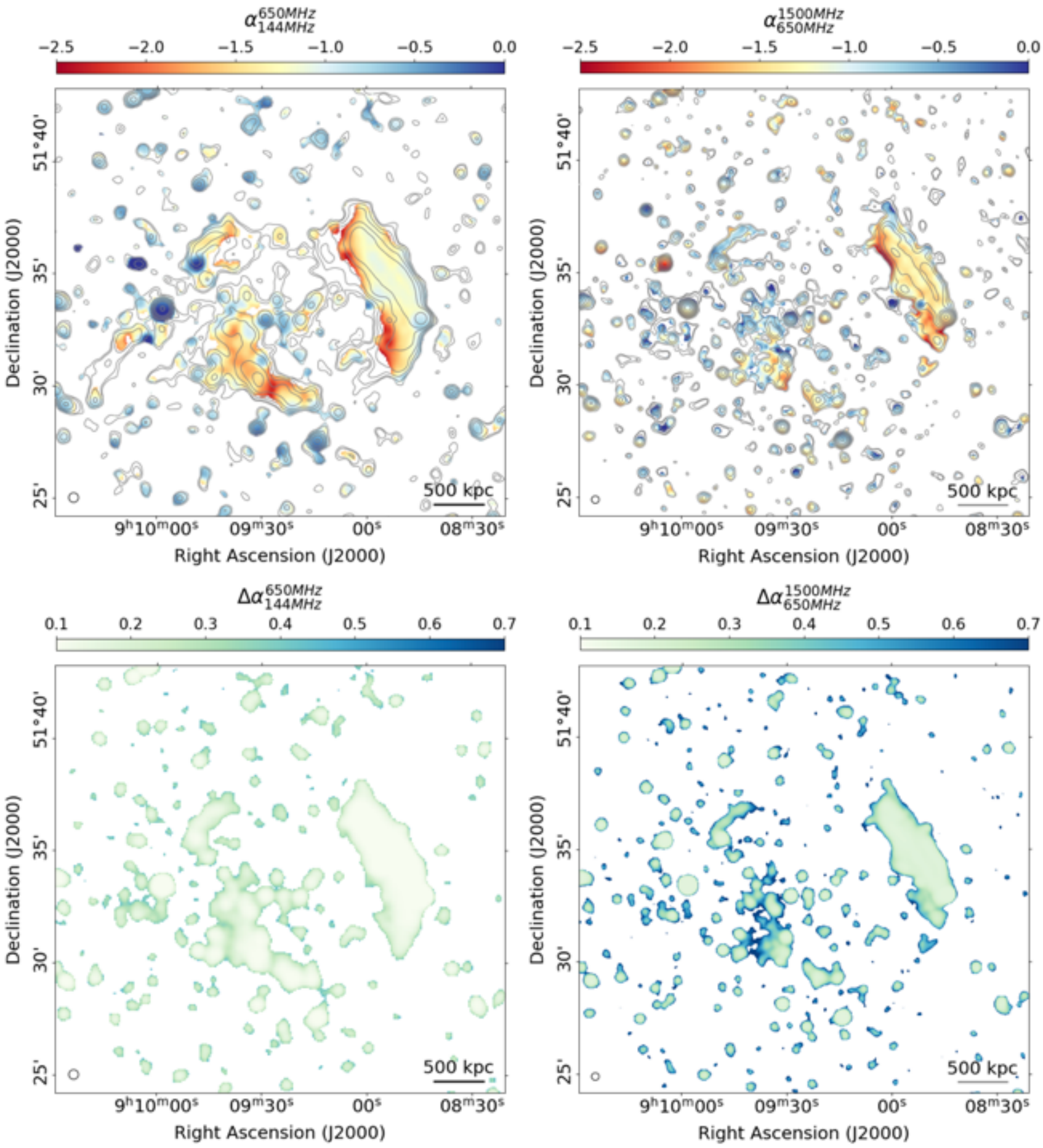

Figure 4.5: Spectral index maps at higher frequencies. *Left*: Map and corresponding error between HBA–uGMRT Band 4 at 20″ resolution, with contours are taken from the HBA image at 20″. *Right:* Map and corresponding error between GMRT Band 4–VLA at 12″ resolution, contours correcpond to the GMRT Band 4 images. In both maps, the contours start at 2σ and increasing in steps of $[2, 3, 6, 12, 24, 48, 96]\sigma$ to avoid obscuring the underlying spectral index structure.

$R1$ and $R2$ are barely visible in the high-frequency maps (**Fig. 4.5**). However, in the 50.6″-resolution spectral index map (**Fig. 4.4**), the source $R1$ seems to have a roughly constant spectral index ~ -1.3 to -1.4. The radio structure in the east E on the other hand has a gradient away from the cluster center, opposite of what is expected for a relic-like emission, going very fast from ~ -1.2 to less than -2. These results confirm the presence of the western radio relic, and reveals unexpected behaviours of the $R1$, $R2$, $R3$ radio sources.

Interestingly, the low-resolution map (**Fig. 4.4**, *right panel*) allows us to study the spectral index of the in-between-regions of halo-*NW* and halo-*R1*. These areas show steep values with $\alpha_{144}^{53} \sim -0.8$ and $\alpha_{144}^{53} \sim -1.1$, respectively. However, we note that the related uncertainties are rather high and the contamination from compact sources cannot be excluded.

4.3.3 Radio surface brightness profiles

The radio halo of A746 has been firstly claimed by van Weeren et al. (2011b), with a total extent of ~ 850 kpc. Nevertheless at lower frequencies, the central diffuse emission appears to be entangled with other diffuse sources that make difficult to set boundaries and manually extract its physical properties. Not only the mentioned overlap with R3 source, but also the possible connection to the NW relic and R1 emission.

Thus, we performed a radial fit to an exponential profile (as done in Murgia et al., 2009; Botteon et al., 2022a; Cuciti et al., 2022) of the form

$$I(r) = I_0\, e^{-r/r_e} \tag{4.2}$$

where I_0 is the central radio surface brightness and r_e the corresponding e-folding radius, i.e. the length-scale at which the surface brightness drops to I_0/e. For this purposed, we used source-subtracted 35″ images described in **Section 2.2.5**. We measured the average surface brightness in concentric annuli of 17″ width ($0.5 \times$ FWHM of the beam) centered on the expected halo center, masking the southern relic $R3$ (**Fig. 4.6**, *left column*). Extracted profiles at 53 and 144 MHz together with best fitting results are shown in **Fig. 4.6**. At 53 MHz, the exponential model has a central brightness of $I_0 = 27 \pm 5\,\mu\mathrm{Jy}\cdot\mathrm{arcsec}^{-2}$ and an e-folding radius of $r_e = 159 \pm 22\,\mathrm{kpc}$. While find a central surface brightness value of $I_0^{144} = 4.0 \pm 0.4\,\mu\mathrm{Jy}\cdot\mathrm{arcsec}^{-2}$ and a characteristic radius of $r_e = 179 \pm 14\,\mathrm{kpc}$ at 144 MHz. We notice that the e-folding radii have consistent values, meaning the surface brightness decline and morphology of the halo does not differ much at the two frequencies. This profile-fitting procedure allows us to define the spatial extent of the diffuse emission. It is customary to fix the size of the halo emission at $3r_e$, as it contains the 80% of the total flux $S_\nu(< 3r_e) = 0.8 S_\nu^\infty$ (Murgia et al. (2009)). That means $3\mathrm{r}_\mathrm{e}^{53} = 477\,\mathrm{kpc}$ and $3\mathrm{r}_\mathrm{e}^{144} = 537\,\mathrm{kpc}$, implying a total extension of ~ 954 kpc and ~ 1.1 Mpc, respectively.

We then estimate halo flux densities integrating the model within $3r_e$, finding $\mathrm{S}_{<3\mathrm{r}_3}^{53} = 254 \pm 50\,\mathrm{mJy}$ and $\mathrm{S}_{<3\mathrm{r}_3}^{144} = 49 \pm 5\,\mathrm{mJy}$. These flux estimates imply an integrated spectral index of $\alpha_{144}^{53} = -1.6 \pm 0.2$, making it an ultra-step spectrum radio halo. From the flux density estimate, we can derive the $k-$corrected halo power as

$$P_\nu = 4\pi D_L^2 S_\nu (1+z)^{-(\alpha+1)}, \tag{4.3}$$

where D_L is the luminosity distance, S_ν is the flux density at the frequency ν, z is the redshift and α is the spectral index. For values of $D_L = 1146.6\,Mpc$, $\mathrm{S}_{144\,\mathrm{MHz}} = \mathrm{S}_{<3\mathrm{r}_3}^{144} = 49 \pm 5\,\mathrm{mJy}$, $z = 0.232 \pm 0.01$ and $\alpha = -1.6 \pm 0.2$, we find $\mathrm{P}_{<3\mathrm{r}_3}^{144} = (8.7 \pm 0.9) \times 10^{24}\,\mathrm{W/Hz}$. Our measured radio power at 144 MHz is fully consistent with the expected value of $P_{144,exp} = 9.57{\times}10^{24}\ W/Hz$,

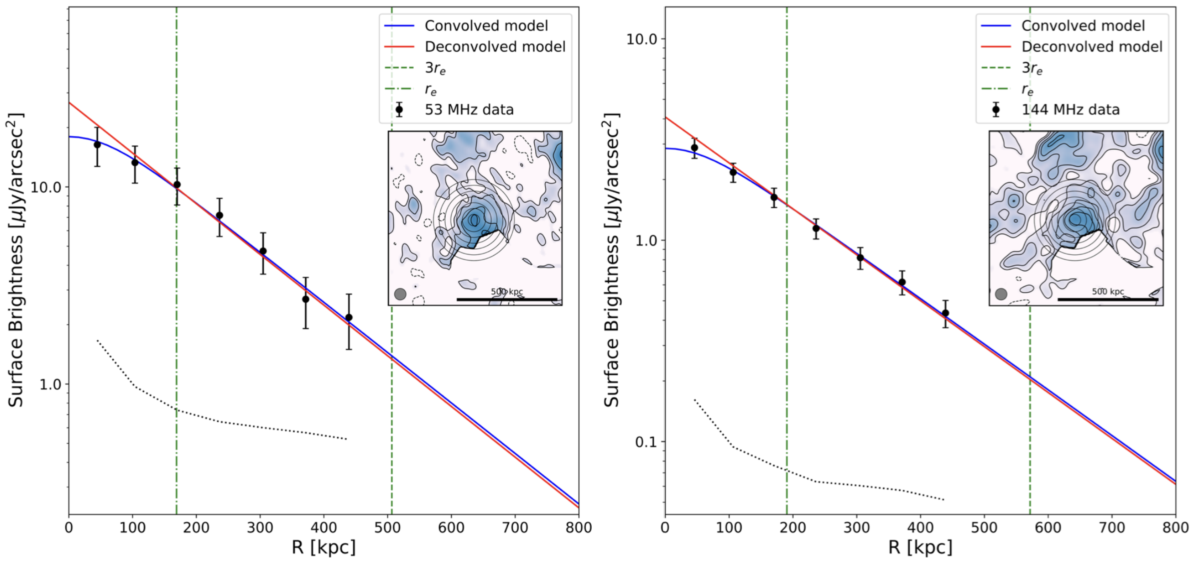

Figure 4.6: Radial surface brightness profile of the radio halo in Abell 746. *Left*: Profile at 53 MHz, obtained from LOFAR LBA 35″ resolution image, with the southern diffuse emission masked. Best-fit parameters $I_0 = 27 \pm 5\,\mu\text{Jy} \cdot \text{arcsec}^{-2}$ and $r_e = 159 \pm 22\,\text{kpc}$. *Right*: Profile at 53 MHz, obtained from LOFAR HBA 35″ resolution image, with the southern diffuse emission masked. Best-fit parameters $I_0^{144} = 4.0 \pm 0.4\,\mu\text{Jy} \cdot \text{arcsec}^{-2}$ and $r_e = 179 \pm 14\,\text{kpc}$. The characteristic e-folding radii corresponding to r_e and $3r_e$ are highlighted by green vertical lines. The solid lines represent the convolved (blue) and deconvolved (red) modelled profiles.

obtained from the best-fit $P_{150\,MHz} - M_{500}$ scaling relation (Cuciti et al., 2023), considering A746 cluster mass of $M_{500} = 5.34 \pm 0.40\,M_\odot$.

These results support the turbulent re-acceleration model prediction. Massive clusters undergoing major mergers typically host halos with flatter spectra ($\alpha \sim -1.3$), detectable up to GHz frequencies, from which the $P_{1.4\,GHz} - M_{500}$ relations are derived (Cassano et al., 2010; Cuciti et al., 2015, 2021). In contrast, less energetic mergers in lower-mass systems ($M_{500} \lesssim 6 \times 10^{14}\,M_\odot$) are predicted to produce USSRHs that fade at higher frequencies and therefore follow the same correlation at lower frequencies $P_{150\,MHz} - M_{500}$ (van Weeren et al., 2021; Cuciti et al., 2023).

4.3.4 Radio Mach number

The diffusive shock acceleration (DSA) model predicts a clear relation between the the shock Mach number $\mathcal{M}$ and the volume-integrated radio spectral index (which we derived in **Section 4.3.1**). In particular, the power-law index of the energy distribution of electrons injected by the shock, δ_{inj}, is related to the Mach number as (Drury, 1983; Blandford & Eichler, 1987):

$$\delta_{\text{inj}} = 2\,\frac{\mathcal{M}^2 + 1}{\mathcal{M}^2 - 1}\,, \tag{4.4}$$

where $\delta_{\rm inj}$ is the electron momentum energy distribution index $\mathrm{d}N/\mathrm{d}p \propto p^{-\delta_{\rm inj}}$, and is connected to the injection spectral index of the radio emission by $\alpha_{\rm inj} = -(\delta_{\rm inj}-1)/2$. Moreover, in the case of a steady-state balance between particle acceleration and radiative losses is assumed, the observed, volume-integrated spectral index $\alpha_{\rm int}$ is related to the injection index through (Kardashev, 1962) as $\alpha_{\rm int} = \alpha_{\rm inj} + 0.5$. Therefore, the Mach number can be directly derived from the observed spectral index using:

$$\mathcal{M} = \sqrt{\frac{2\alpha_{\rm inj} - 3}{2\alpha_{\rm inj} + 1}}, \tag{4.5}$$

allowing us to estimate $\mathcal{M}$ directly from the radio flux density measurements. Thus, for the different relic structures we obtain $\mathcal{M}_{\rm NW} = 2.8 \pm 0.3$, $\mathcal{M}_{\rm R1} = 2.6 \pm 0.3$, $\mathcal{M}_{\rm R2} \sim 2.25$ and $\mathcal{M}_{R3} = 2.3 \pm 0.1$. According to the standard DSA theory, such low Mach numbers ($\mathcal{M} \lesssim 3$) are not efficient at accelerating electrons from the thermal pool. This points to the need for pre-existing populations of seed electrons, likely provided by fossil plasma or past AGN activity, in order to produce the observed synchrotron emission (e.g. Pinzke et al., 2013; Kang, 2016; Wittor et al., 2021). In this cluster, this scenario is totally plausible not only due to the large number of radio sources distributed throughout the cluster volume, but also because specific AGN sources (see **Tab. A1**) strategically located near the observed relic structures. Moreover, the similarity in Mach numbers across different relic features may also suggest a relatively uniform shock propagation within the ICM, although little we know about the geometry of the merger, and therefore projection effects and spectral aging could influence these estimates.

4.4 Merger Discussion

A746 galaxy clusters is a a highly disturbed merger systems, with multi-wavelength data available (optical, X-ray and radio data are schematically represented in **Fig. 4.7**). XMM-Newton observations presented in Rajpurohit et al. (2024) reveals a disturbed X-ray morphology, where four surface brightness discontinuities were identified, three of which were classified as merger-driven shock fronts (SB1, SB2, SB4 in **Fig. 4.7**). Of these only SB1 and SB2 could be connected to the relics.

Using optical data from Subaru/Hyper Suprime-Cam, HyeongHan et al. (2024) carried out a weak-lensing analysis and identified three mass peaks (represented in yellow, and cyan circles indicating the BCGs for each subhalo in **Fig. 4.7**): a central main peak (S) and two extensions toward the north (N) and west (W) tracing the cluster galaxy and X-ray distributions. The main peak aligns with the geometric center of the disturbed X-ray morphology and the radio halo, while the radio relics (NW and R3) are not symmetrically distributed with respect to this center.

From the radio perspective, A746 looks like a relatively standard double-relic system, but the position of the halo as well as the position and spectral gradient of the southern candidate relic seem not to line up with this assumption. Moreover, other patches of radio source $R1$ and $R2$ with a relic-shape morphology are present, although without a clear evidence of spectral index gradient in the radio maps.

The apparent symmetry of the diffuse radio emission (NW and R3 relics) together with the

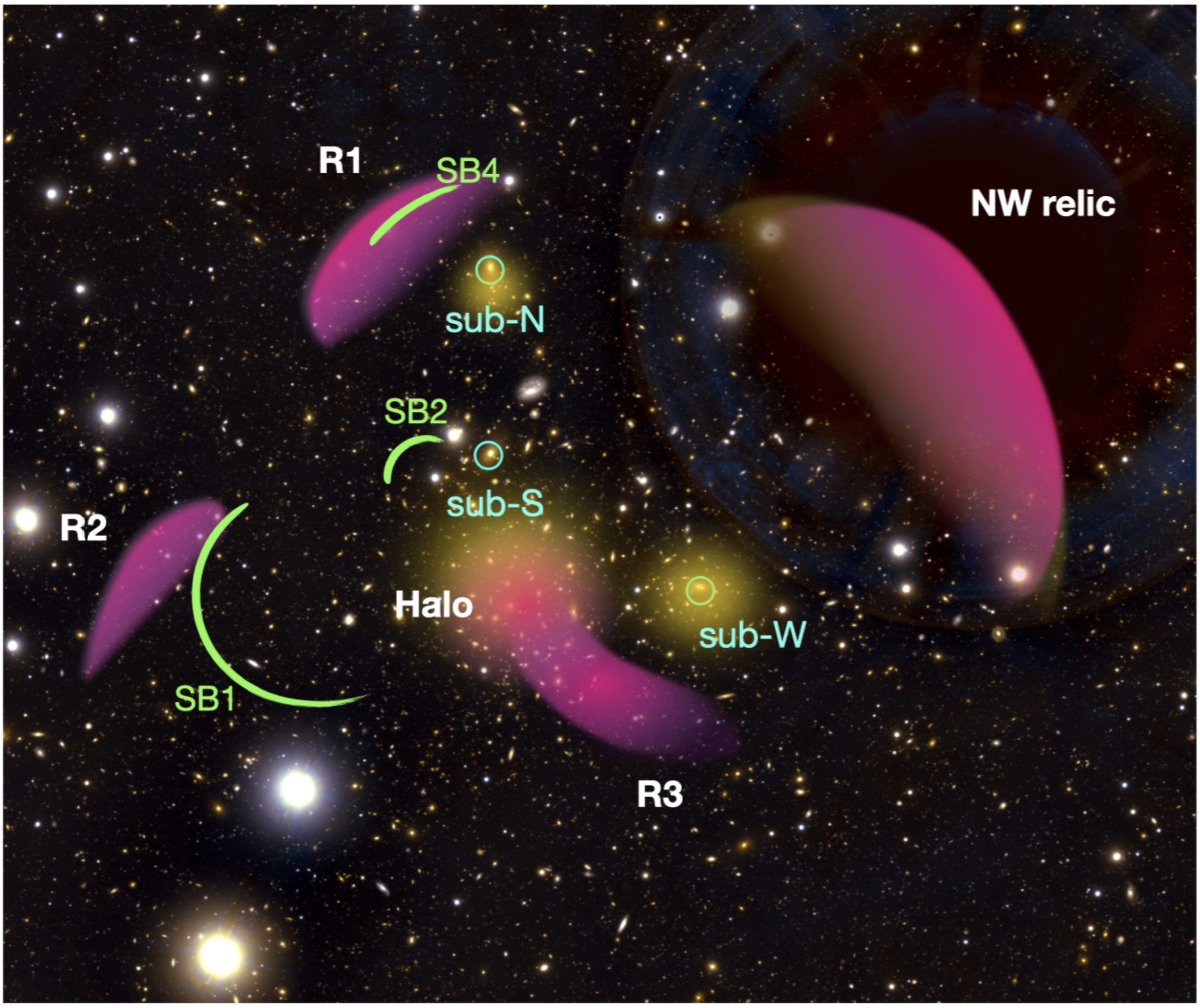

Figure 4.7: Schematic view of A746. Magenta: radio emission. Yellow: Galaxy number density map (adapted from HyeongHan et al. 2024). Cyan circles: BCGs for each subhalo (HyeongHan et al., 2024). Lime lines (SB1, SB2, SB4) indicative the shock positions detected in Rajpurohit et al. (2024).

high degree of polarization measured at the NW relic, would initially suggest a standard near head-on binary merger occurring along the east–west direction. However, this interpretation doesn't fit with other observational constraints. The main southern substructure (S) as well as the radio halo lies in unusually close proximity to the R3 relic, while the western substructure (W) sits roughly equidistant between the two relics. Furthermore, the mass and galaxy density distributions are not bimodal, as typically seen in binary merger systems. Instead, both the galaxy and mass distributions reveal three significant substructures arranged in a roughly triangular configuration, which is mirrored in the morphology of the X-ray emitting ICM. This suggests that the same sequence of dynamical events shaping the dark matter and galaxy distributions also impacted the thermal gas. While a triangular ICM shape is not a unique signature of a triple merger, such a configuration can naturally arise when multiple subclusters interact sequentially or along different axes. This peculiar morphology is observed in some triple merger systems (Ma et al., 2009; Chadayammuri et al., 2024) and has also been reproduced in numerical simulations. For example, the triple merger scenario simulated by **?** involved two equal-mass clusters and a smaller third subcluster on an off-axis trajectory and gave rise to a triangular X-ray morphology.

To reconcile observational discrepancies described above, HyeongHan et al. (2024) propose that A746 has undergone two successive mergers involving three distinct subclusters. In their scenario, the first, near head-on collision occurred along the east–west axis between the S and W subclusters, generating the double radio relics observed today (NW and R3). Shortly thereafter, a third subcluster, associated with the northern mass peak, passed through the system from south to north. This secondary merger event likely perturbed the trajectories of the first two subclusters and may have given rise to the northern relic (R1). However, it remains difficult to incorporate in this picture also the position and spectral characteristic (steep-spectrum) of the radio halo in this picture.

Another possible scenario is that R1 and R2, being the most peripheral features, were produced during an earlier stage by a separate, less energetic merger event. R3 and the NW relics may actually constitute a genuine double relic system, but affected by a significant projection effect. In this picture, the R3 structure would lie behind the central halo emission, with only its tip visible in the south. The observed flat spectral index values at this southern edge (with $\alpha \sim -0.5$) would then represent the injection region of the shock, analogous to the flattest spectral indices seen at the outer edge of the NW relic.

Overall, the combination of multi-wavelength data supports a scenario where Abell 746 is experiencing at least a triple merger, with relics and halo emission tracing shocks and turbulence associated with two distinct merger phases. Yet, the projection effects, overlapping emission, and lack of symmetry in the radio structures make it difficult to pin down a single, clean merger axis or sequence.

4.5 Conclusions

In this work, we performed an analysis of the radio structures present in Abell 746. We have presented new LOFAR LBA obsertvations, combined with LOFAR HBA, uGMRT band 4 and VLA data.

The main findings are summarized below:

- The new LBA data confirm the presence of the radio relic west of the centre (NW) as previously found in van Weeren et al. (2011b) and Botteon et al. (2022a). In addition, we detect three further relic-like structures R1, R2, and R3 (also reported in Raja et al. 2024b) and provide a clearer characterisation of a central radio halo, that appears superimposed with an arc-like southern emission R3 that morphologically resembles a potential counter-relic to the NW.
- The main western relic has a size of 8.1 × 0.5 Mpc, and integrated spectral index $\alpha_{int} = -1.30 \pm 0.04$, corresponding to a Mach number of $M_{NW} = 2.8 \pm 10.3$. While the NW relic exhibits all the canonical properties of relics (arc-shape, bright and flat spectral index at the outer edge, and spectral steepening downstream due to ageing), the nature of the other structures is puzzling. None of the others relic-like structures shows the radial spectral index decline. R1 and R2 display irregular morphologies and patchy spectral index distributions, whereas R3 exhibits spectral flattening in the inward direction. One possible explanation for such a feature could be the presence of a radio galaxy with a head-tail morphology; however, no AGN is detected at the southern edge of R3 (where the spectral index flattens to $\alpha \sim -0.5$). This lack of an optical or radio counterpart makes the AGN-origin scenario for R3 unlikely. Considering the R1, R2, R3 radio structures as relics, we derived their Mach numbers assuming the standard DSA scenario from the volume-integrated spectral index measurements. The low Mach numbers ($\mathcal{M} \lesssim 3$) derived for these sources ($\mathcal{M}_{\rm NW} = 2.8 \pm 0.3$, $\mathcal{M}_{\rm R1} = 2.6 \pm 0.3$, $\mathcal{M}_{\rm R2} \sim 2.25$, $\mathcal{M}_{R3} = 2.3 \pm 0.1$) points to the need for pre-existing populations of seed electrons, likely provided by fossil plasma or past AGN activity, of which the cluster appears to be abundantly rich. This morphological alignment suggests that the fossil plasma–assisted acceleration mechanism is a plausible scenario for the formation of these radio relics.
- We tried to disentangle the radio halo from the southern radio structure by fitting the surface brightness profile to the expected exponential profile for halos sources (Murgia et al., 2009), while while conservatively masking the potential contribution from R3 (see **Fig. 4.6**). The resulting e-folding radii of the radio halo is $r_{e,LBA} = 159 \pm 22\, kpc$ at 53 MHz and $r_{e,HBA} = 179 \pm 14\ kpc$ at 144 MHz. This fit enables us to define an unbiased halo extent (minimally contaminated by relics emission and embedded sources) and compute the integrated flux within $3r_e$ at both frequencies: $\rm S^{53}_{<3r_3} = 254 \pm 50$ mJy and $\rm S^{144}_{<3r_3} = 49 \pm 5$ mJy. These flux estimates imply an integrated spectral index of $\alpha^{53}_{144} = -1.6 \pm 0.2$, therefore we classify it as an ultra-step spectrum radio halo.
- Finally, being an ultra-steep spectrum halo in a relatively low-mass system, we also evaluated the halo radio power and compared it with the latest results about the radio power mass correlation at 150 MHz Cuciti et al. (2023). We find a value of $P^{144}_{<3r_3} = (8.7 \pm 0.9) \times 10^{24}\ W/Hz$ in excellent agreement with the expected value of $P_{144,exp} = 9.57 \times 10^{24}\ W/Hz$, obtained from the best-fit $P_{150\,MHz} - M_{500}$ scaling relation by Cuciti et al. (2023).
- We should be cautious in considering R3 counter relic in the double relic structure formed with NW, as there is a strong contamination of sources and overlap with other diffuse radio emission, such as the central halo. As a matter of fact, the observed upturn in the

halo's integrated spectral index (**Fig. 4.2**) points to a scenario where the relic emission is contributing to the overall volume-integrated halo spectrum. A possible scenario is that R1 and R2, being the most peripheral features, were produced during an earlier stage by a separate, less energetic merger event. R3 and the NW relics may actually constitute a genuine double relic system, but affected by a significant projection effect. In this picture, the R3 structure would lie behind the central halo emission, with only its tip visible in the south. The observed flat spectral index values at this southern edge (with $\alpha \sim -0.5$) would then represent the injection region of the shock, analogous to the flattest spectral indices seen at the outer edge of the NW relic.

A.1 Sources

	Source	RA	DEC	z	type
NW	FIRST J090844.3+513300	09 08 44.37	+51 33 00.77	-	Radio Source (Helfand et al., 2015)
R1	FIRST J090948.5+513529	09 09 48.53	+51 35 29.66	-	AGN Candidate (Helfand et al., 2015)
	SDSS J090945.05+513440.0	09 09 45.04	+51 34 40.05	0.18	Galaxy (Adelman-McCarthy & et al., 2009)
	WISE J090941.05+513529.3	09 09 41.05225	+51 35 29.34	0.21	Galaxy (Cutri & et al., 2012)
R2	J091009.9+513153	09 10 09.91	+ 51 31 53.79	0.42	QSO (Gaia Collaboration, 2020a)
	WISE J091002.71+513205.8	09 10 02.71416	+51 32 05.87	-	Galaxy (Cutri & et al., 2012)
R3	J137.31602760+51.49690839	09 09 15.84	+51 29 48.87	0.29	Galaxy (Golovich et al., 2019)
	ILTJ090921.43+512904.5	09 09 21.43	+51 29 04.51	0.75p	Galaxy (Hardcastle et al., 2023)
	J090924.21+512949.7	09 09 24.21	+51 29 49.73	-	Galaxy (Adelman-McCarthy & et al., 2011)
	SDSS J090932.04+513001.8	09 09 32.04	+51 30 01.84	0.216s	BCG (Gaia Collaboration, 2020b)
	J137.37103600+51.50679057	09 09 29.04	+51 30 24.44	0.213s	Galaxy (Golovich et al., 2019)
	J137.37740880+51.51780296	09 09 30.57	+51 31 04.09	0.216s	Galaxy (Golovich et al., 2019)
	J137.38929390+51.51461624	09 09 33.43	+51 30 52.61	0.312s	Galaxy (Golovich et al., 2019)
	J090935.62+513043.4	09 09 35.61	+51 30 43.49	0.41p	Galaxy (Abazajian et al., 2009)
Halo	J09094355+5131151	09 09 43.56	+51 31 15.88	0.519s	QSO (Gaia Collaboration, 2020b)
	J137.38836700+51.53910279	09 09 33.20	+51 32 20.77	0.210s	Galaxy (Golovich et al., 2019)
	SDSS J090940.34+513240.5	09 09 40.34	+51 32 40.56	0.215s	Galaxy (Gaia Collaboration, 2020b)
	FIRST J090928.7+513259	09 09 28.73	+51 32 59.25	-	Radio Galaxy (Helfand et al., 2015)
	J090938.21+513302.1	09 09 38.21	+51 33 02.1	0.34p	Galaxy (Alam & et al., 2016)
	2MASX J09093863+5133268	9 09 38.60	+51 33 27.24	0.288s	BCG (Golovich et al., 2019)
	J090934.39+513403.2	09 09 34.39	+51 34 03.25	0.23p	Galaxy (Adelman-McCarthy & et al., 2009)
	EDR3 1016390094905004160	09 09 25.09	+51 33 54.16	0.33p	Galaxy Gaia Collaboration (2020b)
	8001589733003678	09 09 40.90	+51 34 00.16	1.04p	Galaxy (Duncan, 2022)

Table A1: List of detected compact point radio sources with optical counterpart, manually subtracted from the extended radio emission. They correspond to the red circles of **Fig. 4.2**.

A.2 LOFAR LBA and HBA source subtracted images at different resolutions

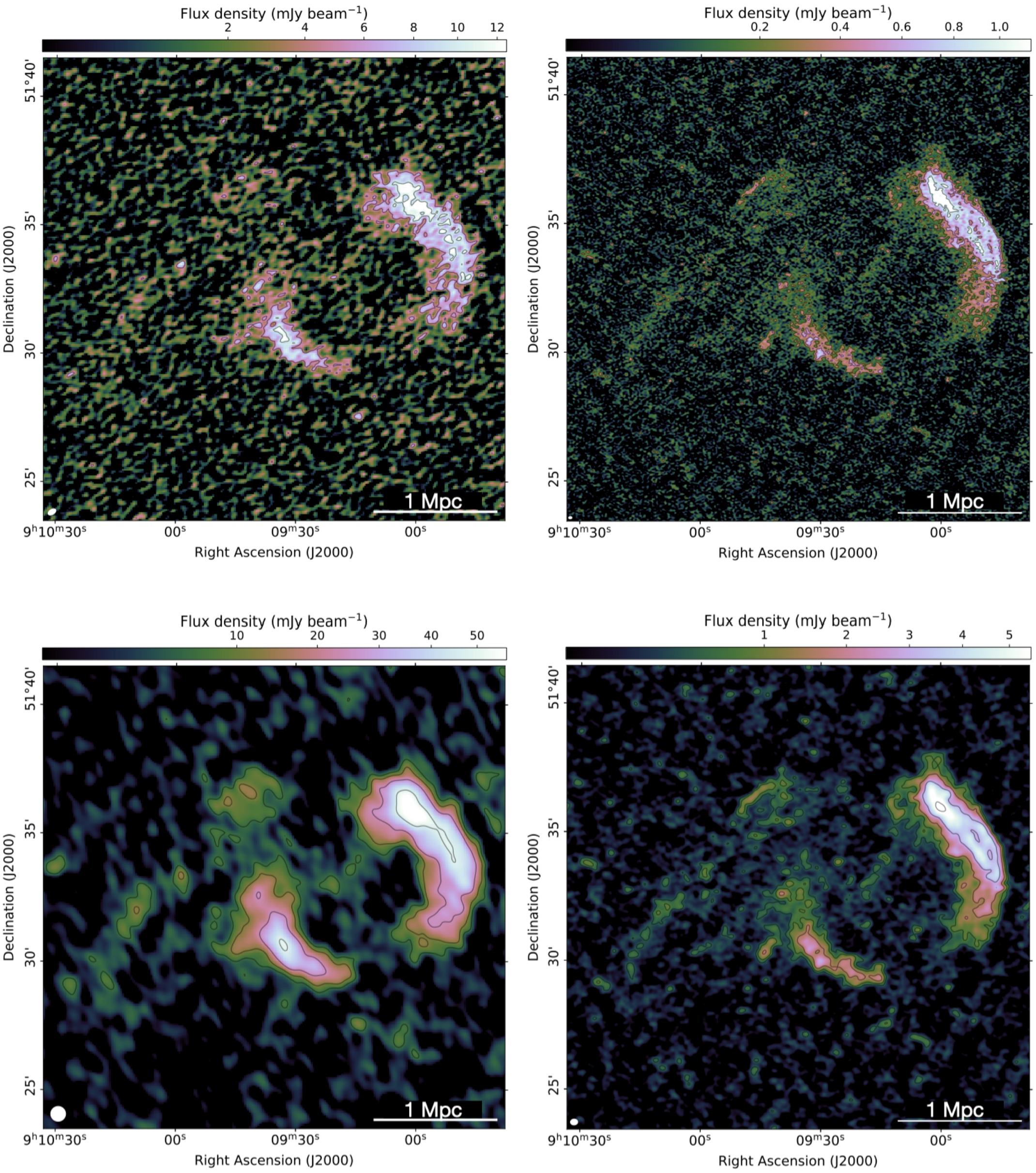

Figure A1: Source subtracted radio images at 53 MHz (left column) and 144 MHz (right column). *Top left:* 53 MHz image at $12'' \times 12''$ resolution with $\sigma = 130\,\mu$Jy/b. *Bottom left:* 53 MHz image at $35''$ resolution with $\sigma = 2\,$mJy/b. *Top right:* 144 MHz image at $8'' \times 5''$ resolution with $\sigma = 1.6\,$mJy/b. *Bottom right:* 144 MHz image at $16.8'' \times 13.6''$ resolution with $\sigma = 78\,\mu$Jy/b.

5 Conclusion and Outlook

Cosmic magnetic fields and cosmic-ray acceleration are important pieces of the puzzle in understanding the Universe. These non-thermal components act on many different scales (from galaxies to clusters and beyond) and trace some of the most energetic processes in the Universe. Radio observations are the primary tools to study them. Not only they are complementary to other observational windows essential to determine the cluster dynamics, but they also offer direct access to turbulence and shocks generated during cluster mergers, thereby indirectly tracing the assembly of structure formation. Moreover, they serve as important constraints for MHD cosmological simulation and theoretical formation mechanism models, which predict the occurrence and properties of diffuse radio sources.

In this dissertation, I presented the research I conducted during my PhD. This is focused on non-thermal phenomena in galaxy clusters, spanning from radio galaxies to diffuse emission, such as radio halos and relics. For this, I mainly employed LOFAR observations < 100 MHz, the lowest radio window observable from Earth, which I then proceeded to combine with higher frequency radio data, to fully characterise the spectral properties of the radio sources.

In **Chapter 2**, I investigated the interaction between radio galaxies and the ICM, which is ultimately related to cosmic-rays life cycles in clusters. By studying the galaxy cluster ZwCl 0634.1+4747, I highlighted the importance of ram pressure effects, usually associated with gas-deprived normal galaxies, in bending radio galaxy jets and affecting their spectral properties. The low-frequencies observations presented in this project show that these disturbed jets can reach very long distances, filling the $\sim$ Mpc-scale cluster volume with mildly-relativistic electrons. Thanks to the combination of ultra-low and low- radio observations, I was able to accurately measure the spectrum along the tails showing that all three radio tails in ZwCl 0634.1+4747 exhibit curved spectra. Instead of getting steeper, the spectraflatten along the tails, maintaining a rather constant (steep) spectrum for hundreds of kpc downstream from the AGN core. This implies the presence of a mechanisms able to re-energized aged electron, making them visible again at low radio frequencies. I investigated different scenarios and I concluded that the observed spectral properties of the tails are most consistent with a scenario where turbulence is driven into the tails as a result of their interaction with the ICM. If this is indeed the case, and given that such spectral signatures are seen in all three radio galaxies in ZwCl 0634.1+4747, this process may be more common than previously thought. Thus, providing a “straightforward” explanation for how a population of relativistic electrons can be sustained across such a long timescale and distances within the ICM.

In **Chapter 3**, I presented the first ultra-low-frequency observations of the “Sausage” cluster (CIZA J2242.8+5301) at 45 MHz using LOFAR LBA. This dataset involved a complex data reduction process, which I personally led. The thermal-noise limited 45 MHz image I was able to obtain shows, among other things, the capabilities of LOFAR LBA calibration pipeline in producing high-fidelity images of diffuse radio emission in clusters. Being one of the most studied double-relic systems, I combined the new low-frequency information with the plethora of radio data available up to 3 GHz, providing new insights into the morphology and spectral properties complex system of diffuse, relic-like sources. By computing spectral index and curvature maps, I showed that the flattest spectrum and zero spectral curvature area, i.e., the site of fresh particle acceleration, coincides with the outer edge of the northern relic. This matches expectations from the DSA scenario, where the injection region at the shock front exhibits these spectral characteristics before radiative losses set in downstream region. In the second part of this project, I proceeded with a more in depth analysis of the northern relic's surface brightness profile. Despite being the text-book example of a edge-on viewed shock, the the eastern part of the northern relic displays a remarkably symmetric profile, with wings extending on either side of the peak. This is inconsistent with the standard picture of particle acceleration at a single, sharp shock followed by downstream spectral ageing. To investigate this, I used an analytical toy model that includes projection effects, magnetic field variation and shock deformation to provide more realistic description of the observed emission. Each of these additional effects increasingly improved the model's match to the data, yet it was not possible to fully reproduce the observed profiles across different frequencies and resolutions. These results show that, even in the most idealized radio relic example, the physics of radio relics is a complex interplay of factors.

In **Chapter 4**, I investigated an extremely disturbed and morphologically complex merging cluster, in contrast to the idealized textbook example of Chapter 3. Abell 746 hosts multiple diffuse radio sources, including a classical relic, several relic-like structures, and a central radio halo over imposed to other diffuse emission. I performed a multi-frequency study across 53–1400 MHz range in order to characterize the morphology and spectral properties of the system in order to explain its merger history. While the main relic showed typical properties of classical relics in terms of morphology and integrated spectral shape, the additional relic-like structure show patchy morphology and no radial spectral steepening from the supposed shock edge to the cluster center. All relics show low mach number ($\mathcal{M} < 3$), expected to be inefficient to accelerate particle from the thermal pool and implying the presence of pre-accelerated seed electron population, likely connected to the many radio galaxies present in the cluster. Interestingly, A746 also host a ultra-steep spectrum radio halo, a population of sources that is expected to be more predominant at low-frequency. In fact, I was able to characterize and classify it, using exponential surface brightness profile fitting of low-frequency data, yielding a spectral index of $\alpha_{53}^{144} = -1.6 \pm 0.2$. The present of a ultra-steep spectrum radio halo in this triple-merger system is consistent with the expectation from turbulent re-acceleration scenario, where ultra steep spectrum radio halos inhabit low-mass clusters.

5.1 Future works

Despite the great progress made in the last few years, our knowledge of non-thermal physics in galaxy clusters is still incomplete. The opening of the low-frequency (< 300 MHz) radio window has revolutionized cluster science, both in terms of new discoveries (e.g., mega-halos **Section 1.3.1.1**, hybrid sources **Section 1.3.1.2** or GReET sources **Section 1.4.1**), and significant statistical samples (Cuciti et al., 2023; Cassano et al., 2023; Jones et al., 2023b), bringing with it exciting new questions.

Among them, and particularly relevant to this thesis, are: How common are low-efficiency re-acceleration phenomena in clusters? Would low-efficiency phenomena, as the one described in Chapter 2 be able to produce and sustain a population of mildly relativistic CR in the ICM? And to what extent do these mechanisms contribute to the overall population of mildly relativistic cosmic rays in the ICM? To investigate this, we need a large sample of radio galaxies with disturbed morphologies in clusters and proper low-frequency coverage in order to detect deviation from standard ageing and thus characterize the re-acceleration mechanisms. Such study would represent a natural extension of the work presented in Chapter 2 and will become feasible thanks to the upcoming LoLSS survey (de Gasperin et al., 2023), which will complete the picture initiated by LoTSS, providing ultra-low-frequency coverage of a large fraction of the northern sky.

One of the most exciting challenges over the next years is the use of Very Long Baseline Interferometry (VLBI) with LOFAR LBA, meaning incorporating the international stations when observing < 100 MHz. That would overcome the (possibly) only downside of LBA observations, the relative low-resolution compared to higher frequency instruments which prevent very detailed studies. The LBA-VLBI dataset for the CIZA J2242.8+5301 cluster, presented in Chapter 3, is already available and I started working on them using the at-the-time available working pipeline. This preliminary attempt highlighted the need to adapt and fine-tune the calibration strategy for LBA-VLBI applications. Thanks to CIZA J2242.8+5301 higher-frequency studies (Di Gennaro et al., 2018) and recent simulations (Lee et al., 2024), we know that relics (especially the northern relic in the Sausage cluster) are far from being homogeneous structures, but are intrinsically made of filamentary substructures, most probably shaped by the inhomogeneities of the ICM medium they propagate through. Achieving arcsecond-resolution for CIZA J2242.8+5301, would allow us to resolve $\sim$ few kpc-scale substructures in Mpc-scale sources. In the future, I plan to analyze this dataset to explore the new possibilities offered by LOFAR LBA combined with VLBI baselines and to probe the sub-structure of radio relics.

Finally, among the ideal targets for low-frequency observations are USSRHs, as the one presented in Chapter 4. At the moment only a handful of steep-spectrum radio halos are known, many of them relying on higher-frequencies non-detection (i.e. upper limit) to constrain their spectral shape. Based on the theoretical re-acceleration scenario (described in **Section 1.3**), these sources are predicted to become more common at lower-frequencies and in lower-mass systems. To address this, I led a successful proposal as principal investigator for LOFAR LBA observations targeting a sub-sample of 13 clusters hosting radio halos in the Planck-LoTSS-DR2 catalogue (Botteon et al., 2022a), with $M < 5 \times 10^{14} M_{\odot}$ and $z < 0.3$. This project, which I plan to take over in the future, will represent the first systematic study of USSRHs in this mass regime, allowing us to constrain the connection between halo spectral steepness and cluster mass. According to Cassano et al. (2023), the model predicts that $70 - 80\%$ of the halos detected in PSZ2 clusters in LoTSS-DR2 have a steep spectrum, a prediction that remains unconfirmed, as follow-up observations at other frequencies are needed to fully characterize their spectral properties. Efforts to which my project will directly contribute.

In the early 2010s, standard reviews on non-thermal radio emission in clusters would state *"the next decade represents a golden age for studies of non-thermal component in galaxy clusters"*. It is something not to take for granted that such expectations would be met. Yet, with the benefit of my relatively limited experience, I believe those expectations were met and surpassed. In about ten years, the cluster-radio community has witnessed a true revolution, made by many discoveries and a big community effort in developing working calibration pipelines able to produce incredible science images. Even more exciting is that these next years, with upcoming surveys and new instruments, will keep producing amazing results. Radio astronomy is stepping into a golden future.

Acknowledgments

My PhD years have seen the most personal and professional growth of my life. They have been an incredible sequence of successes, progress, and achievements I would have never expected as well as inevitable moments of disappointment and failure that taught me even more. These experiences have added to my (still in the making) list of lessons learned, which I will carefully carry with me in the years to come. As success does not come from the work of a person alone, I feel this is the right moment to express my gratitude to the people who accompanied me on this journey.

First, I want to thank my supervisor Marcus Brüggen, for the great enthusiasm he has always shown for research, which taught me a lesson or two about how curiosity and passion should guide scientific practice. The same enthusiasm and commitment that he brings into everyday life at the Hamburg Observatory, which I've seen evolve into a place where people enjoy spending time together, within or beyond research duties. Next, I want to thank my supervisor Francesco De Gasperin, for always providing new points of view, his knowledge at the cutting edge of our field and the support when it came to solving data-reduction-related, never-ending issues. Although our collaboration was mainly virtual, I am grateful for his availability and guidance throughout these years. I want to thank you both for the time you devoted to my scientific growth, the useful discussions which greatly improved the quality of my research and advice for my career. But most of all, thank you for always having my back when times got tough.

Lastly, I would like to thank the examination committee of my doctoral defence, composed of Jochen Liske, Jan-Torge Schindler and Luisa Lucie-Smith, for taking the time to evaluate my work and the one you will dedicate during the defence.

Now, trying not to get too emotional, let's start thanking the many people who offered both professional and emotional support throughout this rollercoaster of a PhD journey. To Marco, amazing friend and flatmate, who was the first to welcome me when I arrived in Hamburg. Sharing the house, the job and even friends might easily drive people to want to kill each other, while I am truly glad I had you by my side. To the "Gang", the people I started the PhD with, who have now either moved on to new adventures or are about to complete their own doctoral studies. To Thomas, Henrik, Gabriella, Thorben, Antonio, Lovorka and Kathrin. You have always offered a shoulder to lean on, shared struggles, given me useful advice and celebrated success, with a lot of laughter along the way. I am glad to call you friends more than colleagues. It is not just about the friends that are with you from the start, but also the ones you make along the way. Thanks to my amazing Chilean buddies: Diego for gifting me with carefree music moments that always improved my mood, and Carolina, for your sweet friendship and for sharing our crazy crochet obsession.

In addition to that, a big thanks to all the people at the observatory, who day by day became part of my everyday life. I hope I brought a bit of positive energy and good company to yours, too.

Thanks to Dragana, Sarah, Angelina, Martin, Philip, Jörg, Volker and all the others. Additional thanks to Volker, with whom I shared a few semesters of teaching for the Radio Lab, and who supported me in handling both the radio telescope and the students.

I have the impression this section is already becoming quite long. I guess this comes with the privilege of meeting a lot of great people along the way. Outside academia, thank you to Seba, Ankit, Hadaba, Sasha, Adri and Caro. It is not easy to feel home when you are living abroad, but you made it possible. Thank you for the time spent exploring Hamburg and everything the city could offer.

A special mention goes to my lifetime friends who, although far from my everyday struggles, have always made me feel their support above all else. Thank you to Vittoria, Claudia, Talisa, Caterina and Margherita. And to my university friends, Elena, Matilde, Silvia. I thank you for rooting for me, listening to me and never failing to make me feel your vicinity. Even if our lives have taken different paths, we always find the time for each other.

Thanks to my parents, for their gentle and discreet presence. With their constant *Buongiorno* and *Buonanotte* messages, never interfering, but always there. Like saying, “We trust you can do this, but just in case, here is your safety net.”

Lastly, a great thanks to Stratos, for your love and endless support. For your patience, when I could not believe in myself. For your curiosity, which taught me to look at the world with new eyes and appreciate the little things. For the simplest moments, like walking along the Alster, sitting on a bench on a sunny day and just enjoying Hamburg at its prime. It would not been the same without you.

6 Bibliography

Abdo, A. A., Ackermann, M., Ajello, M., et al. 2010, ApJ, 708, 1254

Ackermann, M., Ajello, M., Allafort, A., et al. 2010, ApJ Let., 717, L71

Adam, R., Goksu, H., Brown, S., Rudnick, L., & Ferrari, C. 2021, A&A, 648, A60

Ade, P. A. R., Arnold, K., Atlas, M., et al. 2015, Phys. Rev. D, 92, 123509

Ahnen, M. L., Ansoldi, S., Antonelli, L. A., et al. 2016, A&A, 589, A33

Akaike, H. 1974, IEEE Transactions on Automatic Control, 19, 716

Akamatsu, H. & Kawahara, H. 2013, PASJ, 65, 16

Akamatsu, H., van Weeren, R. J., Ogrean, G. A., et al. 2015, A&A, 582, A87

Allen, S. W., Evrard, A. E., & Mantz, A. B. 2011, Ann. Rev. A&A, 49, 409

Alpaslan, M., Driver, S., Robotham, A. S. G., et al. 2015, MNRAS, 451, 3249

Arnaud, M., Pratt, G. W., Piffaretti, R., et al. 2010, A&A, 517, A92

Ascasibar, Y. & Markevitch, M. 2006, ApJ, 650, 102

Baade, W. & Zwicky, F. 1934, Physical Review, 46, 76

Bacchi, M., Feretti, L., Giovannini, G., & Govoni, F. 2003, A&A, 400, 465

Basu, K. 2012, MNRAS, 421, L112

Becker, R. H., White, R. L., & Helfand, D. J. 1994, in Astronomical Society of the Pacific Conference Series, Vol. 61, Astronomical Data Analysis Software and Systems III, ed. D. R. Crabtree, R. J. Hanisch, & J. Barnes, 165

Beduzzi, L., Vazza, F., Cuciti, V., et al. 2024, A&A, 690, A67

Bellomi, E., ZuHone, J. A., Weinberger, R., et al. 2024, ApJ, 974, 234

Beresnyak, A. & Miniati, F. 2016, ApJ, 817, 127

Biava, N., Bonafede, A., Gastaldello, F., et al. 2024, A&A, 686, A82

Biava, N., de Gasperin, F., Bonafede, A., et al. 2021, MNRAS, 508, 3995

Bîrzan, L., McNamara, B. R., Nulsen, P. E. J., Carilli, C. L., & Wise, M. W. 2008, ApJ, 686, 859

Blandford, R. & Eichler, D. 1987, Phys. Rep., 154, 1

Blandford, R. D. & Ostriker, J. P. 1978, ApJ Let., 221, L29

Blumenthal, G. R. & Gould, R. J. 1970, Reviews of Modern Physics, 42, 237

Bonafede, A., Brüggen, M., van Weeren, R., et al. 2012, MNRAS, 426, 40

Bonafede, A., Brunetti, G., Rudnick, L., et al. 2022, arXiv e-prints, arXiv:2203.01958

Bonafede, A., Feretti, L., Giovannini, G., et al. 2009a, A&A, 503, 707

Bonafede, A., Feretti, L., Murgia, M., et al. 2010, A&A, 513, A30

Bonafede, A., Giovannini, G., Feretti, L., Govoni, F., & Murgia, M. 2009b, A&A, 494, 429

Bonafede, A., Intema, H. T., Bruggen, M., et al. 2014, MNRAS, 444, L44

Bond, J. R., Kofman, L., & Pogosyan, D. 1996, Nature, 380, 603

Boselli, A. & Gavazzi, G. 2014, A&A Rev., 22, 74

Böss, L. M., Steinwandel, U. P., & Dolag, K. 2023, ApJ Let., 957, L16

Botteon, A., Brunetti, G., van Weeren, R. J., et al. 2020a, ApJ, 897, 93

Botteon, A., Cassano, R., van Weeren, R. J., et al. 2021a, ApJ Let., 914, L29

Botteon, A., Gastaldello, F., & Brunetti, G. 2018a, MNRAS, 476, 5591

Botteon, A., Giacintucci, S., Gastaldello, F., et al. 2021b, A&A, 649, A37

Botteon, A., Shimwell, T. W., Bonafede, A., et al. 2018b, MNRAS, 478, 885

Botteon, A., Shimwell, T. W., Bonafede, A., et al. 2019, A&A, 622, A19

Botteon, A., Shimwell, T. W., Cassano, R., et al. 2022a, A&A, 660, A78

Botteon, A., van Weeren, R. J., Brunetti, G., et al. 2020b, MNRAS, 499, L11

Botteon, A., van Weeren, R. J., Brunetti, G., et al. 2022b, Science Advances, 8, eabq7623

Boxelaar, J. M., van Weeren, R. J., & Botteon, A. 2021, Astronomy and Computing, 35, 100464

Brienza, M., Godfrey, L., Morganti, R., et al. 2017, A&A, 606, A98

Brienza, M., Rajpurohit, K., Churazov, E., et al. 2025, arXiv e-prints, arXiv:2502.18244

Brienza, M., Shimwell, T. W., de Gasperin, F., et al. 2021, Nature Astronomy, 5, 1261

Brüggen, M. 2013, Astronomische Nachrichten, 334, 543

Brunetti, G., Giacintucci, S., Cassano, R., et al. 2008, Nature, 455, 944

Brunetti, G. & Jones, T. W. 2014, International Journal of Modern Physics D, 23, 1430007

Brunetti, G. & Lazarian, A. 2007, MNRAS, 378, 245

Brunetti, G., Zimmer, S., & Zandanel, F. 2017, MNRAS, 472, 1506

Bruno, L., Botteon, A., Shimwell, T., et al. 2023a, A&A, 678, A133

Bruno, L., Brunetti, G., Botteon, A., et al. 2023b, A&A, 672, A41

Bruno, L., Venturi, T., Dallacasa, D., et al. 2024, A&A, 690, A329

Buote, D. A. 2001, ApJ Let., 553, L15

Burns, J. O. 1998, Science, 280, 400

Burns, J. O., O'Dea, C. P., Gregory, S. A., & Balonek, T. J. 1986, ApJ, 307, 73

Bykov, A. M., Marcowith, A., Amato, E., et al. 2020, SSR, 216, 42

Capetti, A., Massaro, F., & Baldi, R. D. 2017, A&A, 601, A81

Carilli, C. L., Perley, R. A., Dreher, J. W., & Leahy, J. P. 1991, ApJ, 383, 554

Carilli, C. L. & Taylor, G. B. 2002, Ann. Rev. A&A, 40, 319

Carlstrom, J. E., Holder, G. P., & Reese, E. D. 2002, Ann. Rev. A&A, 40, 643

Carretti, E., Brown, S., Staveley-Smith, L., et al. 2013, MNRAS, 430, 1414

Cassano, R. & Brunetti, G. 2005a, MNRAS, 357, 1313

Cassano, R. & Brunetti, G. 2005b, MNRAS, 357, 1313

Cassano, R., Brunetti, G., Norris, R. P., et al. 2012, A&A, 548, A100

Cassano, R., Brunetti, G., & Setti, G. 2006, MNRAS, 369, 1577

Cassano, R., Cuciti, V., Brunetti, G., et al. 2023, A&A, 672, A43

Cassano, R., Ettori, S., Brunetti, G., et al. 2013, ApJ, 777, 141

Cassano, R., Ettori, S., Giacintucci, S., et al. 2010, ApJ Let., 721, L82

Cassano, R., Gitti, M., & Brunetti, G. 2008, A&A, 486, L31

Cavagnolo, K. W., Donahue, M., Voit, G. M., & Sun, M. 2009, ApJ Suppl., 182, 12

Cavaliere, A. & Fusco-Femiano, R. 1976, A&A, 49, 137

Chadayammuri, U., Bogdán, Á., Schellenberger, G., & ZuHone, J. 2024, arXiv e-prints, arXiv:2407.03142

Chandra, P., Ray, A., & Bhatnagar, S. 2004, ApJ Let., 604, L97

Chandrasekhar, S. 1961, Hydrodynamic and hydromagnetic stability

Churazov, E., Forman, W., Jones, C., & Böhringer, H. 2003, ApJ, 590, 225

Churazov, E., Khabibullin, I., Lyskova, N., Sunyaev, R., & Bykov, A. M. 2021, A&A, 651, A41

Clarke, T. E., Randall, S. W., Sarazin, C. L., Blanton, E. L., & Giacintucci, S. 2013, ApJ, 772, 84

Cohen, A. S. & Clarke, T. E. 2011, AJ, 141, 149

Colafrancesco, S. & Blasi, P. 1998, Astroparticle Physics, 9, 227

Condon, J. J., Cotton, W. D., Greisen, E. W., et al. 1998, AJ, 115, 1693

Croston, J. H., Hardcastle, M. J., Mingo, B., et al. 2019, A&A, 622, A10

Cuciti, V., Brunetti, G., van Weeren, R., et al. 2018, A&A, 609, A61

Cuciti, V., Cassano, R., Brunetti, G., et al. 2021, A&A, 647, A51

Cuciti, V., Cassano, R., Brunetti, G., et al. 2015, A&A, 580, A97

Cuciti, V., Cassano, R., Sereno, M., et al. 2023, A&A, 680, A30

Cuciti, V., de Gasperin, F., Brüggen, M., et al. 2022, Nature, 609, 911

Cutri, R. M., Skrutskie, M. F., van Dyk, S., et al. 2003, 2MASS All Sky Catalog of point sources.

Dallacasa, D., Brunetti, G., Giacintucci, S., et al. 2009, ApJ, 699, 1288

Dawson, W. A., Jee, M. J., Stroe, A., et al. 2015, ApJ, 805, 143

de Gasperin, F. 2017, MNRAS, 467, 2234

de Gasperin, F., Brunetti, G., Brüggen, M., et al. 2020a, A&A, 642, A85

de Gasperin, F., Dijkema, T. J., Drabent, A., et al. 2019, A&A, 622, A5

de Gasperin, F., Edler, H. W., Williams, W. L., et al. 2023, arXiv e-prints, arXiv:2301.12724

de Gasperin, F., Intema, H. T., Shimwell, T. W., et al. 2017, Science Advances, 3, e1701634 de Gasperin, F., Intema, H. T., van Weeren, R. J., et al. 2015a, MNRAS, 453, 3483

de Gasperin, F., Lazio, T. J. W., & Knapp, M. 2020b, A&A, 644, A157

de Gasperin, F., Ogrean, G. A., van Weeren, R. J., et al. 2015b, MNRAS, 448, 2197

de Gasperin, F., Rudnick, L., Finoguenov, A., et al. 2022, A&A, 659, A146

de Gasperin, F., Vink, J., McKean, J. P., et al. 2020c, A&A, 635, A150

de Gasperin, F., Williams, W. L., Best, P., et al. 2021, A&A, 648, A104

de Jong, J. M. G. H. J., van Weeren, R. J., Sweijen, F., et al. 2024, A&A, 689, A80

De Luca & Molendi. 2004, A&A, 419, 837

Di Gennaro, G., van Weeren, R. J., Cassano, R., et al. 2021a, A&A, 654, A166

Di Gennaro, G., van Weeren, R. J., Hoeft, M., et al. 2018, ApJ, 865, 24

Di Gennaro, G., van Weeren, R. J., Rudnick, L., et al. 2021b, ApJ, 911, 3

Di Gennaro, G., van Weeren, R. J., Rudnick, L., et al. 2021c, ApJ, 911, 3

Dominguez-Fernandez, P., Bruggen, M., Vazza, F., et al. 2021, MNRAS, 500, 795

Domínguez-Fernández, P., Brüggen, M., Vazza, F., et al. 2021, MNRAS, 507, 2714

Domínguez-Fernández, P., Ryu, D., & Kang, H. 2024, A&A, 685, A68

Donnert, J., Vazza, F., Brüggen, M., & ZuHone, J. 2018, SSR, 214, 122

Donnert, J. M. F., Stroe, A., Brunetti, G., Hoang, D., & Roettgering, H. 2016, MNRAS, 462, 2014

Douglass, E. M., Blanton, E. L., Randall, S. W., et al. 2018, ApJ, 868, 121

Dressler, A. 1980, ApJ, 236, 351

Drury, L. O. 1983, Reports on Progress in Physics, 46, 973

Duchesne, S. W., Johnston-Hollitt, M., & Bartalucci, I. 2021, PASA, 38, e053

Duchesne, S. W., Johnston-Hollitt, M., Riseley, C. J., Bartalucci, I., & Keel, S. R. 2022, MNRAS, 511, 3525

Eckert, D., Finoguenov, A., Ghirardini, V., et al. 2020, The Open Journal of Astrophysics, 3, 12

Edler, H. W., de Gasperin, F., Brunetti, G., et al. 2022, A&A, 666, A3

Ensslin, T. A., Biermann, P. L., Klein, U., & Kohle, S. 1998, A&A, 332, 395

Ensslin, T. A., Biermann, P. L., Kronberg, P. P., & Wu, X.-P. 1997, ApJ, 477, 560

Ensslin, T. A. & Brüggen, M. 2001, in Clusters of Galaxies and the High Redshift Universe Observed in X-rays, ed. D. M. Neumann & J. T. V. Tran, 58

Enßlin, T. A. & Brüggen, M. 2002, MNRAS, 331, 1011

Enßlin, T. A. & Gopal-Krishna. 2001, A&A, 366, 26

Enßlin, T. A. & Vogt, C. 2003, A&A, 401, 835

Fabian, A. C. 1994, Ann. Rev. A&A, 32, 277

Fanaroff, B. L. & Riley, J. M. 1974, MNRAS, 167, 31P

Feretti, L. & Giovannini, G. 2008, in A Pan-Chromatic View of Clusters of Galaxies and the Large-Scale Structure, ed. M. Plionis, O. López-Cruz, & D. Hughes, Vol. 740, 24

Feretti, L., Giovannini, G., Klein, U., et al. 1998, A&A, 331, 475

Fermi, E. 1949, Physical Review, 75, 1169

Finner, K., Jee, M. J., Cho, H., et al. 2025, ApJ Suppl., 277, 28

Finoguenov, A., Sarazin, C. L., Nakazawa, K., Wik, D. R., & Clarke, T. E. 2010, ApJ, 715, 1143

Forman, W. & Jones, C. 1982, Ann. Rev. A&A, 20, 547

Fusco-Femiano, R. 2004, Astrophysics and Space Science, 294, 37

Fusco-Femiano, R., Dal Fiume, D., Feretti, L., et al. 1999, ApJ Let., 513, L21

Garon, A. F., Rudnick, L., Wong, O. I., et al. 2019, AJ, 157, 126

Gendron-Marsolais, M., Hlavacek-Larrondo, J., van Weeren, R. J., et al. 2017, MNRAS, 469, 3872

Gendron-Marsolais, M. L., Hull, C. L. H., Perley, R., et al. 2021, ApJ, 911, 56

Ghirardini, V., Eckert, D., Ettori, S., et al. 2019, A&A, 621, A41

Ghizzardi, S., Rossetti, M., & Molendi, S. 2010, A&A, 516, A32

Giacintucci, S., Markevitch, M., Cassano, R., et al. 2017, ApJ, 841, 71

Giacintucci, S., Venturi, T., Markevitch, M., et al. 2022, ApJ, 934, 49

Giacintucci, S., Venturi, T., Murgia, M., et al. 2007, A&A, 476, 99

Gitti, M., Brighenti, F., & McNamara, B. R. 2012, Advances in Astronomy, 2012, 950641

Gitti, M., Brunetti, G., Cassano, R., & Ettori, S. 2018, A&A, 617, A11

Gitti, M., Brunetti, G., Feretti, L., & Setti, G. 2004, A&A, 417, 1

Golovich, N., Dawson, W. A., Wittman, D. M., et al. 2019, ApJ Suppl., 240, 39

Gómez, P. L. & Calderón, D. 2020, AJ, 160, 152

Gopal-Krishna, Patra, D., & Joshi, R. 2024, arXiv e-prints, arXiv:2403.11290

Govoni, F., Murgia, M., Feretti, L., et al. 2005, A&A, 430, L5

Govoni, F., Murgia, M., Xu, H., et al. 2013, A&A, 554, A102

Greisen, K. 1966, Phys. Rev. Let., 16, 748

Groeneveld, C., van Weeren, R. J., Botteon, A., et al. 2025a, A&A, 693, A99

Groeneveld, C., van Weeren, R. J., Botteon, A., et al. 2025b, A&A, 693, A99

Groeneveld, C., van Weeren, R. J., Miley, G. K., et al. 2022, A&A, 658, A9

Gunn, J. E. & Gott, III, J. R. 1972, ApJ, 176, 1

Ha, J.-H., Ryu, D., & Kang, H. 2018, ApJ, 857, 26

Hardcastle, M. J. 2013, MNRAS, 433, 3364

Hardcastle, M. J., Birkinshaw, M., & Worrall, D. M. 1998, MNRAS, 294, 615

Hardcastle, M. J. & Croston, J. H. 2020, NARev, 88, 101539

Hardcastle, M. J., Shimwell, T. W., Tasse, C., et al. 2021, A&A, 648, A10

Harwood, J. J., Hardcastle, M. J., Croston, J. H., & Goodger, J. L. 2013, MNRAS, 435, 3353

Harwood, J. J., Mooney, S., Morabito, L. K., et al. 2022, A&A, 658, A8

Hewish, A., Bell, S. J., Pilkington, J. D. H., Scott, P. F., & Collins, R. A. 1968, Nature, 217, 709

Hill, G. J. & Lilly, S. J. 1991, ApJ, 367, 1

Hill, J. M. & Longair, M. S. 1971, MNRAS, 154, 125

Hlavacek-Larrondo, J., Li, Y., & Churazov, E. 2022, in Handbook of X-ray and Gamma-ray Astrophysics, ed. C. Bambi & A. Sangangelo, 5

Hoang, D. N., Brüggen, M., Botteon, A., et al. 2022, A&A, 665, A60

Hoang, D. N., Shimwell, T. W., Stroe, A., et al. 2017, MNRAS, 471, 1107

Hoang, D. N., Shimwell, T. W., van Weeren, R. J., et al. 2018, MNRAS, 478, 2218

Hoeft, M. & Brüggen, M. 2007, MNRAS, 375, 77

Hudson, D. S., Mittal, R., Reiprich, T. H., et al. 2010, A&A, 513, A37

HyeongHan, K., Cho, H., Jee, M. J., et al. 2024, ApJ, 962, 100

HyeongHan, K., Jee, M. J., Rudnick, L., et al. 2020, ApJ, 900, 127

Ignesti, A., Brunetti, G., Shimwell, T., et al. 2022, A&A, 659, A20

Inchingolo, G., Wittor, D., Rajpurohit, K., & Vazza, F. 2022, MNRAS, 509, 1160

Intema, H. T., Jagannathan, P., Mooley, K. P., & Frail, D. A. 2017, A&A, 598, A78

Jacob, S. & Pfrommer, C. 2017, MNRAS, 467, 1478

Jaffe, W. J. & Perola, G. C. 1973, A&A, 26, 423

Jansky, K. G. 1933, Nature, 132, 66

Jee, M. J., Stroe, A., Dawson, W., et al. 2015, ApJ, 802, 46

Jones, A., de Gasperin, F., Cuciti, V., et al. 2023a, A&A, 680, A31

Jones, A., de Gasperin, F., Cuciti, V., et al. 2023b, A&A, 680, A31

Jones, T. W., Nolting, C., O'Neill, B. J., & Mendygral, P. J. 2017, Physics of Plasmas, 24, 041402

Kale, R. & Dwarakanath, K. S. 2010, ApJ, 718, 939

Kale, R., Dwarakanath, K. S., Bagchi, J., & Paul, S. 2012, MNRAS, 426, 1204

Kale, R., Shende, K. M., & Parekh, V. 2019, MNRAS, 486, L80

Kale, R., Venturi, T., Giacintucci, S., et al. 2015, A&A, 579, A92

Kang, H. 2016, Journal of Korean Astronomical Society, 49, 145

Kang, H. 2021, arXiv e-prints, arXiv:2108.01876

Kang, H. & Ryu, D. 2011, ApJ, 734, 18

Kardashev, N. S. 1962, SOVAST, 6, 317

Katz-Stone, D. M., Rudnick, L., & Anderson, M. C. 1993, ApJ, 407, 549

Kempner, J. C., Blanton, E. L., Clarke, T. E., et al. 2004, in The Riddle of Cooling Flows in Galaxies and Clusters of galaxies, ed. T. Reiprich, J. Kempner, & N. Soker, 335

Kierdorf, M., Beck, R., Hoeft, M., et al. 2017, A&A, 600, A18

Klamer, I., Subrahmanyan, R., & Hunstead, R. W. 2004, MNRAS, 351, 101

Kocevski, D. D., Ebeling, H., Mullis, C. R., & Tully, R. B. 2007, ApJ, 662, 224

Koester, B. P., McKay, T. A., Annis, J., et al. 2007, ApJ, 660, 239

Koribalski, B. S., Duchesne, S. W., Lenc, E., et al. 2024, MNRAS, 533, 608

Kotera, K. & Olinto, A. V. 2011, Ann. Rev. A&A, 49, 119

Kraichnan, R. H. & Nagarajan, S. 1967, Physics of Fluids, 10, 859

Kravtsov, A. V. & Borgani, S. 2012, Ann. Rev. A&A, 50, 353

Kundu, S., Vaidya, B., & Mignone, A. 2021, ApJ, 921, 74

Kuntz & Snowden. 2008, A&A, 478, 575

Laing, R. A., Bridle, A. H., Parma, P., et al. 2008a, MNRAS, 386, 657

Laing, R. A., Bridle, A. H., Parma, P., & Murgia, M. 2008b, MNRAS, 391, 521

Lal, D. V. 2020, AJ, 160, 161

Lane, W. M., Cotton, W. D., van Velzen, S., et al. 2014, MNRAS, 440, 327

Large, M. I., Mathewson, D. S., & Haslam, C. G. T. 1959, Nature, 183, 1663

Lau, E. T., Kravtsov, A. V., & Nagai, D. 2009, ApJ, 705, 1129

Leahy, D. A. & Roger, R. S. 1998, ApJ, 505, 784

Leccardi, A. & Molendi, S. 2008, A&A, 486, 359

Leccardi, A., Rossetti, M., & Molendi, S. 2010, A&A, 510, A82

Ledlow, M. J. & Owen, F. N. 1996, AJ, 112, 9

Lee, W., Pillepich, A., ZuHone, J., et al. 2024, A&A, 686, A55

Lehle, K., Nelson, D., Pillepich, A., Truong, N., & Rohr, E. 2024, A&A, 687, A129

Lenok, V. 2022, Phd thesis, Karlsruher Institut für Technologie (KIT)

Lindner, R. R., Baker, A. J., Hughes, J. P., et al. 2014, ApJ, 786, 49

Locatelli, N. T., Rajpurohit, K., Vazza, F., et al. 2020, MNRAS, 496, L48

Loi, F., Murgia, M., Govoni, F., et al. 2017, MNRAS, 472, 3605

Loi, F., Murgia, M., Vacca, V., et al. 2020, MNRAS, 498, 1628

Longair, M. S. 2011, High Energy Astrophysics

Lovisari, L., Forman, W. R., Jones, C., et al. 2017, ApJ, 846, 51

Lovisari, L. & Reiprich, T. H. 2019, MNRAS, 483, 540

Lusetti, G., Bonafede, A., Lovisari, L., et al. 2024, A&A, 683, A132

Lyutikov, M. 2006, MNRAS, 373, 73

Ma, C.-J., Ebeling, H., & Barrett, E. 2009, ApJ Let., 693, L56

Maguire, C. A., Carley, E. P., Zucca, P., Vilmer, N., & Gallagher, P. T. 2021, ApJ, 909, 2

Mahatma, V. H., Hardcastle, M. J., Williams, W. L., et al. 2018, MNRAS, 475, 4557

Mandal, S., Intema, H. T., Shimwell, T. W., et al. 2019, A&A, 622, A22

Mandal, S., Intema, H. T., van Weeren, R. J., et al. 2020, A&A, 634, A4

Mao, M. Y., Sharp, R., Saikia, D. J., et al. 2010, MNRAS, 406, 2578

Markevitch, M. 2006, in ESA Special Publication, Vol. 604, The X-ray Universe 2005, ed. A. Wilson, 723

Markevitch, M. 2010, arXiv e-prints, arXiv:1010.3660

Markevitch, M. 2012, in Twelfth Marcel Grossmann Meeting on General Relativity, ed. A. H. Chamseddine, 397–410

Markevitch, M., Gonzalez, A. H., David, L., et al. 2002, ApJ Let., 567, L27

Markevitch, M., Govoni, F., Brunetti, G., & Jerius, D. 2005, ApJ, 627, 733

Markevitch, M. & Vikhlinin, A. 2001, ApJ, 563, 95

Markevitch, M. & Vikhlinin, A. 2007, Phys. Rep., 443, 1

Markevitch, M., Vikhlinin, A., Mazzotta, P., & VanSpeybroeck, L. 2000, arXiv e-prints, astro

Massey, F. J. J. 1951, Journal of the American Statistical Association, 46, 68

Mather, J. C., Cheng, E. S., Cottingham, D. A., et al. 1994, ApJ, 420, 439

Mather, J. C., Cheng, E. S., Eplee, Jr., R. E., et al. 1990, ApJ Let., 354, L37

McMullin, J. P., Waters, B., Schiebel, D., Young, W., & Golap, K. 2007, in Astronomical Society of the Pacific Conference Series, Vol. 376, Astronomical Data Analysis Software and Systems XVI, ed. R. A. Shaw, F. Hill, & D. J. Bell, 127

McNamara, B. R. & Nulsen, P. E. J. 2007, Ann. Rev. A&A, 45, 117

Migkas, K., Schellenberger, G., Reiprich, T. H., et al. 2020, A&A, 636, A15

Mignone, A., Massaglia, S., & Bodo, G. 2004, Astrophysics and Space Science, 293, 199

Miley, G. 1980, Ann. Rev. A&A, 18, 165

Miley, G. K. 1973, A&A, 26, 413

Mingo, B., Croston, J. H., Hardcastle, M. J., et al. 2019, MNRAS, 488, 2701

Mohan, N. & Rafferty, D. 2015, PyBDSF: Python Blob Detection and Source Finder, Astrophysics Source Code Library, record ascl:1502.007

Mohr, J. J., Evrard, A. E., Fabricant, D. G., & Geller, M. J. 1995, ApJ, 447, 8

Molendi, S. & Pizzolato, F. 2001, ApJ, 560, 194

Morabito, L. K., Deller, A. T., Röttgering, H., et al. 2016, MNRAS, 461, 2676

Morabito, L. K., Jackson, N., de Jong, J., et al. 2025, Astrophysics and Space Science, 370, 19

Morabito, L. K., Jackson, N. J., Mooney, S., et al. 2022, A&A, 658, A1

Morganti, R., Jurlin, N., Oosterloo, T., et al. 2021, Galaxies, 9, 88

Mroczkowski, T., Nagai, D., Basu, K., et al. 2019, SSR, 215, 17

Mukherjee, D., Bodo, G., Rossi, P., Mignone, A., & Vaidya, B. 2021, MNRAS, 505, 2267

Müller, A., Pfrommer, C., Ignesti, A., et al. 2021, MNRAS, 508, 5326

Murgia, M., Eckert, D., Govoni, F., et al. 2010, A&A, 514, A76

Murgia, M., Govoni, F., Feretti, L., et al. 2004, A&A, 424, 429

Murgia, M., Govoni, F., Markevitch, M., et al. 2009, A&A, 499, 679

Murgia, M., Govoni, F., Vacca, V., et al. 2024, MNRAS, 528, 6470

Nair, D. G., Morganti, R., Brienza, M., et al. 2024, A&A, 691, A287

Nasa High Energy Astrophysics Science Archive Research Center (Heasarc). 2014, HEAsoft: Unified Release of FTOOLS and XANADU, Astrophysics Source Code Library, record ascl:1408.004

Neronov, A. & Vovk, I. 2010, Science, 328, 73

Nolting, C., Jones, T. W., O'Neill, B. J., & Mendygral, P. J. 2019a, ApJ, 876, 154

Nolting, C., Jones, T. W., O'Neill, B. J., & Mendygral, P. J. 2019b, ApJ, 885, 80

Norris, R. P. 2017, Nature Astronomy, 1, 671

Nulsen, P. E. J., McNamara, B. R., Wise, M. W., & David, L. P. 2005, ApJ, 628, 629

O'Dea, C. P. & Owen, F. N. 1985, AJ, 90, 927

O'Donoghue, A. A., Eilek, J. A., & Owen, F. N. 1993, ApJ, 408, 428

Oegerle, W. R. & Hill, J. M. 2001, AJ, 122, 2858

Offringa, A. R., McKinley, B., Hurley-Walker, N., et al. 2014, MNRAS, 444, 606

Offringa, A. R. & Smirnov, O. 2017, MNRAS, 471, 301

Ogrean, G. A., Brüggen, M., Röttgering, H., et al. 2013, MNRAS, 429, 2617

Ogrean, G. A., Brüggen, M., van Weeren, R., et al. 2014, MNRAS, 440, 3416

Ohmura, T., Asano, K., Nishiwaki, K., Machida, M., & Sakemi, H. 2023, arXiv e-prints, arXiv:2305.04795

O'Neill, B. J., Jones, T. W., Nolting, C., & Mendygral, P. J. 2019a, ApJ, 884, 12

O'Neill, B. J., Jones, T. W., Nolting, C., & Mendygral, P. J. 2019b, ApJ, 887, 26

Osinga, E., van Weeren, R. J., Brunetti, G., et al. 2024, A&A, 688, A175

O'Sullivan, S. P., Brüggen, M., Van Eck, C. L., et al. 2018, Galaxies, 6, 126

Owen, E. R., Wu, K., Inoue, Y., Yang, H. Y. K., & Mitchell, A. M. W. 2023, Galaxies, 11, 86

Owen, F. N. & Rudnick, L. 1976, ApJ Let., 205, L1

Pacaud, F., Pierre, M., Refregier, A., et al. 2006, Monthly Notices of the Royal Astronomical Society, 372, 578–590

Pacholczyk, A. G. 1970, Radio astrophysics. Nonthermal processes in galactic and extragalactic sources

Pal, S. & Kumari, S. 2023a, Journal of Astrophysics and Astronomy, 44, 17

Pal, S. & Kumari, S. 2023b, Journal of Astrophysics and Astronomy, 44, 17

Pâris, I., Petitjean, P., Aubourg, É., et al. 2014, A&A, 563, A54

Parma, P., Murgia, M., Morganti, R., et al. 1999, A&A, 344, 7

Pasini, T., Edler, H. W., Brüggen, M., et al. 2022, A&A, 663, A105

Pearce, C. J. J., van Weeren, R. J., Andrade-Santos, F., et al. 2017, ApJ, 845, 81

Penzias, A. A. & Wilson, R. W. 1965, ApJ, 142, 419

Perley, R. A. & Butler, B. J. 2013, ApJ Suppl., 204, 19

Petrosian, V. & East, W. E. 2008, ApJ, 682, 175

Pfrommer, C. & Enßlin, T. A. 2004, A&A, 413, 17

Pfrommer, C. & Jones, T. W. 2011, ApJ, 730, 22

Pinzke, A., Oh, S. P., & Pfrommer, C. 2013, MNRAS, 435, 1061

Piras, S., Horellou, C., Conway, J. E., et al. 2024, A&A, 687, A267

Pizzo, R. F., de Bruyn, A. G., Bernardi, G., & Brentjens, M. A. 2011, A&A, 525, A104

Planck Collaboration, Ade, P. A. R., Aghanim, N., et al. 2014, A&A, 571, A29

Planck Collaboration, Ade, P. A. R., Aghanim, N., et al. 2016a, A&A, 594, A27

Planck Collaboration, Ade, P. A. R., Aghanim, N., et al. 2016b, A&A, 594, A13

Poole, G. B., Fardal, M. A., Babul, A., et al. 2006, MNRAS, 373, 881

Pratt, G. W., Arnaud, M., Piffaretti, R., et al. 2010, A&A, 511, A85

Pyrzas, S., Steenbrugge, K. C., & Blundell, K. M. 2015, A&A, 574, A30

Quintana, H. & Lawrie, D. G. 1982, AJ, 87, 1

Rahaman, M., Raja, R., Datta, A., Burns, J. O., & Rapetti, D. 2022, MNRAS, 515, 2245

Raja, R., Rahaman, M., Datta, A., et al. 2020, MNRAS, 493, L28

Raja, R., Rahaman, M., Datta, A., & Smirnov, O. M. 2024a, ApJ, 975, 125

Raja, R., Smirnov, O. M., Venturi, T., Rahaman, M., & Yang, H. Y. K. 2024b, ApJ, 977, 83

Rajpurohit, K., Lovisari, L., Botteon, A., et al. 2024, ApJ, 966, 38

Rajpurohit, K., van Weeren, R. J., Hoeft, M., et al. 2022, ApJ, 927, 80

Rajpurohit, K., Vazza, F., Hoeft, M., et al. 2020, A&A, 642, L13

Ramos-Ceja, Pacaud, F., Reiprich, T. H., et al. 2019, A&A, 626, A48

Rickel, M., Moravec, E., Gordon, Y. A., et al. 2025, arXiv e-prints, arXiv:2502.04198

Riley, J. M. & Branson, N. J. B. A. 1973, MNRAS, 164, 271

Riseley, C. J., Bonnassieux, E., Vernstrom, T., et al. 2022a, MNRAS, 515, 1871

Riseley, C. J., Rajpurohit, K., Loi, F., et al. 2022b, MNRAS, 512, 4210

Rodman, P. E., Turner, R. J., Shabala, S. S., et al. 2019, MNRAS, 482, 5625

Roettiger, K., Burns, J. O., & Stone, J. M. 1999, ApJ, 518, 603

Rossetti, M., Gastaldello, F., Eckert, D., et al. 2017, MNRAS, 468, 1917

Rudnick, L., Brüggen, M., Brunetti, G., et al. 2022, ApJ, 935, 168

Ruszkowski, M., Lee, D., Brüggen, M., Parrish, I., & Oh, S. P. 2011, ApJ, 740, 81

Ruszkowski, M. & Pfrommer, C. 2023, A&A Rev., 31, 4

Ryle, M. & Hewish, A. 1960, MNRAS, 120, 220

Ryle, M. & Windram, M. D. 1968, MNRAS, 138, 1

Ryu, D., Kang, H., & Ha, J.-H. 2019, ApJ, 883, 60

Sanders, J., Walker, S., ZuHone, J., & Bellomi, E. 2018, Chandra News, 25, 1

Sanders, J. S., Biffi, V., Brüggen, M., et al. 2022, A&A, 661, A36

Sanders, J. S., Dennerl, K., Russell, H. R., et al. 2020, A&A, 633, A42

Sanders, J. S., Fabian, A. C., Russell, H. R., Walker, S. A., & Blundell, K. M. 2016a, MNRAS, 460, 1898

Sanders, J. S., Fabian, A. C., Taylor, G. B., et al. 2016b, MNRAS, 457, 82

Santos, J. S., Rosati, P., Tozzi, P., et al. 2008, A&A, 483, 35

Sarazin, C. L. 1988, X-ray emission from clusters of galaxies

Savini, F., Bonafede, A., Brüggen, M., et al. 2019, A&A, 622, A24

Savini, F., Bonafede, A., Brüggen, M., et al. 2018, MNRAS, 478, 2234

Schellenberger, G., Giacintucci, S., Lovisari, L., et al. 2022, ApJ, 925, 91

Schwarz, G. 1978, Annals of Statistics, 6, 461

Sebastian, B., Lal, D. V., & Pramesh Rao, A. 2017, AJ, 154, 169

Shimwell, T. W., Hardcastle, M. J., Tasse, C., et al. 2022, A&A, 659, A1

Shimwell, T. W., Luckin, J., Brüggen, M., et al. 2016, MNRAS, 459, 277

Shimwell, T. W., Röttgering, H. J. A., Best, P. N., et al. 2017, A&A, 598, A104

Shimwell, T. W., Tasse, C., Hardcastle, M. J., et al. 2019, A&A, 622, A1

Shulevski, A., Brienza, M., Massaro, F., et al. 2024, A&A, 682, A171

Sijbring, D. & de Bruyn, A. G. 1998, A&A, 331, 901

Simionescu, A., Werner, N., Urban, O., et al. 2012, ApJ, 757, 182

Slee, O. B., Roy, A. L., Murgia, M., Andernach, H., & Ehle, M. 2001, AJ, 122, 1172

Smirnov, O. M. & Tasse, C. 2015, MNRAS, 449, 2668

Sommer, M. W., Basu, K., Intema, H., et al. 2017, MNRAS, 466, 996

Springel, V., Frenk, C. S., & White, S. D. M. 2006, Nature, 440, 1137

Srivastava, S. & Singal, A. K. 2020, MNRAS, 493, 3811

Stroe, A., Harwood, J. J., Hardcastle, M. J., & Röttgering, H. J. A. 2014a, MNRAS, 445, 1213

Stroe, A., Rumsey, C., Harwood, J. J., et al. 2014b, MNRAS, 441, L41

Stroe, A., Shimwell, T., Rumsey, C., et al. 2016, MNRAS, 455, 2402

Stroe, A., van Weeren, R. J., Intema, H. T., et al. 2013a, A&A, 555, A110

Stroe, A., van Weeren, R. J., Intema, H. T., et al. 2013b, A&A, 555, A110

Stroe, A., van Weeren, R. J., Intema, H. T., et al. 2013c, A&A, 555, A110

Stuardi, C., Bonafede, A., Lovisari, L., et al. 2021, MNRAS, 502, 2518

Stuardi, C., O'Sullivan, S. P., Bonafede, A., et al. 2020, A&A, 638, A48

Subramanian, K. 2016, Reports on Progress in Physics, 79, 076901

Sunyaev, R. A. & Zeldovich, Y. B. 1972, Comments on Astrophysics and Space Physics, 4, 173

Sweijen, F., van Weeren, R. J., Röttgering, H. J. A., et al. 2022, Nature Astronomy, 6, 350

Tasse, C., Hugo, B., Mirmont, M., et al. 2018, A&A, 611, A87

Tasse, C., Shimwell, T., Hardcastle, M. J., et al. 2021, A&A, 648, A1

Timmerman, R., van Weeren, R. J., Callingham, J. R., et al. 2022, A&A, 658, A5

Tiwari, J. & Singh, K. P. 2022, MNRAS, 509, 3321

Tribble, P. C. 1993, MNRAS, 261, 57

Van der Tol, S. 2009, PhD thesis, Technical University of Delft, Netherlands

van Haarlem, M. P., Wise, M. W., Gunst, A. W., et al. 2013a, A&A, 556, A2

van Haarlem, M. P., Wise, M. W., Gunst, A. W., et al. 2013b, A&A, 556, A2

van Weeren, R. J., Andrade-Santos, F., Dawson, W. A., et al. 2017, Nature Astronomy, 1, 0005

van Weeren, R. J., Bonafede, A., Ebeling, H., et al. 2012, MNRAS, 425, L36

van Weeren, R. J., Brüggen, M., Röttgering, H. J. A., & Hoeft, M. 2011a, Journal of Astrophysics and Astronomy, 32, 505

van Weeren, R. J., Brüggen, M., Röttgering, H. J. A., et al. 2011b, A&A, 533, A35

van Weeren, R. J., Brunetti, G., Brüggen, M., et al. 2016, ApJ, 818, 204

van Weeren, R. J., de Gasperin, F., Akamatsu, H., et al. 2019, SSR, 215, 16

van Weeren, R. J., Hoeft, M., Röttgering, H. J. A., et al. 2011c, A&A, 528, A38

van Weeren, R. J., Intema, H. T., Röttgering, H. J. A., Brüggen, M., & Hoeft, M. 2011d, Mem. Soc. Astron. Ital., 82, 569

van Weeren, R. J., Röttgering, H. J. A., & Brüggen, M. 2011e, A&A, 527, A114

van Weeren, R. J., Röttgering, H. J. A., Brüggen, M., & Cohen, A. 2009a, A&A, 508, 75

van Weeren, R. J., Röttgering, H. J. A., Brüggen, M., & Cohen, A. 2009b, A&A, 508, 75

van Weeren, R. J., Röttgering, H. J. A., Brüggen, M., & Hoeft, M. 2010, Science, 330, 347

van Weeren, R. J., Shimwell, T. W., Botteon, A., et al. 2021, A&A, 651, A115

van Weeren, R. J., Timmerman, R., Vaidya, V., et al. 2024, A&A, 692, A12

Vardoulaki, E., Backöfer, V., Finoguenov, A., et al. 2025, A&A, 695, A178

Varenius, E., Conway, J. E., Martí-Vidal, I., et al. 2016, A&A, 593, A86

Varenius, E., Conway, J. E., Martí-Vidal, I., et al. 2015, A&A, 574, A114

Vazza, F. & Botteon, A. 2024, Galaxies, 12, 19

Vazza, F., Brüggen, M., Gheller, C., et al. 2017, Classical and Quantum Gravity, 34, 234001

Vazza, F., Brüggen, M., Wittor, D., et al. 2016, MNRAS, 459, 70

Vazza, F., Brunetti, G., Brüggen, M., & Bonafede, A. 2018, MNRAS, 474, 1672

Veilleux, S., Maiolino, R., Bolatto, A. D., & Aalto, S. 2020, A&A Rev., 28, 2

Venkatesan, T. C. A., Batuski, D. J., Hanisch, R. J., & Burns, J. O. 1994, ApJ, 436, 67

Venturi, T., Giacintucci, S., Brunetti, G., et al. 2007, A&A, 463, 937

Venturi, T., Rossetti, M., Brunetti, G., et al. 2017, A&A, 603, A125

Veronica, A., Su, Y., Biffi, V., et al. 2022, Astronomy & Astrophysics, 661, A46

Vikhlinin, A., Markevitch, M., & Murray, S. S. 2001, ApJ, 551, 160

Vikhlinin, A. A. & Markevitch, M. L. 2002, Astronomy Letters, 28, 495

Voit, G. M. 2005, Reviews of Modern Physics, 77, 207

Völk, H. J. & Atoyan, A. M. 2000, ApJ, 541, 88

Werner, N., Durret, F., Ohashi, T., Schindler, S., & Wiersma, R. P. C. 2008, SSR, 134, 337

Whittingham, J., Pfrommer, C., Werhahn, M., Jlassi, L., & Girichidis, P. 2024, arXiv e-prints, arXiv:2411.11947

Whyley, A., Randall, S. W., Clarke, T. E., et al. 2024, arXiv e-prints, arXiv:2402.04876

Wik, D. R., Sarazin, C. L., Finoguenov, A., et al. 2009, ApJ, 696, 1700

Wilber, A., Brüggen, M., Bonafede, A., et al. 2019, A&A, 622, A25

Wilber, A., Brüggen, M., Bonafede, A., et al. 2018, MNRAS, 473, 3536

Wittor, D. 2023, Universe, 9, 319

Wittor, D., Brüggen, M., Grete, P., & Rajpurohit, K. 2023, MNRAS, 523, 701

Wittor, D., Ettori, S., Vazza, F., et al. 2021, MNRAS, 506, 396

Wittor, D., Hoeft, M., Vazza, F., Brüggen, M., & Domínguez-Fernández, P. 2019a, MNRAS, 490, 3987

Wittor, D., Hoeft, M., Vazza, F., Brüggen, M., & Domínguez-Fernández, P. 2019b, MNRAS, 490, 3987

Wittor, D., Vazza, F., & Brüggen, M. 2016, Galaxies, 4, 71

Xu, H., Li, H., Collins, D. C., Li, S., & Norman, M. L. 2011, ApJ, 739, 77

Zaroubi, S., de Bruyn, A. G., Harker, G., et al. 2012, MNRAS, 425, 2964

Zhang, C., Zhuravleva, I., Kravtsov, A., & Churazov, E. 2021, MNRAS, 506, 839

Zhang, X., Simionescu, A., Gastaldello, F., et al. 2023, A&A, 672, A42

Zhou, R., Newman, J. A., Mao, Y.-Y., et al. 2021, MNRAS, 501, 3309

Zhou, Y., Xu, H., Zhu, Z., et al. 2022, MNRAS, 517, 1299

Zucca, P., Morosan, D. E., Rouillard, A. P., et al. 2018, A&A, 615, A89

ZuHone, J. A., Markevitch, M., Ruszkowski, M., & Lee, D. 2013, ApJ, 762, 69